Two Dimensional Hybrid Simulations of Small Scale Obstacles in the Solar Wind

by

Matthew William Hopcroft

Thesis

Submitted to the University of Warwick

for the degree of

Doctor of Philosophy

Department of Physics

March 2001

Contents

List of Figures

Acknowledgments

Firstly, I would like to thank Professor Sandra C. Chapman for her continual support throughout the last $3\frac{1}{2}$ years, in particular for convincing me things weren't as bad as they seemed time and again. Thanks also to the rest of the research group for creating such a good atmosphere during my stay, and to Chris and Andy for rescuing me from the dark side of IT, when necessary.

The work in this thesis was funded by EPSRC and utilized facilities funded by PPARC.

This thesis could not have been produced without the support of my parents — thanks especially for the use of your cars! Thanks to Anne-Marie for always being there to cheer me up and chill me out.

Finally, thanks to all those I've met at Anchor House, and my old friends at RaW. Good luck for the future to you all.

Declaration

I hereby declare that this thesis is my own work, except where explicitly stated, and that it has not been submitted for a degree at the University of Warwick, or any other University.

M. Hopcroft

March, 2001.

Abstract

The structure and dynamics of the solar wind interaction with two small scale obstacles (of the order of a pickup ion gyroradius) is examined. These are a comet, comparable to Grigg-Skjellerup, and a weakly ionospheric planet. We also perform a pilot study of an intrinsically magnetized planet in such flow, in preparation for a future three-dimensional simulation. Here, we use two-dimensional hybrid simulations (particle ions, fluid electrons) and consider different solar wind Alfvén Mach number flow (M_A) and interplanetary magnetic field orientation relative to this plane. This allows control of the available wave types.

The cometary simulations display magnetosonic "turbulence" as M_A is increased, when the field is perpendicular to the simulation plane. If we allow parallel propagating modes by setting the field parallel to the plane, we find the "turbulence" significantly changes in scale and extent, suggesting resonant growth of Alfvén ion cyclotron waves in the presence of magnetosonic "turbulence" occurs. Free energy is available from picked up cometary ions. The process depends on the cometary ion density, which strongly varies, and we conclude this explains the broadband nature of the disturbances.

In the perpendicular field orientation, the planetary source produces a novel two tail structure which continuously strips the planetary ionosphere. We find these tails have very distinct characteristics, resulting in the wake being filled relatively quickly downstream, by complex structure. At higher M_A, magnetosonic "turbulence" again appears. Switching the field parallel to the plane causes massive field line draping and pile-up, and causes instability. A long lasting wake appears, and we conclude that a three-dimensional simulation is required.

The magnetized ionospheric planet pilot study proved difficult to scale accurately in two dimensions. The planetary field failed to penetrate the solar wind, however it appears the simulation would be stable and achieve equilibrium in three dimensions.

Abbreviations

1D - One dimensional

2D - Two dimensional

3D - Three dimensional

AIC - Alfvén-ion cyclotron

AMPTE - Active Magnetospheric Particle Tracer Explorers

BS - Bow shock

EUV - Extreme ultra violet

HT - de Hoffman-Teller (frame of reference)

IMF - Interplanetary magnetic field

IPT - Io plasma torus

KH - Kelvin-Helmholtz

LT - Lower tail

M_A - Alfvén Mach number

MGS - Mars Global Surveyor

MHD - Magnetohydrodynamic

MS - Magnetosonic

N - Normal (frame of reference)

PIC - Particle-in-cell

p.p.c. - Particles per cell

PVO - Pioneer Venus Orbiter

SLAMS - Short large-amplitude magnetic structures

SW - Solar wind

ULF - Ultra low frequency

UT - Upper tail

UV - Ultra violet

Chapter 1

Introduction

1.1 Interplanetary Space

The area of space surrounding the planets in the solar system is known as the heliosphere, and conditions within it are dominated by the Sun. It is permeated by the solar wind (SW) and interplanetary magnetic field (IMF), and has global structure. The SW is a stream of ionized particles that continuously flows outwards from the Sun and interacts with obstacles placed in its path. It originates largely from the solar coronal holes — regions of open field in the corona that allow ionized material to escape the solar atmosphere. Although a precise mechanism has yet to be found, this material is accelerated to high speeds by heating in the corona. Due to the conditions present here, the SW carries a frozen-in magnetic field with it — the IMF. The furthest extent of the heliosphere is far beyond the orbit of Earth, when this out-flowing material encounters the interstellar medium at around 160 A.U. (*Baumjohann and Treumann*, 1996).

Although the Sun's intrinsic magnetic field contains many higher order moments, a fairly simple dipole arrangement is sufficient to explain the average heliospheric structure. The field lines near the North and South poles of the Sun are

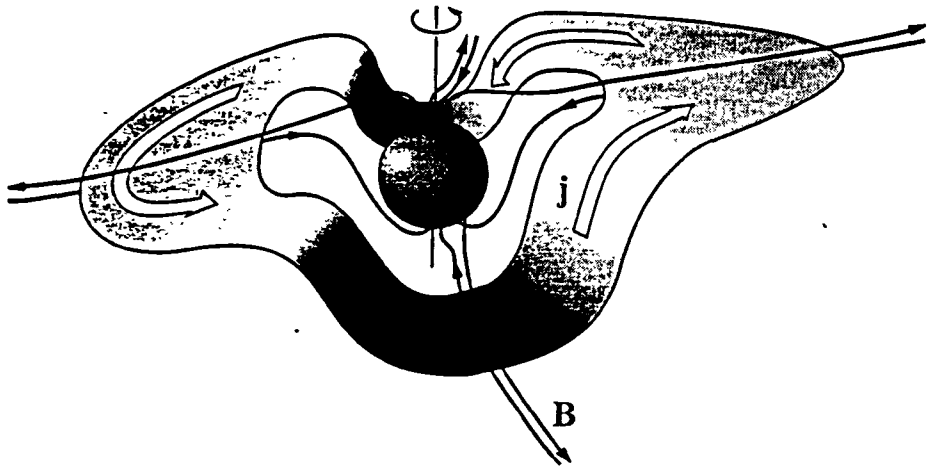

Figure 1.1: Topology of the SW current sheet which can deviate from the ecliptic plane. After *Baumjohann and Treumann* (1996).

normally those left open allowing fast streams of SW particles to escape. As these opposite pointing fields spread out into space they are separated from each other by a current sheet, roughly in the ecliptic plane. However, where the current sheet deviates from this plane (as shown in figure 1.1), space is filled with the appropriately directed IMF, either towards or away from the Sun.

The field direction thus changes whenever the warped current sheet is crossed, such that the field in the ecliptic plane is divided into sectors as shown in figure 1.2. The spiraling of the field in figure 1.2 is due to the rotation of the Sun, which still has one end of the field lines anchored in the corona as the SW expands outwards. This expansion increases with distance from the Sun due to increased SW velocity further out, a fact predicted before spacecraft observations by *Parker* (1958). Along with increased flow velocity it is also found that particle number density decreases according to an approximate inverse square law with distance, at least up to a few A.U., and temperature also decreases, though less predictably (*Baumjohann and Treumann*, 1996).

All the above time-averaged results and observations conceal the true nature

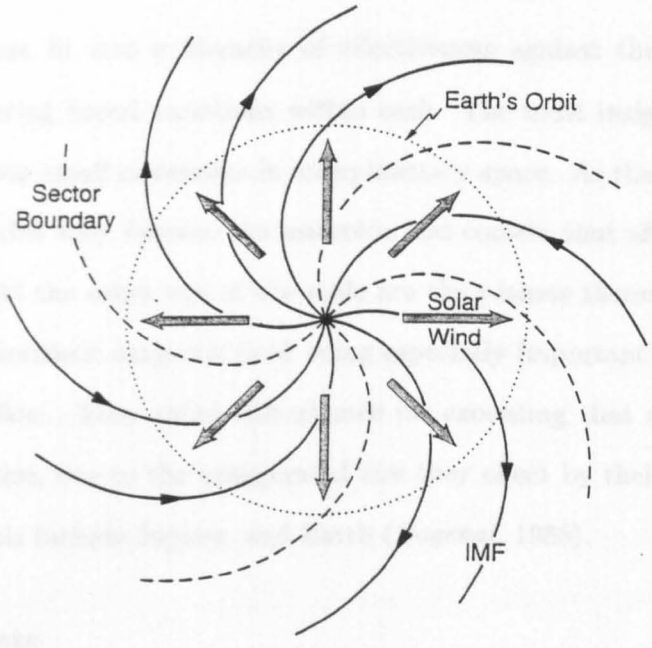

Figure 1.2: The resulting Parker spiral of IMF, split into alternately directed sectors. After *Baumjohann and Treumann* (1996).

of the SW: that of a turbulent flow with structures only on the largest scales (*Goldstein and Roberts*, 1999), which is affected by events on the solar surface such as coronal mass ejections, flares and sunspot activity. Solar activity in general follows an 11 year cycle, however the SW varies on a much smaller time scale. Because of this, "typical" parameters are hard to quote, however many sources try (*Krall and Trivelpiece*, 1986; *Baumjohann and Treumann*, 1996; *Parks*, 1991). The variation of the SW and the obstacles it interacts with thus provides a plethora of different scenarios and consequent effects at various flow speeds, densities and size scales.

1.2 Obstacles to the Solar Wind

For the purposes of this discussion, the obstacles faced as the SW flows outwards from the Sun will be divided into three categories: comets and other very small sources: obstacles with an exosphere; magnetized obstacles. All the obstacles in

the solar system fit into a hierachy of effectiveness against the SW, with these categories covering broad variations within each. The most insignificant obstacles are the numerous small meteorites in interplanetary space. As these increase in size and differ in orbit they become the asteroids and comets that affect the SW as it passes them. At the other end of the scale are the planets themselves, with those with a strong intrinsic magnetic field being especially important when interacting with the SW flow. They cause disturbance far exceeding that associated with a body of their size, due to the exaggerated size they effect by their magnetosphere. Examples of this include Jupiter, and Earth (*Bagenal*, 1985).

1.2.1 Comets

Comets are thought to originate from the formative years of the solar system and consist of material that has been distorted into a usually highly elliptic orbit about the Sun. As the comet approaches the Sun every cycle, the increased radiation causes sublimation of the comets' surface constituents. They vary greatly in size, and due to this and their movement throughout space, have proved useful for many years in providing natural experiments of the SW interaction under different conditions. Of the comets encountered so far, the icy conglomerate model, or "dirty snowball" model first thought up in the 1950's (*Whipple*, 1950) seems to most accurately describe their structure: that of a small nucleus sublimating ices of light elements and molecules, with dust particles mixed in. A prime example was Halley, encountered in 1986 by a fleet of craft and whose coma was found to mainly consist of water (80% by volume), with other ions such as $^{12}C^{+}$, $^{12}CH^{+}$, $^{16}O^{+}$, Na^{+} and $^{32}S^{+}$ also identified (*Krankowsky et. al.*, 1986).

The structure of a comet as viewed from Earth first gave credence to the existence of the SW, before spaceflight, by the presence of twin tails as it approaches the Sun (see figure 1.3) (*Johnstone*, 1985). The more diffuse tail in figure 1.3 results

from the motion of neutral dust particles under the influence of solar radiation pressure, as had always been thought. *Biermann* (1951) predicted the existence of a particulate SW to explain the more clearly defined and often structured second tail which depends on the relative velocity vector between the SW and comet motion. The tails of comets also display other interesting events such as disconnections, symmetrical rays either side of the main plasma tail, and tail streamers. These are believed to be due to field line draping effects (see section 1.3.2) or sudden changes in SW configuration.

Different processes are possible for the ionization of neutral particles once in the coma surrounding a cometary nucleus. The effectiveness of each depends on parameters such as the neutral density and proximity to the Sun, and is not known exactly, but the three ones generally considered are photo-ionization by solar radiation, charge exchange with a SW proton, and ionization by impacts (*Johnstone*, 1985). The second of these produces no net gain in ionization, but does increase the net mass ionized and produces fast neutral hydrogen. The observation of such ionic components within a cometary environment can place limits on the rates of each type of process, as for the case of Halley in *Huddleston et. al.* (1994), which found evidence for higher ionization rates and loss rates due to charge exchange than had been expected. It is then possible to predict that the increased numbers of fast neutrals could lead to the associated higher ionization rate, for example.

Because comets are such healthy examples of space plasma physics effects, they have been subject to many spacecraft missions, and a general picture of their structure has been constructed, as shown in figure 1.4. Two such missions are the International Cometary Explorer (ICE) mission to Giacobini-Zinner (*Von Rosenvinge et. al.*, 1986; *Richardson et. al.*, 1986) and the Giotto encounter with both Halley and Grigg-Skjellerup (*Reinhard*, 1986). The latter of these proved particularly fruitful due to the matching payload at two comets of different size. They pro-

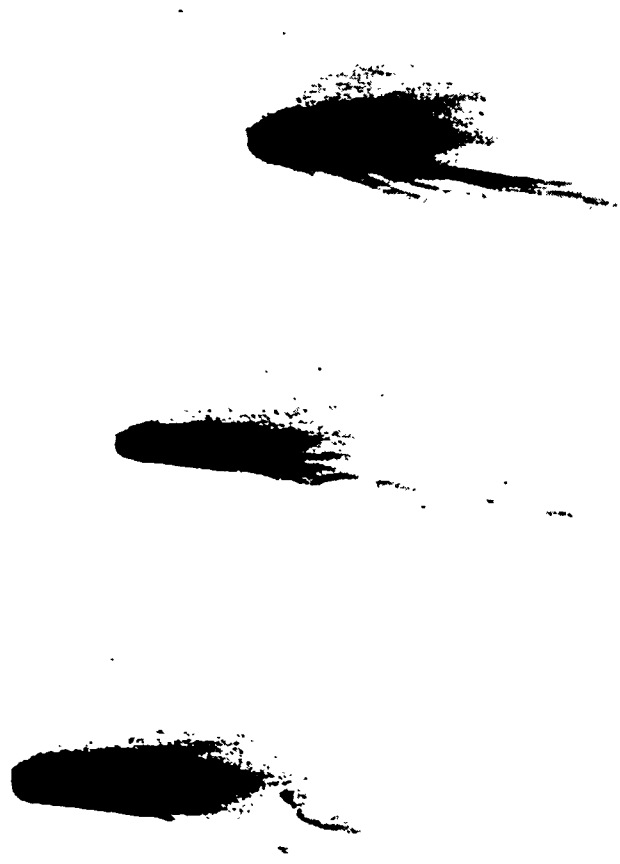

Figure 1.3: Twin tails of an observed comet. Taken on three successive days of the 1986 Halley approach, the diffuse tail is due to dust, whilst the sharper tail depends on ions interacting with the IMF. After *Parks* (1991).

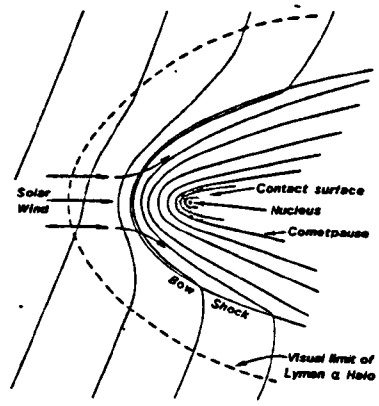

Figure 1.4: Sketch of cometary structure, after *Luhmann* (1991).

vided detailed enough results to confirm an ion density proportional to $\frac{1}{r^2}$ at Grigg-Skjellerup in a ring distribution until reaching the shock itself (*Coates et. al.*, 1993) and possible scattering of water group ions at Halley (*Huddleston et. al.*, 1993b). Both comets were found to be qualitatively similar (*Johnstone et. al.*, 1993) with both experiencing a magnetic pile-up boundary, suggesting this is common to all comets (*Mazelle et. al.*, 1995). *Johnstone* (1995) suggested that with proper scaling, the results from Halley give similar structures to those observed at Grigg-Skjellerup, supporting the idea of a largely universal structure. The main difference observed between these two very differently scaled comets involved observations of the shock: Halley had clearly defined shocks both inbound and outbound, whereas the inbound pass at Grigg-Skjellerup was interpreted more as a "bow wave" (*Rème et. al.*, 1993; *Coates et. al.*, 1997).

The waves produced by these comets were extensively studied. Low wavenumber waves were formed at Halley, possibly by a fire-hose instability (*Coates et. al.*, 1996). but dependent upon the pickup ion distribution. It is well known that cometary environments consist of cool heavy ion beams that are capable of exciting a non-resonant ion beam instability, such as magnetosonic (MS) and Alfvén oscillations (*Treumann and Baumjohann*, 1997; *Winske and Gary*, 1986). The

cometary exploration mission data provided more examples of such disturbances. *Shevchenko et. al.* (1995) compared theoretical calculations of upstream magneto-hydrodynamic (MHD) wave activity with Giotto data, suggesting that in time left hand polarized waves travelling both towards and away from the Sun are produced and that these may cause heating of the cometary ions. Such waves were detected at Grigg-Skjellerup (*Neubauer et. al.*, 1993). However, *Tsurutani et. al.* (1987), looking at Giacobini-Zinner data, suggested observations there were consistent with a right-hand resonant ion beam instability in the sunward direction. Investigations using a test-particle approach into the effects of MS turbulence at Giacobini-Zinner by *Srivastava et. al.* (1993) revealed that such waves travelling obliquely to the IMF can be extremely effective at accelerating particles in the coma. In addition to acceleration of the particles, *Kojima et. al.* (1989) also performed hybrid simulations suggesting a cometary environment is capable of heating SW protons, by wave-wave and wave-particle interactions. Mirror modes have been detected in the Halley data (*Glassmeier et. al.*, 1993), and *Verheest et. al.* (1999) have proposed a mechanism by which electromagnetic turbulence between the water group and proton gyrofrequencies could be produced at such comets, dependent upon sufficient mass loading. Such a process might then only be applicable to larger comets. In addition to these, other wave types have been seen. These have included whistler waves seemingly associated with steepened MS wavefronts (*Tsurutani et. al.*, 1989), and apparent observations of Kelvin-Helmholtz (KH) instabilities in cometary ion tails with wavelengths approximately that of the tail radius (*Ray*, 1982).

With such varied data, many attempts have been made to match theoretical and numerical models to that observed. Two-fluid simulations have been performed (*Bogdanov et. al.*, 1996) and subsequently checked with limited hybrid simulations (*Lipatov et. al.*, 1997) which show several stages of cometary structure as the source rate builds. These range from the smallest sources, giving cycloidal motion within a

tail with stratified clumping of heavy ions along it, to a full bow shock (BS) at larger production rates. The structuring of the tail at low production rates seems to occur via a dripping effect of the heavy ions, when their density is comparable to that of the SW (*Sauer et. al.*, 1996a). At the intermediate rates of production, before a full BS develops, the relative drifting between protons and heavy ions is thought to produce steepened waves which produce multiple Mach cones, additional boundaries, and might be useful in explaining tail rays (*Sauer and Dubinin*, 1999a). Theoretical work by *Huddleston et. al.* (1993a) compared the density gradient expected at Grigg-Skjellerup with data obtained by Giotto, to reveal that they are unexpectedly steep and leading to suggested explanations why.

Of course the largest comets such as Halley are most suited to a MHD approach for modeling the expected location of plasma boundaries (*Murawski et. al.*, 1998), however these still have some discrepancies with the quantitative results from data (*Israelevich et. al.*, 1999). Attempts have also been made to use MHD models to interpret data at smaller sources such as Grigg-Skjellerup (*Schmidt et. al.*, 1993), but mainly for large-scale effects such as production rate or spacecraft trajectory. More general MHD cometary modeling, not directly related to missions, has shown possible reconnection of field lines occurring in the tail and at the subsolar point when the IMF orientation changes (*Ogino et. al.*, 1986). However, as these were only two-dimensional (2D) models, limited cross-over of results to the three-dimensional (3D) scenario can be assumed.

In addition to the above fly-bys of natural comets and subsequent theory, in 1984-5 two artificial ionic releases were made into the SW and Earth's magnetosheath: the AMPTE releases. Although it has since been noted (*Brecht and Thomas*, 1987) that the resulting physical processes were somewhat different to those at a comet, the initial experiments were intended to produce a short-lived artificial comet for observation (*Valenzuela et. al.*, 1986). One of the most surprising results

was that the "comet" exhibited lateral motion instead of acceleration along the direction of SW flow. This has since been explained as lateral momentum transfer in the $\underline{V} \times \underline{B}$ direction (*Chapman and Dunlop*, 1986) and subsequently modeled using 3D particle simulations (*Brecht and Thomas*, 1987) and one-dimensional (1D) and 3D hybrid simulations (*Chapman and Schwartz*, 1987; *Delamere et. al.*, 1999). The resulting structure was one of a diamagnetic cavity producing an asymmetric pickup tail. A "snowplough" effect accelerated the bulk of the released ions whilst SW protons were either reflected at the snowplough, thus obtaining larger gyroradii, or transmitted through it (*Chapman and Schwartz*, 1987). Those protons reflected initially in the magnetosheath releases could then be retransmitted as their motion would not carry them far enough away laterally to avoid the shock-like transition region a second time (*Chapman*, 1989). It was shown that such retransmission at quasi-perpendicular shocks produces clearly defined downstream density clumping at regular intervals (*Burgess et. al.*, 1989). The structure produced by the AMPTE releases was also associated with various observed waves (*Woolliscroft et. al.*, 1986), and these too have been analyzed with reference to application at other sources (*Sauer et. al.*, 1999b).

1.2.2 Obstacles with an exosphere

The next broad category under consideration is that of planets or moons with an ionosphere of some extent. The variability between the levels of ionosphere present, together with ongoing discussions regarding intrinsic magnetic fields at some obstacles, as shall be seen, means many could be described like this. Here I shall summarize three: Venus, Mars and Io.

All obstacles possessing an atmosphere of neutrals are subjected to the Sun's ultraviolet (UV) ionizing radiation, which will ionize a proportion of particles. The level of ionization present will determine the conductivity of the obstacle and there-

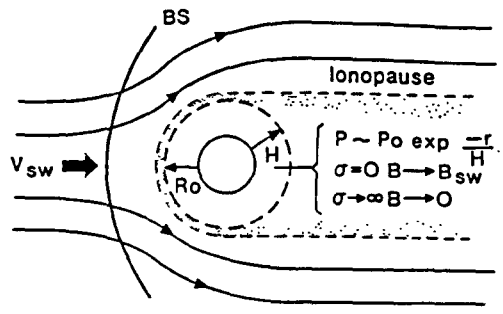

Figure 1.5: Interaction of the SW with an obstacle possessing a dense ionosphere. After *Bagenal* (1985).

fore its resulting interaction, with more dense atmospheres also being subject to impact ionization (*Bagenal*, 1985). If the ionosphere is dense, the conductivity approaches infinity and the SW is excluded from within and forced to flow around the obstacle as shown in figure 1.5.

At some point in the atmosphere, a pressure balance is set up such that the atmospheric pressure balances those of the IMF and SW ram pressure, as shown in equation (1.1) (*Bagenal*, 1985).

$$\rho_{sw} v_{sw}^2 + \frac{B_{IMF}^2}{2\mu_0} \approx P \tag{1.1}$$

The symbols are as shown in figure 1.5. If the conductivity created by ionization in the atmosphere fails to rise much above zero, the IMF drapes throughout the ionosphere allowing freshly ionized neutrals to be picked up (see section 1.3.1 and figures 1.6 and 1.7).

Venus is the most explored planet undergoing such an interaction. It has been subjected to over a dozen missions, including that of the Pioneer Venus Orbiter (PVO) summarized by *Russell* (1992). Venus' atmosphere is 96% CO_2 with sulphuric acid clouds and a surface temperature of 460^oC (*Russell*, 1992). It has been cited often in the mass media of the last decade as an example of "runaway greenhouse effect", as it is enveloped by a thick atmosphere. A BS forms, although it is weaker

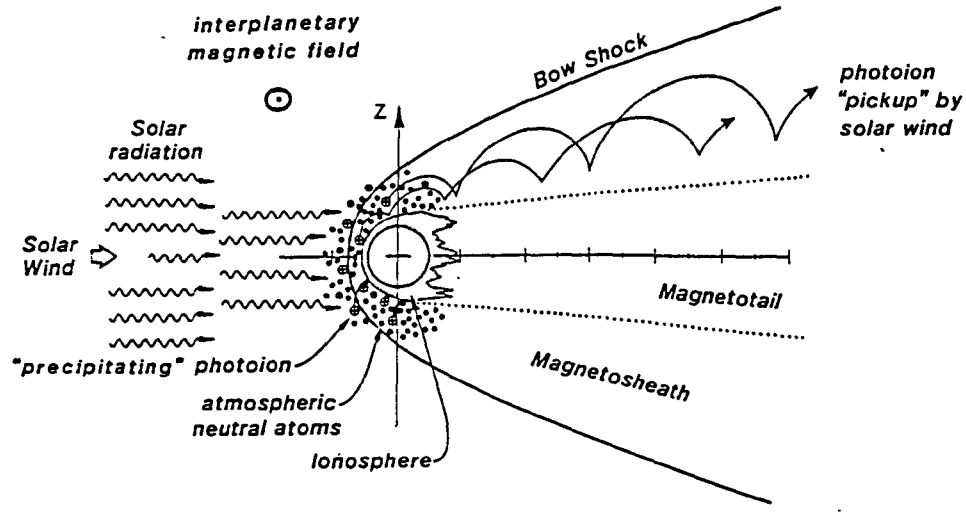

Figure 1.6: Pickup ion motion at Venus. After *Luhmann* (1990).

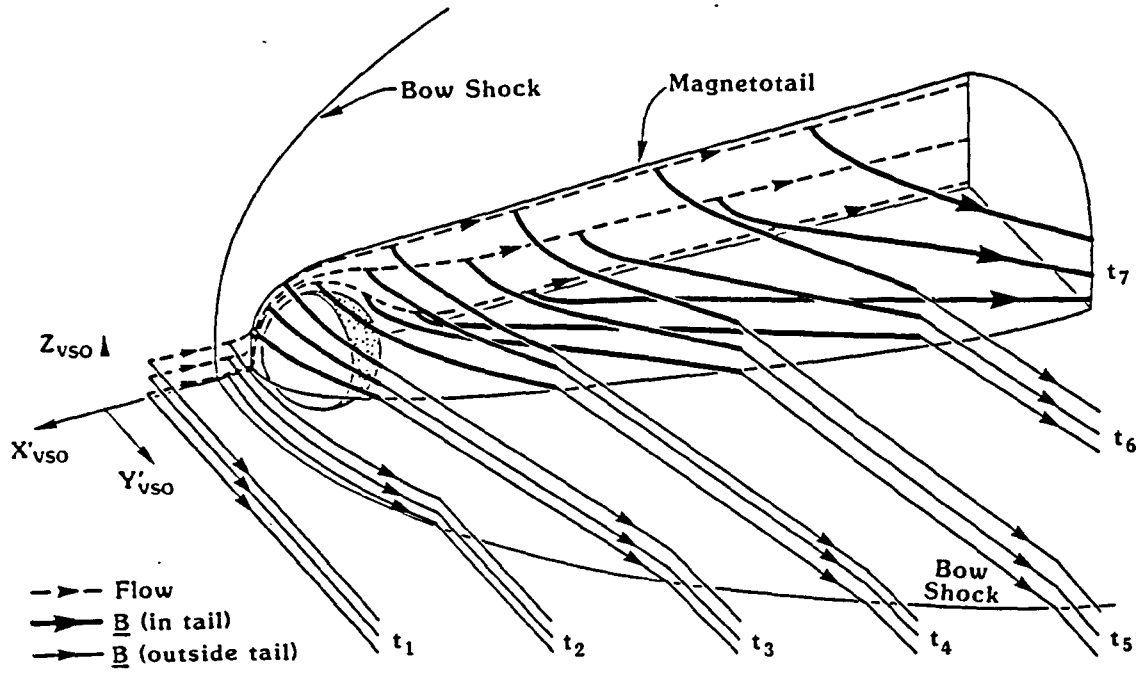

Figure 1.7: Schematic of field line draping occurring at Venus. After *Saunders and Russell* (1986).

than that at Earth and not truly collisionless, as pointed out by *Brecht* (1995), and so must be modeled differently. Behind this lies a subsonic magnetosheath, similar to at Earth, although there is of course no intrinsic magnetic field at Venus. This is supported by a lack of correlation of magnetic field observations to surface features, and the fact that the current sheet in the tail appears to depend entirely on the IMF orientation (*Russell et. al.*, 1980).

Due to the extremely dense atmosphere we expect high ionization and conductivity, and the IMF to be largely excluded. This is confirmed by observations, although interaction at the planetary end of flux lines still causes field line draping as shown in figure 1.7. These field lines also allow the escape of some ionospheric constituents along them. Observations also encounter occasional small regions of enhanced magnetic field labeled "flux ropes", which are believed to be caused by shearing effects at the ionopause, or the dragging of field lines through the interior.

The ionization processes at work at Venus vary over the solar cycle, and from dayside to nightside. Due to the extensive coverage of the PVO (although mainly at solar maximum) these have been studied. In the review by *Knudsen* (1992) it is stated that most dayside ionization is due to solar EUV radiation, however on the nightside this is replaced by horizontally transported ions, and a downward flux of O^+ and electron impacts. The nightside of Venus has also been found to exhibit ionospheric "holes", consisting of low density and high magnetic field strength, with an orientation suggestive of a link to field line draping. The predominant ion picked up by the SW at Venus is O^+. *Moore and McComas* (1992) have observed the effects of such pickup ions in the tail of Venus and have found a different effect depending upon the region the ions originate from, as shown schematically in figure 1.8. Ions originating in the magnetic barrier transfer to the central tail with small gyroradii, whilst those originating higher up in the ionosphere are picked up with larger gyroradii in the magnetosheath. The relative importance of the different ionization

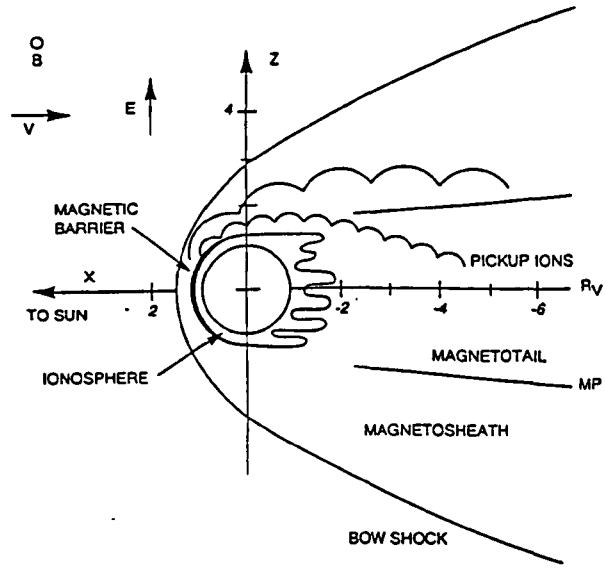

Figure 1.8: Dependence of pickup ion motion on original location of the particle. Ions originating from the magnetic barrier transfer to the tail with small gyroradii. After *Moore and McComas* (1992).

processes at Venus has also been investigated by *Bauske et. al.* (1998) (using a MHD code similar to *Kallio et. al.* (1998), but with mass loading effects included in more detail). who suggested that photoionization was the most important, over impact ionization and charge exchange. They included hydrogen and oxygen pickup ions. *Kallio et. al.* (1998) used only oxygen mass loading and switched this on or off to represent to a first approximation the interaction at solar maximum or minimum. Their results gave good agreement with data. A review of other MHD modeling of Venus (and Mars) is given in *Spreiter and Stahara* (1992), including an orientation with the IMF aligned with the SW flow velocity.

There is still discussion regarding the similarities between Venus and Mars: some authors cite many similarities in the observations at Mars to those at Venus (*Cloutier et. al.*, 1999), yet there has been much discussion over Mars' magnetization state (*Vaisberg.* 1992). MHD simulations by *Krymskii et. al.* (1995) investigated the horizontal magnetic field component at Mars and concluded that a field was present

by comparison of electron density profiles. However, this could be due to either an intrinsic field (unlike Venus) or an "overpressure" condition, as experienced at Venus, where the IMF is pushed down throughout the ionosphere. Mars' atmosphere is less dense than that at Venus and so would be less likely to stand-off the SW, however a BS still forms (*Bagenal*, 1985). More recent results from the Mars Global Surveyor (MGS) (*Acuña et. al.*, 1998) detected no significant overall field, yet found regions of magnetic field increased, particularly over the oldest terrain, suggesting the anomalies were crustal in origin. It was noted that these could affect BS variability, but that overall the interaction would be similar to that at Venus. This interpretation is not universal: 3D hybrid simulations by *Brecht et. al.* (1993) compared the results of Phobos 2 observations to their dayside only simulation to find magnetic field agreement and the lack of a traditional subsolar shock front, unlike at Venus. They note that in many ways the interaction is more like that at the AMPTE releases (see section 1.2.1), however acknowledge that massloading effects were not included in their simulations. This model has since been improved (*Brecht*, 1997a) to entirely enclose the planet, represented by a conducting sphere, yet still with no ionosphere. 2D tests with an ionosphere were performed, however the 3D results were found to fit observations more closely without. The model was also used to investigate the impact of SW protons with the planet (*Brecht*, 1997b) after earlier work (*Brecht et. al.*, 1993) had suggested they penetrate deep into the ionosphere. The results suggested that proton deposition was dependent upon orientation between the IMF and SW velocity and magnitude, but could compete with photoionization and hence lead to more ion formation than expected.

A two-fluid MHD code has been used by *Liu et. al.* (1999), which generally matches observed average BS location well and predicts a rate of oxygen ion escape tailward consistent with Phobos 2 observations. This was a quantitative improvement over the work by *Fox* (1997), whose model obtained escape rates higher than

observed and with the major constituent of O^{2+}, not O^{+}, although this work was aimed at explaining atmospheric evolution on Mars.

Mars shares confusion over the interpretation of boundary layers similar to some comets: *Dubinin et. al.* (1996) have examined a boundary layer in the Phobos 2 data which appears impermeable by SW protons, consisting mainly of planetary ions, like a magnetopause (although they emphasize not like Earth's). The interaction is dominated by the IMF orientation and hence asymmetric. Elsewhere *Dubinin and Lundin* (1995) propose a massloading boundary based on observations of a sudden drop in proton flux, whilst admitting to the possibility that such boundaries may become confused. The importance of the IMF orientation to the interaction is highlighted further by the work of *Russell et. al.* (1990) who used Phobos 2 data to look for MHD waves upstream of the BS. They found turbulence upstream when the field was connected to the shock thus allowing ions to travel upstream, and weak left hand elliptically polarized waves at the proton gyrofrequency, possibly due to pickup processes. Otherwise they concluded the data was quite quiet. More recently *Delva and Dubinin* (1998) looked for ULF waves here and concluded the situation was qualitatively similar to that at Venus and Earth, with more turbulence appearing deeper into the foreshock. They also stated somewhat in contradiction to *Russell et. al.* (1990), that Mars had *more* activity than Venus or Earth upstream of the foreshock, possibly due to the role of planetary ions.

The final obstacle considered in this category is the innermost major moon of Jupiter, Io. It lies within the rotation dominated magnetosphere of Jupiter, in a region known as the Io plasma torus (IPT) and is unusual in that its wake appears in front of the moon: a scenario caused by the rotating plasma of Jupiter's magnetosphere overtaking it. Because of this unique location, there is still much not understood about its interaction. It is known (*Bagenal*, 1985) that Io is a source of plasma in the IPT, with estimated production rates giving about 10^{28} ions needed

per second to maintain the status quo. The torus has an inner, cold plasma region and outer warm plasma, which gives UV emission. However, it is not known for sure that Io is the dominant source within the IPT: *Horányi and Cravens* (1996) have postulated that it is produced by Jupiter's ionosphere, and claim to have good agreement with observed brightness distributions. This highlights the problem that little fly-by data is available at Io. Much of what is known is thus found from ground-based observations (*Thomas*, 1993a,b, 1996; *Thomas and Lichtenberg*, 1997) of ionic components within the IPT, such as by *Thomas* (1995) who detected S^+, S^{2+}, O^+ and O^{2+}, and reported on their radial velocity dependence. *Frank et. al.* (1996) use data from the 1995 Galileo fly-by, however, to also report the presence of SO_2^+ ions and argue that the plasma environment at Io could lead to a reduced magnetic field without the need for a field intrinsic to Io. *Cheng and Paranicas* (1996) use the same fly-by to justify a thermoremanent magnetic moment at Io, caused by cooling of the surface layers in a stronger field than that now surrounding the moon. The issue is an open one.

Due to the conductivity of Io, it also supports an electrodynamic circuit via its motion through the magnetic field of Jupiter, and it is known that decametric arcs occur in relation to this. It provides another tool for understanding the system as a whole, and the generation of such emissions (*Queinnec and Zarka*, 1998).

1.2.3 Small magnetized obstacles

The most studied object in the solar system with a magnetosphere is, of course, the Earth itself. Its field is strong enough to allow it to greatly enhance its interaction with the SW: the obstacle the Earth presents to this flow is disproportionately large due to the magnetic dipole contained within the relatively small body. Such an interaction represents the pinnacle here, as does that at Jupiter (albeit different to Earth's) which due to its magnetosphere is the largest object in our solar system,

bigger than the Sun (*Bagenal*, 1985). Both of these examples have been well studied and as such a summary here is impractical. More importantly, both examples differ hugely from those in this study in terms of spatial scale. The obstacles herein are all termed "small scale" due to the obstacle and its interaction region being of the same approximate size as a pickup ion gyroradius in undisturbed flow at the obstacle. Both Earth and Jupiter's magnetospheres are much greater than this unit length and as such may involve different physical processes.

However, the solar system also provides an example of an appropriately scaled magnetosphere in the form of Mercury, the innermost planet. Although only visited once by the Mariner 10 spacecraft (*Dunne*, 1974), which performed three fly-bys in 1974-75, the planet is thought to possess a magnetic field of its own (*Ness et. al.*, 1974). The spacecraft detected signatures of a magnetic tail, magnetopause and BS crossings reviewed by *Ness* (1979). The resulting picture of Mercury's magnetosphere is shown in figure 1.9, along with a scaled overlay of the Earth's plasmasphere.

As Mercury's field is so much weaker than that at Earth (4×10^{-4}Earth's (*Bagenal*, 1985)), it more than proportionately reduces with the planets size. This creates at least two major differences. The first is that the cusp regions on Mercury reach much lower latitudes than on Earth, and the second is that there are no regions of trapped particles in the magnetosphere, unlike the Earth which has a plasmasphere in the inner magnetosphere (*Bagenal*, 1985). On a dipole scaled to Mercury, this region would be within the planet (see figure 1.9). More predictably, the BS has a stand-off distance of $\sim 2R_{Me}$ (*Ness et. al.*, 1974) at the subsolar point and can be as low as to impinge the surface depending upon SW ram pressure. Indeed *Siscoe and Christopher* (1975) have estimated this to occur for just under 1% of the time.

Most of the magnetospheric constituents are captured SW particles, how-

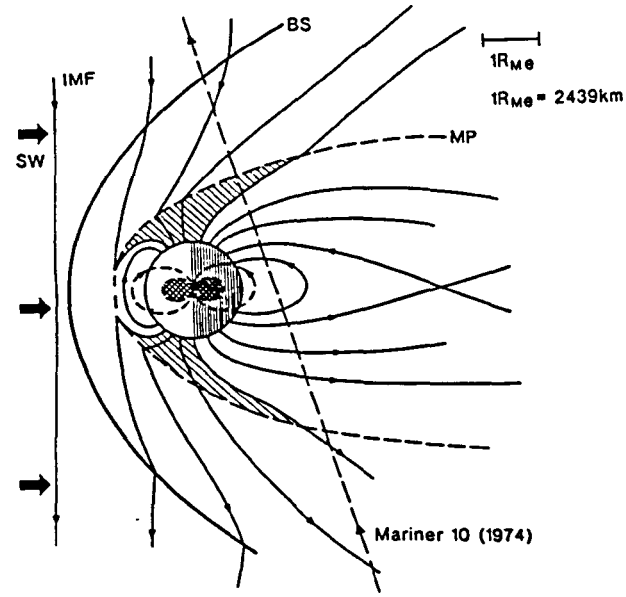

Figure 1.9: Mercury's magnetosphere with the polar cusp regions hatched. Shown also is the scaled plasmasphere of Earth, double hatched and within the planet. After *Bagenal* (1985).

ever this impinging flow of SW onto the surface enables sputtering of constituent substances with subsequent photoionization to form a thin exosphere at Mercury (*Lammer and Bauer*, 1997). Some observations have placed a hot sodium component of the exosphere at altitudes in excess of $700km$, and *Lammer and Bauer* (1997) use particle surface sputtering to explain the higher ejection energies needed for such a population. Surface sputtering could also account for other heavier species such as oxygen and potassium. *Potter* (1995) suggests an alternative *chemical* sputtering mechanism which could also produce water ice when applied to metal silicates. Observations by radar of polar craters have suggested water ice may be contained within them (*Butler et. al.*, 1993). This method would also require a lower surface concentration of heavy elements to create the observed exospheric densities than that of physical sputtering, but would only give products at the surface thermal temperature.

The Mariner 10 nightside passes of Mercury also observed bursts of energetic particles which *Siscoe et. al.* (1975) interpreted as being the equivalent of Earth's substorms only on a shorter timescale due to the smaller spatial scale and lack of a damping ionosphere at Mercury. As no further missions have been sent the question remains largely unanswered, however more recently *Luhmann et. al.* (1998) have argued that the observations do not necessarily imply periods of energy storage and release within the magnetosphere. Instead they propose Mercury simply reacts to changes in the IMF, particularly its southward component, by restructuring the magnetosphere.

Missions in the last decade have also confirmed the presence of magnetic fields associated with asteroids, which although more like weak point sources are worth briefly summarizing. The Galileo spacecraft observed magnetic fluctuations upon passing the asteroids Gaspra and Ida (*Wang et. al.*, 1995). The size of these meant the disturbances took the form of whistler wave propagation almost uniquely along the field lines. *Kivelson et. al.* (1995) concluded that the interaction at the smaller asteroid, Gaspra, showed evidence of a magnetic dipole larger than the obstacle itself, whilst ambiguous SW conditions at the time of the Ida fly-by gave uncertain results. The observations have been followed up by numerical work by *Wang and Kivelson* (1996) and *Baumgärtel et. al.* (1994). *Wang and Kivelson* (1996) use both analytical work and Hall MHD and 1D particle simulations to investigate the interaction at such asteroids. They show that a dipole field present at Gaspra would produce the observed interaction, particularly field line draping, whilst *Baumgärtel et. al.* (1994) use 2D Hall MHD modeling to produce similar magnetic fields to those observed using a dipole strength of $10^{14} Am^2$.

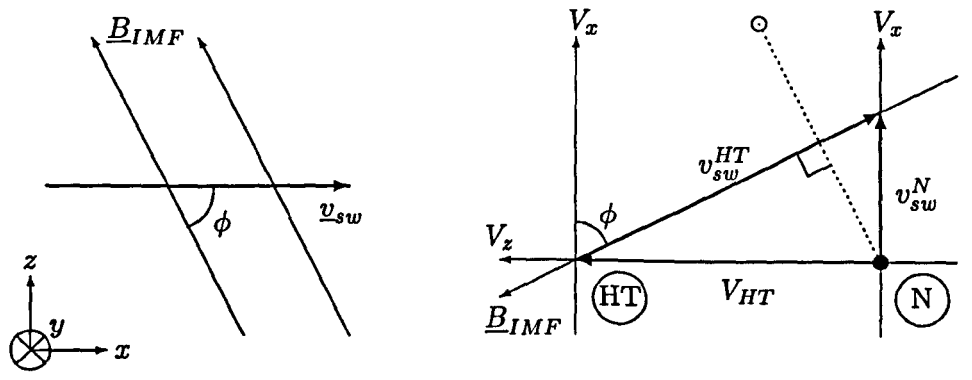

Figure 1.10: The de Hoffman-Teller frame of reference moves with velocity $V_{HT} = v_{sw}^{N} \tan\phi$ in the z-direction, as shown in the velocity space diagram on the right.

1.3 Effects at Obstacles

1.3.1 Pickup and massloading

These processes are closely related as they are opposite extremes of the mechanism by which freshly ionized particles are accelerated up to the local SW flow speed. First, consider the case of a single, ionized test particle in SW flow. It is convenient to transfer to the de Hoffman-Teller (HT) frame of reference shown in both real and velocity space in figure 1.10 (*Schwartz*, 1985).

In figure 1.10, $\hat{\underline{x}}$ is parallel to $\underline{v}_{sw}$ and the IMF is contained in the xz-plane. The HT frame then moves with velocity given by equation (1.2) in the z-direction.

$$v_{HT} = v_{sw}^{N} \tan\phi \tag{1.2}$$

In equation (1.2), v_{sw}^{N} is the SW velocity in the Normal (N) frame at rest and the transformation occurs in the z-direction, as seen in figure 1.10. In the HT frame, the electric field experienced by particles is zero, equation (1.3), as $\underline{v}_{sw}^{HT}$ and

$\underline{B}_{IMF}$ are parallel.

$$\underline{E}^{HT} = -\underline{v}_{sw}^{HT} \times \underline{B}_{IMF} = 0 \tag{1.3}$$

This means any particle motion can now be decomposed into a guiding centre motion, $v_{\parallel}^{HT}$, and a gyromotion component, $v_{\perp}^{HT}$, as there is no net drift perpendicular to $\underline{B}_{IMF}$. A single, ionized particle is now added with an initial velocity, v^N, assumed to be small enough relative to v_{sw} that it can be ignored in the N frame. This appears at the origin of the N axes as shown in figure 1.10. However, in the HT frame this particle now has a perpendicular gyromotion velocity of $v_{sw}^N \sin\phi$ and subsequently traces a ring in velocity space, also as shown in figure 1.10. Viewing this motion from the N frame adds a perpendicular guiding centre drift of $v_{sw}^N \sin\phi$, such that the maximum velocity obtained on a cycle is $2v_{sw}^N \sin\phi$. As this is much larger than any initial velocity the particle may have had on ionization, it justifies the assumption made.

The process becomes more important when *many* particles are being ionized within the locality for two reasons. Firstly, the acceleration of these particles is to the detriment of the SW: as they gain momentum, it loses. Many such particles can thus decelerate SW flow: the effect of massloading. Massloading is known to be important at comets, Venus and Titan (*Bagenal*, 1985; *Johnstone*, 1985) and contributes to other effects such as field line draping (see section 1.3.2). Secondly, the ring-type distribution formed in velocity space as shown in figure 1.11 proves important.

The diagram in figure 1.11 assumes $\phi = 90°$ in the above derivation and uses the notation given therein. In reality, the particles fill a torus in velocity space , as shown dotted in figure 1.11, rather than the ring derived above. This spread is due to the initial particle velocities, assumed negligible above, and small variations to

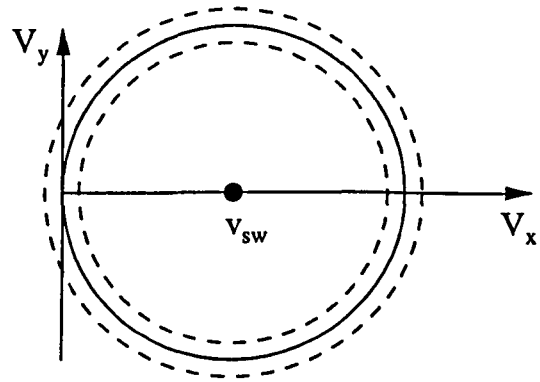

Figure 1.11: Pickup ion ring distribution in velocity space.

the magnetic field over an orbit which cause small deviations in gyration (indeed, larger gyrations may take the particle into somewhat different conditions). The important point is that such a distribution contains a large amount of free energy which can feed into instabilities as discussed, for example, by *Winske and Gary* (1986) and *Gray et. al.* (1996). The simulations presented in chapters 4 - 6 take $\phi = 90°$ for simplicity.

A similar mechanism to that described above can take place at shocks: particles such as SW protons can be reflected off the shock front and hence gain energy and a large gyroradius. *Burgess et. al.* (1989) has shown that such reflection can only occur if the particle already has a high energy compared to the rest of the distribution, a result supported by *Scholer and Kucharek* (1999) who conclude that pickup ions passing through a shock are one order of magnitude more likely to be reflected than ambient SW. Such ions would already have excess energy compared to the SW.

1.3.2 Obstacle scaling

The physical processes that occur at an obstacle vary according to its size. This involves two measures: the ionic production rate, and the spatial extent of this

production. It is important to consider both.

The production of ions at a source can be a very complicated procedure involving many different ionization mechanisms. Fundamentally, it depends on the neutral particle density present, and hence the neutral production rate of the source. It also depends on the ionization rate of these neutrals, which is species dependent. Of course, there is usually a mixture of species produced at any given source as well as the multiple ionization mechanisms possible. For the cometary case, water group ions are most abundant (see section 1.2.1). The major ionization processes considered are usually photoionization, charge exchange and impact ionization.

The spatial extent of the source region depends on the amount of mass being produced as described above, but also on the distance that neutrals might travel before becoming ionic. It thus depends on the ejection velocity of the particles away from the centre of the source region, as well as the ionization rate.

These descriptions of the parameters that affect source size assume a cometary type source. The addition of a planetary surface, especially that possessing a magnetic field, will modify things. One such example is found in magnetic field line draping. This can be caused by either sufficient massloading decelerating the SW flow near a source such that the "frozen-in" field is held up in that region and hence draped, or alternatively by the presence of a conducting planet. The diffusion time for the magnetic field to pass through such an obstacle is then $\tau_d \sim \mu_0 \sigma L^2$, where σ is the conductivity of the planet and L its characteristic size (*Bagenal*, 1985): whereas the time for convection of flow past the obstacle is $\tau_c \sim \frac{L}{V}$ where V is the flow velocity. For sufficiently high σ, the diffusion time for the field is longer than that convected past in the flow, and the field becomes built up in front of the planet and draped at the sides.

The small scale simulations presented in this thesis use a source region of roughly one pickup ion gyroradius in undisturbed flow in diameter. The neutral

production rates are not defined as these alone do not control the physics: it depends on the rate of ionic mass production and the source region extent combined. However, figure 1.12 shows calculated neutral source rates used in this study as can be best found, added to a figure displaying the three comets that have been subjected to fly-by missions.

The normalized production rate used in figure 1.12 is given in equation (1.4), in which Q_h is the neutral production rate, ν_i the ionization rate, B_∞ the magnetic field far from the source, and $v_{ej.}$ the radial ejection velocity of the particles, all in Gaussian units (*Bogdanov et. al.*, 1996).

$$\sigma_h = \frac{Q_h \nu_i e}{B_\infty v_{ej.} c} \tag{1.4}$$

For these simulations, values of $\nu_i = 1.5 \times 10^{-4} s^{-1}$, $B_\infty = 18nT$ $(1.8 \times 10^{-4} G)$ and $v_{ej.} = 1.9 kms^{-1}$ were taken. The x-axis in figure 1.12 is the Alfvén Mach number (M_A) of the flow in which such sources were examined. It can be seen that my source production rates are most comparable to those of Grigg-Skjellerup.

1.3.3 Shocks

In a regular fluid, shocks are formed by waves travelling faster than the sound speed, which causes them to steepen and eventually form a shock front in which excess steepening is balanced by diffusion, as shown in figure 1.13.

In a plasma, waves exist which can act as sound waves for the purposes of shock formation. At plasma shocks, such as the Earth's BS, we typically find $\lambda_{collisions} \gg \lambda_D$ (λ_D is the Debye length - see Chapter 2) and so diffusion is inadequate to balance the shock. Plasma shocks can be balanced by dissipation of the wave front instead, similar to the process that forms solitons. Consequently, shocks form in space in front of many obstacles albeit for different reasons (*Bagenal*, 1985).

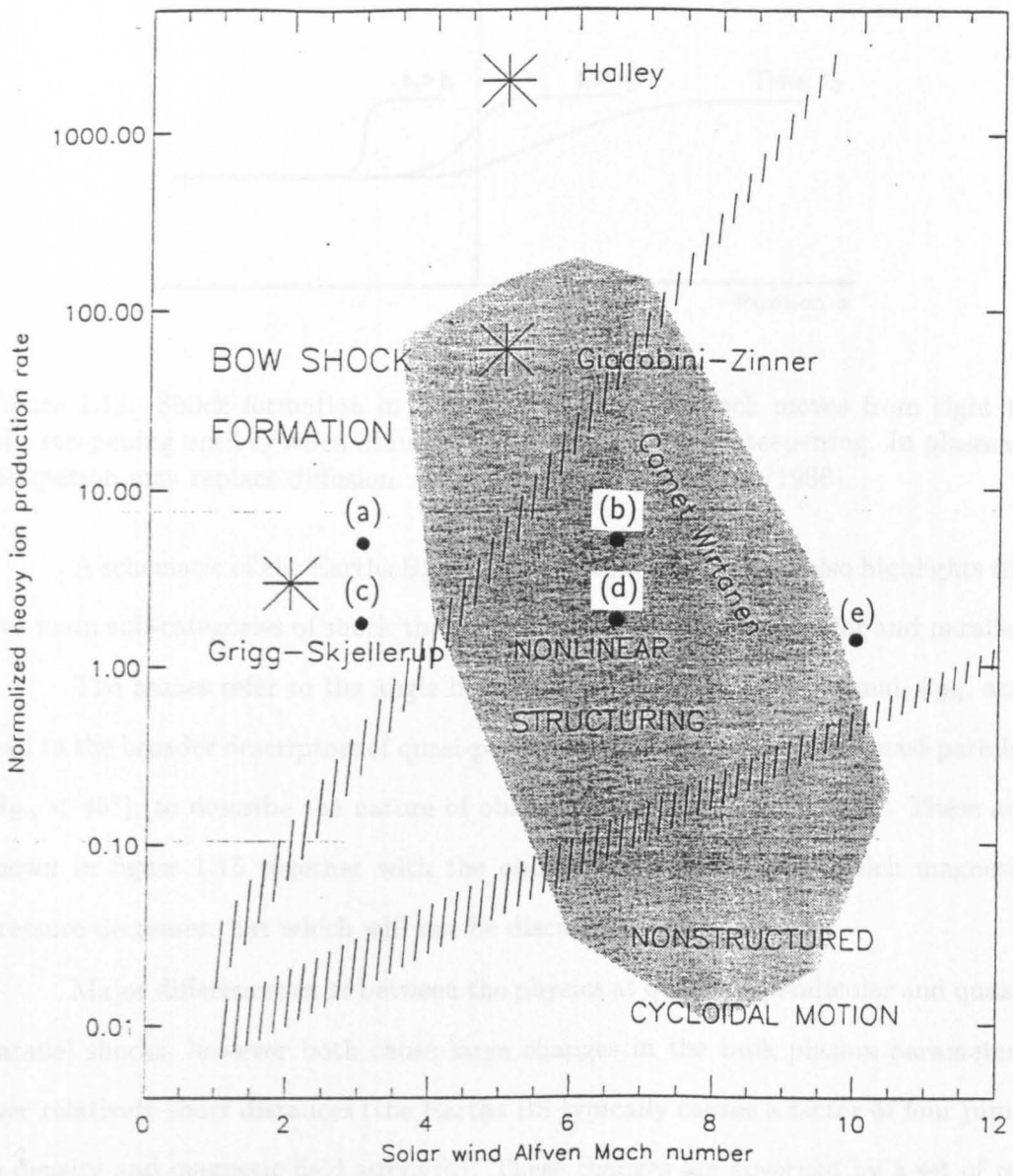

Figure 1.12: Plot showing the location in σ_h - M_A space of the three comets studied by spacecraft missions. The space is divided into regions denoting the structure type observed by *Bogdanov et. al.* (1996). Also shown are the simulations in this thesis of: (a) cometary source with $\sigma_h = 5.25$, $M_A = 3.0$; (b) cometary source with $\sigma_h = 5.25$, $M_A = 6.6$; (c) planetary source with $\sigma_h = 1.97$, $M_A = 3.0$; (d) planetary source with $\sigma_h = 1.97$, $M_A = 6.6$. Point (e) shows the location of the simulation in figure 1(b) of *Bogdanov et. al.* (1996). After *Bogdanov et. al.* (1996).

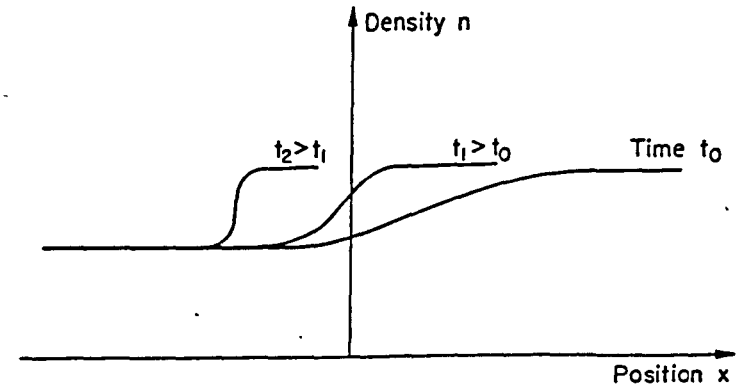

Figure 1.13: Shock formation in a regular fluid. The shock moves from right to left, steepening until t_2 when diffusion balances out further steepening. In plasmas, dissipation may replace diffusion. After *Krall and Trivelpiece* (1986).

A schematic of the Earths BS is shown in figure 1.14 which also highlights the two main sub-categories of shock that will be discussed: perpendicular and parallel.

The names refer to the angle between the IMF and shock normal, θ_{Bn}, and lead to the broader descriptors of quasi-perpendicular ($\theta_{Bn} > 45°$) and quasi-parallel ($\theta_{Bn} < 45°$). to describe the nature of oblique shocks ($0 < \theta_{Bn} < 90°$). These are shown in figure 1.15 together with the oblique slow shock, over which magnetic pressure decreases, but which will not be discussed here.

Major differences exist between the physics at quasi-perpendicular and quasi-parallel shocks, however both cause large changes in the bulk plasma parameters over relatively short distances (the Earths BS typically causes a factor of four jump in density and magnetic field strength). These changes are governed by a set of relations, the Rankine-Hugoniot relations, which allow the calculation of downstream parameters in terms of upstream values (*Baumjohann and Treumann*, 1996) over length scales suitable for ideal MHD. The simplest of these are those governing magnetic field normal to the shock and mass conservation, given in equations (1.5) and (1.6).

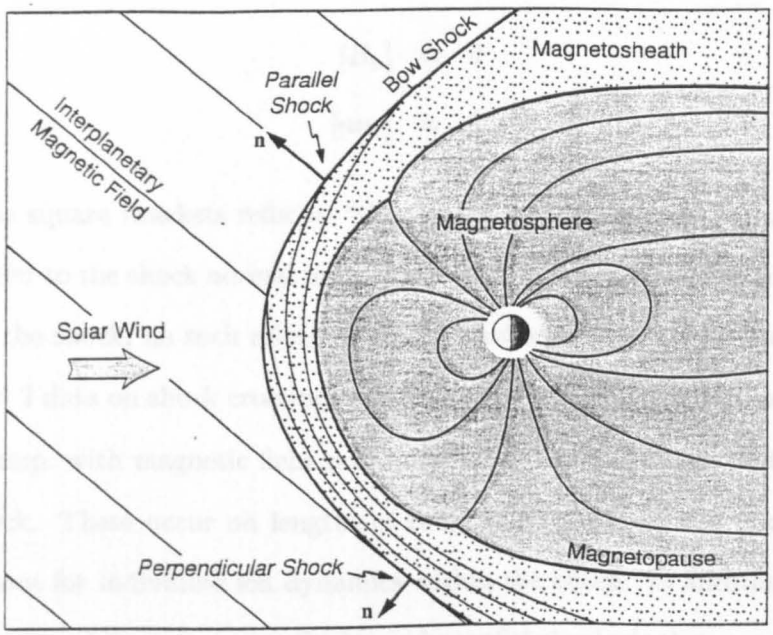

Figure 1.14: Schematic of the Earth's BS, showing parallel and perpendicular regions. After *Baumjohann and Treumann* (1996).

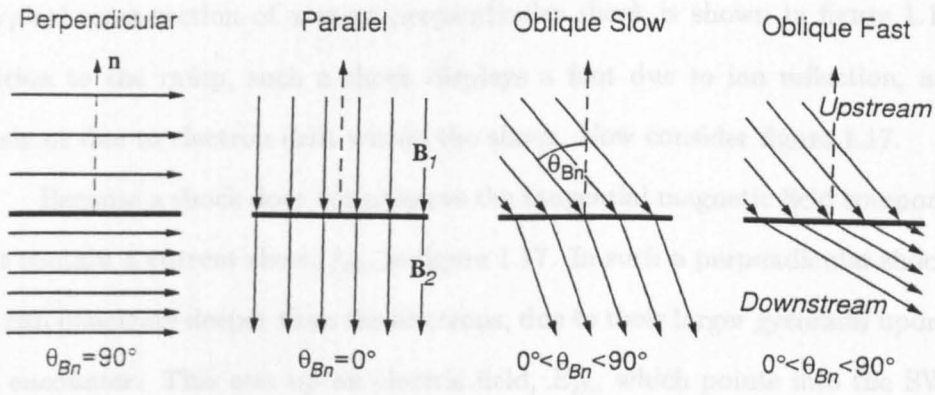

Figure 1.15: The different geometries of shock normal and magnetic field. The oblique slow shock is not discussed here. After *Baumjohann and Treumann* (1996).

$$[B_n] = 0 \quad (1.5)$$

$$[nv_n] = 0 \quad (1.6)$$

The square brackets refer to "the change over the shock", values with subscript n refer to the shock normal component only. On smaller length scales, close to or within the shock, no such relations hold. *Newbury et. al.* (1998) have examined ISEE1 and 2 data on shock crossings and reported the existence of subramps within a shock ramp, with magnetic field variations of similar magnitude to that over the whole shock. These occur on lengths of roughly 0.1 - $0.2\frac{c}{\omega_{pi}}$ and obviously could be important for individual ion dynamics within the shock. In addition, one of the main differences between perpendicular and parallel shocks is the ramp width itself. Data from fly-by missions and multifluid modeling by *Zank et. al.* (1994) indicates quasi-parallel shock ramps are much more extended.

Quasi-perpendicular shocks

A typical cross-section of a quasi-perpendicular shock is shown in figure 1.16. In addition to the ramp, such a shock displays a foot due to ion reflection, and an overshoot due to electron drift within the shock. Now consider figure 1.17.

Because a shock does not preserve the tangential magnetic field component it must contain a current sheet, j_{sh}, in figure 1.17. In such a perpendicular shock, the ions can penetrate deeper than the electrons, due to their larger gyroradii upon their first encounter. This sets up an electric field, E_{sh}, which points into the SW and acts to reflect ions with too little energy to overcome the potential. Those reflected gyrate once more infront of the shock where they are accelerated (see section 1.3.1) and carry a current, j_f. This more than compensates for the effect of j_{sh} reducing the magnetic field, to create the enhanced field of the shock foot. In reality another

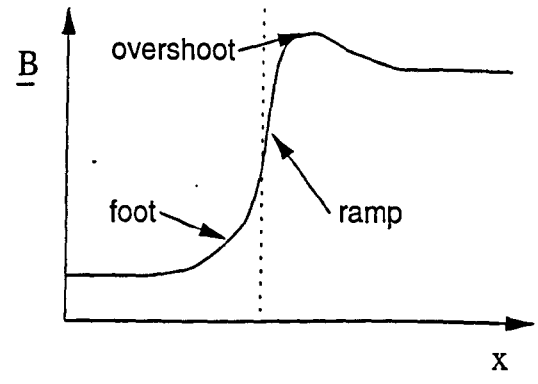

Figure 1.16: A schematic of the cross-section of magnetic field through a quasi-perpendicular shock.

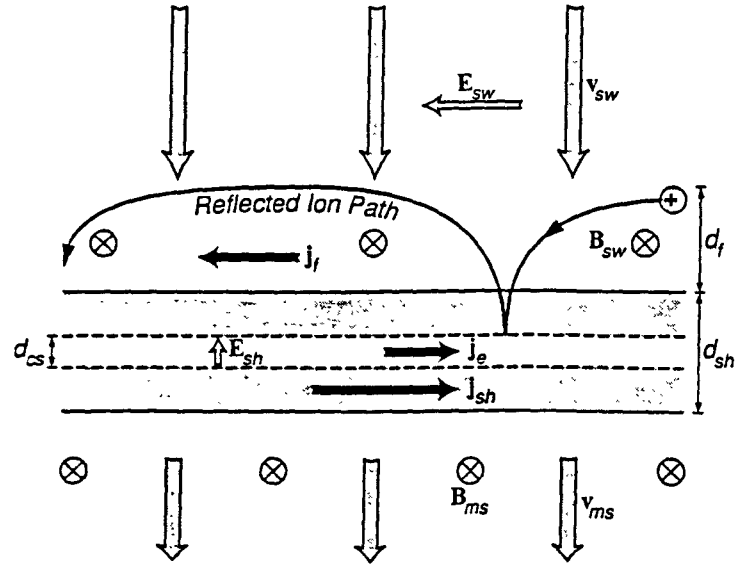

Figure 1.17: The currents and fields present in a perpendicular shock that lead to the structure in figure 1.16. After *Baumjohann and Treumann* (1996).

population adds to the creation of the shock foot also: work by *Burgess et. al.* (1989) used 1D hybrid simulations to closely follow various energy ranges of the incoming SW protons and found that high energy ions were also reflected due to non-adiabatic motion within the shock layer. Together, these mean the shock foot has a spatial extent of roughly one ion gyroradius. The electrons do not contribute to its formation directly.

The electric field within the shock also acts to attract electrons. Due to the small spatial scale of their gyroradii they then experience an $E_{sh} \times B$ drift over the narrow layer in which this exists, that the ions do not. This drift gives rise to an electron current, j_e, which increases the effect of j_{sh} by cumulative addition, and so causes the magnetic overshoot (*Baumjohann and Treumann*, 1996).

The possibility of backstreaming ions due to reflection at such a shock enables ion beam instabilities to form. The most likely of these are Alfvén-ion cyclotron (AIC) and mirror mode waves in the area immediately downstream of the shock. *McKean et. al.* (1995a,b) have performed 2D hybrid simulations to examine whether such modes are created at the shock and convected downstream, or produced in the magnetosphere itself. They found the shock and convection mechanism to be most likely due to the mixture of both modes seen in observations. The waves feed off temperature anisotropies of reflected ions, with heavier species taking longer to lose such anisotropy downstream of the shock.

Quasi-parallel shocks

In general these are more complicated than quasi-perpendicular shocks due to the ions and electrons ability to travel relatively far upstream along connected field lines. This forms regions known as foreshocks, which contain particles that have travelled along the field lines whilst simultaneously being swept back by the SW flow. As electrons travel faster, their foreshock region stays closer to the field line itself, and

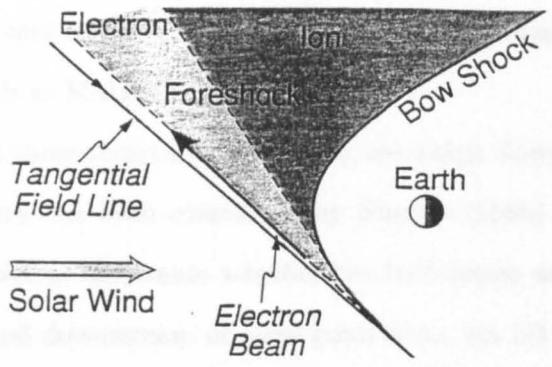

Figure 1.18: Electron and ion foreshock geometry, highlighting the greater area of the electron foreshock due to their relatively high speed. After *Treumann and Baumjohann* (1997).

as such covers a larger area than that of the ions which have a relatively low velocity. This is shown in figure 1.18.

When particles are reflected into the foreshock they excite many instabilities and scatter in velocity space into a kidney beam and, eventually, ring distribution. The dominant instability in the ion foreshock is the AIC right hand resonant instability (*Treumann and Baumjohann*, 1997), however the diffuse ion distribution that results can then drive a left hand resonant instability. Observations at the Earth's quasi-parallel shock have revealed many structures such as shocklets and short large-amplitude magnetic structures (SLAMS), some of which are thought to take part in shock reformation. *Scholer* (1993); *Scholer et. al.* (1993) and *Dubouloz and Scholer* (1995) have performed 1D and 2D hybrid simulations of SLAMS and their interaction with the shock. They conclude that most upstream wave phenomena are different stages of the same process of shock reformation involving SLAMS. More oblique shocks reform on larger scales as the waves steepen and radiate whistlers upon being swept into the existing shock. The process is less coherent along the shock at higher Mach numbers. The formation of SLAMS themselves has been studied by *Dubouloz and Scholer* (1993), who claim that the growth and steepening of a right hand resonant mode scatters the initially backstreaming ions so that a left

hand mode results, and together these generate enhanced magnetic structures on the same scale length as SLAMS.

The result of these structures when they are swept downstream into the region behind the shock has been considered by *Burgess* (1995) and *Scholer et. al.* (1997) who attempted to determine whether the turbulence was due to upstream waves being convected downstream or local generation, via 1D hybrid simulations. They considered nearly parallel shocks and found the aforementioned beam instabilities at around $M_A = 8$. They also detected non resonant right hand ion-ion instabilities in the presence of high beam density and a large velocity discrepancy between it and the flow. At even larger Mach numbers, shock generated waves were found to dominate the turbulence, whilst more oblique shocks than those studied were expected to show dominance of upstream convected waves. The acceleration of protons was also considered for quasi-parallel shocks by *Giacalone et. al.* (1997) when compared to varying Mach number and upstream wave activity. They found low Mach numbers to give poor acceleration with the density compression across the shock being less than that predicted by Rankine-Hugoniot relations. The efficiency did increase with Mach number up to $M_A = 10$, however, and upstream wave activity was found to have no effect on the acceleration efficiency, but did affect the energy going into the acceleration of high energy particles.

The shocks formed at obstacles are caused by different processes: at comets due to massloading; at Venus due to currents in the ionosphere; and at Earth due to the magnetosphere. Some obstacles display many boundaries (see section 1.2.1) and in the last decade bi-ion MHD fluid simulations performed by *Sauer et. al.* (1994, 1995) and *Sauer et. al.* (1996b) have possibly explained these as something akin to shocks of different species: protons and a second heavier species. The results showed

a second boundary behind the initial proton shock which appeared impervious to proton flow, which they labeled "protonopause". The magnetic field penetrates this boundary on the back of the electrons which follow the picked up heavy ions through, and it appears when the density of heavy ions reaches that of the already shocked SW. The BS is seemingly split to give a deflection of protons whilst decelerating the heavy ions' speed to that of the proton flow. This heavier species could be either cometary pickup ions, or SW alpha particles. A similar code used by *Sauer et. al.* (1996c) showed that at lower source rates, magnetoacoustic oscillations produced striations related to periodic formation of discontinuities.

Chapter 2

Plasma Equations

2.1 The Vlasov Equation

This chapter will look at the equations used to describe a plasma, starting with the Vlasov equation. A plasma is represented by a distribution function, $f(\underline{x}, \underline{v}, t)$, which is evolved by the generalized Boltzmann equation from statistical mechanics, as given in equation (2.1) (*Baumjohann and Treumann*, 1996).

$$\frac{\partial f}{\partial t} + \underline{v}.\nabla f + \underline{a}.\nabla_v f = \left(\frac{\partial f}{\partial t}\right)_c \tag{2.1}$$

In equation (2.1), f is the plasma distribution function, whilst $\underline{v}$ and $\underline{a}$ represent velocity and acceleration respectively. The symbol ∇ has its usual meaning, with ∇_v representing differentiation with respect to each velocity component in turn. The term on the right represents interparticle collisional effects on the propagation of f: if it is absent the equation preserves phase space density (see Liouvilles theorem in *Baumjohann and Treumann* (1996)).

2.1.1 Distribution function

The most detailed description available of a plasma is to describe the three spatial and three velocity variables for every particle in the plasma at all time. Such a function is impractical to use, so a reduced, single particle distribution function is considered: if $F(\underline{x}_1, ...\underline{x}_N, \underline{v}_1, ...\underline{v}_N, t)$ is the full description of an N-particle plasma, then the reduced version is given by equation (2.2) (*Krall and Trivelpiece*, 1986).

$$f(\underline{x}, \underline{v}, t) = \int_{-\infty}^{\infty} F d\underline{x}_2 ... d\underline{x}_N d\underline{v}_2 ... d\underline{v}_N \tag{2.2}$$

This gives the probability of a particle being present in any region of phase space at a given time, and is assumed to be a sufficient description as the particle will explore that space. The normalization condition for the existence of the particle is given in equation (2.3).

$$\int_{-\infty}^{\infty} f(\underline{x}, \underline{v}, t) d\underline{x} d\underline{v} = N \tag{2.3}$$

The Vlasov equation is now obtained from equation (2.1) by considering the specific case of a space plasma. Excluding ionospheres, typical space plasmas are effectively collisionless: the mean free path of a particle in the SW is around 1AU. The term on the right is thus set to zero. Additionally, the Lorentz force is substituted for the acceleration of the particles. Acceleration due to interparticle Coulomb interactions is neglected because we assume distances much greater than the Debye length on which these act.

2.1.2 Debye length

As plasmas consist of positively and negatively charged particles, regions of enhanced charge attract opposing particles which then act as a shield. Plasmas are differentiated from other ionized gases by considering this shielding effect when acting on a Coulomb potential. The Debye length is defined in equation (2.4), where T_e and n_e refer to the electron temperature and number density, and other symbols have their usual meaning (*Chen*, 1984).

$$\lambda_D = \sqrt{\frac{k_B T_e \varepsilon_0}{n_e e^2}} \tag{2.4}$$

To qualify as a plasma, the Debye sphere, which has radius λ_D, must contain enough electrons to shield a potential applied at its centre. The Debye shielding thus implies particle motion is dominated by global electric and magnetic fields: the reason that numerical modeling on a grid is a valid description. In most plasmas, λ_D is small compared to the plasma dimensions.

These factors result in the Vlasov equation for the evolution of space plasmas, equation (2.5), in which q and m are the charge and mass of the particle under consideration. It already has some restriction on its use because the plasma must be collisionless.

$$\frac{\partial f}{\partial t} + \underline{v}.\nabla f + \frac{q}{m}(\underline{E} + \underline{v} \times \underline{B}).\nabla_v f = 0 \tag{2.5}$$

The inclusion of electric and magnetic fields in the description also necessitates a method of their calculation: a task fulfilled by the full electrodynamic Maxwells equations listed in equations (2.6) - (2.9) (*Chen*, 1984).

$$\nabla.\underline{B} = 0 \tag{2.6}$$

$$\nabla.\underline{E} = \frac{\rho_q}{\epsilon_0} \tag{2.7}$$

$$\nabla \times \underline{E} = -\frac{\partial \underline{B}}{\partial t} \tag{2.8}$$

$$\nabla \times \underline{B} = \mu_0 \underline{J} + \epsilon_0 \mu_0 \frac{\partial \underline{E}}{\partial t} \tag{2.9}$$

These are given here for a free space medium in which currents and charges are allowed to flow and exist respectively, using the permittivity, ϵ_0, and permeability, μ_0, of free space. Other symbols have their usual meanings, with ρ_q the charge density.

2.2 Fluid Description

The Vlasov equation gives a good description of a plasma, but does not use measurable quantities, such as density and temperature. A fluid description of the plasma describing motion as a whole is more useful.

From the distribution function, $f_\alpha(\underline{x}, \underline{v}, t)$, of ion species α the bulk plasma variables for that species can be found by taking velocity moments (*Krall and Trivelpiece*, 1986). Briefly, variables such as number density that depend only on position and time, can be found from the distribution function, that depends on these plus velocity, by integrating over all velocity space. Successive variables can be found by multiplying $f_\alpha(\underline{x}, \underline{v}, t)$ by velocity an appropriate number of times before integrating. Examples of number density and bulk velocity are given in equations (2.10) and (2.11) (*Krall and Trivelpiece*, 1986).

$$n_\alpha(\underline{x}, t) = \int f_\alpha(\underline{x}, \underline{v}, t) d^3v \tag{2.10}$$

$$\underline{V}_\alpha(\underline{x}, t) = \frac{1}{n_\alpha(\underline{x}, t)} \int \underline{v} f_\alpha(\underline{x}, \underline{v}, t) d^3v \tag{2.11}$$

The sequence is infinite, however those beyond the first few are rarely used: the pressure and heat tensors of a plasma are the next two (*Krall and Trivelpiece*, 1986). Other measurable quantities can be found by modification of these, such as charge density and current density from equations (2.10) and (2.11) respectively. The variables enable the description of a plasma to be reduced to a fluid description, however less detail is produced.

In a similar manner to that described above, moments of the Vlasov equation can also be taken. They give equations of continuity or conservation for the fluid variables. It can be shown that the zeroth order moment of the Vlasov equation results in that of particle number conservation given in equation (2.12) (*Krall and Trivelpiece*, 1986).

$$\frac{\partial n_\alpha}{\partial t} + \nabla.(n_\alpha \underline{V}_\alpha) = 0 \tag{2.12}$$

In equation (2.12) n_α is the number density of the plasma species whilst $\underline{V}_\alpha$ is the bulk velocity, both as found in equations (2.10) and (2.11). Again, successive moments of the Vlasov equation can be taken, the next one results in the conservation of momentum, equation (2.13).

$$m_\alpha n_\alpha \frac{\partial \underline{V}_\alpha}{\partial t} + m_\alpha n_\alpha \underline{V}_\alpha.\nabla \underline{V}_\alpha - n_\alpha q_\alpha (\underline{E} + \underline{V}_\alpha \times \underline{B}) + \nabla.\underline{\underline{P}}_\alpha = 0 \tag{2.13}$$

Equation (2.13) now contains $\underline{\underline{P}}_\alpha$, the pressure tensor. Indeed, each successive moment includes another variable in addition to those in the previous equation. The set of fluid equations always has one more unknown variable than equations to solve for, and are said to lack closure. An extra equation is needed to give a closed set, often an assumption about the pressure as shall be seen in Chapter 3.

Fluid equations are much more practical to use than the Vlasov equation, however as well as assuming a collisionless plasma with dimensions much larger than

the Debye length, the individual particle kinetic effects are lost. A fluid modeled plasma thus loses some physical processes, an obvious example being wave-particle interactions.

2.3 Magnetohydrodynamics

The equations in section 2.2 represent each ion species and electrons separately. MHD attempts to merge all species into a single fluid representation. Firstly, the equations in section 2.2 are reduced to their single fluid counterparts, aided by the definition of single fluid variables given in equations (2.14) - (2.19) (*Krall and Trivelpiece*, 1986).

$$\begin{aligned} n &= \frac{\sum_\alpha n_\alpha m_\alpha}{\sum_\alpha m_\alpha} \\ &= \frac{m_e n_e + m_i n_i}{m_e + m_i} \end{aligned} \tag{2.14}$$

$$\begin{aligned} \rho_m &= \sum_\alpha n_\alpha m_\alpha \\ &= m_e n_e + m_i n_i \end{aligned} \tag{2.15}$$

$$\begin{aligned} \rho_q &= \sum_\alpha n_\alpha q_\alpha \\ &= q(n_i - n_e) \end{aligned} \tag{2.16}$$

$$\begin{aligned} \underline{V} &= \frac{\sum_\alpha n_\alpha m_\alpha \underline{V}_\alpha}{\sum_\alpha n_\alpha m_\alpha} \\ &= \frac{m_e n_e \underline{V}_e + m_i n_i \underline{V}_i}{m_e n_e + m_i n_i} \end{aligned} \tag{2.17}$$

$$\begin{aligned} \underline{J} &= \sum_\alpha q_\alpha n_\alpha \underline{V}_\alpha \\ &= e\left(n_i \underline{V}_i - n_e \underline{V}_e\right) \end{aligned} \tag{2.18}$$

$$\begin{aligned} \underline{\underline{P}} &= \sum_\alpha \overline{n}_\alpha m_\alpha \int (\underline{v} - \underline{V})(\underline{v} - \underline{V}) f_\alpha d\underline{v} \\ &= \overline{n}_e m_e \int (\underline{v} - \underline{V})(\underline{v} - \underline{V}) f_e d\underline{v} + \overline{n}_i m_i \int (\underline{v} - \underline{V})(\underline{v} - \underline{V}) f_i d\underline{v} \end{aligned} \tag{2.19}$$

Equations (2.14) - (2.19) first describe the variable in terms of numerous

different species, α, and then assuming only electrons and a single ionic species. They show the single fluid variables of number density, mass density, charge density, centre of mass velocity, current density and pressure respectively. All symbols have their usual meanings with the pressure variable, the sum of each species' individual centre of mass pressure, using $\overline{n}_\alpha$, the average number density, in the calculation.

The single fluid MHD equations are now found by writing separate fluid equations for each species, multiplying throughout by the appropriate mass, and adding these together. Using the above substitutions, equation (2.20), the MHD equation of continuity, can easily be found.

$$\frac{\partial n}{\partial t} + \nabla n \underline{V} = 0 \tag{2.20}$$

The equation of momentum conservation is complicated by the presence of a nonlinear term, which is dealt with by using $m_e \ll m_i$ and the application of quasineutrality, $n_i \approx n_e$. It is thus implied that the centre of mass of the fluid is that of the ions, whilst quasineutrality requires application on length scales $L \gg \lambda_D$ only, such that local charge concentrations are shielded. The MHD equation for the conservation of momentum is then equation (2.21). MHD also makes use of Ohm's law and, as for the separate fluid equations, requires an equation of closure for the system. The application of quasineutrality also affects the range of the model on a temporal scale.

$$\rho_m \frac{\partial \underline{V}}{\partial t} + \rho_m \left(\underline{V}.\nabla\right) \underline{V} = \rho_q \underline{E} + \underline{J} \times \underline{B} - \nabla.\underline{\underline{P}} \tag{2.21}$$

2.3.1 The plasma frequency

This fundamental frequency concerns oscillations due to charge separation on a minute scale, as shown schematically in figure 2.1. In this block of plasma the

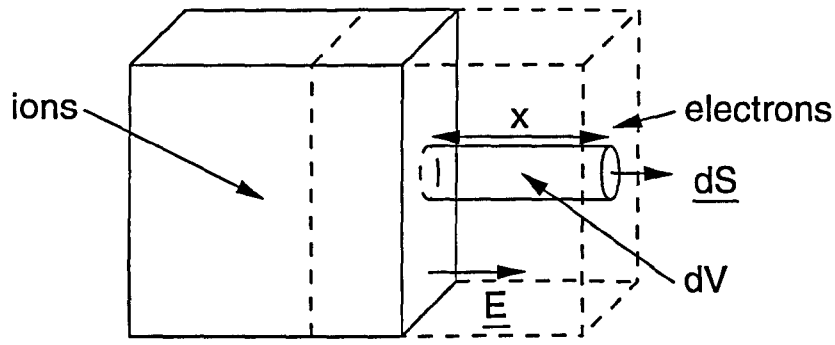

Figure 2.1: Schematic figure of charge separation leading to oscillations at the plasma frequency.

electrons are displaced from the ions, creating a charge separation and electric field. Taking equation (2.7) (Maxwell 2) and integrating over the volume element, dV, gives equation (2.22).

$$\int \nabla . \underline{E} dV = \int \frac{\rho}{\varepsilon_0} dV \tag{2.22}$$

Using Gauss' theorem on the left, and $\rho = -en_e$, $dV = xdS$ on the right, before removing the integrals, gives the electric field as $\underline{E} = \frac{-en_e x}{\varepsilon_0}$. Substitution of this into the Lorentz force law ($\underline{B} = 0$) subsequently gives equation (2.23), which when compared to a standard oscillator equation reveals the frequency of the resulting oscillations, the plasma frequency ω_{pe}, as equation (2.24) (*Chen*, 1984).

$$m_e \frac{d^2x}{dt^2} = \frac{-e^2 n_e x}{\varepsilon_0} \tag{2.23}$$

$$\omega_{pe} = \sqrt{\frac{n_e e^2}{m_e \varepsilon_0}} \tag{2.24}$$

This is given for the electrons as they react quickest to shield a non-uniform charge. On a temporal scale, the assumption of quasineutrality implies considered

times are much greater than $\frac{1}{\omega_{pe}}$, such that a low frequency limit has been taken, $\omega \ll \omega_{pe}$.

The application of a low frequency limit changes equations (2.7) and (2.9) of Maxwells equations. It can be assumed that free charges do not accumulate, $\rho_q = 0$ everywhere, with immediate effect on equation (2.7). Secondly, the displacement current in equation (2.9) can be taken as negligible compared to the conduction current and dropped (*Krall and Trivelpiece*, 1986).

The resulting versions of Maxwells equations (which will also be used for normalization in Chapter 3) are given in equations (2.25) - (2.28). These are valid for consideration of length scales greater than the Debye length, and low frequency phenomena. In a quasineutral plasma, $\nabla.\underline{E}$ is undefined, but we include it here for completeness in the knowledge it is not used in this study.

$$\nabla.\underline{B} = 0 \tag{2.25}$$

$$\nabla.\underline{E} = 0 \tag{2.26}$$

$$\nabla \times \underline{E} = -\frac{\partial \underline{B}}{\partial t} \tag{2.27}$$

$$\nabla \times \underline{B} = \mu_0 \underline{J} \tag{2.28}$$

Note that MHD does not differentiate between the species of ions present and as such is restricted to time and length scales larger than those associated with the gyroradius and gyrofrequency (see section 2.4.1) of the most massive species. This is both the attraction, and a drawback: it enables the modeling of very large scale interactions with relatively little computational resources, whilst it also means all of the microphysics is lost. This drawback leads to the use of intermediate schemes as shall be discussed in section 2.4.

2.3.2 Magnetic Reynolds number

Ideal MHD also gives the phenomenon of a "frozen in" magnetic field for space plasmas (*Krall and Trivelpiece*, 1986). Substituting for $\underline{E}$ from Ohm's law in equation (2.27), before substituting for $\underline{J}$ from equation (2.28) and using an appropriate vector identity results in equation (2.29) (*Krall and Trivelpiece*, 1986).

$$\frac{\partial \underline{B}}{\partial t} = \nabla \times (\underline{V} \times \underline{B}) + \frac{\eta}{\mu_0} \nabla^2 \underline{B} \tag{2.29}$$

The magnetic Reynolds number, R_M, is now defined by comparing the strengths of the two terms on the right of equation (2.29), to give equation (2.30). In this, L is the length scale over which the conditions under consideration exist. Space plasmas usually have $L \to \infty$, so equation (2.30) generally gives $R_M \gg 1$ — corresponding to a negligible diffusion scenario where the second term on the right of equation (2.29) approaches zero. Most space plasmas are then said to have the magnetic field "frozen in", giving implications for such things as field line draping at obstacles.

$$R_M = \frac{V \mu_0 L}{\eta} \tag{2.30}$$

2.3.3 Plasma beta

This is another parameter used to describe a plasma, the ratio of thermal to magnetic pressure. It is given by equation (2.31) strictly only for a plasma that is in isotropic equilibrium and quasineutral (*Baumjohann and Treumann*, 1996). It uses the magnetic field strength, B, and isotropic pressure, p. In non-isotropic plasmas, where pressure is a tensor value, separate pressures perpendicular or parallel to the magnetic field can be used to give corresponding values of β. Different species within a plasma may also have different β due to different thermal conditions.

$$\beta = \frac{2\mu_0 p}{B^2} \tag{2.31}$$

2.4 Hybrid Description

The code used in this study is a hybrid of fluid equations for the electrons and a representation of $f(\underline{x}, \underline{v}, t)$ for the ions. Vlasov codes which solve for f in velocity space exist, but their resolution is generally more difficult than that of a particle-in-cell (PIC) technique, which approximates f by a series of uniform height delta-functions, one at each location in phase space occupied by a meta-particle in the simulation. For N meta-particles the formal description is given by equation (2.32).

$$f(\underline{x}, \underline{v}, t) = \frac{1}{N} \sum_{1}^{N} \delta\left(\underline{v} - \underline{v}_{\#}(t)\right) \delta\left(\underline{x} - \underline{x}_{\#}(t)\right) \tag{2.32}$$

In such a description the peaks of a given (e.g. Maxwellian) distribution are well resolved by many delta-functions, whilst the physically important tails are less so. It is important to ensure these areas are adequately represented by using more meta-particles. The validity of the plasma approximation allows this description, in which meta-particles move around a grid under the influence of field values calculated on the corners of each cell and interpolated to their position. All the microphysics is kept in the simulation to the level afforded by the dynamic range of the distribution function representation. The drawback is the computational expense at representing many meta-particles.

Hybrid codes maintain as much kinetic-scale physics as possible whilst allowing large simulations to be performed using practical resources, by representing one or more of the heavier ion species using PIC techniques and saving computationally by using a fluid description of the rest.

The code used in this study represents two species of ions using PIC techniques: the SW protons and heavy source ions. This partially frees it from the MHD restrictions: the length scales of the heaviest ions are now included kinetically. The restriction still holds for the heaviest particles using a fluid description, however as $m_e \ll m_i$, this still gives a far greater range of physics than MHD. The electrons are described by the fluid momentum equation (2.13), with one more approximation: they are inertialess, $m_e \to 0$. This means no electron cyclotron resonance occurs in the simulation, and the Fourier domain is numerically damped (*Press et. al.*, 1986). Taking equation (2.13) for an electron fluid, and using this approximation gives equation (2.33). Here, $\underline{V_i}$ is the ion bulk velocity, used in substitution for the electron bulk velocity by equation (2.34), under conditions of quasineutrality.

$$\underline{E} = -\underline{V_i} \times \underline{B} + \frac{1}{en_e}\left(\underline{J} \times \underline{B} - \nabla.\underline{\underline{P_e}}\right) \tag{2.33}$$

$$\underline{J} = e\left(n_i\underline{V_i} - n_e\underline{V_e}\right) \tag{2.34}$$

The source ions and SW protons are treated kinetically using the Lorentz equations of motion, equations (2.35) and (2.36), which treat particles (numbered by #) on an individual basis.

$$\underline{v_\#} = \frac{d\underline{x}_\#}{dt} \tag{2.35}$$

$$m_\# \frac{d\underline{v}_\#}{dt} = q_\#\left(\underline{E} + \underline{v}_\# \times \underline{B}\right) \tag{2.36}$$

2.4.1 Gyrofrequency

Assume the fields in equation (2.36) are constant. Then, by writing $\underline{v}_\# = \underline{v}_{\#\perp} + \underline{v}_{\#\|}$, substituting and separating into two separate equations, it immediately becomes

apparent that the particle experiences constant acceleration parallel to the magnetic field. For the perpendicular motion, it helps to perform the frame transformation $\underline{v}_{\#\perp} = \underline{v}'_{\#\perp} + \underline{v}_d$, such that $\underline{v}_d \times \underline{B} = -\underline{E}_\perp$ ($\underline{v}_d$ is the electric field drift velocity). Substitution of this into the perpendicular equation results in equation (2.37), in which the gyrofrequency equation (2.38), has already been substituted.

$$\frac{d\underline{v}'_{\#\perp}}{dt} = \underline{v}'_{\#\perp} \times \underline{\Omega}_{\#} \tag{2.37}$$

$$|\underline{\Omega}_{\#}| = \frac{eB}{m_{\#}} \tag{2.38}$$

This is the frequency in radians/second of the particles orbital motion around the field line. Finally, by letting $\underline{v}'_{\#\perp} = \frac{d\underline{R}_{g\#}}{dt}$ and substituting for the first term on the right of equation (2.37) before integrating and rearranging, the particles gyroradius given in equation (2.39) can be found.

$$R_{g\#} = \frac{|\underline{v}'_{\#\perp}|}{|\underline{\Omega}_{\#}|} = \frac{m_{\#} v_{\#\perp}}{eB} \tag{2.39}$$

The gyrofrequency (or cyclotron frequency) and gyroradius are thus particle specific (*Baumjohann and Treumann*, 1996). In a constant electric field, a drift motion, $\underline{v}_d$, of the guiding centre is also experienced.

Equations (2.27) and (2.28) from Maxwell's equations complete the set used in this study. The code allows for heavy ion/proton - wave interactions to be represented yet needs fewer resources than a full PIC simulation. Consequently, there is a balance between the computational requirement for the code, and the physics it can resolve. The global simulations of small body interactions with the SW presented here include physics down to the the scale of the SW proton motion.

Chapter 3

Structure of Study

3.1 Simulations Performed

This study aims to determine the global momentum transfer mechanisms present at interactions of the SW with small bodies such as comets and small magnetized obstacles. Three distinct sets of simulations were performed, distinguished by the source region represented in each. These lead up to a pilot study for a Mercury type obstacle via a cometary source and an absorbing planet with a weak ionosphere. This progression allows comparison between the results at each stage and a more informative analysis of the mechanisms occurring.

Throughout, the source regions are referred to as being "small-scale". This description refers to the spatial extent of the source region being of the order of a heavy ion gyroradius in undisturbed flow. This is a characteristic scale length of such plasma interactions, and so the physics produced by such obstacles can prove interesting. The simulations are performed using normalized units of the system, so can be scaled to other obstacles. This generality means comparisons with Grigg-Skjellerup and Venus, in addition to Mercury are possible.

The code used is a 2D (or $2\frac{1}{2}$D) hybrid code. It considers the electrons

as a charge-neutralizing fluid whilst the SW protons and heavy source ions are represented by meta-particles following the Lorentz equations of motion around a 2D grid. This allows resolution of the ion dynamics and hence a greater range of physics than possible with a two-fluid, or MHD simulation. The study is thus able to detect ion kinetic scale mechanisms for momentum transfer.

3.2 Code Algorithm

Codes such as that used here are sometimes referred to as $2\frac{1}{2}$D (*Lipatov et. al.*, 1997) as all vectors are calculated self-consistently in $3D$, but are functions of only x and y. This restriction to a 2D plane affords better simulation control: certain processes can be eliminated by altering the field orientation. This keeps the physics simpler when trying to answer a specific question, but means that certain comparisons between simulation and data (such as BS stand-off distance) are unsafe.

3.2.1 Normalization used

Like most scientific computer simulations this code uses normalized variables instead of those measured in real units to generalize the results. On the equations governing the plasma (see section 2.4) we choose the normalizations listed in equations (3.1) - (3.8).

$$t' = t\Omega_p \tag{3.1}$$

$$\underline{x}' = \underline{x}\frac{\Omega_p}{v_A} \tag{3.2}$$

$$\underline{v}' = \frac{\underline{v}}{v_A} \tag{3.3}$$

$$\rho' = \frac{\rho}{\rho_0} \tag{3.4}$$

$$\underline{B}' = \frac{\underline{B}}{B_0} \tag{3.5}$$

$$\underline{E}' = \frac{\underline{E}}{v_A B_0} \tag{3.6}$$

$$\underline{J}' = \frac{\underline{J} m_p}{v_A \rho_0 e} \tag{3.7}$$

$$P_e' = \frac{P_e \mu_0}{B_0^2} \tag{3.8}$$

Unprimed variables refer to the parameter in question measured in SI units, primed versions to the normalized variable. Equations (3.1) - (3.8) give the normalized versions of time, space, velocity, mass density, magnetic field, electric field, current density and electron pressure respectively. In addition they utilize the proton cyclotron frequency, equation (2.38), the Alfvén velocity, equation (3.9), and a substitution for the the permeability of free space given in equation (3.10). Mass is normalized to one proton mass, m_p, whilst the values of ρ_0 and B_0 are fixed unitary quantities representing the initial mass density and IMF strength respectively.

$$v_A = \frac{B_0}{\sqrt{\mu_0 \rho_0}} \tag{3.9}$$

$$\mu_0 = \frac{B_0^2}{v_A^2 \rho_0} \tag{3.10}$$

When applied to the plasma equations listed in section 2.4, the normalized equations found for use in the code are equations (3.11) - (3.15).

$$\frac{d\underline{x}'_{\#}}{dt'} = \underline{v}'_{\#} \tag{3.11}$$

$$\frac{d\underline{v}'_{\#}}{dt'} = \frac{1}{m}\left(\underline{E}' + \underline{v}'_{\#} \times \underline{B}'\right) \tag{3.12}$$

$$\nabla' \times \underline{E}' = -\frac{\partial \underline{B}'}{\partial t'} \tag{3.13}$$

$$\nabla' \times \underline{B}' = \underline{J}' \tag{3.14}$$

$$\underline{E}' = -\underline{V}'_i \times \underline{B}' + \frac{1}{\rho'}\left(\underline{J}' \times \underline{B}' - \nabla' P'_e\right) \tag{3.15}$$

Symbols with "#" as a subscript refer to values attached to a particular particle, whilst ∇' is the normalized version (using the inverse normalization of x') of grad. The variable V'_i is the normalized ionic bulk velocity. Equations (3.11) and (3.12) are the normalized Lorentz equations of motion; equations (3.13) and (3.14) are low frequency, normalized versions of two of Maxwells equations (see section 2.3); and equation (3.15) is for calculating the electric field, and derived from electron momentum considerations (see section 2.4).

3.2.2 Description of simulation algorithm

Equations (3.11) - (3.15) are used to iterate the particle positions, velocities and the field values forward in time. They are not a closed set due to the presence of P_e in equation (3.15) (see section 2.2). Hence, one more equation is needed and in the hybrid code used here, this is to set the electron pressure, P_e, constant according to equation (3.16), where β_e refers to the electron plasma parameter defined in equation (2.31). Note that as only the gradient of P_e is present in equation (3.15), a similar effect could be achieved by setting $P_e = 0$.

$$P'_e = \rho_0 \beta_e \tag{3.16}$$

Before the description of the code algorithm, clarification of what each variable refers to and how they are labeled is given. Two types of variable are present in the calculation: particle variables stored in arrays of size $\sim 10^6$ values (one per particle); and grid variables stored in arrays of size $\sim 10^4 - 10^5$ values (one per grid cell). Few particle variables are used: position (in 2D) and velocity (in 3D) for each particle. Other variables such as magnetic field, mass density, electric field, and bulk velocity of each species are grid variables. In the description that follows, particle variables are denoted by a subscript "#" to imply an individual particle number. Grid based variables are denoted by a subscript "ij" for the i^{th} row and j^{th} column of the grid. The timestep at which each variable is known or required is displayed as a superscript value such as "$n+1$", but due to the algorithm used, some quantities are found on the half-timestep only (*Terasawa et. al.*, 1986; *Hockney and Eastwood*, 1981). All variables are normalized, however the primes will be dropped here and throughout for clarity.

Each iterative step conveniently breaks into three stages: advancing the particle positions; updating the magnetic field; and advancing the particle velocities.

Advancing the particle positions

At the start of each timestep the values of only a limited number of variables are known: the position and velocity of each meta-particle, $\underline{x}_{\#}^{n}$ and $\underline{v}_{\#}^{n+\frac{1}{2}}$, and the grid variables of magnetic field and mass density, $\underline{B}_{ij}^{n}$ and ρ_{ij}^{n}. Additionally, the constant value of $\underline{P}_{ij}^{n}$ is known. Stage 1 is to leapfrog the particle positions onwards using their velocities at the half timestep (*Birdsall and Langdon*, 1991), via a centre-differenced expansion of equation (3.11), giving equation (3.17).

$$\underline{x}_{\#}^{n+1} = \underline{x}_{\#}^{n} + \Delta t \underline{v}_{\#}^{n+\frac{1}{2}} + O\left(\Delta t^3\right) \tag{3.17}$$

The last term on the right hand side of equation (3.17) gives the level of accuracy in this differenced equation with regards to the timestep, Δt. The code is second order accurate, as will be seen. As the leapfrog scheme is symplectic (area preserving in phase space) this level of accuracy suffices. Equation (3.17) calculates the new position at timestep $n+1$ for each particle, from its old position and velocity. This occurs for all SW protons and heavy source ions present in the grid, with x and y components treated independently.

The updated positions are now used in the calculation of bulk plasma variables at the grid points: the mass density and bulk ionic velocity, which are needed for stage 2. These depend on $f_i(\underline{x}, \underline{v}, t)$, and are found by use of a shape function to interpret the effect of each meta-particle on the bulk variables at its neighbouring grid cells. A second order shape function is employed, $S(X, Y)$, more details of which can be found in *Birdsall and Langdon* (1991). It applies a weighting to the nine nearest grid cells from each meta-particle dependent upon their distance from it: the meta-particle has less influence at more distant cells, but the total weighting of each meta-particle within a species is equivalent.

Mass density is calculated first, via equation (3.18) as it is needed for substitution into the bulk velocity calculation, equation (3.19). The summations are over all meta-particles, and the variable g is a weighting factor dependent upon the species of the particle concerned. After stage 1, the new meta-particle positions, and the grid variables of mass density and bulk velocity are known.

$$\rho_{ij}^{n+1} = \sum_{\#} gS\left(X_j - x_{\#}^{n+1}, Y_i - y_{\#}^{n+1}\right) + O\left(dx^3\right) \tag{3.18}$$

$$\underline{V}_{ij}^{n+\frac{1}{2}} = \sum_{\#} \frac{\underline{v}_{\#}^{n+\frac{1}{2}} g\left(S\left(X_j - x_{\#}^{n+1}, Y_i - y_{\#}^{n+1}\right) + S\left(X_j - x_{\#}^{n}, Y_i - y_{\#}^{n}\right)\right)}{\left(\rho_{ij}^{n+1} + \rho_{ij}^{n}\right)} + O\left(dx^3\right) \tag{3.19}$$

Updating the magnetic field

Stage 2 involves the calculation of the magnetic field at timestep $n+1$, using equations (3.13), (3.14) and (3.15). Equation (3.15) is used to substitute for $\underline{E}$ in equation (3.13), before Ampérès law, equation (3.14), is used to eliminate $\underline{J}$ from the result. After these substitutions equation (3.20), suitable for the calculation of $\underline{B}_{ij}^{n+1}$ is found.

$$\frac{\partial \underline{B}}{\partial t} = \nabla \times \left[\underline{V}_i \times \underline{B} - \frac{(\nabla \times \underline{B}) \times \underline{B}}{\rho} + \frac{\nabla P_e}{\rho}\right] \tag{3.20}$$

As the magnetic field is present on both sides of this equation a rational Runge-Kutta algorithm (*Wambecq*, 1978; *Terasawa et. al.*, 1986) is used to solve it. This solves for $\underline{B}_{ij}^{n+1}$ by starting from $\underline{B}_{ij}^{n}$, so the square brackets of equation (3.20) should effectively contain "$\underline{E}_{ij}^{n+\frac{1}{2}}$". This requires the use of $\underline{V}_{ij}^{n+\frac{1}{2}}$ and $\rho_{ij}^{n+\frac{1}{2}}$, of which only $\underline{V}_{ij}^{n+\frac{1}{2}}$ has already been found. Because of this $\rho_{ij}^{n+\frac{1}{2}}$ is found by a simple time average at each grid cell, equation (3.21). Substitution of both the bulk velocity and mass density at each grid cell into equation (3.20) and the subsequent solution for $\underline{B}_{ij}^{n+1}$ is then possible. Rational Runge-Kutta is accurate up to and including terms second order in time, so gives $\underline{B}_{ij}^{n+1} + O\left(\Delta t^3\right)$.

$$\rho_{ij}^{n+\frac{1}{2}} = \frac{\rho_{ij}^{n+1} + \rho_{ij}^{n}}{2} \tag{3.21}$$

Advancing the particle velocities

This stage calculates the particles new velocities on the next half-timestep and is potentially the most complicated as it involves the extrapolation of grid variables to the particles exact position via an inverse shape function. It therefore also takes up substantial computing resources. The calculation uses equation (3.12), and similarly to stage 2, equations (3.15) and (3.14) are used to substitute for the electric field and current density respectively, to give equation (3.22).

$$\frac{d\underline{v}_{\#}}{dt} = \frac{1}{m}\left\{\left[-\underline{V}_i \times \underline{B} + \frac{1}{\rho}\left((\nabla \times \underline{B}) \times \underline{B} - \nabla P_e\right)\right] + \underline{v}_{\#} \times \underline{B}\right\} \tag{3.22}$$

1. As the calculation will find $\underline{v}_{\#}^{n+\frac{3}{2}}$ from $\underline{v}_{\#}^{n+\frac{1}{2}}$ we require the square brackets to effectively contain "$\underline{E}_{ij}^{n+1}$" this time, and hence need ρ^{n+1} and $\underline{V}^{n+1}$ (no "ij" subscripts as these need extrapolation to the particles exact location) for use in equation (3.22). Now, ρ_{ij}^{n+1} is known, but not $\underline{V}_{ij}^{n+1}$. An estimate is required: an act complicated by the fact $\underline{V}_{ij}^{n+\frac{3}{2}}$ is still unknown. Consequently, equation (3.23) is used.

$$\underline{V}_{ij}^{n+1} = \frac{3\underline{V}_{ij}^{n+\frac{1}{2}} - \underline{V}_{ij}^{n-\frac{1}{2}}}{2} + O\left(\Delta t^2\right) \tag{3.23}$$

2. The mass density, bulk velocity and magnetic field values used in equation (3.22) are required to be known at the exact position of the particle — not just on grid points. An inverse shape function (*Birdsall and Langdon*, 1991) is used to reverse the process applied in stage 1 to calculate such grid variables, as shown in equation (3.24).

$$\underline{B}^{n+1} = \sum_j \left(\sum_i \underline{B}_{ij}^{n+1} S\left(X_j - x_{\#}^{n+1}, Y_i - y_{\#}^{n+1}\right)\right) + O\left(dx^3\right) \tag{3.24}$$

3. The final term on the right hand side of equation (3.22) uses the particles individual velocity, however this too is needed at timestep "$n+1$" so an average as

shown in equation (3.25) is made. This contains the updated particle velocity, $\underline{v}_{\#}^{n+\frac{3}{2}}$, which is unknown as yet.

$$\underline{v}_{\#}^{n+1} = \frac{\underline{v}_{\#}^{n+\frac{1}{2}} + \underline{v}_{\#}^{n+\frac{3}{2}}}{2} \tag{3.25}$$

Upon substitution of equation (3.25); the position-wise extrapolated values of mass density, bulk velocity, equation (3.23) and magnetic field, equation (3.24); and the application of centred-differencing to the left hand side of equation (3.22), equation (3.26) results.

$$\begin{aligned} \frac{\underline{v}_{\#}^{n+\frac{3}{2}} - \underline{v}_{\#}^{n+\frac{1}{2}}}{\Delta t} &= \frac{1}{m}\left\{-\underline{V}^{n+1} \times \underline{B}^{n+1} + \frac{1}{\rho^{n+1}}\left[(\nabla \times \underline{B}^{n+1}) \times \underline{B}^{n+1} - \nabla P_e\right]\right\} \\ &+ \frac{1}{m}\left\{\left(\frac{\underline{v}_{\#}^{n+\frac{1}{2}} + \underline{v}_{\#}^{n+\frac{3}{2}}}{2}\right) \times \underline{B}^{n+1}\right\} + O\left(\Delta t^2\right) \end{aligned} \tag{3.26}$$

Rearranging all unknowns to the left hand side then gives equation (3.27).

$$\begin{aligned} \underline{v}_{\#}^{n+\frac{3}{2}} - \left(\underline{v}_{\#}^{n+\frac{3}{2}} \times \frac{\Delta t \underline{B}^{n+1}}{2m}\right) &= \underline{v}_{\#}^{n+\frac{1}{2}} + \frac{\Delta t}{m}\left[\left(\frac{\underline{v}_{\#}^{n+\frac{1}{2}}}{2} - \underline{V}^{n+1}\right) \times \underline{B}^{n+1}\right] \\ &+ \frac{\Delta t}{m\rho^{n+1}}\left[(\nabla \times \underline{B}^{n+1}) \times \underline{B}^{n+1} - \nabla P_e\right] \\ &+ O\left(\Delta t^3\right) \end{aligned} \tag{3.27}$$

Note that the error from equation (3.23) is multiplied by a further Δt to give accuracy to terms in second order. Equation (3.27) can now be written in matrix form. The right hand side contains only known quantities and the left can be written as a product of two matrices: a column matrix containing the desired solutions of $\underline{v}_{\#x}^{n+\frac{3}{2}}$, $\underline{v}_{\#y}^{n+\frac{3}{2}}$ and $\underline{v}_{\#z}^{n+\frac{3}{2}}$, and a square matrix involving terms of $\frac{\Delta t B^{n+1}}{2m}$. Applying the inverse of this matrix to both sides of the equation then yields solutions for the three components of the particles velocity.

After an iterative step, the variables known are $\underline{x}_{\#}^{n}$, $\underline{x}_{\#}^{n+1}$, $\underline{v}_{\#}^{n+\frac{1}{2}}$, $\underline{v}_{\#}^{n+\frac{3}{2}}$, $\underline{B}_{ij}^{n}$, $\underline{B}_{ij}^{n+1}$, ρ_{ij}^{n}, ρ_{ij}^{n+1}, $\underline{V}_{ij}^{n+\frac{1}{2}}$, and an estimate of $\underline{V}_{ij}^{n+1}$. In addition, other values such as the current density, electric field, and electron bulk velocity are written out at opportune points to data files. The timestep ends by reassigning the new values as old and starting again from stage 1.

3.3 Computational Limitations

Applying a numerical scheme to a physical problem involves discretization by the application of a spatial grid and iterative advancement of the solution. Additionally, the distribution function is represented in this study by meta-particles. These approximations imply restrictions on resolution, information transfer speed and frequency which affect the solution stability, and are summarized here.

3.3.1 Nyquist frequency

The choice of grid cell and timestep size affects the frequencies a simulation will be capable of transmitting. In real co-ordinates this corresponds to the requirement for adequate resolution. By setting discrete divisions, a limit is placed on the sampling available: waves can only be sampled at grid cells. Any with a higher frequency (smaller wavelength) will be undetectable, or indistinguishable from longer wavelengths. Discretized time and space thus partitions ω-k space into allowed and unstable frequencies. The lower limits are prescribed by the total size of the grid and the length of the run: more timesteps and a larger grid allow lower frequencies to be measured. Equation (3.28) shows the general form of a Fourier series frequency, from which maxima and minima can be found (*Garcia*, 1994).

$$f_k = \frac{k-1}{N\Delta x} \tag{3.28}$$

The region of detectable frequencies is reduced further by aliasing (*Garcia*, 1994). Different frequencies at symmetrically opposite ends of the spectrum available according to equation (3.28) produce the same transform as their counterpart making them indistinguishable. The result is that the maximum frequency a Fourier transform of data with timestep Δt could resolve is halved from that given by taking $k = N$ in equation (3.28), to the Nyquist frequency given in equations (3.29) and (3.31). The factor of 2π in these equations is due to them corresponding to angular frequencies in the simulations presented here. Aliasing also applies to spatial frequencies, or wavenumber, k, such that the maximum and minimum frequencies that are stable in these simulations are given by equations (3.29) - (3.32).

$$\omega_{\max} = \frac{2\pi}{2\Delta t} \tag{3.29}$$

$$\omega_{\min} = \frac{2\pi}{N\Delta t} \tag{3.30}$$

$$k_{\max} = \frac{2\pi}{2\Delta x} \tag{3.31}$$

$$k_{\min} = \frac{2\pi}{N_x\Delta x} \tag{3.32}$$

The electrons in the hybrid code are treated using fluid equations, and as such do not suffer resolution criteria. However, the requirement that the Nyquist frequencies in space and time be large enough that the available ω-k space can readily accommodate the proton cyclotron frequency branch of the dispersion relation translates, in real co-ordinates, to a resolution condition on the motion of the proton meta-particles at small scales, as given in equations (3.33) and (3.34).

$$\Delta t < \Omega_p^{-1} \tag{3.33}$$

$$\Delta x < R_{gp} \tag{3.34}$$

Here Ω_p and R_{gp} are as defined in section 2.4.1. If these are met at small scales for the protons, they are automatically met for the source ions. Their resolution at large extremes of length and time is dictated by the minimum frequencies in ω-k space given by equations (3.30) and (3.32). These translate to real co-ordinates by ensuring the motion fits adequately within the simulation grid and that the simulation proceeds long enough for that motion to evolve.

What if frequencies are excited outside this stable range? Although the hybrid algorithm assumes a low frequency regime (see Chapter 2), a smoothing function is employed to aid the elimination of high frequency noise that could become unstable. It is given in equation (3.35) and is applied to the magnetic field every 40 timesteps and to the mass density, ρ_{ij}, every 50 timesteps. It distributes the value at any given cell over its eight nearest neighbours, with weightings as shown in figure 3.1, to filter out spurious peaks (*Birdsall and Langdon*, 1991).

$$\begin{aligned} \underline{B}^n_{ij}\,(smoothed) \;=\; & \frac{1}{16}\left[4\underline{B}^n_{ij} + 2\left(\underline{B}_{i-1,j} + \underline{B}_{i+1,j} + \underline{B}_{i,j-1} + \underline{B}_{i,j+1}\right)\right] + \\ & \frac{1}{16}\left(\underline{B}_{i-1,j-1} + \underline{B}_{i-1,j+1} + \underline{B}_{i+1,j-1} + \underline{B}_{i+1,j+1}\right) \end{aligned} \tag{3.35}$$

Such peaks could be caused by too low a dynamic range of the plasma distribution function. Using only a limited number of particles per cell (p.p.c.) as a representation means the simulation could drop below the lower limit of one particle per cell, particularly in simulations which produce a wake. Even dropping near this limit could produce unstable values for the mass density in cells concerned, which in turn would affect other quantities via its use as a denominator in equation (3.15). Ideally, sufficient representation of $f(\underline{x}, \underline{v}, t)$ would prevent this, although the limit

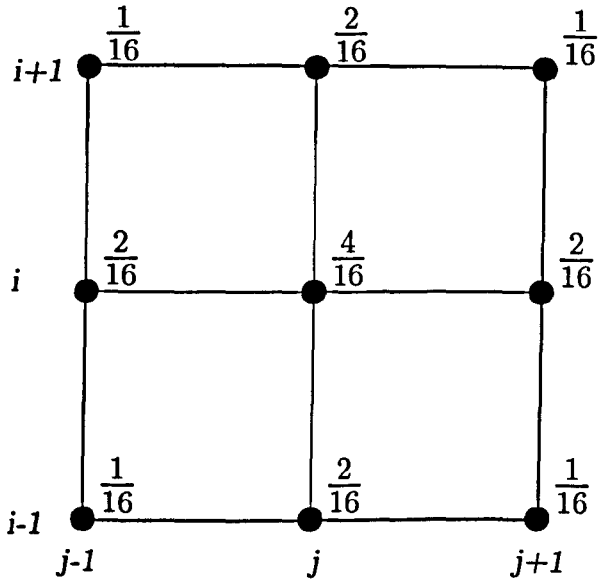

Figure 3.1: The weighting applied to each of a cells eight nearest neighbours and itself in the smoothing function given in equation (3.35).

of the technique means it can never be ruled out. Consequently the code enforces a minimum density of one fifth the initial value in all cells. This unphysical correction is recorded whenever it occurs, so that an assessment of the solutions validity can be made.

3.3.2 Stability conditions

This hybrid code is in a low frequency regime so the algorithm does not allow the excitation of physical effects at frequencies outside the range of the Nyquist frequencies: these are naturally damped. However, there are other stability conditions that are necessary over the whole range of solutions.

The foremost of these is the Courant condition (*Garcia*, 1994), which concerns the rate of information transfer across the simulation grid and is given in equation (3.36). Here Δx and Δt represent the grid cell size and timestep respectively, whilst $v_{\#}$ and v_{ϕ} represent the maximum velocities of particles and waves

within the simulation. In reality it is rare to know the maximum velocities *a priori*, as there may be energization mechanisms present that accelerate particles beyond the Courant velocity leading to unphysical wave growth. An estimate is then made which accommodates most, but maybe not all particles within the Courant condition. To manage this eventuality the hybrid code counts those particles violating equation (3.36), halves their velocity and records the number of such occurrences. Providing such violations are kept to a minimum, the solution should still be valid.

$$\frac{\Delta x}{\Delta t} > v_{\#}, v_{\phi} \tag{3.36}$$

Statistical noise will always be present in the simulation due to the representation of the plasma distribution function by meta-particles. This must be sufficiently well represented to ensure that effects seen in the simulations are due to the instability of non-linear physical processes, rather than growth of this numerical noise. In particular, unstable velocity distributions that could lead to wave energization should be well resolved, however these too cannot be predicted *a priori*. Such key areas of phase space have been shown to have an exaggerated effect on outcomes if not properly resolved (*Leroy et. al.*, 1981, 1982).

Statistically, the number of p.p.c., n, will vary at any time by $\pm\sqrt{n}$. This in turn will affect the noise generated in bulk plasma variables in stage 1 of an iterative step which will scale according to $\pm\frac{1}{\sqrt{n}}$. This can then proliferate through all the other linearized equations. An obvious preference, then, is for a large number of p.p.c., however this carries unfavourable implications with regards to computer resources needed. A figure of 25 p.p.c. is considered sufficient for the hybrid code in this study to maintain accuracy. However, increasing this to 100 p.p.c. and repeating the simulation serves two purposes: the resulting solution contains less noise and, more importantly, a comparison of the two data sets will reveal if any features

present in the first were caused by statistical noise growth, due to their reduced presence in the second. Physically generated instabilities will remain unchanged in both simulations. Most of the results presented here use 100 p.p.c., after initially being performed with 25 p.p.c.

All the possible sources of non-physical instabilities discussed in this section mean proof is required that physically produced phenomena aren't hidden by numerical noise. If one perturbs quantities of density, magnetic field and bulk velocity in the ideal MHD equations, assumes wave like solutions, and linearizes the resulting equations, it is possible to obtain dispersion relations for waves propagating along the magnetic field (*Baumjohann and Treumann*, 1996). That for low frequency Alfvén waves is given in equation (3.37).

$$\omega \approx k v_A \tag{3.37}$$

At higher frequencies two branches separate off from this to form the ion cyclotron wave and whistlers, given by equation (3.38).

$$\omega = \Omega_p, \frac{k^2 v_A^2}{\Omega_p} \tag{3.38}$$

It should be possible to generate this dispersion relation using the hybrid code in this study, except for the high frequency response of the electron whistler branch which, due to a fluid description, will never level off on an ω-k plot (see section 2.4). To ensure this dominates any instability due to numerical noise, the 2D grid was filled entirely with SW protons flowing in the x-direction with $B_{IMF} = B_y$. No source was present. A B_x Gaussian perturbation, and similar distortion to the particle velocities in the region of this Gaussian was then added to the underlying field and velocity distribution. The width of the disturbance was such that it would

decay to excite a range of wavenumbers, and the magnitude of both the magnetic and velocity perturbations obeyed Walens relation (*Baumjohann and Treumann*, 1996). The simulation was then started, during which the Gaussian decayed into a spectrum of wave modes. Magnetic field data near the outflowing edge of the simulation was recorded in 1D (parallel to the outflow edge) and throughout time. Afterwards, a 2D Fourier transform was taken of this data, the result of which is displayed in figure 3.2. This clearly shows the dominance of the low frequency Alfvén branch described by equation (3.37), and the splitting of this into the two branches described in equation (3.38), over any numerical instability growth. The high frequency response is also sufficiently attenuated before the Nyquist frequency on each axis.

3.4 Simulation Geometry

3.4.1 Co-ordinate system

The simulations use an object centred solar ecliptic co-ordinate system with the source region centred at (0,0) in the 2D grid, which represents the solar ecliptic plane. The IMF is then alternated between lying in the plane, $B_{IMF} = B_y$, or perpendicular to it, $B_{IMF} = -B_z$, to give two perspectives of an essentially 3D problem. The SW flow is from $-x$ to $+x$, as shown in figure 3.3.

Distances are normalized to units of proton inertial lengths, $\frac{v_A}{\Omega_p}$, but the diagrams in this thesis have axes that give distances in terms of the heavy ion gyroradii in undisturbed flow, to emphasize the scaling relationship. Note that this unit is dependent upon the SW flow velocity due to the pickup process and so is different for the high velocity and low velocity simulations.

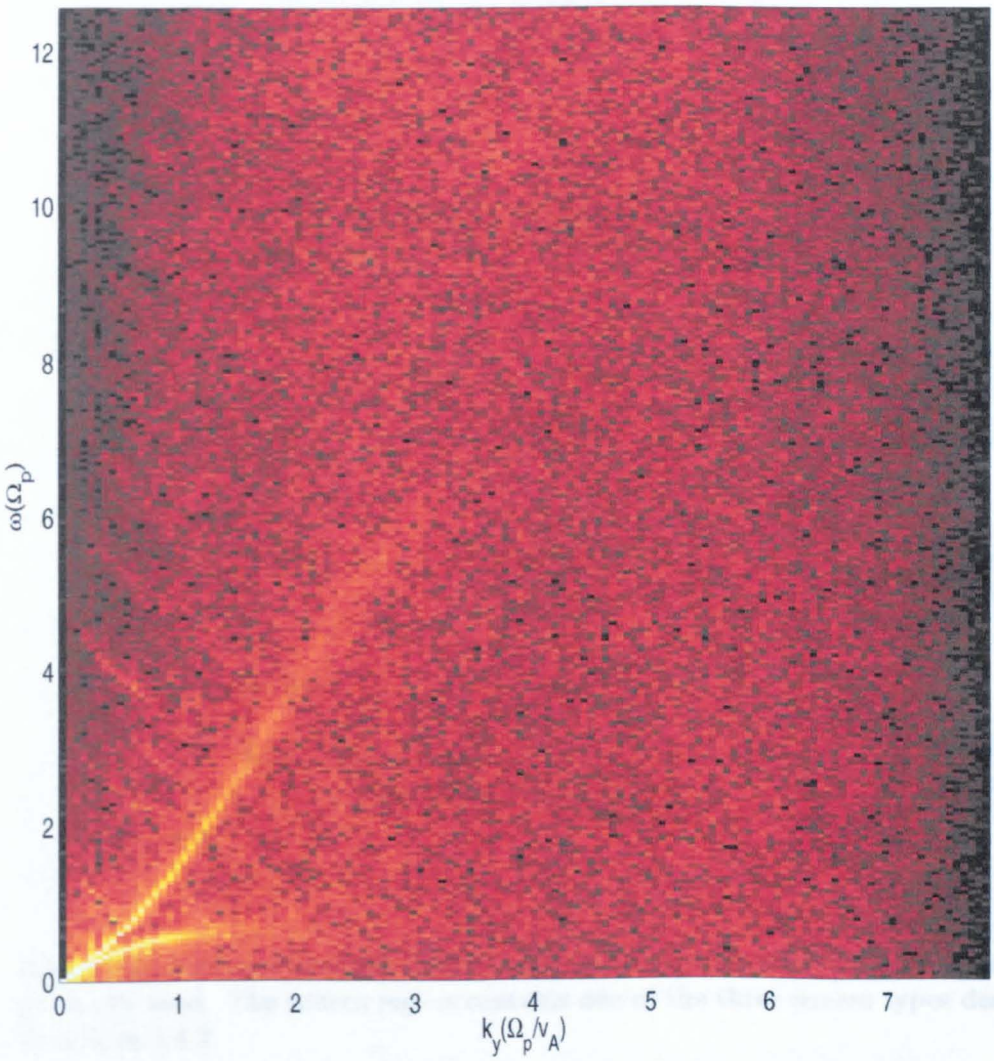

Figure 3.2: Plot of ω versus k from a simulation set up to excite parallel propagating waves. The dispersion relation of Alfvén waves can clearly be seen separating into those of ion-cyclotron and whistler waves.

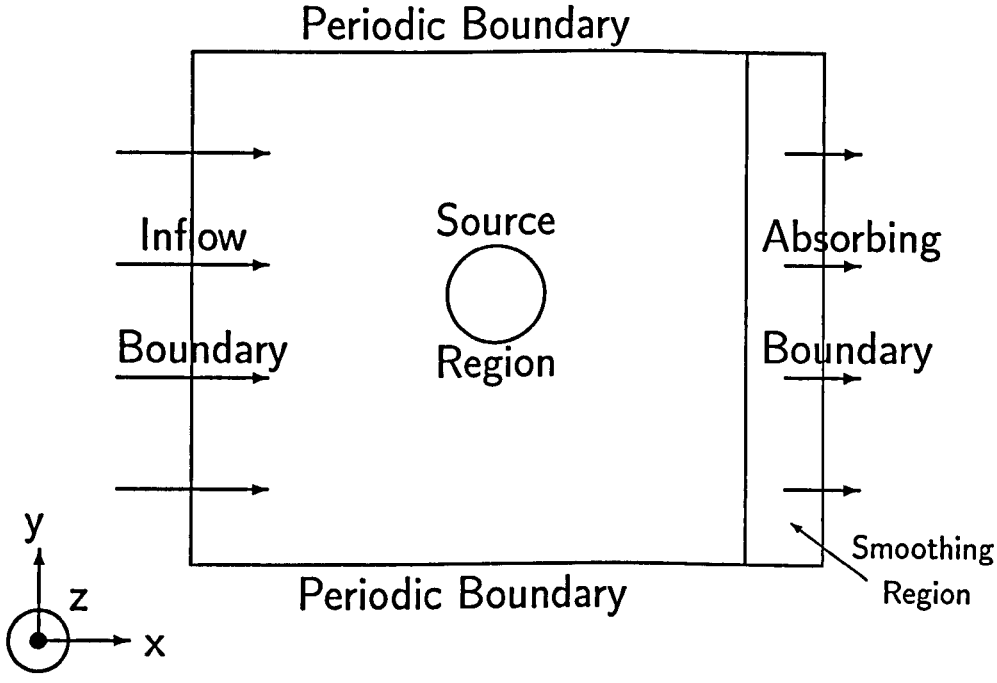

Figure 3.3: A schematic of the simulation grid, not to scale, including the co-ordinate geometry used. The source region contains one of the three source types described in section 3.4.3.

3.4.2 Boundary conditions

The simplest boundaries are the two periodic ones at $y = y_{\min}$ and $y = y_{\max}$. In addition to particle periodicity, the field variables calculated on grid cells near these boundaries consider the opposite side as neighbours for the purposes of taking moments.

The boundary at $x = x_{\min}$ was initially an inflow only boundary. It consists of a column of "bath" cells that are replenished every timestep by fresh SW particles before their velocity carries them into the main grid. Particles crossing in the opposite direction caused a code error trap to activate. In simulations with more dynamic shock fronts, however, this occurred more regularly due to scattering. To allow sufficient upstream space for them to be decelerated and returned to the SW flow direction was impractical computationally, so the boundary was modified to absorb particles and record the number of such occurrences. Provided minimal particles are removed like this, any associated wave growth should be retained. This modification was implemented for the simulations in Chapters 5 and 6.

The final boundary has been modified extensively. It was initially an outflow only boundary (and still is) with particles crossing it being removed and the field quantities having zero gradient across it. At the higher SW flow speeds these conditions were found to be impervious to some magnetic field anomalies formed. These would typically form near the source region, travel down the lobes and then be prevented from exiting the grid and hence grow and become unstable. Consequently an additional smoothing region was added near the boundary. The last ten cells at each point now have smoothing operations performed on $\underline{B_{ij}}$ every timestep, in addition to the regular smoothing discussed in section 3.3.1. The smoothing is linearly increased through these ten, to the final cell in the grid with the result made up of a percentage of the smoothed value, plus a percentage of its original value at

each grid point. The smoothed percentage is increased from 10% in the tenth from final column, to 100% in the final column. This region gradually smoothes waves, before they reach the outflow boundary, and hence the instabilities are prevented from forming.

3.4.3 Source structure

A summary is given of each of the three source types in this study: cometary source, weakly ionospheric planet, and a weakly ionospheric planet with an intrinsic magnetic field.

Cometary source

This consists of two regions producing heavy ions in different distributions, as shown in figure 3.4. The inner core produces around 90% of the ions uniformly, whilst the outer halo distributes the remaining 10% in a $\frac{1}{r^2}$ formation. The radial size of the source is scaled to match that of a Mercury sized obstacle with respect to heavy ion pickup gyroradii in undisturbed flow. The halo considers production up to a scaled altitude of $3000km$.

The production rate for the core is found from a neutral sodium particle density of roughly $8 \times 10^3 cm^{-3}$ up to $300km$ altitude (*Lammer and Bauer*, 1997). From this, the mass density and subsequently ionic mass production rate can be found by using the sodium ionization rate of $1.5 \times 10^{-4} s^{-1}$. Multiplying by the volume over which this production occurs at Mercury, before dividing by the volume over which it is spread at a Mercury sized obstacle with no planet, such as this cometary source, then allows a new ionic mass production rate to be found for the inner core region. As the SW proton density of $17cm^{-3}$ is represented by 100 p.p.c., this ionic production rate can be similarly found in p.p.c., using the same ratio. Multiplying by the total number of cells within the core area, and converting the

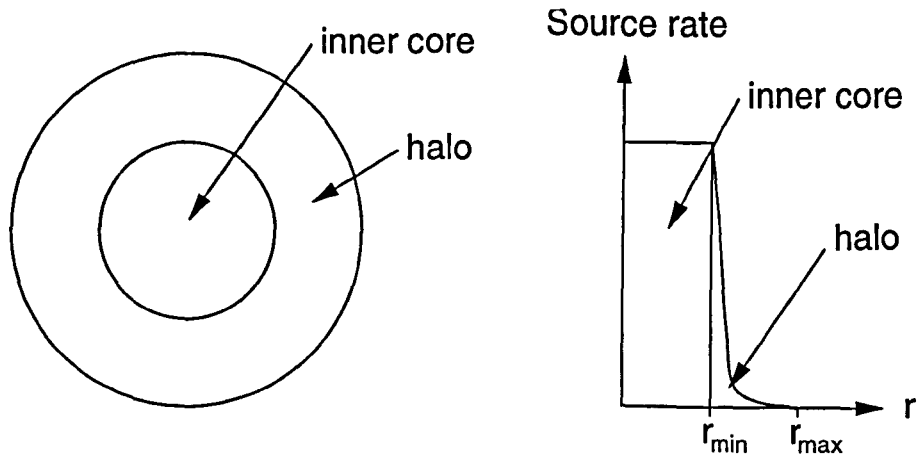

Figure 3.4: Cometary source structure showing the inner core and halo. These produce newborn ions in a manner described by the distribution on the right.

length represented by a timestep into seconds finally allows a rate of production in particles per timestep to be found.

The same calculation for the outer halo uses a neutral sodium particle density of only $90cm^{-3}$ (*Lammer and Bauer*, 1997), but is simplified by not having to compensate for distributing over a larger volume due to no representation of the planet itself in this source structure. The resulting rates of ion production are added every timestep in the simulation regardless of ion transport (or lack of) away from the source, and reducing the cell size or increasing the timestep in a simulation will correspondingly raise the source rate.

Weakly ionospheric planetary source

A planetary surface is now added within the core source region of the obstacle which produces no heavy ions, but does have set conditions. The new source structure can be seen in figure 3.5. The planet region of the source has four qualities:

1. It absorbs particles that stray into it.

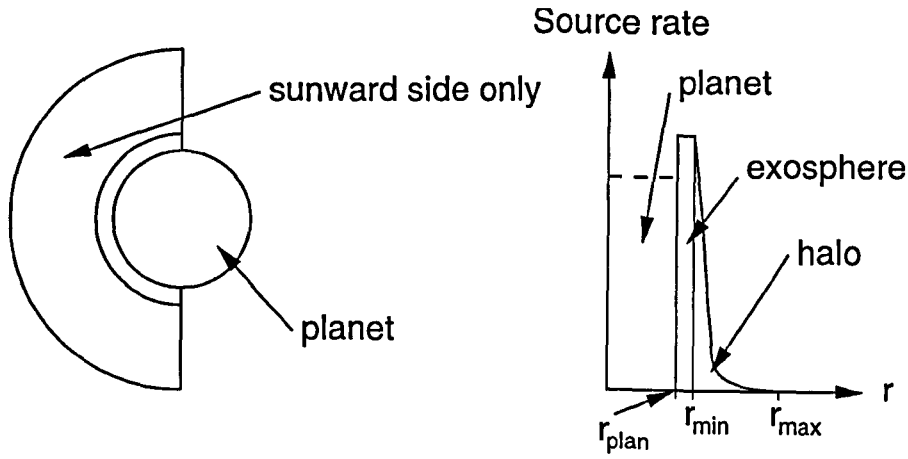

Figure 3.5: Structure used to simulate a weakly ionospheric planet. The central region now contains an absorbing planetary surface and production occurs only on the sunward face.

2. The density has a fixed value, given entirely in terms of heavy ions.

3. All bulk plasma velocity components are zero.

4. The magnetic field is set to zero initially.

Additionally, the source regions are limited to the semi-circle facing into the SW (see figure 3.5) as a negligibly corotating, photoionization dominated ionosphere is assumed. This halves the production rates, otherwise calculated similarly to the cometary case. The IMF is expected to diffuse into the planet throughout the simulation, but slowly as there is no resistive term in the algorithm. Some results in Chapter 5 use a source region extending entirely around the planet, or allow a z-component of velocity within it, however these are labeled as such.

Magnetized planetary source

The pilot study in Chapter 6 uses a source region similar in structure to that above, but with a current flowing within the planet to generate an intrinsic magnetic field, as shown in figure 3.6. The current is tapered at both the centre and edge of the

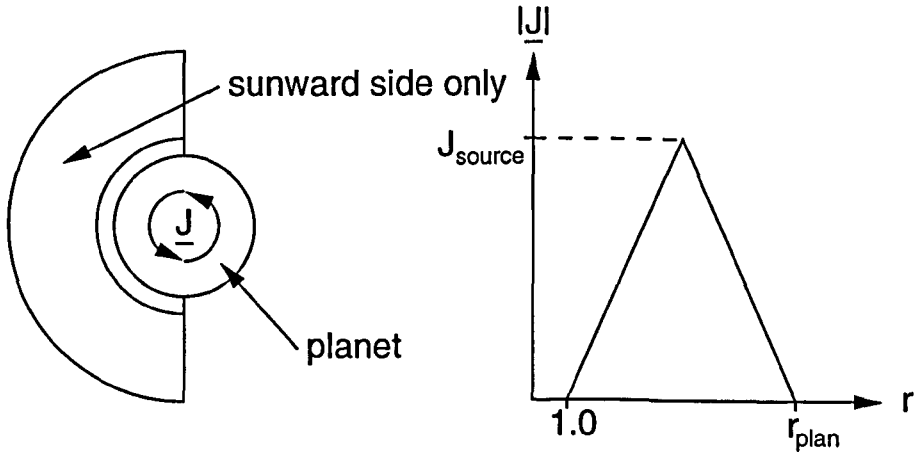

Figure 3.6: Structure used to perform a pilot study of a magnetized, weakly ionospheric planet. The source rates are as in figure 3.5, but here a current, with magnitude dependence shown on the right, is added within the planet to generate a magnetic dipole field.

planet as shown on the right of figure 3.6, and leaves a region of zero current in the centre of radius $1\frac{v_A}{\Omega_p}$ ($r_{plan} = 7.67\frac{v_A}{\Omega_p}$). It is generated by appropriately setting the bulk plasma velocities. Otherwise the planet uses the same source rates as above. The calculation of J_{source} is given in Chapter 6.

3.5 Simulation Practicalities

3.5.1 Initial conditions and end criteria

In all simulations, the grid initially contains only SW protons which have a large velocity in the x-direction and much smaller thermal fluctuations in other directions. Appropriate conditions for the source type in use were also initiated, with heavy ions added accordingly throughout. To reduce initial turbulence, which might adversely affect the downstream boundary, heavy ion production is phased in, such that the source is only fully productive after 800 timesteps. For the cometary sources this simulates increasing production near the Sun. Simulations are stopped when a

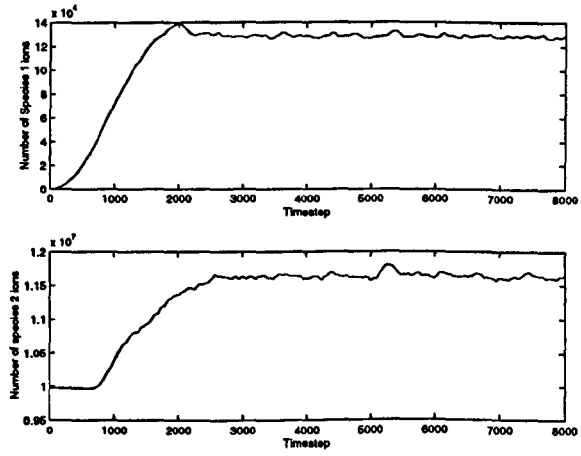

Figure 3.7: Example of a quasi-steady state in both species particle counts. The results of this particular cometary simulation are displayed in figures 4.15, 4.16, 4.19, 4.20 and 4.21. Each timestep is equal to $0.04\Omega_p^{-1}$.

quasi-steady state is achieved in both species' particle counts, typically after 8000 timesteps, as exemplified in figure 3.7.

3.5.2 Cometary ion representation

These simulations consider only one species of heavy ion in addition to the SW protons: a gross simplification. A whole range of ion types have been reported at cometary encounters (*Ogilvie et. al.*, 1986; *Coates et. al.*, 1993; *Krankowsky et. al.*, 1986), with a populous species being the water group (*Huddleston et. al.*, 1993b; *Coates et. al.*, 1993). The most common ionospheric constituents at Venus and Mercury are Oxygen and Sodium respectively (*Knudsen*, 1992; *Lammer and Bauer*, 1997), although others are present. One approximation is thus that the source emits only one species.

Another is to give the heavy ions a mass of only $m_h = 4m_p$. This allows better statistical representation: to add mass to the simulation in larger units means fewer such particles than if the same rate is added in lighter particles, giving better

resolution. The simulation is normalized so this ratio could be scaled. Additionally, the gyroradii of these ions have to fit comfortably within the simulation grid, so using a realistic ratio to represent sodium ions would have been computationally costly.

3.5.3 Physical parameters

As these simulations progress to a pilot study for the interaction of the SW with a Mercury type obstacle, they used suitable SW parameters of $B_0 = 18nT$ (*Ness et. al.*, 1974), $V_{sw} = 630kms^{-1}$ and $n_e = n_p = 17cm^{-3}$ (*Ogilvie et. al.*, 1974), giving a mass density of $\rho_0 = 2.9 \times 10^{-20}kgm^{-3}$. The source region represents an altitude of $300km$ above the Hermean surface for the inner region, and $3000km$ altitude for the halo (*Lammer and Bauer*, 1997). The radius of Mercury is $R_M = 2439km$ (*Dunne*, 1974). Using an Alfvén velocity of $v_A = 95kms^{-1}$, $\Omega_p \approx 1.7s^{-1}$, and preserving the scaling with respect to the reduced heavy ion mass, this gives $R_M = 7.67\frac{v_A}{\Omega_p}$. The number density of sodium atoms was taken as $8 \times 10^3 cm^{-3}$ for the inner region and $90cm^{-3}$ for the outer halo (*Lammer and Bauer*, 1997). Finally, the thermal energy of the SW protons was taken as $T_p = 1.28 \times 10^5 K$, which translates to a velocity of $0.34v_A$ in the simulations, and the source ions were emitted with a radial velocity of only $2km/s$, or $0.02v_A$ (*Lammer and Bauer*, 1997).

3.5.4 Implementation

This took the form of a FORTRAN77 program with an initialization file in which the normalized values of the data in section 3.5.3 were set. Runs varied greatly in length depending on the SW Mach number and source type: planetary runs, and those with low Mach number flow generally produced a broader shock interaction region, needing larger grids, more particles, and a longer runtime. Due to this variety, a selection of machines were used. For low memory requirement runs Sun

workstations within the group lab areas were employed. Runs requiring more memory used an Origin 2000 Onyx2 IRIX system attached to the virtual reality lab at Warwick. Finally, the very large, long duration runs (typically the 100 p.p.c. runs displayed herein) were performed using GRAND, a high performance computing facility funded by PPARC, based at Leicester and on which Warwick had a share of time.

Chapter 4

Cometary Simulations: Results

This chapter displays results of simulations performed using the cometary source described in section 3.4.3 and summarized in *Hopcroft and Chapman* (2001). Results are presented at different SW flow speeds and IMF orientations: either lying in or perpendicular to the plane. The IMF is *always* perpendicular to the SW flow direction, however. These differing conditions produce highly contrasting structures and as a consequence, take different times to settle into quasi-steady states. The results presented may thus appear to be at different times according to their captions, but unless otherwise stated are all shown in a quasi-steady state described in section 3.5.1. This holds throughout Chapters 4, 5 and 6. All units of length are given in cometary, or heavy, ion pickup gyroradii in undisturbed flow. Note that this is dependent upon M_A. Densities are given in units of initial SW density, similarly for magnetic field, which is given in terms of the inflowing IMF strength. Velocities, including that of the inflowing SW, are given in units of the Alfvén velocity, whilst time is given in units of inverse proton gyrofrequency, Ω_p^{-1}. Many of the figures contain two additional markings to aid understanding: a pair of "circles" near the centre of the plot which denote the outer spatial limits of the two source regions described in section 3.4.3; and an 'L'-shape in the bottom left corner, which

highlights one cometary ion pickup gyroradii in undisturbed flow along each axis to emphasize the scaling. Any distortion of the source region circles to ellipses is due entirely to the axis scaling used.

4.1 Slow Solar Wind Flow Simulations

4.1.1 IMF in the simulation plane

The first set of simulations are performed at low SW flow speeds with $M_A = 3.0$, $M_{MS} = 2.75$. Figure 4.1 shows total mass density (both SW protons and cometary ions) on a $\log_{10}$ scale for a simulation with the IMF in the plane of the simulation, $\underline{B}_{IMF} = B_y$. The arrows show the bulk velocity of the flow in the plane relative to the inflowing SW value of $3.0v_A$ at the left-hand edge. This result is a good example of a standard MS shock, although Rankine-Hugoniot jump conditions have proved impossible to verify due to the small normal component of velocity along the shock flanks. It has three regions of interest. The shock front itself is clearly visible as a jump in density and a deflection and reduction in magnitude of the plasma flow (the arrows). A high density tail of cometary ions is seen stretching directly downstream from the source to the absorbing boundary. This is shown more clearly in figure 4.2, which shows the cometary ion mass density only, again on a $\log_{10}$ scale. Finally, either side of the tail are lobe regions, and the density can be seen to gradually reduce from immediately behind the shock to this area. Most importantly, the shock is well-defined and smooth.

The orientation of the IMF in this simulation, and the restriction to a 2D plane, means the source causes field line draping and pile-up as can be seen in figure 4.3, which shows the magnitude of the magnetic field at any point on the colourscale, and the two components in the plane of the simulation as arrows relative to the inflowing IMF arrows. In the high density tail the field magnitude remains

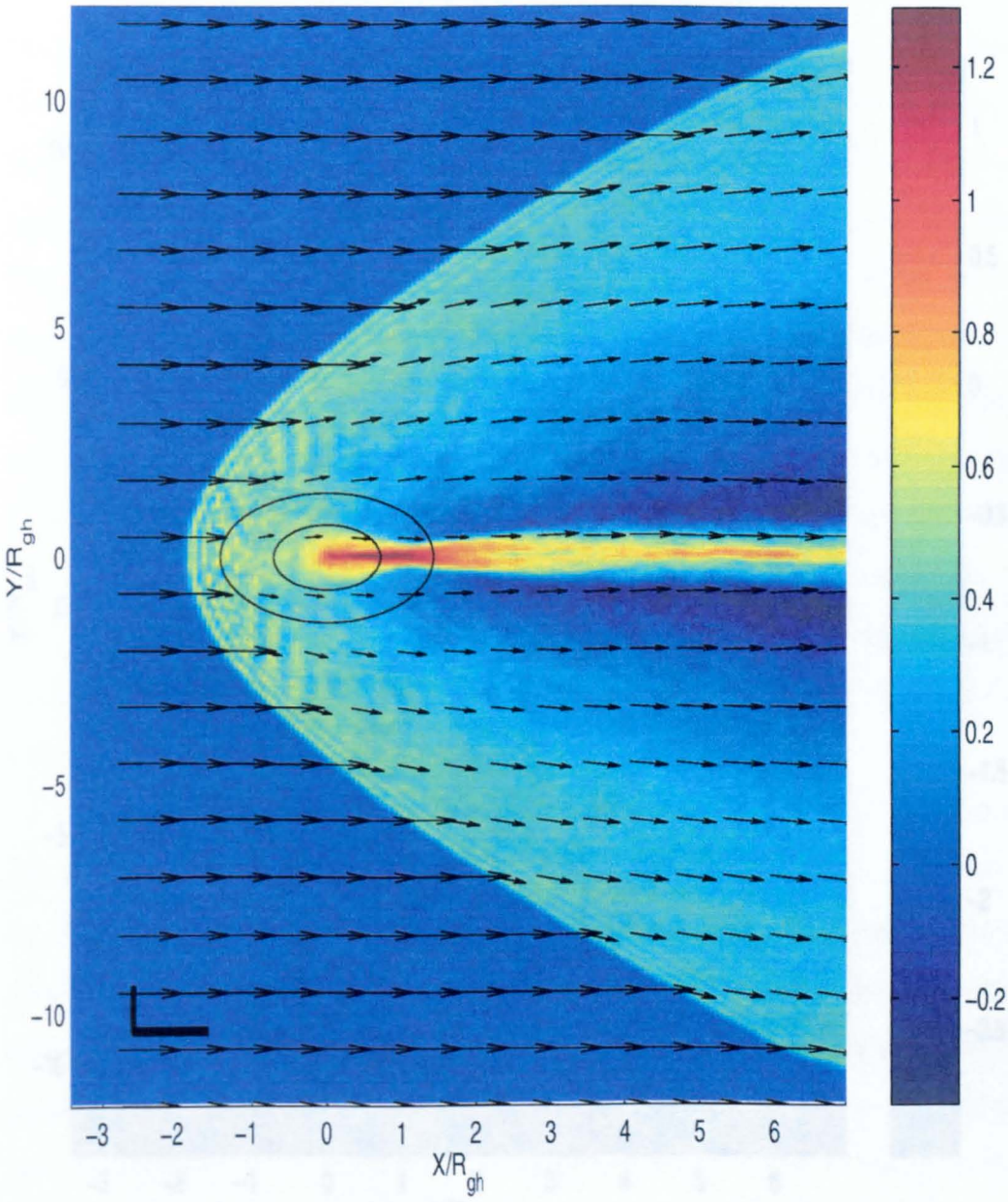

Figure 4.1: Total mass density using a $\log_{10}$ scale for a simulation with a SW Alfvén Mach number of $M_A = 3.0$ and $\underline{B}_{IMF} = B_y$. Taken after $400\Omega_p^{-1}$, the arrows show the bulk flow velocity relative to that of the SW. The "circles" near the centre show the extent of the cometary source regions whilst the "L"-shape, bottom left, shows one cometary pickup gyroradii in each direction to emphasize the scaling.

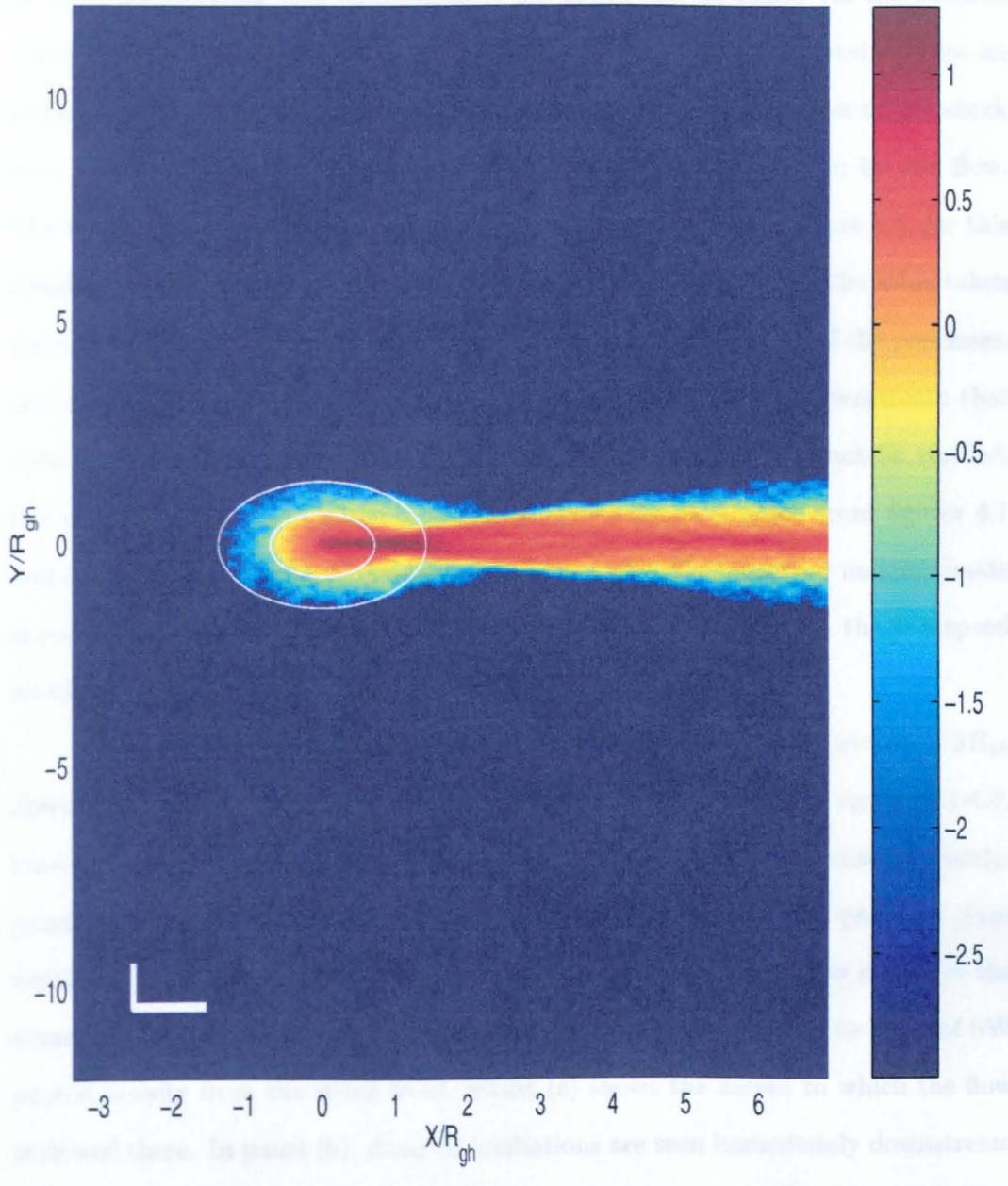

Figure 4.2: Mass density of cometary ions only again on a $\log_{10}$ scale for the same simulation and time as that in figure 4.1. Other markings as before.

relatively low.

By assuming the upstream SW to be an isotropic Maxwellian plasma of protons, the pressure and, subsequently, MS speed can be found via the thermal velocity given to the protons in the simulation. Using this MS speed enables an estimate for the shock angle to be made, assuming information travels to the shock front in the form of MS waves whilst being convected downstream by the flow. The angle calculated using the downstream flow speed, visible in figure 4.4, for this simulation is 32.4° between the SW flow direction and shock front. The value taken form these plots is 39.4°. This calculation is clearly a simplification of the processes, and assumes consideration of a segment of shock sufficiently far downstream that a fluid view may be taken. As the Rankine-Hugoniot relations cannot be verified, the validity of this assumption is unknown. However, it is noted from figures 4.1 and 4.2 that the shock flanks are free of cometary ions. The observed underestimate is seen throughout this chapter, and is likely due to inaccuracies in the MS speed which will vary in the downstream region.

Figure 4.4 displays cross-sections of various parameters at a distance of $3R_{gh}$ downstream of the source centre for the same simulation depicted in figures 4.1-4.3. Panel (a) shows combined mass density and that of the two ion species separately; panel (b) the magnetic field components and overall magnitude; and panel (c) gives similar plots for the bulk velocity. Panel (a) clearly shows the narrow extent of the cometary ion tail in this orientation and the gradual reduction into the lobes of SW proton density from the shock front, whilst (c) shows the extent to which the flow is slowed there. In panel (b), damped oscillations are seen immediately downstream of the shock front in B_x, B_y and $|\underline{B}|$. These are not due to SW proton reflection and subsequent bunching as in *Burgess et. al.* (1989), according to the following argument. In figure 4.4(b), one unit of the y-axis is given by $R_{gh} = \frac{v_{sw}}{\Omega_h} = \frac{v_{sw} m_h}{e B_u}$ where B_u refers to the upstream magnetic field, v_{sw} is the SW velocity and Ω_h the

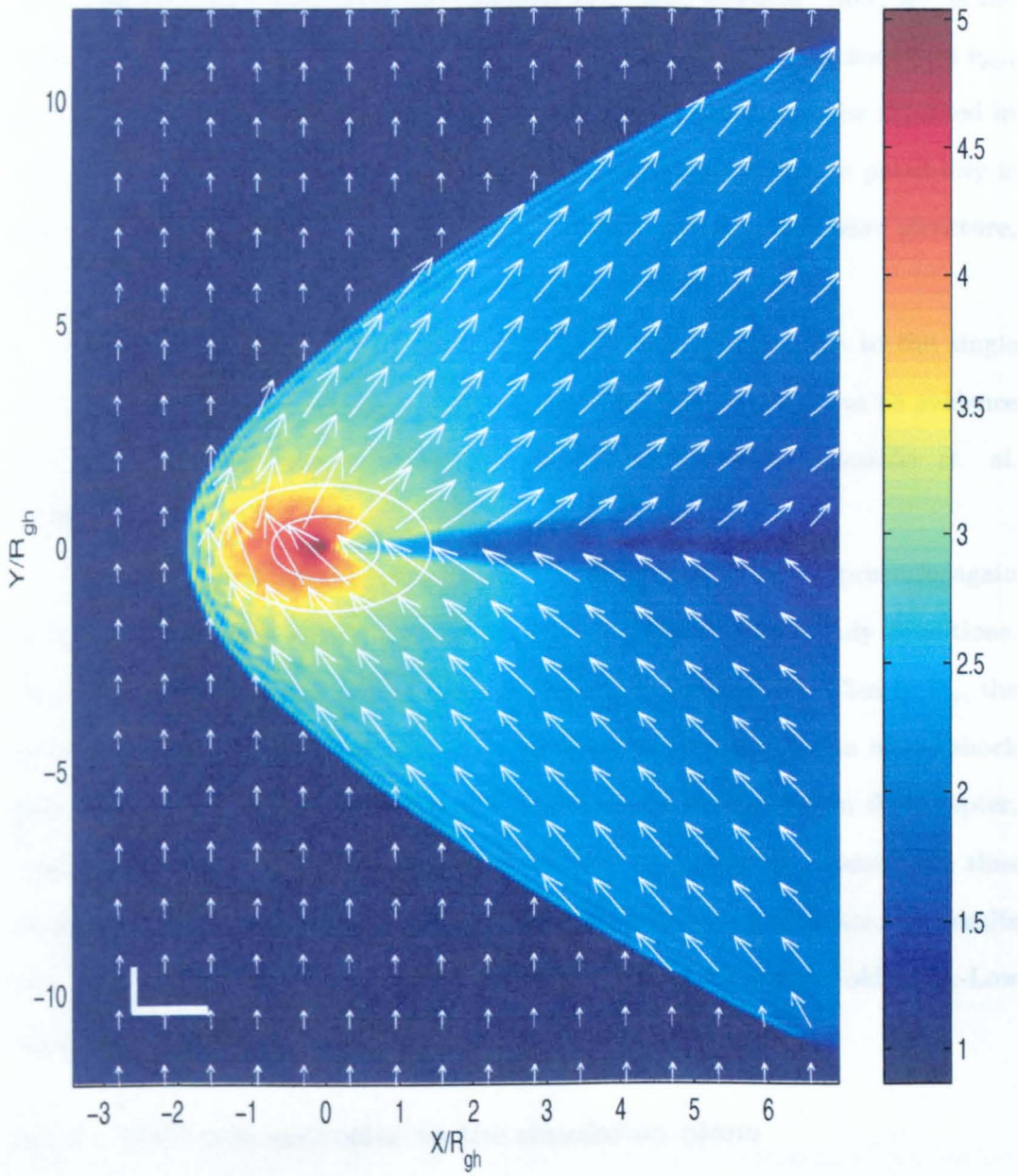

Figure 4.3: Magnetic field magnitude for the same simulation and time as figure 4.1. The white arrows show the component lying in the plane of the simulation.

heavy ion gyrofrequency. As $m_h = 4m_p$ and, from figure 4.4(b), $B_d \approx 2.4B_u$ where B_d is now the downstream value, then $R_{gh} = \frac{4v_{sw}m_p}{eB_u} = \frac{4v_{sw}m_p}{eB_d} \times 2.4 = 9.6\frac{v_{sw}}{\Omega_{pd}}$, where Ω_{pd} is the proton gyrofrequency in the downstream field strength. Now, $\frac{v_{sw}}{\Omega_{pd}}$ is the downstream gyroradius of protons reflected at the shock and hence picked up at v_{sw}, so if this was the cause of the oscillations, approximately ten would be expected in one unit of R_{gh}. As this is clearly not the case in figure 4.4(b), the possibility is discounted. Instead, they are more likely a downstream standing wave structure, with additional numerical Gibbs' effect at the shock front.

The plot of B_z is also interesting for different reasons, due to the single oscillation seen only on passing through the shock. This is thought to be evidence of a rotation of the magnetic field at the shock, as discussed in *Scudder et. al.* (1986).

Finally, figure 4.5 shows cross-sections of the normalized ionic pressure, again for a simulation with $M_A = 3.0$ and $B_{IMF} = B_y$ under quasi-steady conditions. Each component is shown as seen $3R_{gh}$ downstream of the source. Clearly P_{iy}, the parallel component of the pressure, is significantly lower downstream of the shock than the others. This result is repeated for the other simulations in this chapter, except for the most disturbed in section 4.2.2. It is significant because care thus needs to be taken over assumptions of isotropic pressure. In particular, the results may not be produced by MHD or fluid simulations, with Chew-Goldberger-Low theory being necessary (*Krall and Trivelpiece*, 1986).

4.1.2 IMF perpendicular to the simulation plane

The next series of figures 4.6-4.9 show similar results, again at a low SW flow speed of $M_A = 3.0$, but with the IMF initially perpendicular to the plane, $\underline{B}_{IMF} = -B_z$. Because of this, the magnetic field remains perpendicular to the plane for all time, and so $|\underline{B}|$ is effectively $|B_z|$ with no components in the plane (figure 4.8).

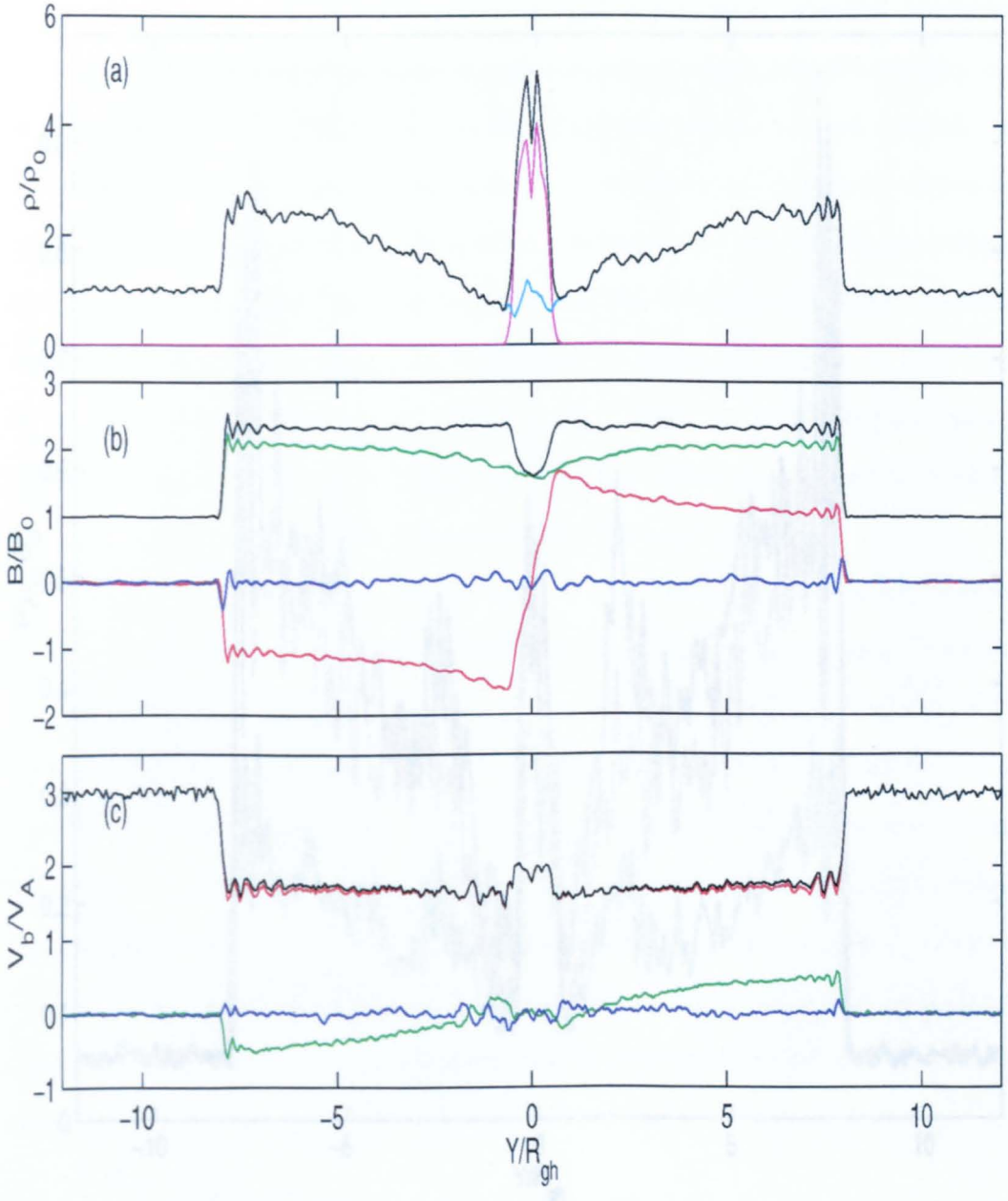

Figure 4.4: Cross-sections taken after $400\Omega_p^{-1}$ at $3R_{gh}$ downstream of the source centre of a simulation with $M_A = 3.0$ and $\underline{B}_{IMF} = B_y$. Panel (a) shows total mass density (black), cometary ion mass density (magenta), and SW proton mass density (cyan). Panel (b) shows the magnetic field magnitude (black) and the three components: x (red), y (green) and z (blue), whilst panel (c) displays the bulk velocity cross-sections under identical colour coding to panel (b).

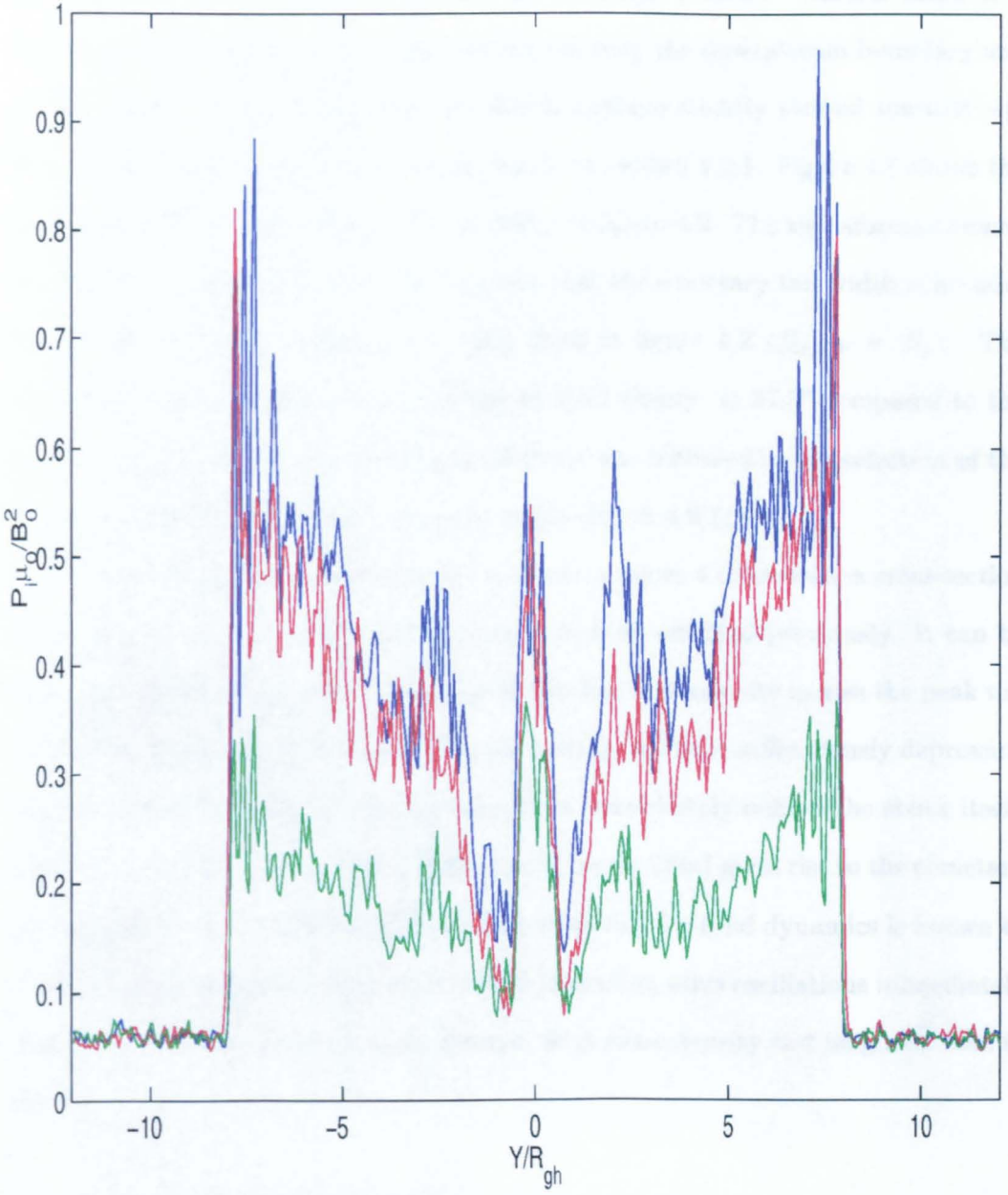

Figure 4.5: Cross-section of normalized ionic pressure components taken after $360\Omega_p^{-1}$ at $3R_{gh}$ downstream of the source centre for the same simulation as in figure 4.4. The conditions were quasi-steady, and give the plots of P_{ix} (red), P_{iy} (green) and P_{iz} (blue). The component parallel to B_{IMF}, P_{iy}, is significantly lower downstream than either of the perpendicular components.

Figure 4.6 shows a plot similar to that in figure 4.1, with the shock front, low density lobe regions and high density tail similarly present. Careful inspection reveals a slight rippling of the cometary ion tail near the downstream boundary and an asymmetry of the global structure which appears slightly skewed towards $-y$. Both these observations are seen more clearly in section 4.2.1. Figure 4.7 shows the mass density of cometary ions only, similarly to figure 4.2. The two aforementioned features are again visible, and it is apparent that the cometary tail width is broader in this field orientation ($\underline{B}_{IMF} = -B_z$) than in figure 4.2 ($\underline{B}_{IMF} = B_y$). The BS angle is again greater than predicted by fluid theory, at 37.5° compared to the 31.5° expected. In this case an additional error was included in the selection of the downstream flow speed, which strongly varies (figure 4.9 (c)).

Figure 4.9 shows similar results to those in figure 4.4, however a cross-section of $|\underline{B}|$ only is presented in panel (b) due to reasons outlined previously. It can be seen that switching the field orientation at this low flow velocity causes the peak tail density to rise by over a factor of 4 (figure 4.9(a)), whilst simultaneously depressing the flow velocity in this locality far more than immediately behind the shock itself. The steep gradient of the velocity difference in figure 4.9(c) gives rise to the cometary ion tail ripple via the KH instability, which from regular fluid dynamics is known to depend on this quantity (*Choudhuri*, 1998). Standing wave oscillations immediately downstream of the shock are again present, with mass density and magnetic field in phase.

4.2 Fast Solar Wind Flow Simulations

4.2.1 IMF perpendicular to the simulation plane

The SW Alfvén Mach number is now increased to $M_A = 6.6, M_{MS} = 6.04$ to examine the effect of a comet passing through a fast stream of SW, or nearing the Sun. Note

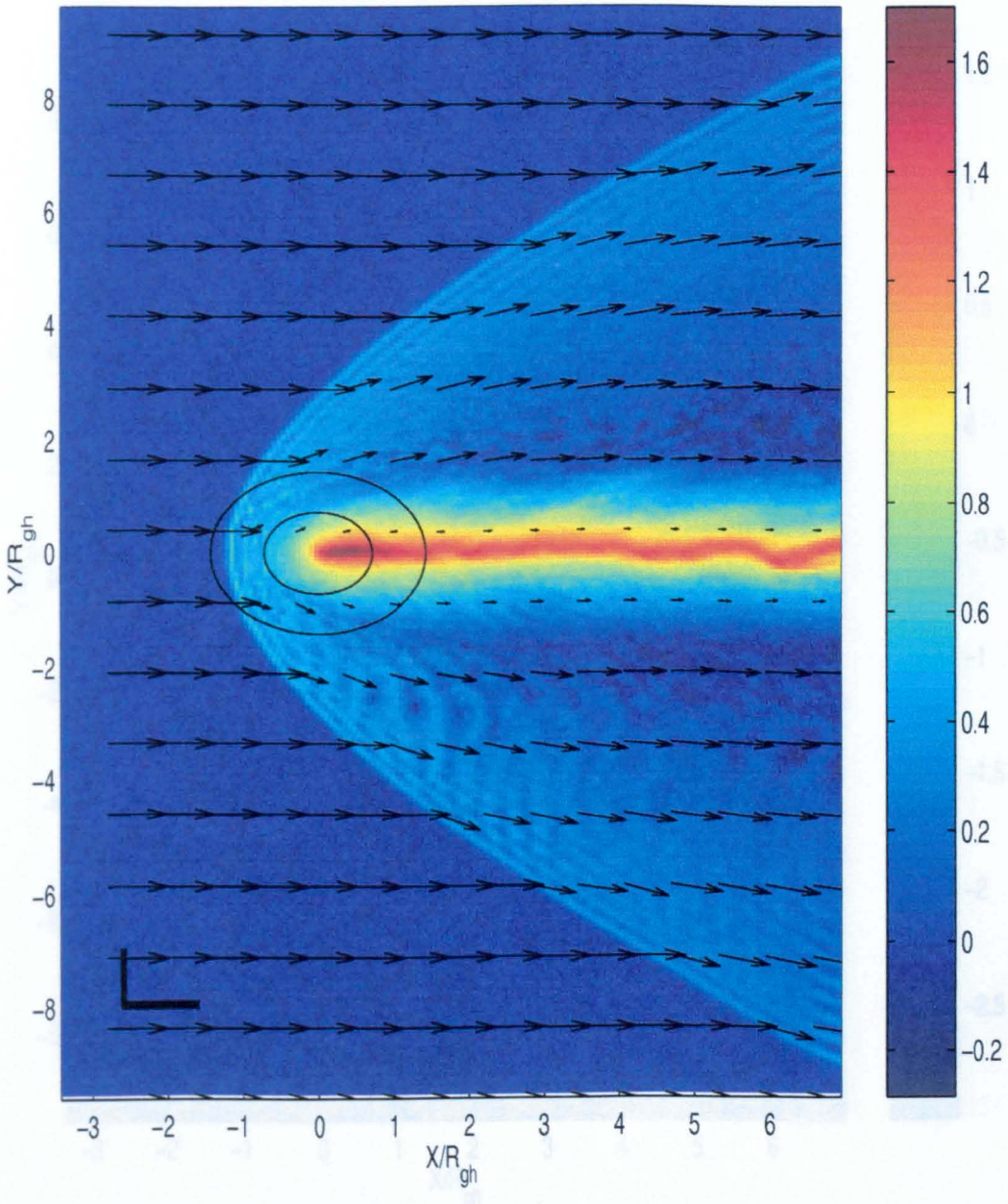

Figure 4.6: Total mass density using a $\log_{10}$ scale for a simulation with SW Alfvén Mach number $M_A = 3.0$ and $\underline{B}_{IMF} = -B_z$ after $720\Omega_p^{-1}$. The arrows show bulk velocity.

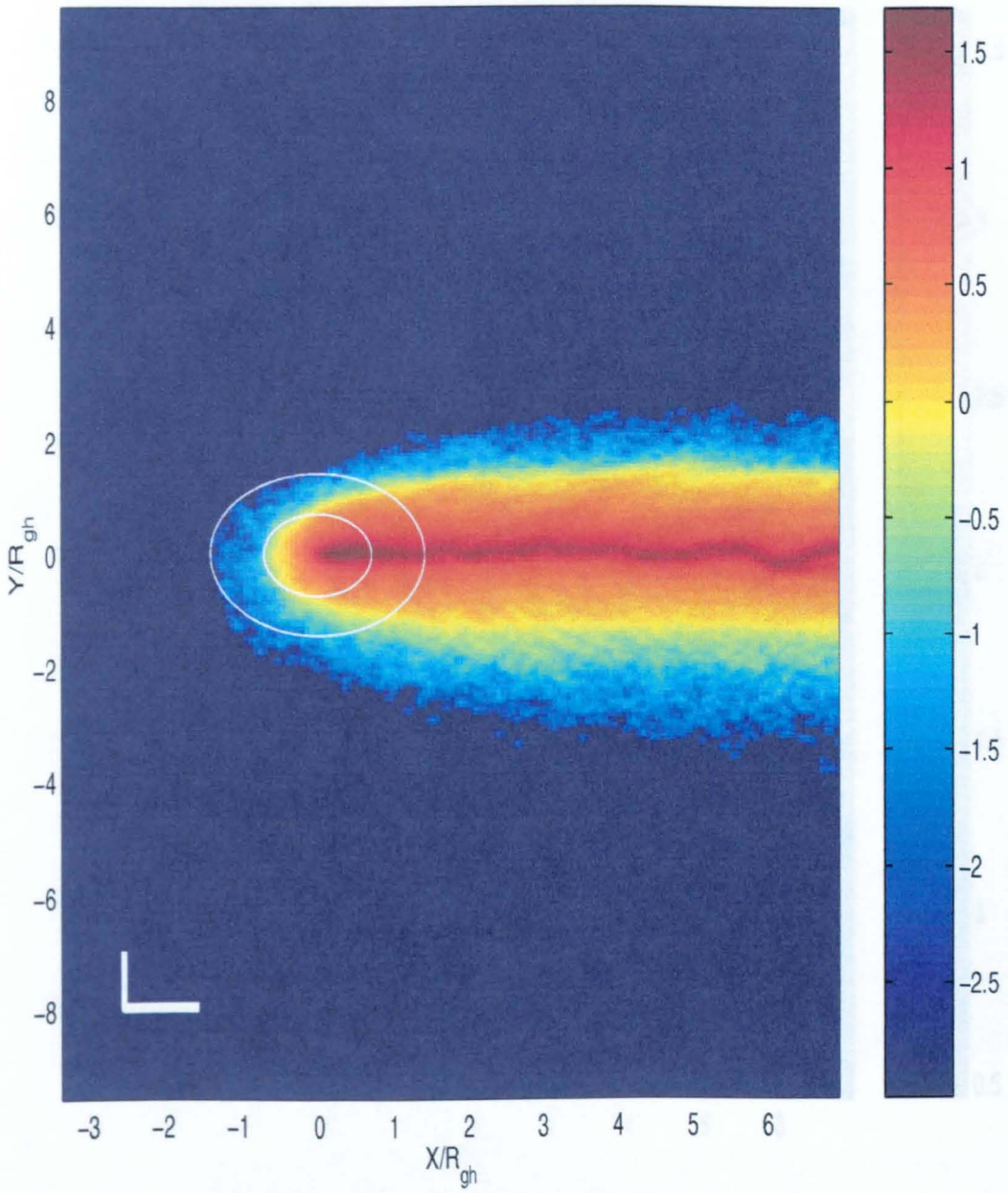

Figure 4.7: Mass density of cometary ions only using a $\log_{10}$ scale for the same simulation as in figure 4.6.

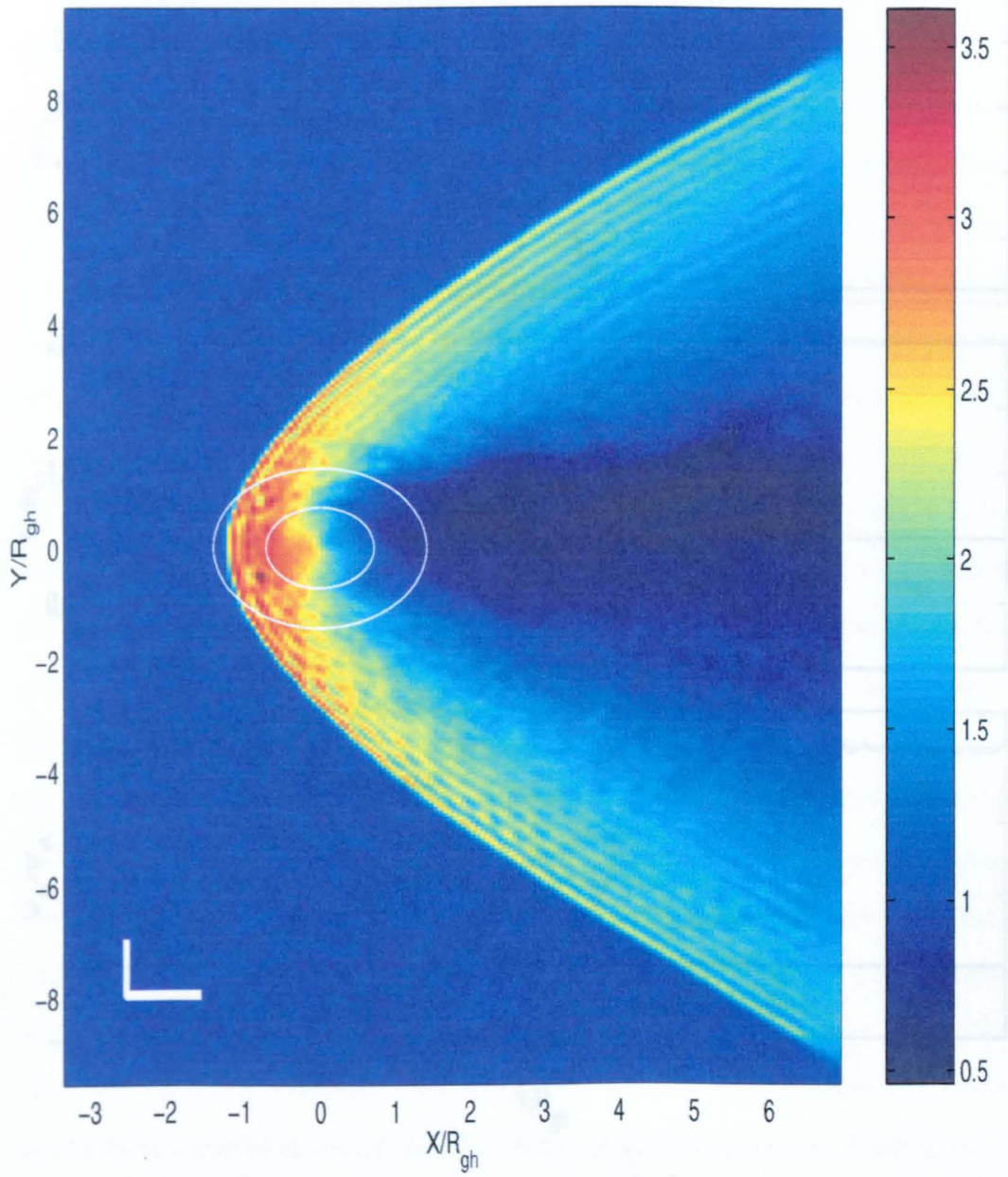

Figure 4.8: Magnetic field magnitude for the same simulation as in figure 4.6. Notice that as $\underline{B}_{IMF} = -B_z$, no components evolve in the plane of the simulation.

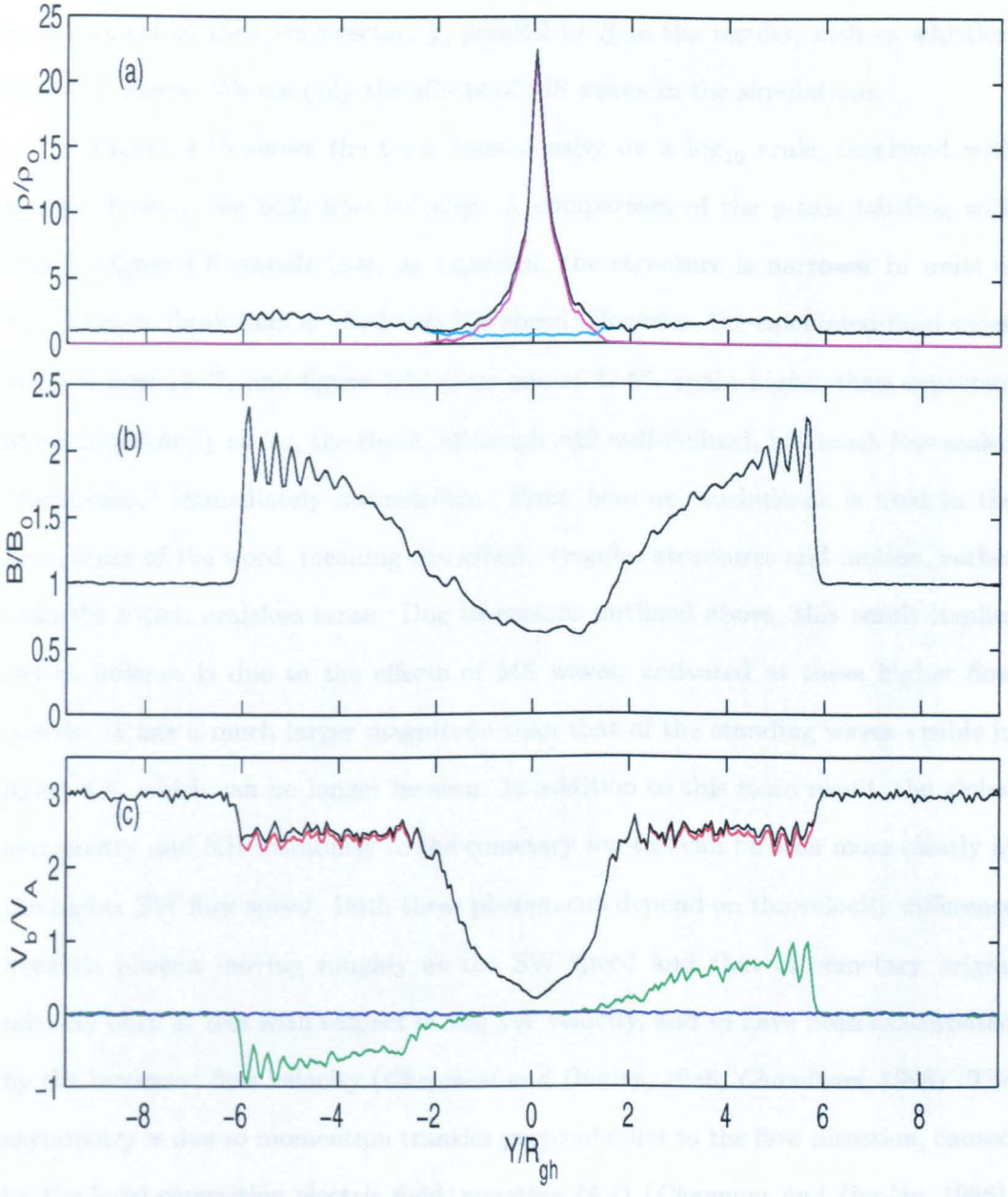

Figure 4.9: Cross-sections of mass density, magnetic field and bulk velocity taken after $720\Omega_p^{-1}$ at $3R_{gh}$ downstream of the source centre of a simulation with $M_A = 3.0$ and $\underline{B}_{IMF} = -B_z$. Colour scheme as for figure 4.4, except that only magnetic magnitude (black) is shown in panel (b) as no other components are present.

that this in turn changes the value of R_{gh}. The IMF is again perpendicular to the plane of the simulation, $\underline{B}_{IMF} = -B_z$, which eliminates the possibility of waves with a component of their wavevector, $\underline{k}$, parallel to $\underline{B}$ in the results, such as whistlers and AIC waves. We see only the effects of MS waves in the simulations.

Figure 4.10 shows the total mass density on a $\log_{10}$ scale, overlayed with arrows showing the bulk flow velocity. A comparison of the y-axis labeling with that in figure 4.6 reveals that, as expected, the structure is narrower in units of R_{gh}, flank to flank than at the lower SW speed. However, the calculated fluid shock angle is now 13.4°, and figure 4.10 gives one of 22.6°, again higher than expected. Most importantly so far, the shock, although still well-defined, has much fine-scaled "turbulence" immediately downstream. From here on, turbulence is used in the loose sense of the word, meaning disturbed, irregular structures and motion, rather than the strict, scaleless sense. Due to reasons outlined above, this result implies the turbulence is due to the effects of MS waves, activated at these higher flow speeds. It has a much larger magnitude than that of the standing waves visible in figure 4.6, which can no longer be seen. In addition to this main result, the global asymmetry and KH instability in the cometary ion tail can be seen more clearly at the higher SW flow speed. Both these phenomena depend on the velocity difference between plasma moving roughly at the SW speed and that of cometary origin, initially born at rest with respect to the SW velocity, and so have been exacerbated by the increased flow velocity (*Chapman and Dunlop*, 1986; *Choudhuri*, 1998). The asymmetry is due to momentum transfer perpendicular to the flow direction, caused by the local convection electric field, equation (4.1) (*Chapman and Dunlop*, 1986), in the initial stages of pickup. In equation (4.1), $\underline{v}$ is the *local* SW bulk velocity, such that in minimally perturbed flow, such as upstream of the BS, it reduces to v_{SW}.

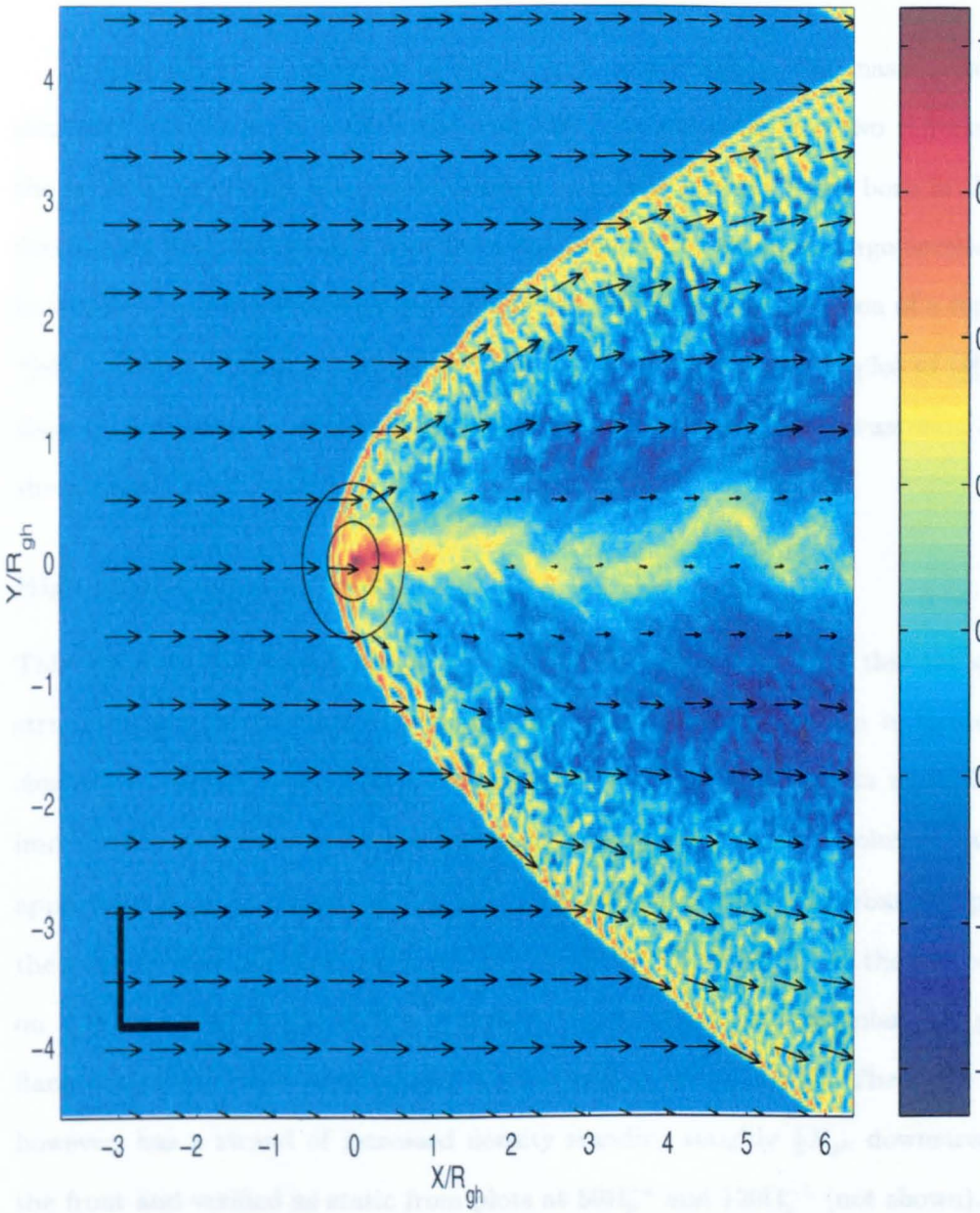

Figure 4.10: Total mass density using a $\log_{10}$ scale after $320\Omega_p^{-1}$ for a simulation with SW flow with $M_A = 6.6$ and $\underline{B}_{IMF} = -B_z$. The arrows show bulk velocity in the plane.

$$\underline{E} = -\underline{v} \times \underline{B} \tag{4.1}$$

This effect is apparent in figure 4.11, which shows the mass density of cometary ions only. It reveals the cometary ions are split into two populations: the majority gradually accelerated downstream, after initially being born in already decelerated flow; whilst those ions born upstream of the shock undergo acceleration in fast flow, and experience pickup type motion leading to the creation of a separate "jet" of ions visible near the front of the source in figure 4.11. A plot of $|\underline{B}|$ (not shown), similar to figure 4.8, merely shows the turbulence seen downstream of the shock again.

High resolution simulation

This simulation has been repeated on a smaller grid cell size to verify that the spatial structures are independent of this, and the result of this is shown in figure 4.12 similarly to figure 4.10. The crucial result is that the structure in mass density immediately downstream of the shock remains at this higher resolution, and so appears to be independent of grid size. The scale size of the disturbances appears the same on a grid of cells of size $0.375\frac{v_A}{\Omega_p} \times 0.375\frac{v_A}{\Omega_p}$ (figure 4.12), to those produced on a grid of cells of size $0.75\frac{v_A}{\Omega_p} \times 0.75\frac{v_A}{\Omega_p}$ (figure 4.10). In particular, the $y > 0$ flank of the simulation appears very similar to that in figure 4.10. The $y < 0$ flank, however, has a strand of increased density standing roughly $\frac{1}{3}R_{gh}$ downstream of the front and verified as static from plots at $80\Omega_p^{-1}$ and $120\Omega_p^{-1}$ (not shown). This is not due to SW proton reflection (*Burgess et. al.*, 1989), by a similar analysis to that in section 4.1.1. It is interesting to note its appearance only on the smaller grid cell simulation in addition to the structuring expected, and its approximate location between the majority of cometary ions in the tail and the picked up, upstream jet

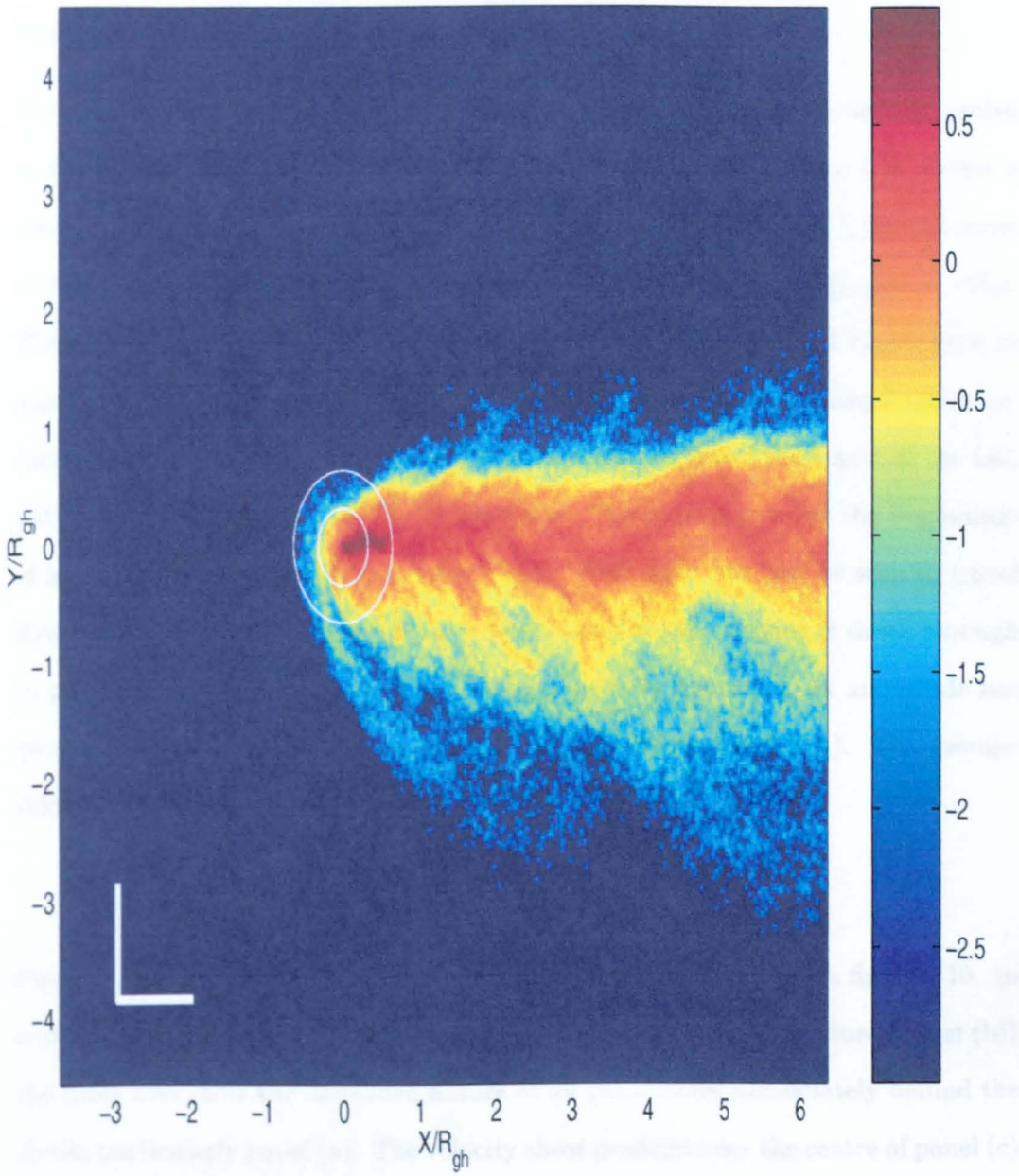

Figure 4.11: Mass density of cometary ions only using a $\log_{10}$ scale for the same simulation as shown in figure 4.10.

which are visible in figure 4.11. Such a plot of cometary ions only for the simulation in figure 4.12 (not shown) reveals identical structure.

Time development of the cometary tail

Waves in the cometary ion tail caused by the KH instability can be seen to evolve in time along its length. Although best viewed as a movie, figure 4.13 shows a sequence of stills of the total mass density, each separated by $10\Omega_p^{-1}$, for the same simulation parameters as that depicted in figure 4.10 ($M_A = 6.6, \underline{B}_{IMF} = -B_z$). These close-ups of the tail show its evolution. Due to numerical constraints in production they were obtained with only 25 p.p.c., rather than the usual 100 p.p.c. used elsewhere. It is seen that a wave takes $\sim 80\Omega_p^{-1}$ to travel the length of the tail, a distance of $6.35R_{gh}$, or $168\frac{v_A}{\Omega_p}$. In particular, this sequence shows the beginnings of a tail ripple in panel (a) at $(x, y) = (1, 0)$. The ripple can first be seen to travel downstream whilst the mass density in the section of tail carrying it drops through to panel (e). As the tail approaches the downstream boundary, its amplitude has grown and mass density appears to increase again in panels (f)-(h). The average velocity of the feature down the tail is thus roughly $\frac{168\frac{v_A}{\Omega_p}}{80\frac{1}{\Omega_p}} = 2.1v_A$.

Figure 4.14 shows cross-sectional data for the simulation displayed in figure 4.10. In addition to providing more evidence for the asymmetry of the structure (panel (b)) the plots also show the disturbed nature of all parameters immediately behind the shock, particularly panel (a). The velocity shear gradient near the centre of panel (c) is over twice that in figure 4.9(c).

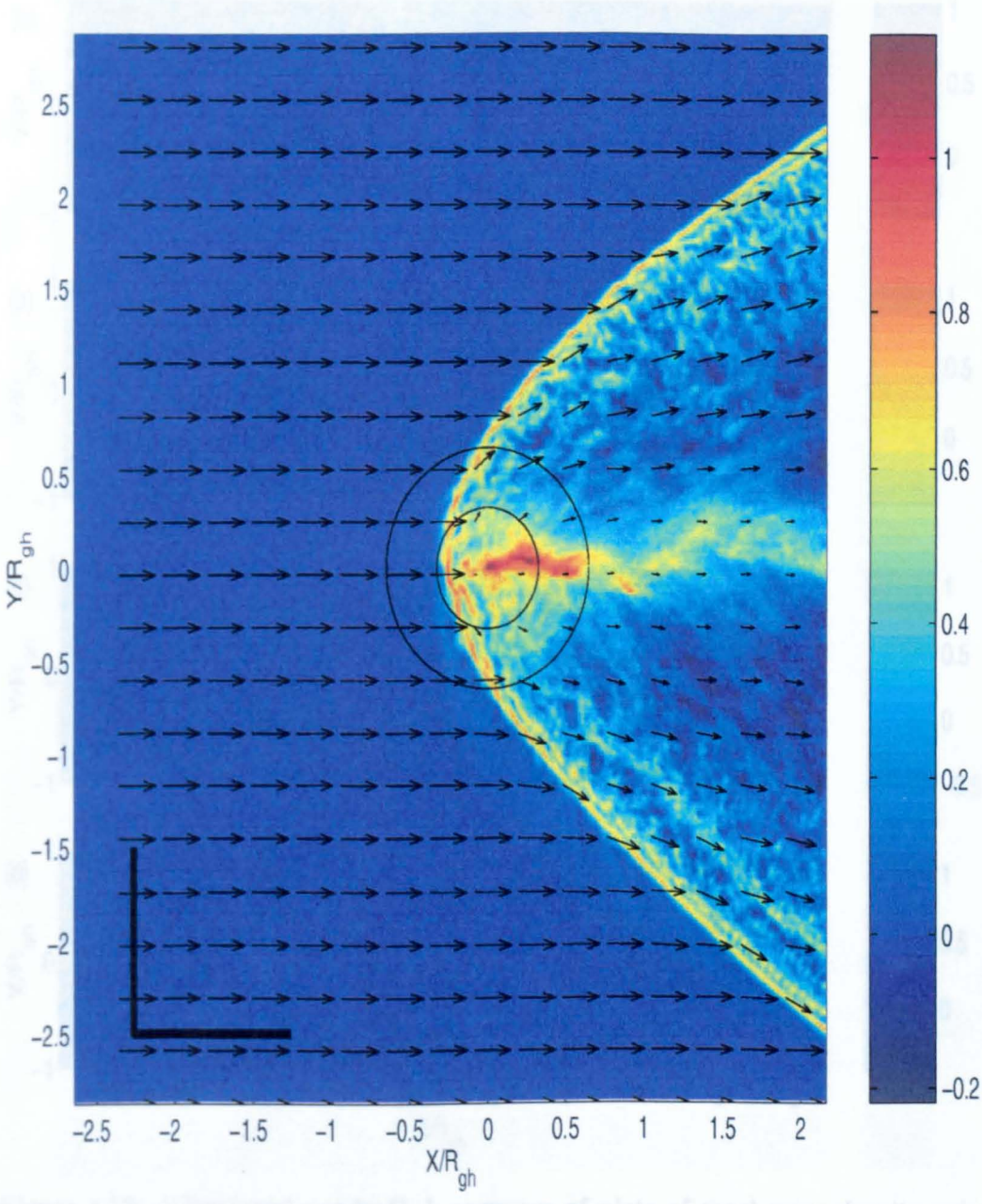

Figure 4.12: Total mass density using a $\log_{10}$ scale for a simulation with $M_A = 6.6$ and $\underline{B}_{IMF} = -B_z$ as in figure 4.10, but using a grid cell of one quarter the size used there. Taken after $160\Omega_p^{-1}$, the arrows show bulk velocity.

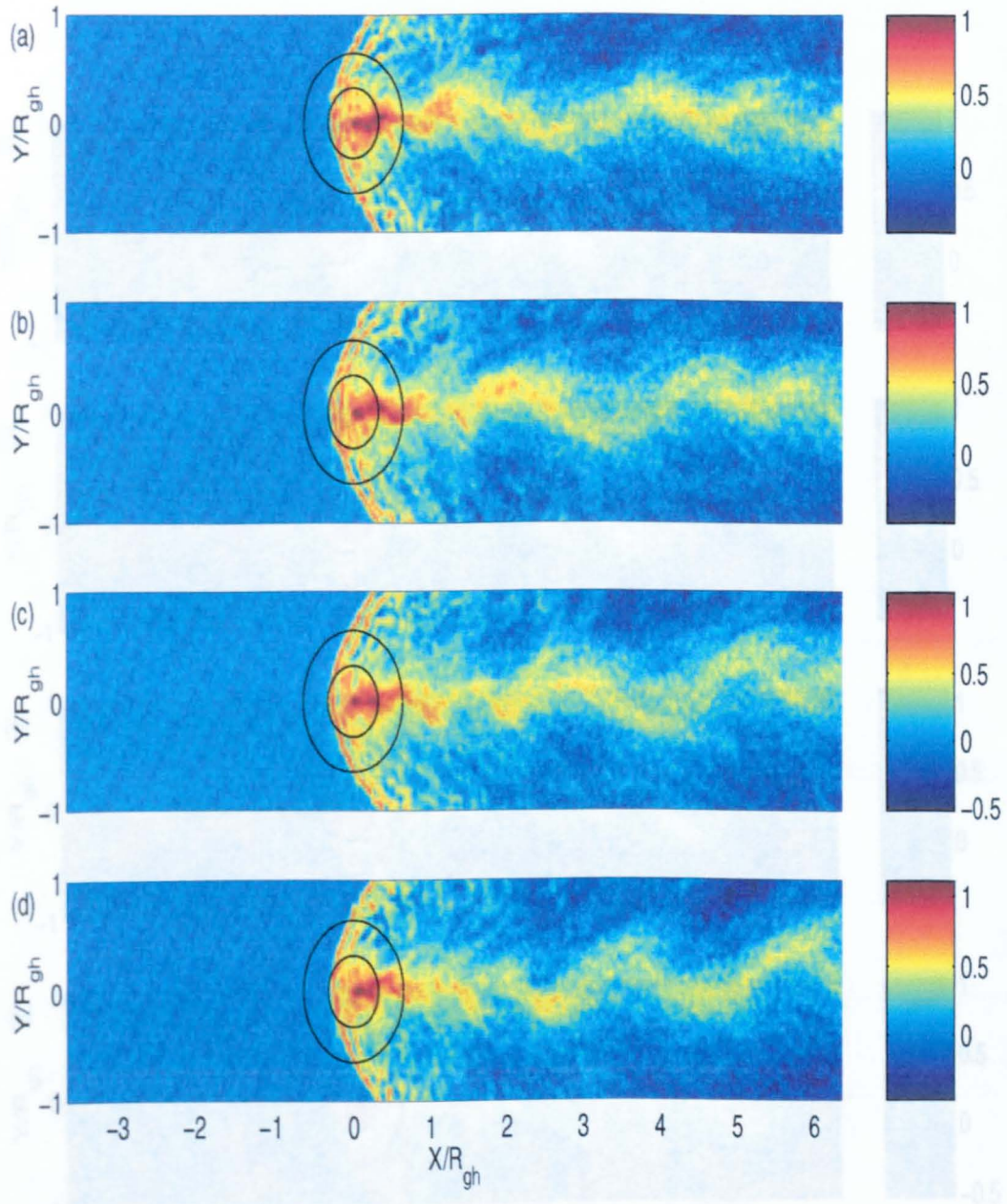

Figure 4.13: (Continued overleaf) A sequence of plots of total mass density using a $\log_{10}$ scale of a simulation with $M_A = 6.6$ and $\underline{B}_{IMF} = -B_z$. The sequence starts in a quasi-steady state (at $330\Omega_p^{-1}$ in panel (a)) and each panel is $10\Omega_p^{-1}$ later than the previous. Notice the KH oscillations in the cometary ion tail progressing downstream. This simulation used only 25 p.p.c. due to numerical constraints.

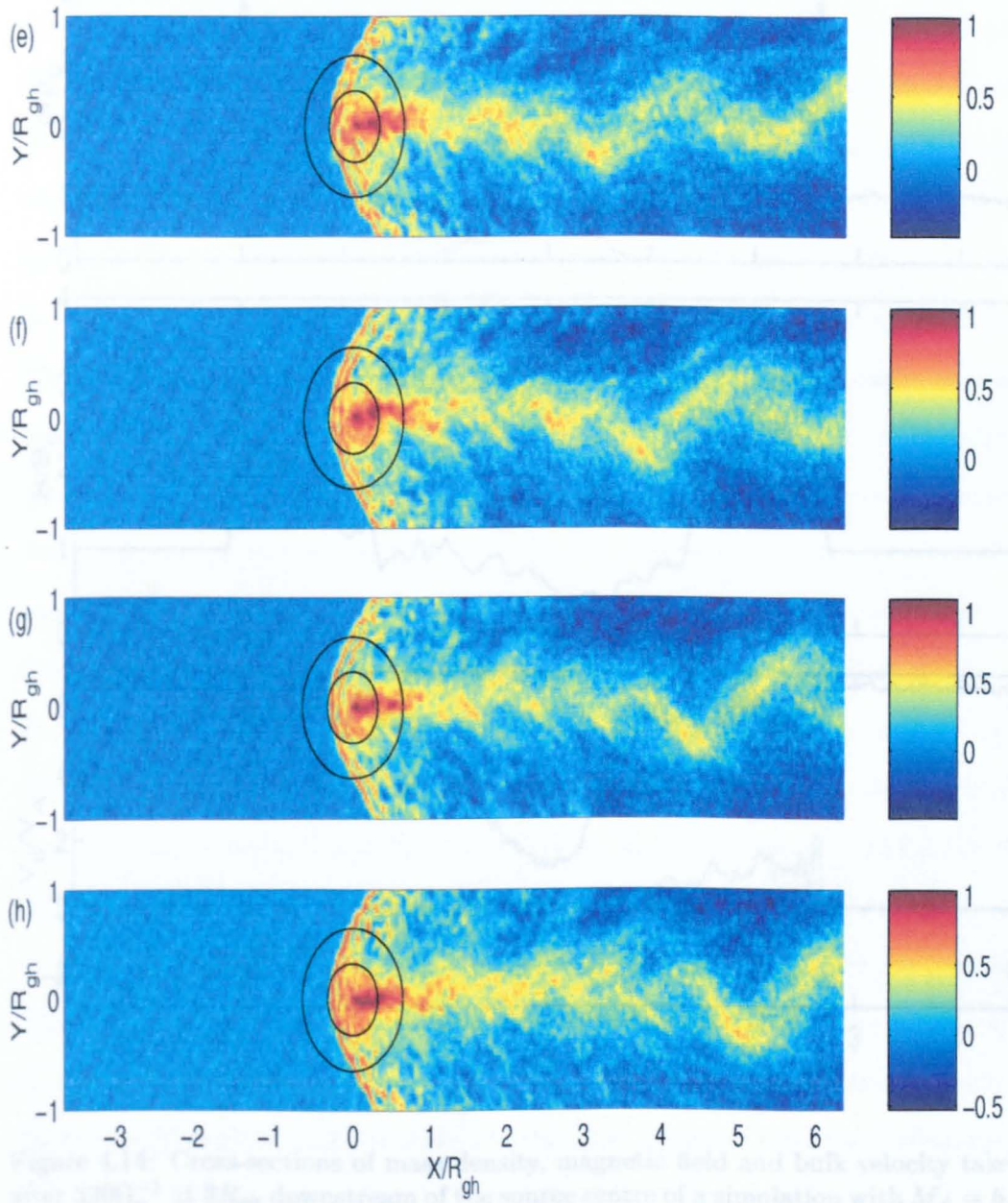
(e)
(f)
(g)
(h)
Y/R_gh
X/R_gh
1
0
−1
−3
−2
−1
0
1
2
3
4
5
6
0.5
−0.5

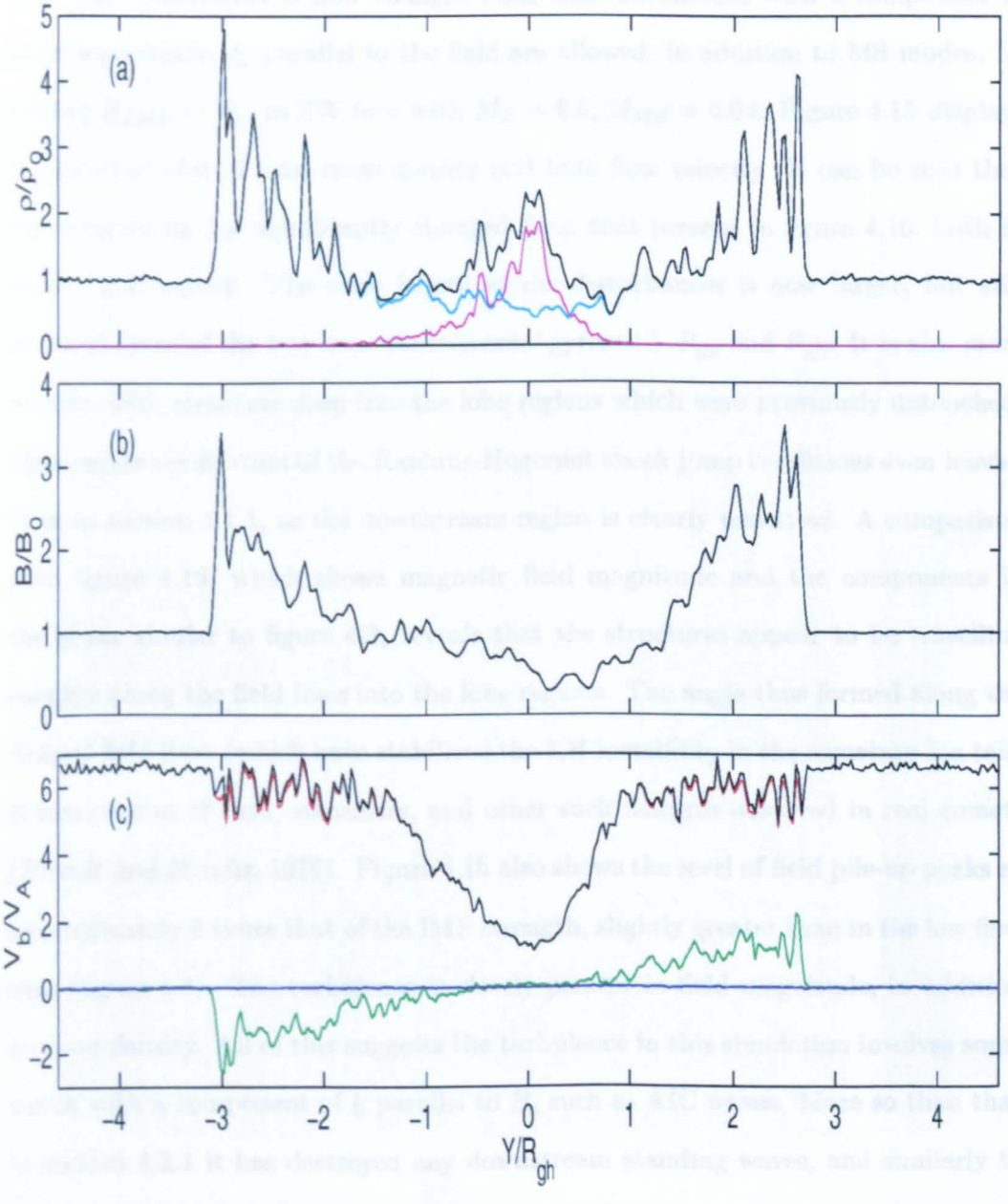

Figure 4.14: Cross-sections of mass density, magnetic field and bulk velocity taken after $320\Omega_p^{-1}$ at $3R_{gh}$ downstream of the source centre of a simulation with $M_A = 6.6$ and $\underline{B}_{IMF} = -B_z$. Colour scheme as for figure 4.4, except that only magnetic field magnitude (black) is shown in panel (b) as no other components are present.

4.2.2 IMF in the simulation plane

The IMF orientation is now changed such that wavemodes with a component of their wavevector, $\underline{k}$, parallel to the field are allowed, in addition to MS modes, by setting $\underline{B}_{IMF} = B_y$, in SW flow with $M_A = 6.6, M_{MS} = 6.04$. Figure 4.15 displays the familiar plot of total mass density and bulk flow velocity. It can be seen that the structuring has significantly changed from that present in figure 4.10, both in nature and extent. The scale length of the disturbances is now larger, but still between those of the two ionic constituents' gyroradii, R_{gp} and R_{gh}. It is also more prolific, with structure deep into the lobe regions which were previously untouched. This makes verification of the Rankine-Hugoniot shock jump conditions even harder than in section 4.1.1, as the downstream region is clearly unsettled. A comparison with figure 4.16, which shows magnetic field magnitude and the components in the plane similar to figure 4.3, reveals that the structures appear to be travelling roughly along the field lines into the lobe regions. The angle thus formed along the draped field lines (which have stabilized the KH instability in the cometary ion tail) is reminiscent of rays, streamers, and other such features observed in real comets (*Brandt and Mendis*, 1979). Figure 4.16 also shows the level of field pile-up peaks at approximately 6 times that of the IMF strength, slightly greater than in the low flow case (figure 4.3). The turbulence is clearly present in field magnitude, in addition to mass density. All of this suggests the turbulence in this simulation involves some waves with a component of $\underline{k}$ parallel to $\underline{B}$, such as AIC waves. More so than that in section 4.2.1 it has destroyed any downstream standing waves, and similarly to there the BS angle is 23.3° compared to the 13.4° expected from fluid calculations.

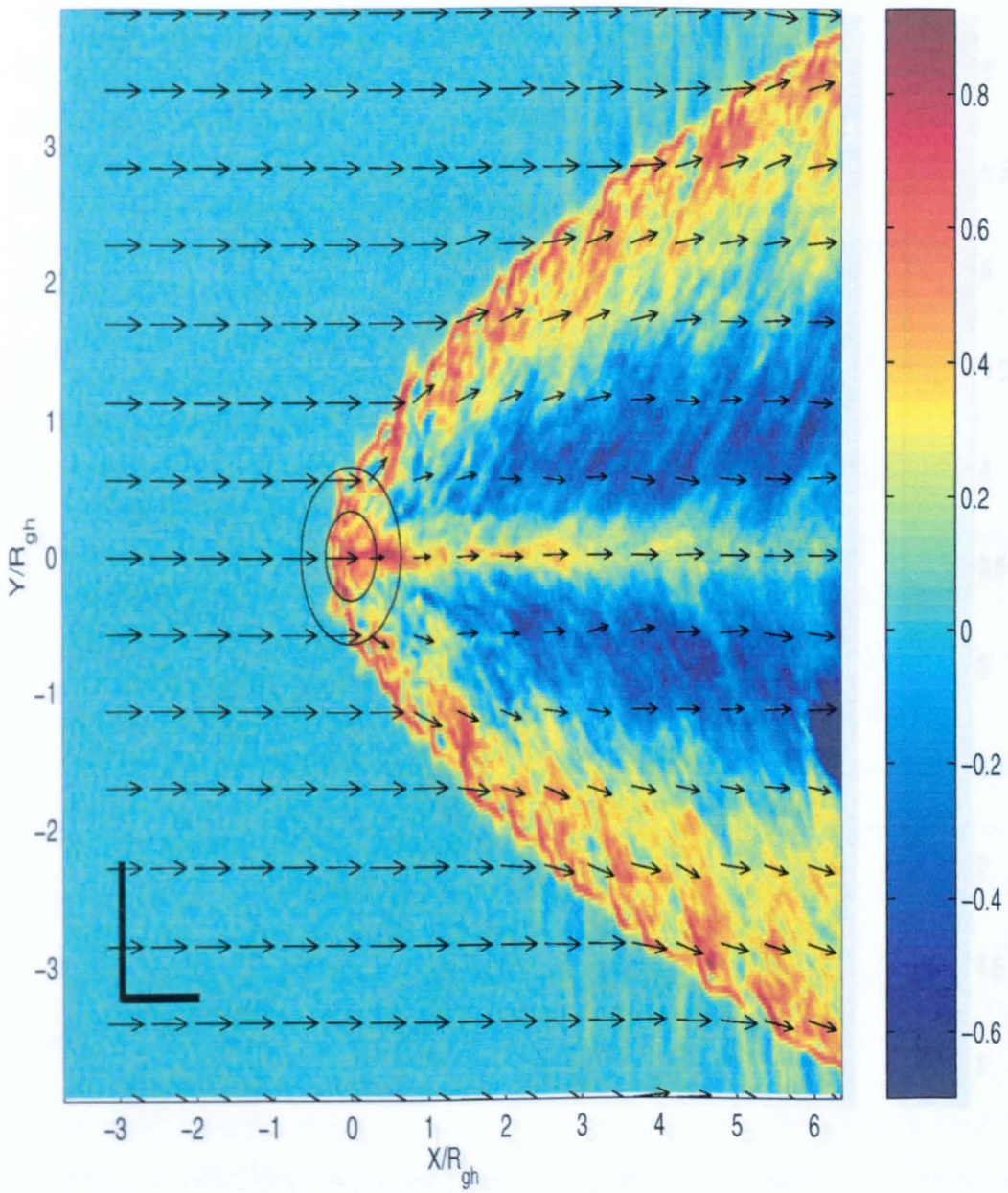

Figure 4.15: Total mass density using a $\log_{10}$ scale for a simulation with $M_A = 6.6$ and $\underline{B}_{IMF} = B_y$. Taken after $320\Omega_p^{-1}$, the arrows show bulk velocity in the plane.

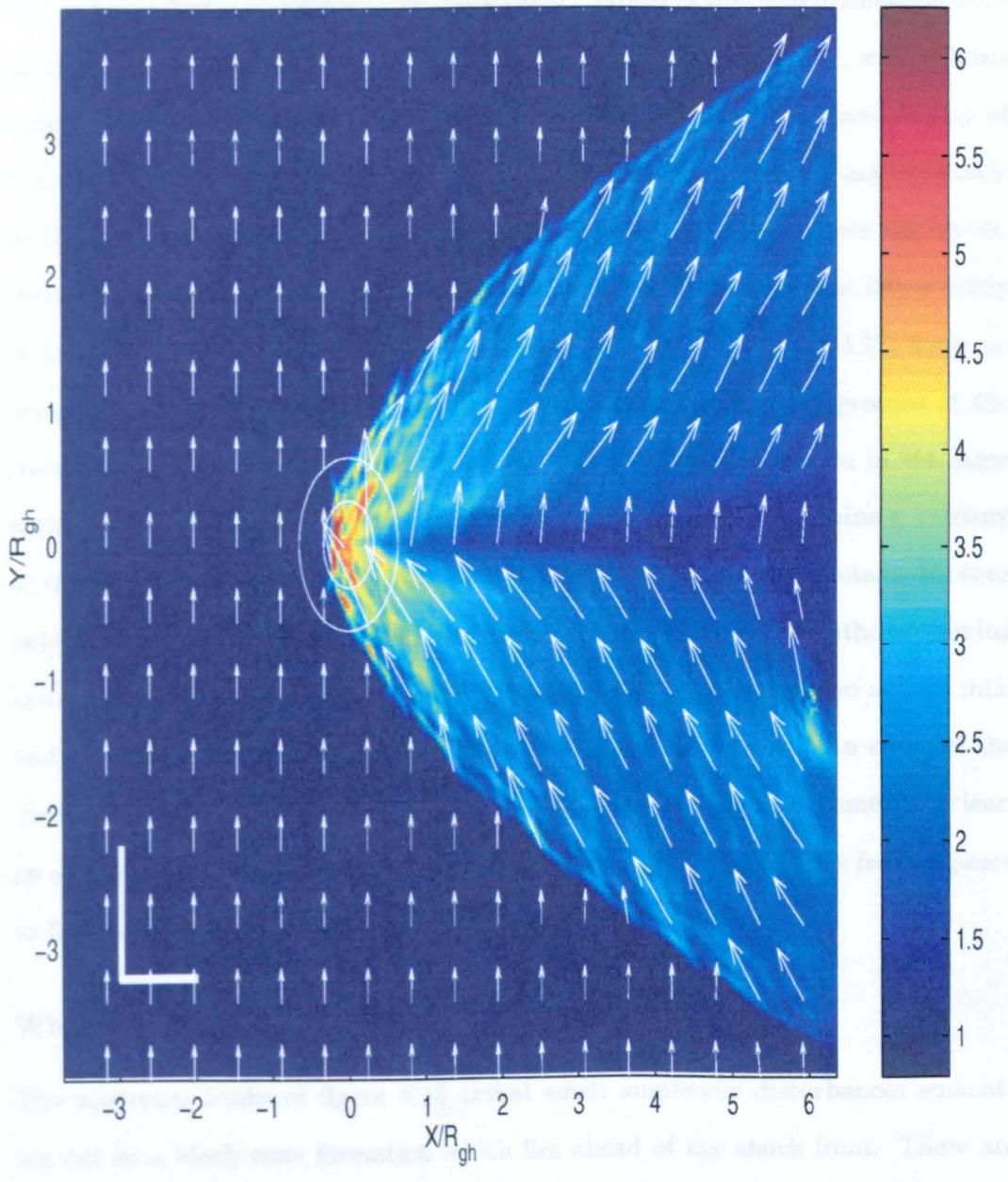

Figure 4.16: Magnetic field magnitude, and components in the plane, for the same simulation and time as in figure 4.15.

High resolution simulation

A simulation with a smaller total grid size and an individual cell size of one quarter that in figure 4.15 was performed to check the structures in this field orientation were independent of cell size. The results of this can be seen in figure 4.17, which shows total mass density and bulk flow, and figure 4.18 which shows the mass density of the cometary ions only. By comparing the two, it can be seen that the main obstacle to the flow is the inner source region, whilst the halo front permeates the shock, thereby allowing cometary ions to be picked up in fast flow also. Most importantly of all, parts of the shock flanks which exhibit turbulence in figure 4.17, show no presence of cometary ions locally in figure 4.18. The structuring of protons at the shock is thus not merely a direct reaction to cometary ion structure in the same region (such as in *Bogdanov et. al.* (1996)) — only the nose contains a mixture of the two species. Sufficiently far along the shock, the structure contains protons only. This suggests the generation mechanism for the structuring is either occurring along all regions of the shock, or takes place in the nose where the two species mix, and then requires a propagation mechanism to reach other areas. An effect of the disturbances along the length of the shock is that the front itself becomes less clear, an example being found near (0.75, 1.0) in figure 4.17, where the shock front appears to fall back discontinuously.

Whistler waves

The upstream flanks of figure 4.15 reveal small amplitude disturbances emanating out in a Mach cone formation which lies ahead of the shock front. These are thought to be whistler waves. Figure 4.19 gives a closer look at these by plotting $\log_{10}\left(\sqrt{B_i^2}\right)$, where $i = x$ in panel (a); $i = y$ in panel (b); $i = z$ in panel (c). This shows more detail of each component at low amplitudes and from the results

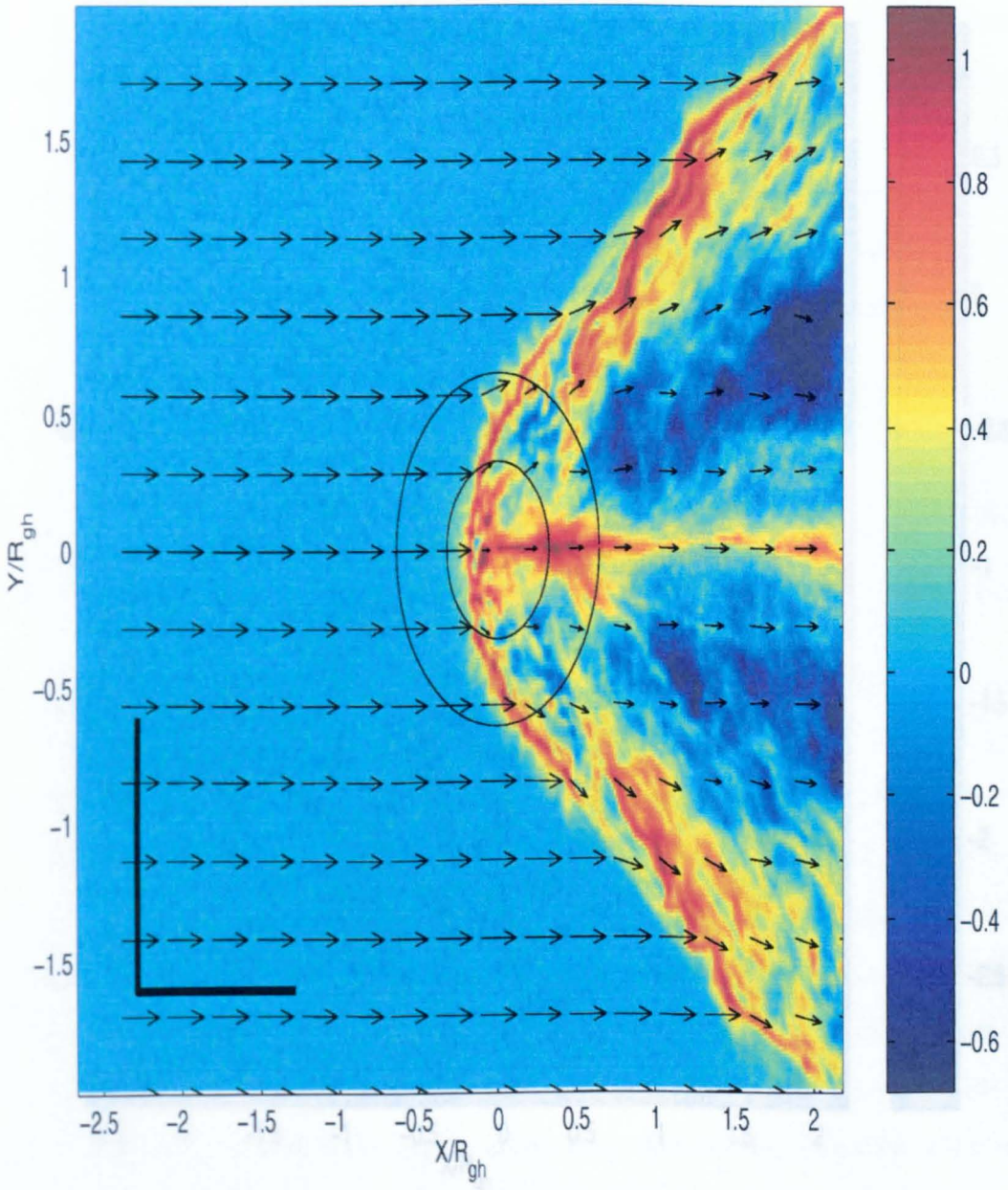

Figure 4.17: Total mass density using a $\log_{10}$ scale for a simulation with $M_A = 6.6$ and $\underline{B}_{IMF} = B_y$, but using a grid cell of one quarter the size used in figure 4.15. Taken after $120\Omega_p^{-1}$, the arrows show bulk velocity.

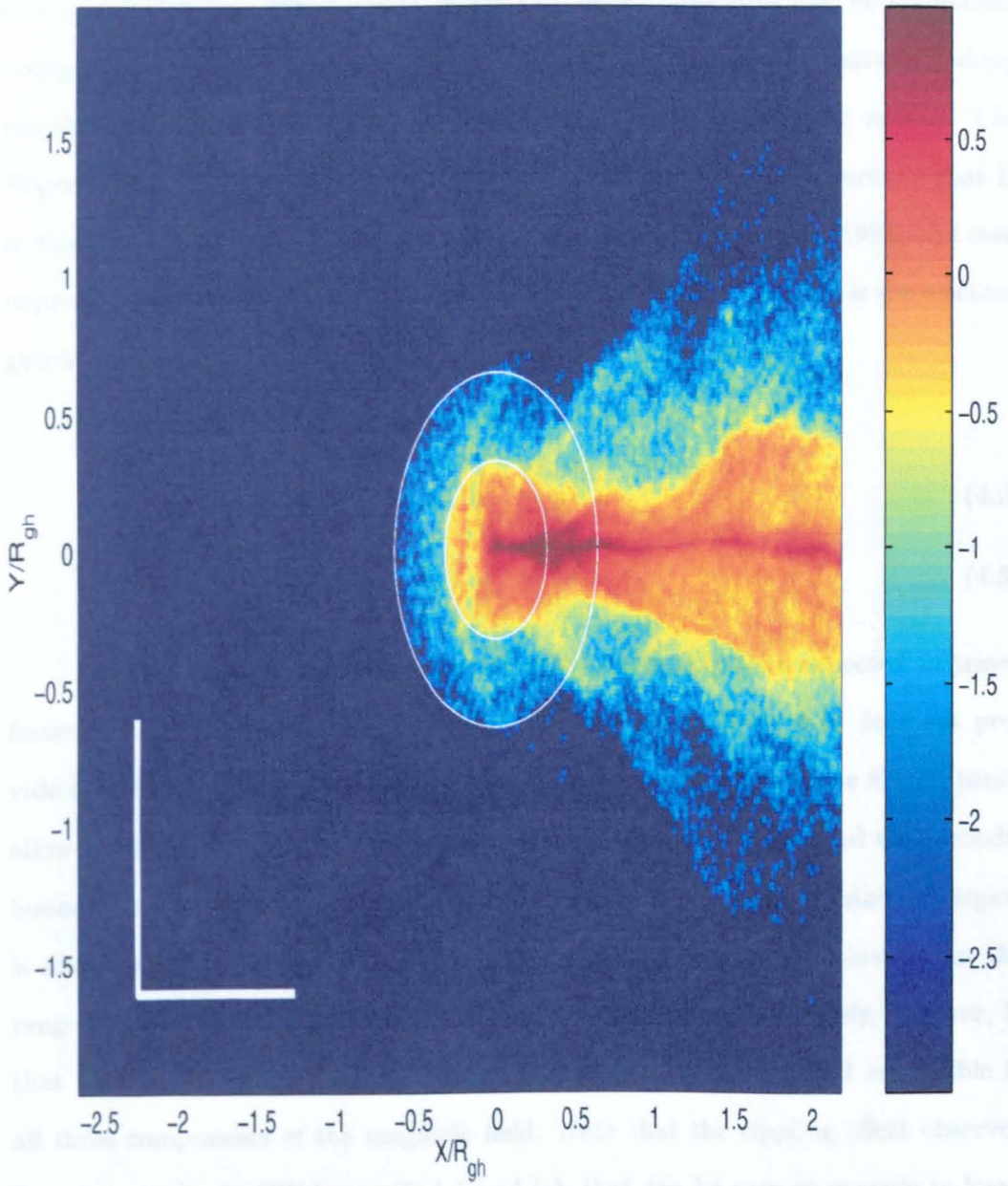

Figure 4.18: Mass density of cometary ions only using a $\log_{10}$ scale for the same simulation as shown in figure 4.17. Notice by comparison that sufficiently far along the flanks there are no cometary ions at the shock.

it can be seen that an effect is felt in all three, in addition to the mass density in figure 4.15. By using "*time=distance/velocity*" and assuming the upstream SW flow speed of $6.6v_A$, the speed at which this front propagates can be estimated. Using panel (c) as the clearest example, it is found the front travels outwards along the IMF at a speed of roughly $9.6v_A$ (other components give similar values). The dispersion relation for whistler waves, in a different, but equivalent form to that in section 3.3.2, is given in equation (4.2) (*Baumjohann and Treumann*, 1996) and consequently their group velocity is given by equation (4.3), in which Ω_e is the electron gyrofrequency, ω_{pe} the plasma frequency, and c the speed of light.

$$\omega = \frac{k^2c^2\Omega_e}{\omega_{pe}^2} \tag{4.2}$$

$$v_g = \frac{2kc^2\Omega_e}{\omega_{pe}^2} \tag{4.3}$$

Larger wavevectors, hence shorter wavelengths, are thus expected to travel faster and form the cone angle observed. Unfortunately figure 4.19 does not provide enough range for spectral analysis to be performed to determine k, and hence allow verification. The cone front can clearly be seen to wrap round the periodic boundaries and thus interfere with much of itself. The limited, untainted region is insufficient for analysis and running the simulation again with three times the range in y would be impractical numerically. Whistlers do seem likely, however, in that they travel upstream of the shock, faster than MS waves, and are visible in all three components of the magnetic field. Note that the rippling effect observed far upstream in the SW in panels (a) and (c), that can be seen to cascade to lower frequency further downstream, is the presence of normal modes of the grid. These are smoothed out as they progress downstream. As they only appear on these plots, they are shown to be low amplitude.

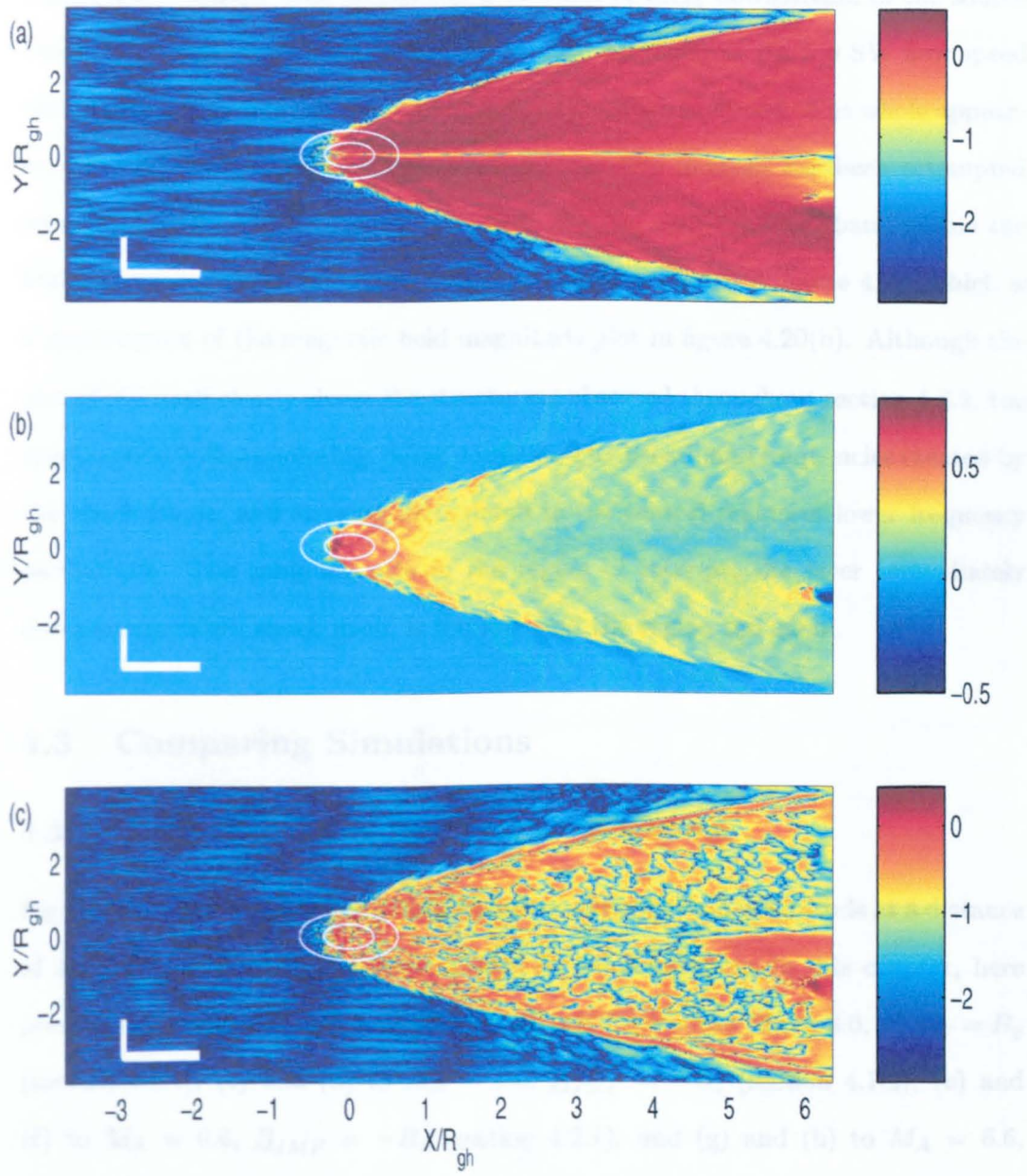

Figure 4.19: Plots of $\log_{10}\left(\sqrt{B_i^2}\right)$ where $i = x$ in panel (a), $i = y$ in panel (b), and $i = z$ in panel (c), for a simulation with $M_A = 6.6$ and $\underline{B}_{IMF} = B_y$ after $320\Omega_p^{-1}$. Notice the disturbances upstream of the shock flanks, which are most clear in panels (a) and (c).

Figure 4.20 displays cross-sections at a distance of $3R_{gh}$ downstream of the source centre for the same simulation as in figure 4.15. Similarly to the low SW flow speed case, figure 4.4, jumps in B_z at the shock front itself are observed. The whole appearance is now much more irregular, however. Spectral analysis has been attempted on several results in this chapter with little success: they are broadband within the limits of resolution. One of the clearest examples is shown in figure 4.21, which is a spectrogram of the magnetic field magnitude plot in figure 4.20(b). Although the plot of $|\underline{B}|$ itself clearly shows the structuring observed throughout section 4.2.2, the spectrogram is disappointing, being dominated by broadband frequencies created by the shock fronts, and showing little detail in the central region of lower frequency oscillations. The sampling rate in the region of interest, the layer immediately downstream of the shock itself, is too low, and the region too small.

4.3 Comparing Simulations

4.3.1 Density and magnetic field cross-sections

Figure 4.22 gives cross-sections of density and magnetic field magnitude at a distance of $3R_{gh}$ downstream of the source centre for all simulations in this chapter, here presented for direct comparison. Panels (a) and (b) refer to $M_A = 3.0$, $\underline{B}_{IMF} = B_y$ (section 4.1.1); (c) and (d) to $M_A = 3.0$, $\underline{B}_{IMF} = -B_z$ (section 4.1.2); (e) and (f) to $M_A = 6.6$, $\underline{B}_{IMF} = -B_z$ (section 4.2.1); and (g) and (h) to $M_A = 6.6$, $\underline{B}_{IMF} = B_y$ (section 4.2.2). It can be seen that other than a slight asymmetry in panels (c) and (d), and effects such as velocity shear and increased density in the tail, both simulations at low SW Mach number are similar, in that they both present well-defined shock jumps with standing waves immediately downstream, gradually

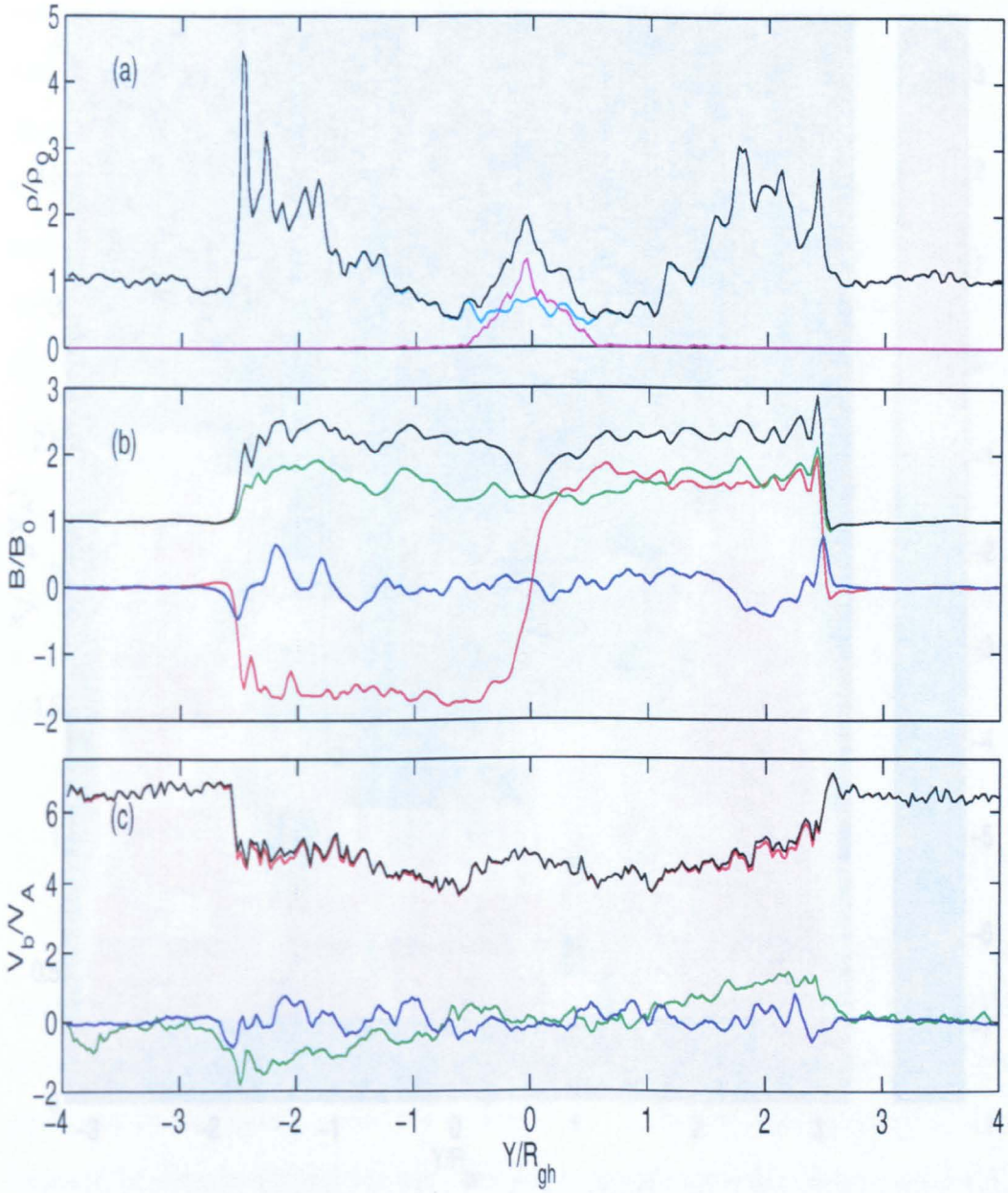

Figure 4.20: Cross-sections of mass density, magnetic field and bulk velocity after $320\Omega_p^{-1}$ at $3R_{gh}$ downstream of the source centre of a simulation with $M_A = 6.6$ and $\underline{B}_{IMF} = B_y$. Colour coding is as for figure 4.4.

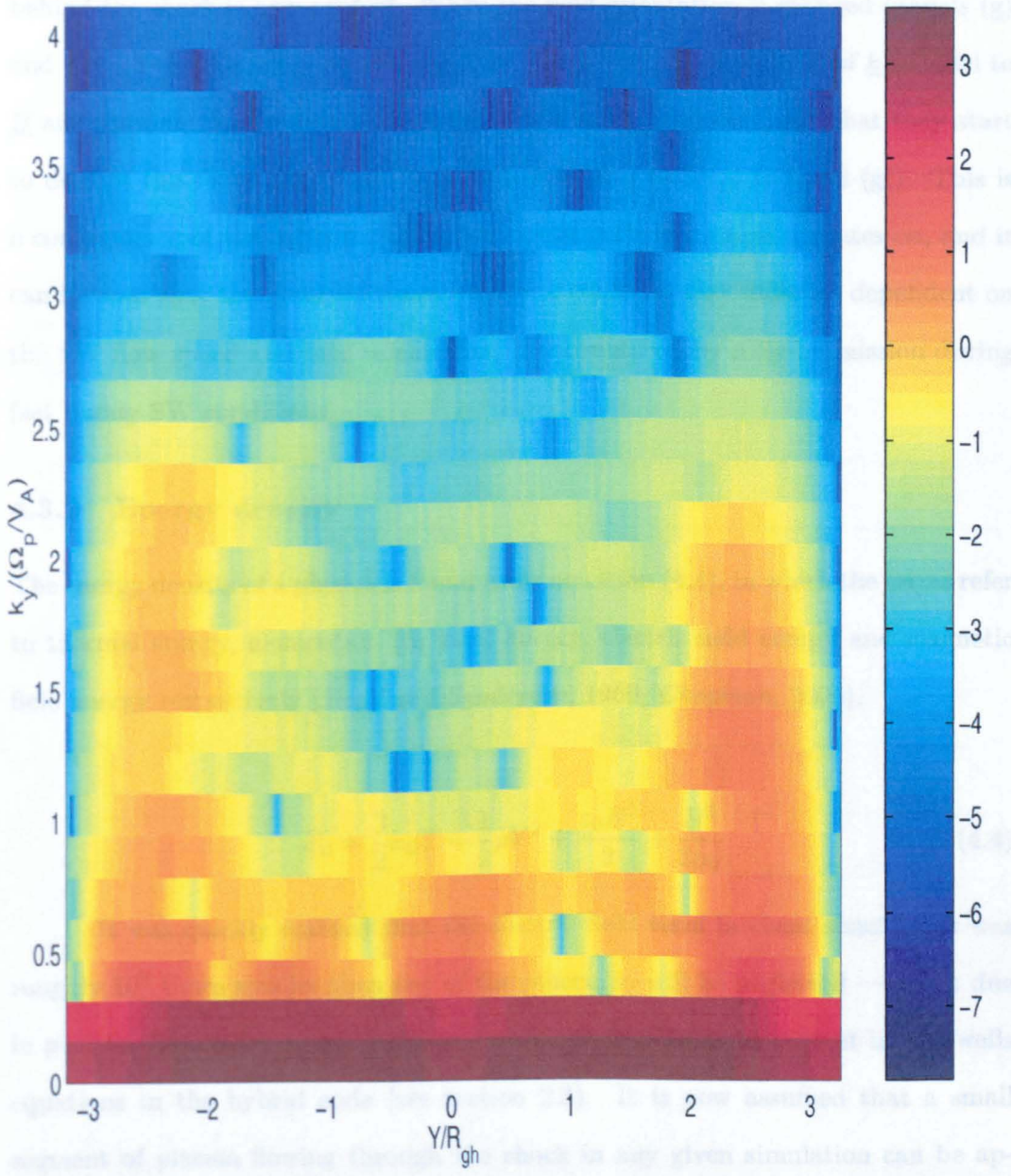

Figure 4.21: Spectrogram of a cross-section of the magnetic field magnitude at $3R_{gh}$ downstream of the source centre for a simulation with $M_A = 6.6$ and $\underline{B}_{IMF} = B_y$ after $320\Omega_p^{-1}$ (the black line in figure 4.20(b)).

damped. When the SW flow speed is raised, with the field perpendicular to the plane (panels (e) and (f)), the shock remains well-defined, but MS turbulence immediately behind the shock is now evident. When the field orientation is changed (panels (g) and (h)) at this high flow speed such that waves with a component of $\underline{k}$ parallel to $\underline{B}$ are allowed, the disturbances become even more irregular, such that they start to disrupt the shock front itself (see for example, $y \sim 2R_{gh}$ in panel (g)). This is a consequence of the increased scale length the turbulence now operates on, and it can be seen that the observed shock structure could be very different dependent on the SW flow speed and field orientation, if encountered by a fly-by mission during fast bursty SW conditions.

4.3.2 Energy density

The energy density of a plasma is found using equation (4.4), in which the terms refer to thermal energy, momentum (or ram) energy, electric field energy and magnetic field energy respectively (*Boyd and Sanderson*, 1969; *Chapman*, 2000).

$$E_d = \frac{3}{2}k_B T + \frac{1}{2}\rho V^2 + \frac{\varepsilon_0 E^2}{2} + \frac{B^2}{2\mu_0} \tag{4.4}$$

It was quickly realized that the electric field term in these simulations was roughly 10^5 times smaller than any of the others, so will be neglected — a fact due in part to the low frequency limit neglect of the displacement current in Maxwells equations in the hybrid code (see section 2.3). It is now assumed that a small segment of plasma flowing through the shock in any given simulation can be approximated by an instantaneous measurement along a streamline it would follow. This is justified by the quasi-steady conditions present.

Figures 4.23 and 4.24 display plots of the three remaining energy density terms along such streamlines at $y = 1.4R_{gh}$. Figure 4.23 shows the results of

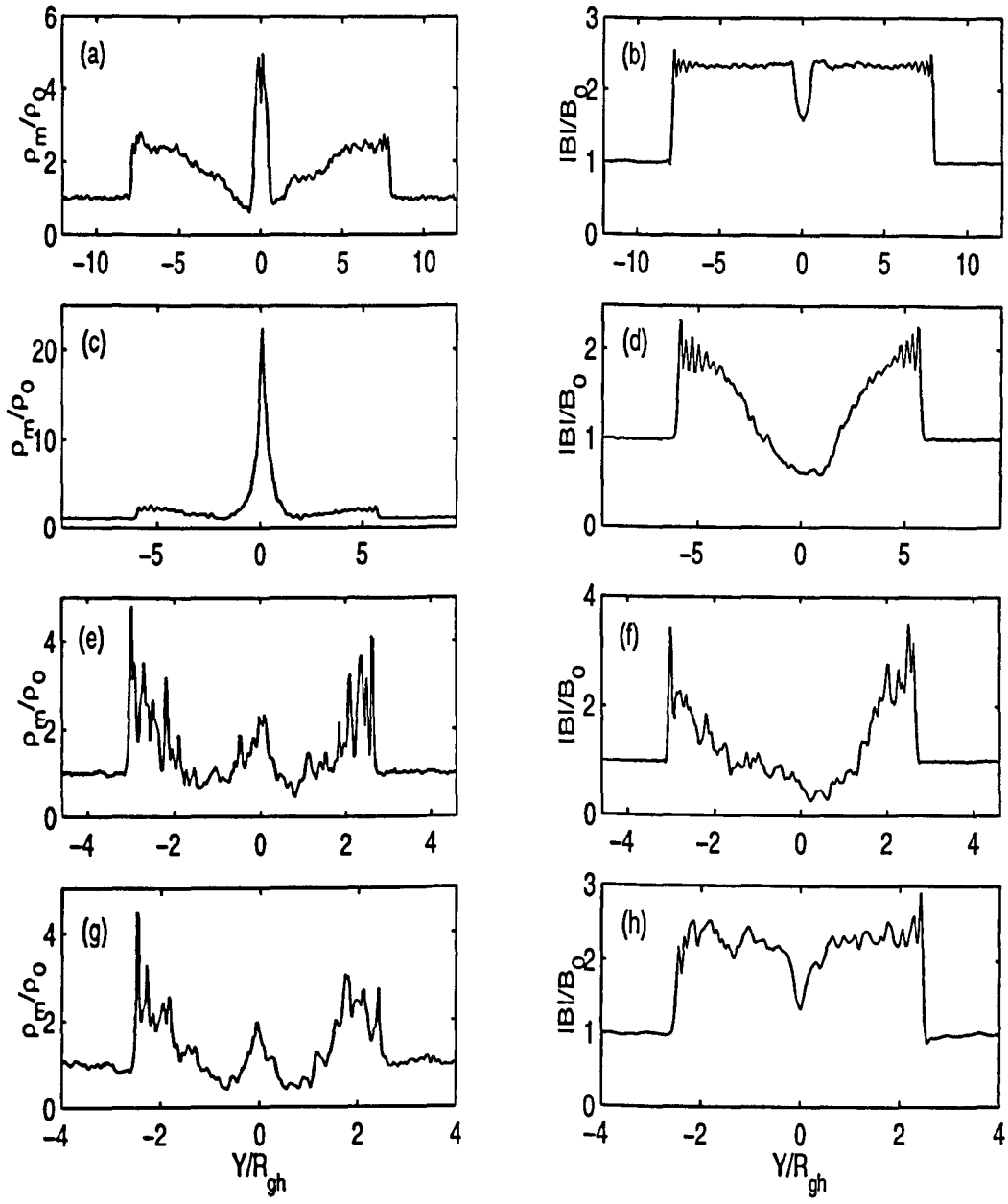

Figure 4.22: Total mass density and magnetic field magnitude cross-sections at $3R_{gh}$ downstream of the source centre for: $M_A = 3.0$, $\underline{B}_0 = B_y$ (panels (a) and (b)); $M_A = 3.0$, $\underline{B}_0 = -B_z$ (panels (c) and (d)); $M_A = 6.6$, $\underline{B}_0 = -B_z$ (panels (e) and (f)); and $M_A = 6.6$, $\underline{B}_0 = B_y$ (panels (g) and (h)). Notice the deteriorating definition of the shock *front* as the downstream disturbances become active on larger scale lengths.

simulations with (a) $M_A = 3.0$, $B_{IMF} = B_y$ (section 4.1.1) and (b) $M_A = 3.0$, $B_{IMF} = -B_z$ (section 4.1.2), whilst figure 4.24 shows those with (a) $M_A = 6.6$, $B_{IMF} = B_y$ (section 4.2.2) and (b) $M_A = 6.6$, $B_{IMF} = -B_z$ (section 4.2.1). The thermal energy density plots are taken at different times due to a mistake in the data writing procedure for pressure. As all plots are taken under quasi-steady state conditions, this should not affect the large-scale structures. The plots are individually normalized to their upstream SW values, which have then been scaled in a ratio suitable for representing approximate SW proportions (fast flowing, cold plasma), whilst clarifying the data on single sets of axes. In figure 4.23 the SW ram energy density (black) is 30 times the SW thermal energy density (red), whilst the magnetic component (blue) is 3 times the SW thermal energy. In figure 4.24 the same ratios are 100 and 3, to reflect the increased ram energy in $M_A = 6.6$ SW flow.

As expected, the energy density typically seems to transfer from the momentum in the SW, to increased thermal and magnetic components downstream. The thermal component generally peaks markedly at the shock front, before tailing off rapidly to a level still above that upstream in the SW. The magnetic field component generally peaks further downstream, and remains at a level above the upstream value whenever $B_{IMF} = B_y$ (figures 4.23(a) and 4.24(a)). When $B_{IMF} = -B_z$ the level of magnetic energy density far downstream appears to drop back to the order of its SW value again.

4.3.3 Normalized source rate

To enable a comparison of the results presented here to those of *Bogdanov et. al.* (1996), the calculation of the normalized production rate used, given by equation (1.4), is required. The source rate used in these cometary simulations was $1 \times 10^8 cm^{-2} s^{-1}$ (*Lammer and Bauer*, 1997) on a Mercury sized comet. Thus, using the radius of Mercury, $2439km$ (*Dunne*, 1974), a total production rate of

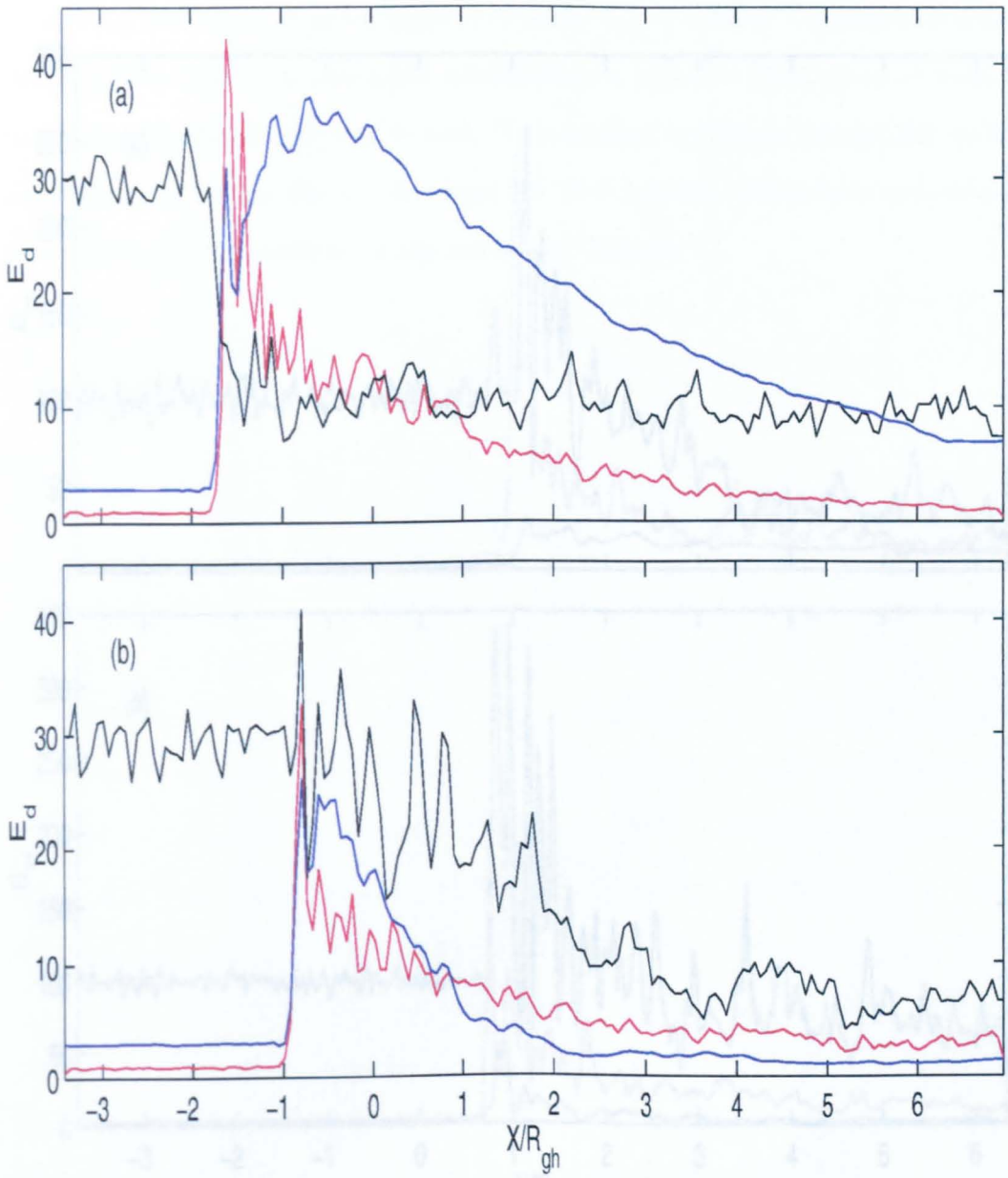

Figure 4.23: Energy density components along $y = 1.4R_{gh}$ for quasi-steady simulations with (a) $M_A = 3.0$, $B_{IMF} = B_y$ and (b) $M_A = 3.0$, $B_{IMF} = -B_z$.The lines show thermal energy density (red), ram energy density (black), and magnetic field energy density (blue), all as given in equation (4.4). All are normalized to their upstream values, which are then scaled approximately as found in the SW. Data in panel (a) is taken after $400\Omega_p^{-1}$ (ram and $\underline{B}$ field) and $360\Omega_p^{-1}$ (thermal). Data in panel (b) is taken after $720\Omega_p^{-1}$ (all components).

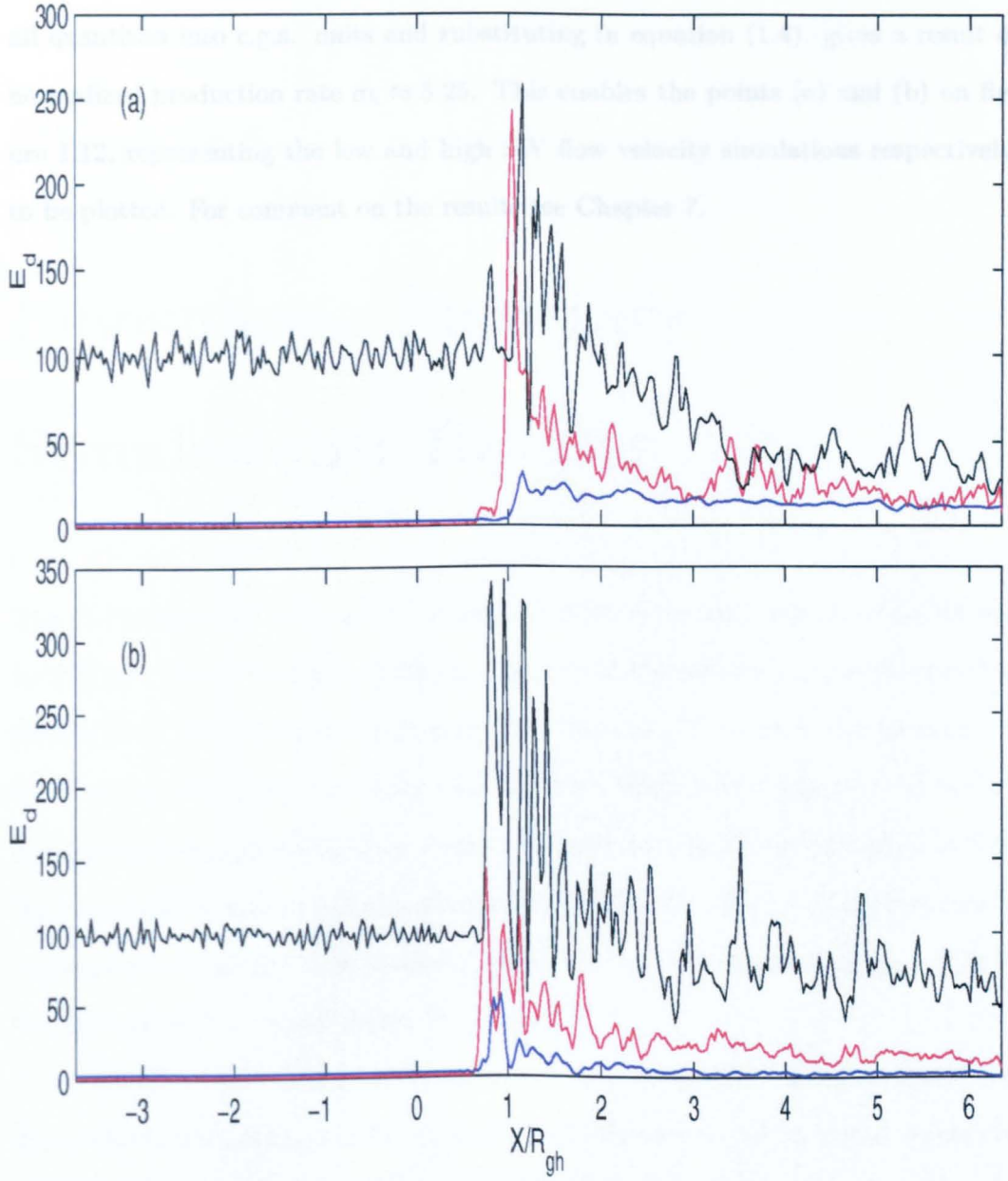

Figure 4.24: Similar plot to figure 4.23 except for simulations with (a) $M_A = 6.6$, $B_{IMF} = B_y$ and (b) $M_A = 6.6$, $B_{IMF} = -B_z$. Upstream values are now scaled differently to reflect the increased ram energy density in fast flow. Data in both panels is taken after $320\Omega_p^{-1}$ (ram and $\underline{B}$ field) and $240\Omega_p^{-1}$ (thermal).

$Q_h = 7.48 \times 10^{25} s^{-1}$ is found. Using this, and $B_{IMF} = 18nT$, ionization rate $\nu_i = 1.5 \times 10^{-4} s^{-1}$ and radial ejection velocity $V_{ej.} = 1.9 kms^{-1}$ before converting all quantities into c.g.s. units and substituting in equation (1.4), gives a result of normalized production rate $\sigma_h \approx 5.25$. This enables the points (a) and (b) on figure 1.12, representing the low and high SW flow velocity simulations respectively, to be plotted. For comment on the results see Chapter 7.

Chapter 5

Ionospheric Planetary Simulations: Results

The study discussed in Chapter 4 is now extended to examine the structure formed by SW flow past a weakly ionospheric source with a planetary core, as described in section 3.4.3. The interaction is thus one of a small moon or planet with no magnetic field, acting as a source of heavy ions via some weak mechanism such as surface sputtering, or irregular deposition such as volcanic activity. Examples might include the outermost moons of Saturn, when located externally to that magnetosphere in supermagnetosonic SW flow (*Bagenal*, 1985). Certain aspects are also applicable to Venus, even with its much denser ionosphere.

Unless otherwise stated, the mass density of the planet is taken fixed at $13\rho_0$. This value is not intended to be physically realistic because, as we would expect, its effect is emphasized by the 2D nature of the obstacle in the simulations. The aim is to attain as realistic as possible an interaction mechanism with the SW as this restriction to 2D allows — a restriction that is most evident in those simulations with $\underline{B}_{IMF} = B_y$ where field line draping dominates the solution. In this geometry the 2D cylindrical obstacle does not permit flux tubes to slip around the obstacle.

An indicator of such difficulties in this respect is the computational requirements for different simulations: those with $B_{IMF} = -B_z$ (section 5.1) typically run for $320\Omega_p^{-1}$ on a grid extending to $x = \pm 5R_{gh}$ in fast flow before giving a quasi-steady state, whilst those with $B_{IMF} = B_y$ (section 5.2) typically require $560\Omega_p^{-1}$ runtime on a grid width of $x = \pm 10R_{gh}$ in fast flow, and still do not evolve into quasi-steady conditions.

5.1 IMF Perpendicular to the Simulation Plane

5.1.1 Slow solar wind flow

Initially, the interaction in supermagnetosonic SW flow with $M_A = 3.0$ ($M_{MS} = 2.75$) was investigated. Figure 5.1 shows the total mass density on a $\log_{10}$ scale and in a quasi-steady state, with the arrows showing bulk velocity. The shock front has retained features of the cometary case under these conditions as it is smooth and displays damped oscillations immediately downstream similarly to section 4.1.2. There is now, however, an additional set of waves restricted to $y < 0$ which appear to be travelling downstream with wavefronts running $y \rightarrow -y$. These are seen more clearly in figure 6.10 which shows the current density carried by SW protons in this simulation, for comparison to those in the magnetized source pilot study. Some analysis is presented there, but they are thought to be due to the asymmetric pickup ion processes in this IMF orientation.

The most striking difference to the cometary results is the tail structure, which has been split into two strands of planetary ions separated by a wake, with different characteristics. These shall be referred to as the "upper tail" (UT) for that in $y > 0$, and "lower tail" (LT) for that in $y < 0$. Figure 5.2 shows the mass density of planetary ions only, for the same simulation as in figure 5.1. The planetary exosphere is being removed by the IMF passing, to create the new two

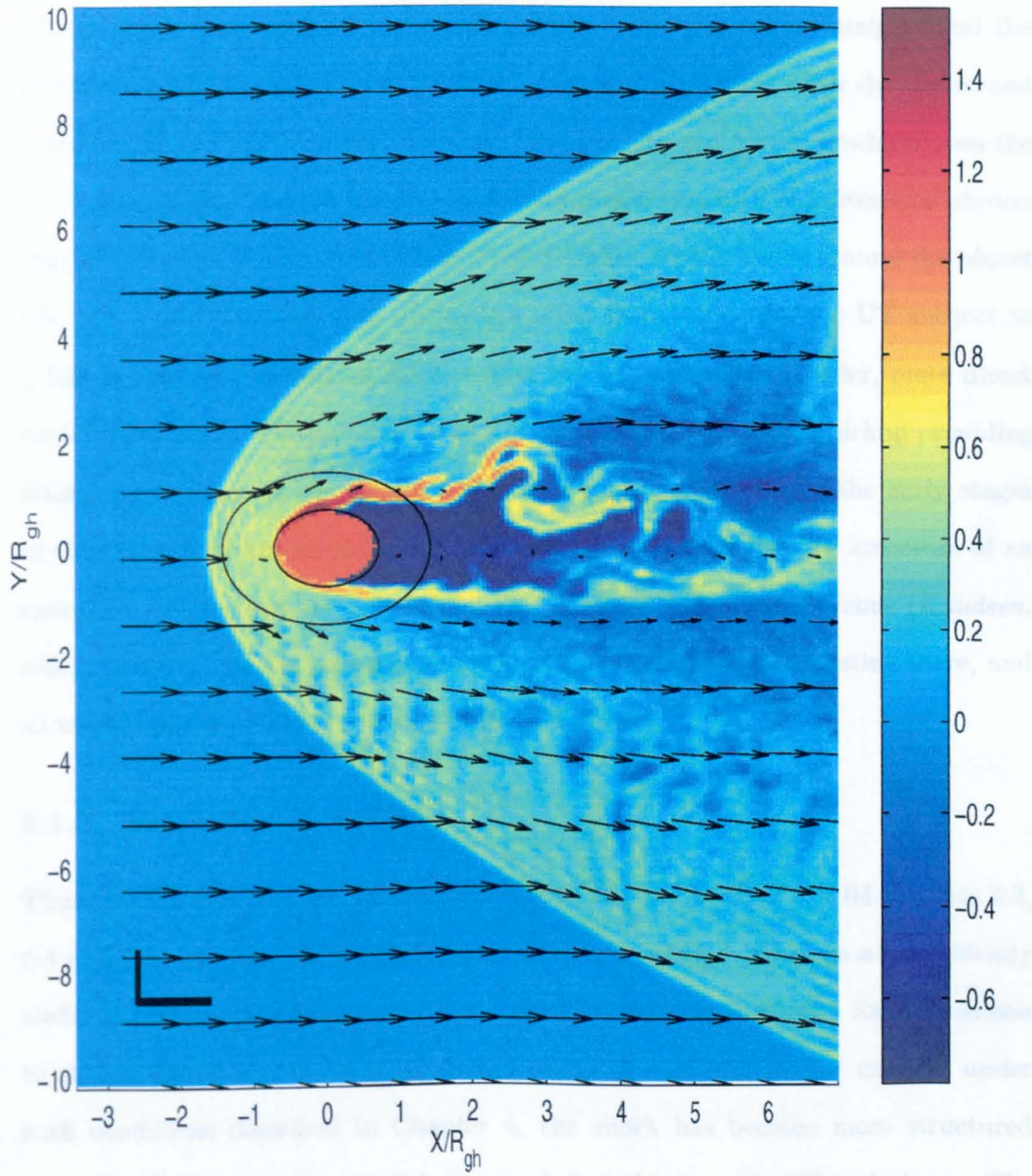

Figure 5.1: Total mass density using a $\log_{10}$ scale for a simulation with a weakly ionospheric planetary source in SW flow with $M_A = 3.0$ and $\underline{B}_{IMF} = -B_z$. That shown is a quasi-steady state, achieved after $720\Omega_p^{-1}$. The arrows show bulk velocity, with other markings as in figure 4.1.

tail structure. As the IMF is relatively free to slip around the obstacle in this orientation the wake is filled in further downstream, albeit in an irregular manner. Interestingly, there appears to be some infill of the wake *immediately* behind the planet by a small population of planetary ions which produce a low density strand within it. Note that the planet itself absorbs particles and is only productive on the $x < 0$ face, to simulate the low level sputtered production by SW proton and photon impact intended. This strand of ions must therefore rapidly move around the planet into the wake. The two tails themselves differ in nature, with the UT subject to a KH instability (see section 5.1.2) whilst the LT presents a broader, more direct path downstream. The increased width of the LT results from ion pickup providing lateral momentum in the $-y$-direction. Ions experiencing this in the early stages of the UT will be absorbed by the planet surface. Overall, the new structure of an exosphere being constantly eroded by the SW has similarities to Venus (*Knudsen*, 1992), however it must be remembered that the ionosphere is corotating there, and so would appear on the $x > 0$ face of the planet also.

5.1.2 Fast solar wind flow

The same source is now placed in SW flow with $M_A = 6.6$, $M_{MS} = 6.04$. Figures 5.3, 5.4 and 5.5 show the resulting structure after only $320\Omega_p^{-1}$, which is a quasi-steady state. Figure 5.3 shows the total mass density and bulk flow velocity for comparison to that in figure 5.1, in lower Mach number flow. Similarly to the changes under such conditions described in Chapter 4, the shock has become more structured immediately downstream and it is assumed that this is again MS turbulence. The global structure also maintains its asymmetry about the line $y = 0$. In comparison to the slower flow case, the shock jump in density has risen slightly, yet that of the tails has dropped dramatically, by a factor of roughly 10. This is seen more clearly in figure 5.4, where the UT seems to have been particularly depleted. This suggests

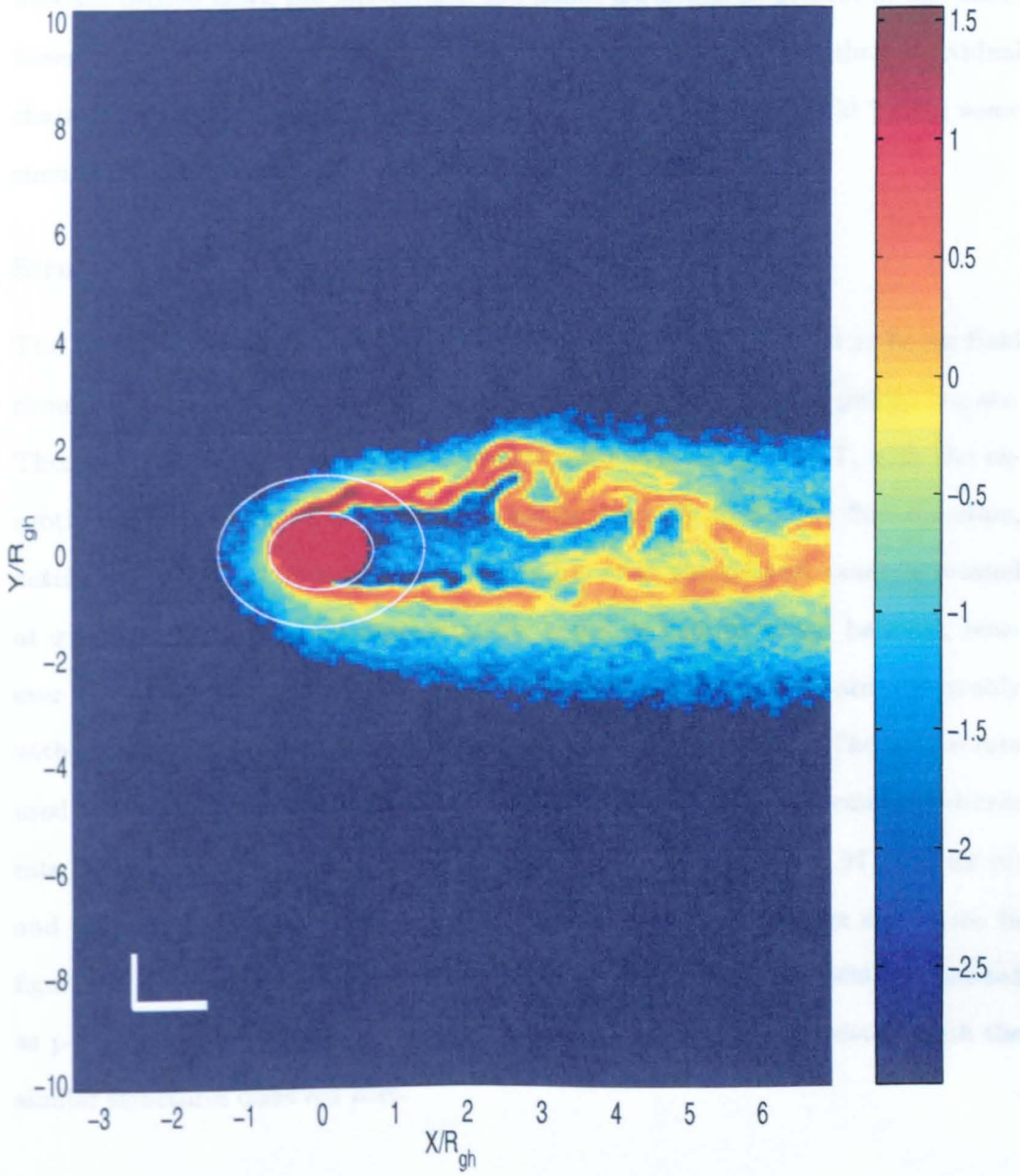

Figure 5.2: Mass density of planetary ions only, using a $\log_{10}$ scale, for the same simulation and time as in figure 5.1.

that in faster flow a larger percentage are forced back onto the planetary surface and absorbed, instead of entering the tail. Additionally, the faster flow will mean ions are carried down the tail quicker and hence fewer will be present at any time, however this will affect both tails equally. The two tails still retain their individual characteristics. Figure 5.5 shows the magnitude of the magnetic field for the same simulation and reveals a slow rate of diffusion through the planet.

Structure of the lower tail

The LT in figure 5.4 appears to display structure like that observed in bi-ion fluid simulations by *Bogdanov et. al.* (1996), in addition to its general pickup ion arc. There are density striations spaced roughly every R_{gh} along the LT, with the exception of the location $x \approx 3R_{gh}$. They appear laterally to the SW flow direction, cutting it top-left to bottom-right in figure 5.4, with the clearest example located at $x = 2R_{gh}$. The particle representation is not as high as would be ideal, however an average separation distance of $27.4\frac{v_A}{\Omega_p}$ is found, which compares favourably with a value of $28.6\frac{v_A}{\Omega_p}$ in figure 1(b) of *Bogdanov et. al.* (1996). The source rate used in figure 5.4, and other simulations in this chapter, gives a normalized source rate by equation (1.4) (from *Bogdanov et. al.* (1996)) of $\sigma_h = 1.97$. Points (c) and (d) can thus be added to figure 1.12, with (d) representing the simulation in figure 5.4. The parameters used in figure 1(b) of *Bogdanov et. al.* (1996) are plotted as point (e), and can be seen to fall in the same region as (d), consistent with the similar structures observed here.

High resolution simulation

Figure 5.6 shows the planetary ion mass density for a simulation with the same source and conditions as figure 5.4, only performed on a grid of one-quarter the cell size. Consequently the total grid size is necessarily reduced, but more detail

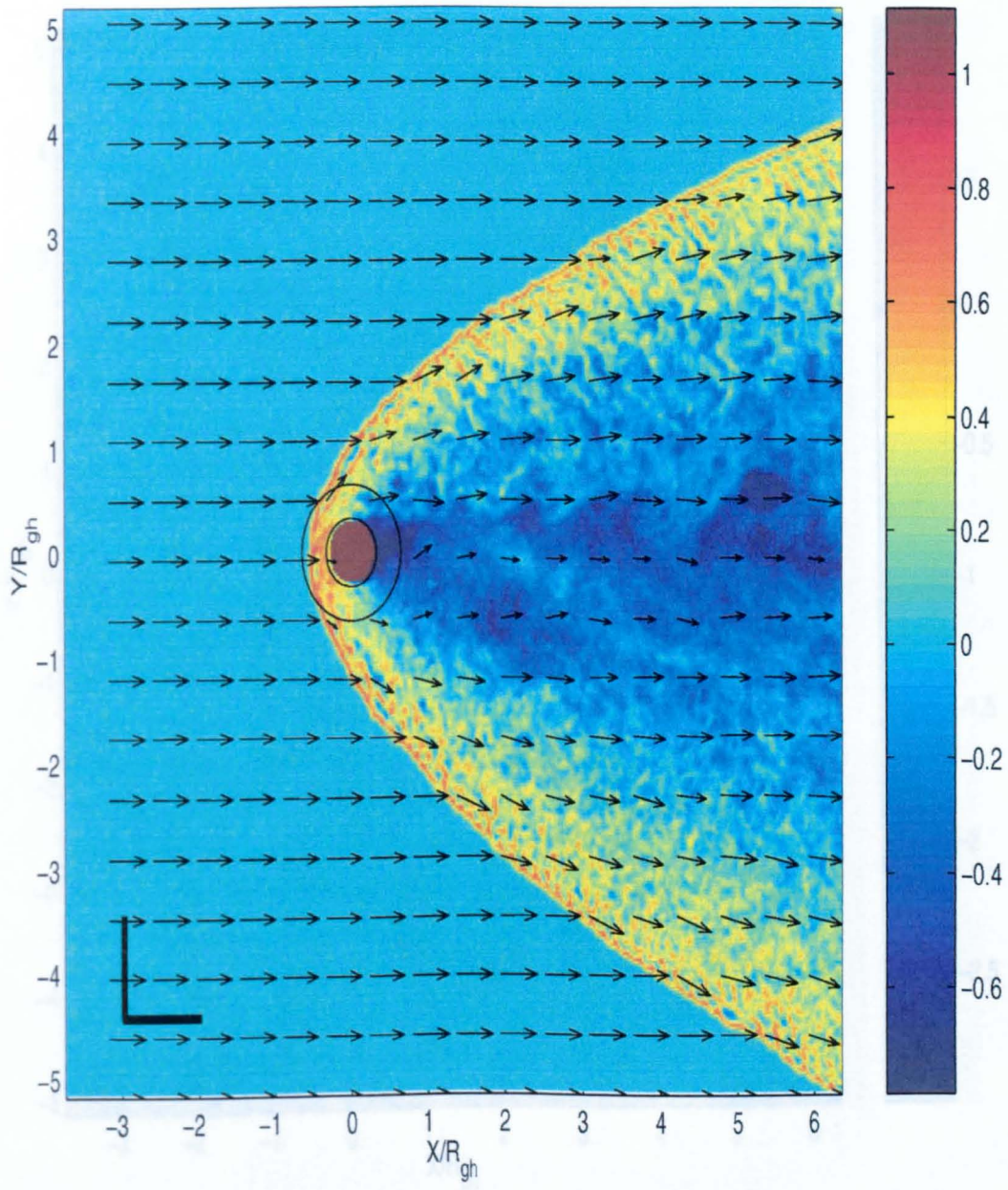

Figure 5.3: Total mass density using a $\log_{10}$ scale for a simulation with $M_A = 6.6$ and $\underline{B}_{IMF} = -B_z$. Taken after only $320\Omega_p^{-1}$ in a quasi-steady state, the arrows show bulk velocity.

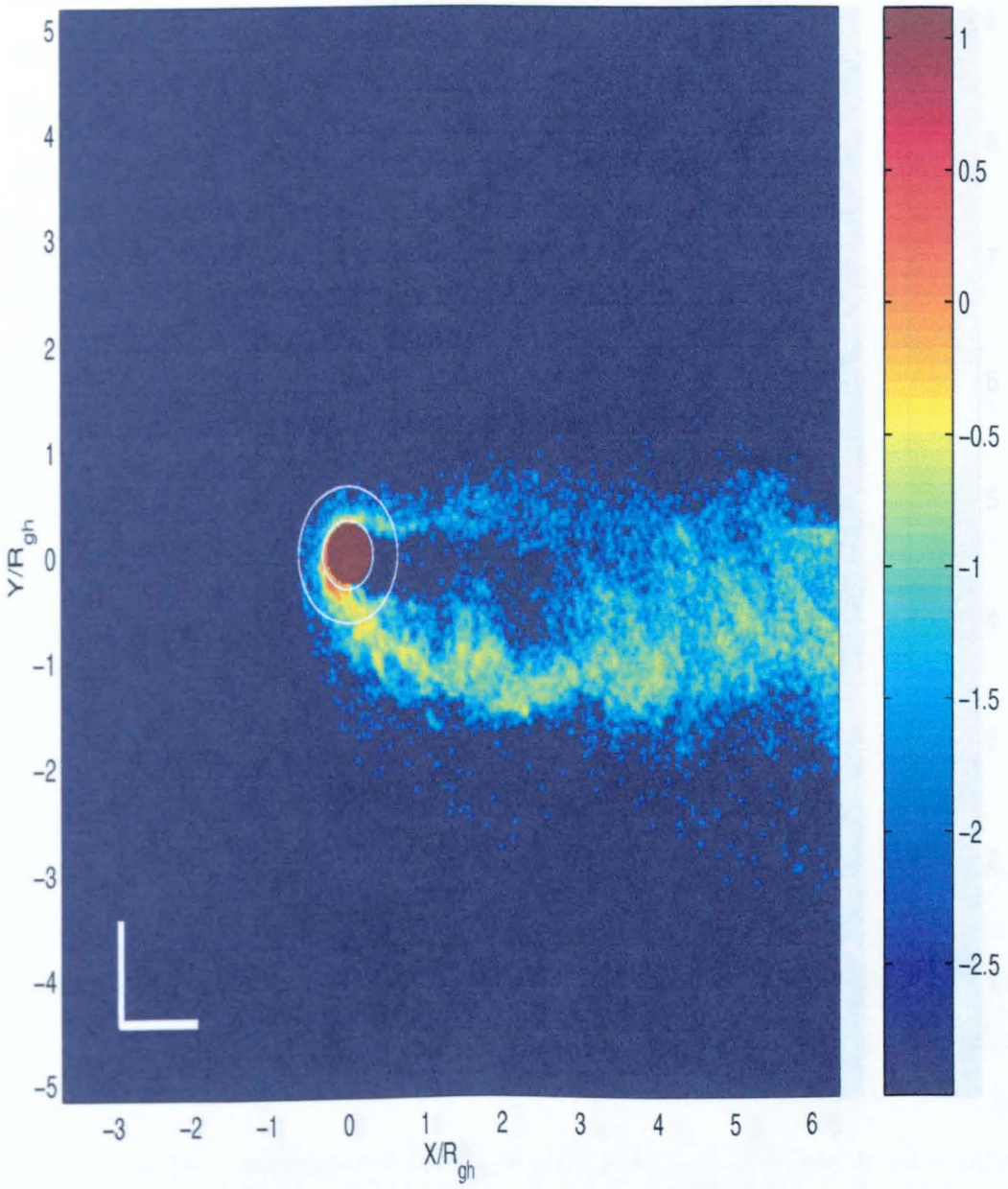

Figure 5.4: Mass density of planetary ions only, using a $\log_{10}$ scale, for the same simulation and time as in figure 5.3.

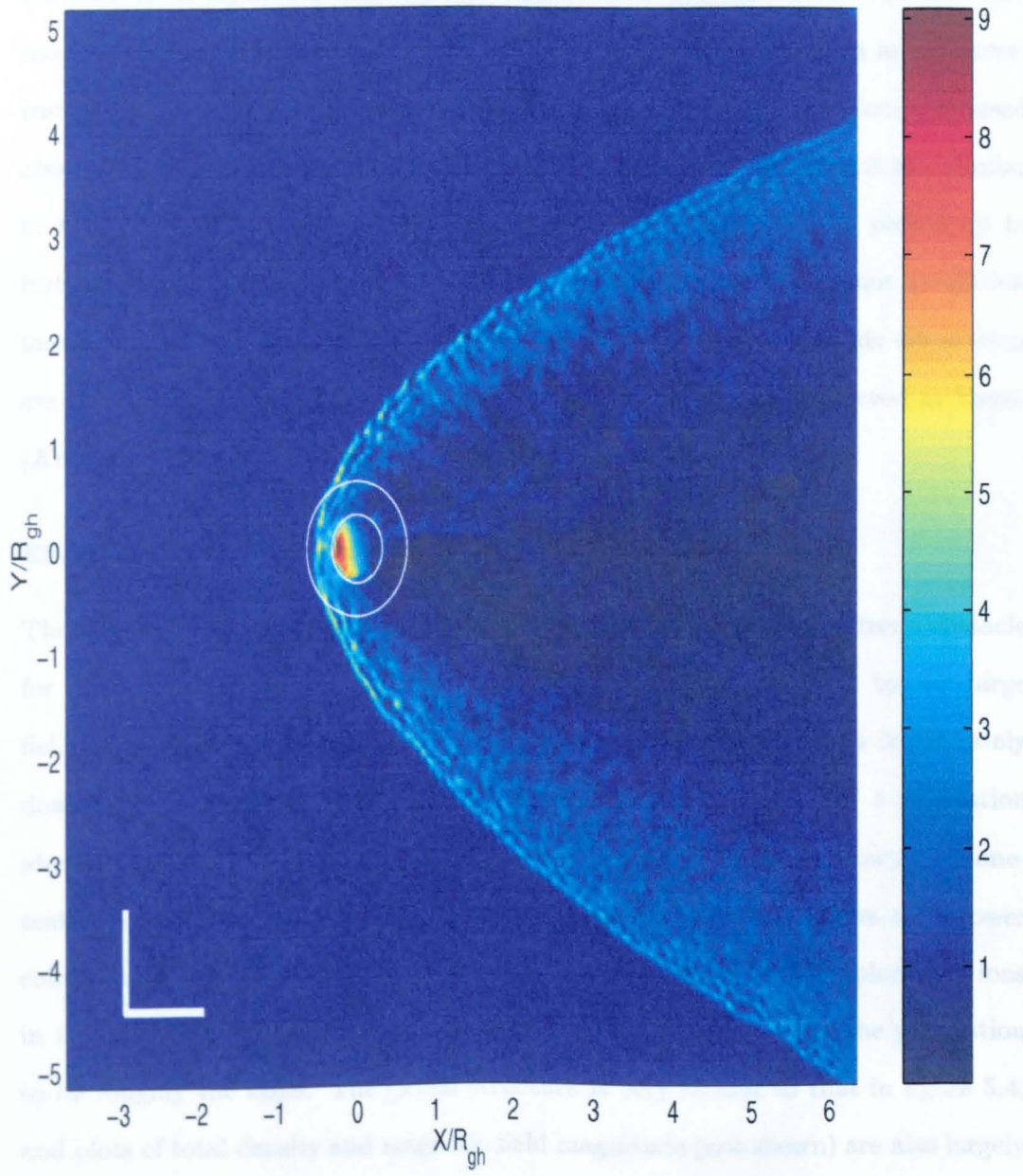

Figure 5.5: Magnetic field magnitude for the same simulation as in figure 5.3. As $\underline{B}_{IMF} = -B_z$, no components of the field evolve in the plane of study.

is produced near the source, with better particle distribution function resolution also realized due to the smaller cells initially containing the same number of meta-particles as in figure 5.4. Most of the observations are confirmed: the two tails have reduced density, especially the UT, with each remaining different in character. Insufficient downstream distance is included to detect the LT striations discussed above, however an upstream "jet" of planetary ions is now clearly visible, similar to that in figure 4.11 of the cometary case, which consists of ions picked up in fast upstream flow. Although visible in retrospect in figure 5.4, poor resolution meant it was hard to detect. In all, the features observed under this orientation are reminiscent of the highly structured wake of planetary ions observed at Venus (*Knudsen*, 1992).

Effect of planetary density

The high planetary density of $13\rho_0$ used in the above simulations is a strong obstacle for the magnetic diffusion to overcome, as figure 5.5 demonstrates by the large field build up on the sunward face of the planet, and low field values immediately downstream. Figure 5.7 shows the planetary ion mass density for a simulation identical to that in figure 5.4, except that the planetary density is now set at one-tenth the previous value, $1.3\rho_0$. The lower planetary density allows a narrower colour range to be used in figure 5.7, giving the impression of more planetary ions in the tail, however careful comparison of the colourscales reveals the population to be roughly the same. The global structure is very similar to that in figure 5.4, and plots of total density and magnetic field magnitude (not shown) are also largely identical. The density at which the planet is set in this orientation thus appears to have little effect.

Figure 5.7 also displays the KH instability in the UT more clearly than figure 5.4. It is found to have a wavelength of $\lambda_{KH} \approx 41\frac{v_A}{\Omega_p}$. From *Treumann and*

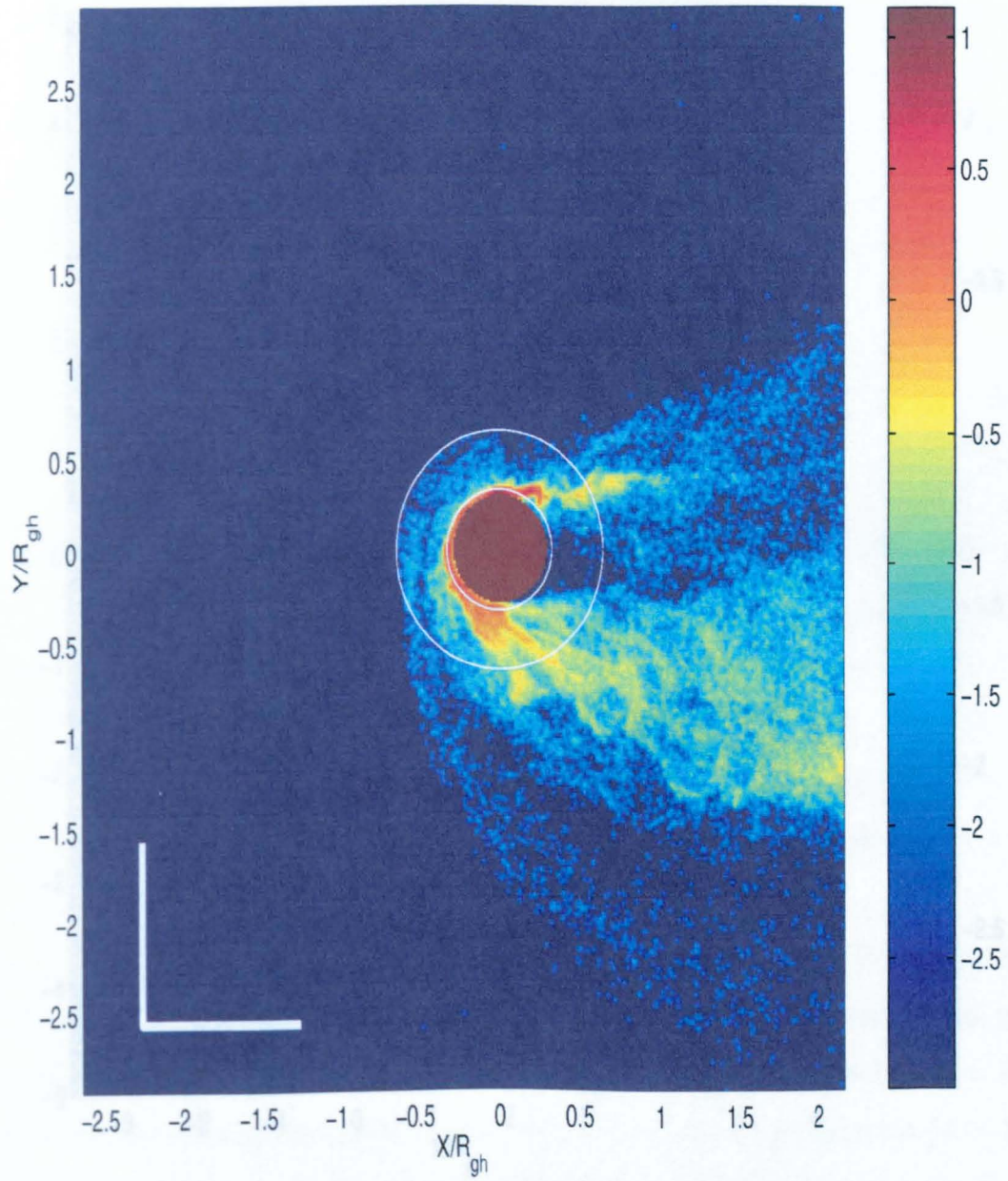

Figure 5.6: Mass density of planetary ions only, using a $\log_{10}$ scale for a simulation with $M_A = 6.6$ and $\underline{B}_{IMF} = -B_z$ as in figure 5.4, but using grid cells of one quarter the size used there. Taken after $160\Omega_p^{-1}$ in a quasi-steady state.

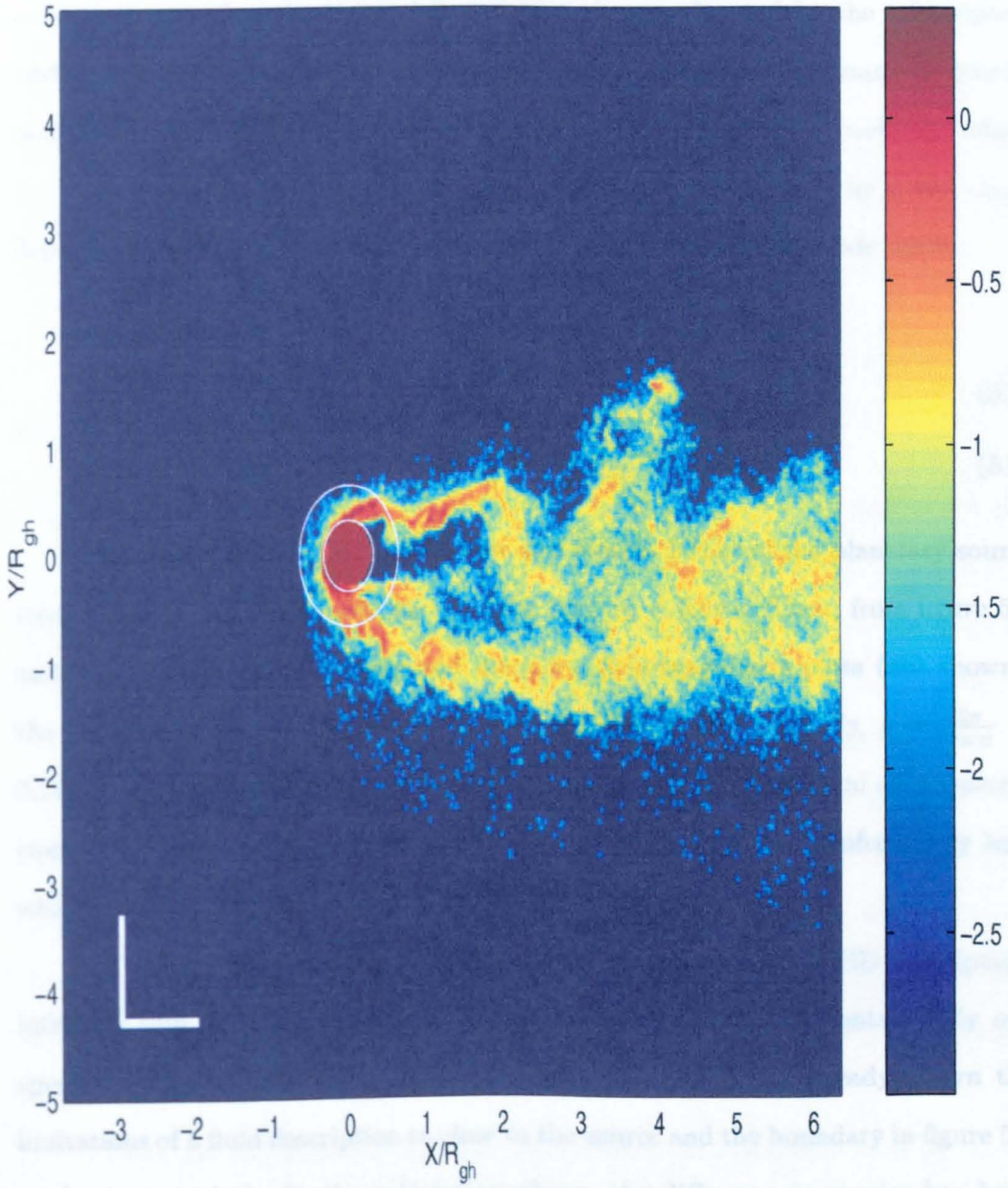

Figure 5.7: Mass density of planetary ions only, using a $\log_{10}$ scale, for a simulation with $M_A = 6.6$ and $\underline{B}_{IMF} = -B_z$. Here the planetary mass density itself has been lowered to $1.3\rho_0$ and the result is little different to that in figure 5.4.

Baumjohann (1997), the solution to the KH dispersion relation is given by equation (5.1), whenever the condition in equation (5.2) is met. These equations describe a scenario at a shear boundary between two plasmas denoted by the subscripts 1 and 2, with plasma 1 flowing at velocity v_0 past plasma 2. The number density and Alfvén velocity in each region are denoted by n_i and v_{Ai} respectively, where $i = 1, 2$, whilst the wavevector and angular frequency are denoted by $\underline{k}$ and ω_{KH}. Equations (5.1) and (5.2) remain the same when normalized into code units.

$$\omega_{KH} = \frac{n_1 \underline{k}.\underline{v}_0}{n_1 + n_2} \tag{5.1}$$

$$(\underline{k}.\underline{v}_0)^2 > \left(\frac{n_1 + n_2}{n_1 n_2}\right)\left[n_1 (\underline{k}.\underline{v}_{A1})^2 + n_2 (\underline{k}.\underline{v}_{A2})^2\right] \tag{5.2}$$

Plasma 1 is taken as the SW flow and plasma 2 that of the planetary source ions, assumed to be produced at rest such that $v_0 = 6.6 v_A$. Then, from figure 5.7 and its associated total density and magnetic field magnitude plots (not shown), the values of v_{A1}, v_{A2}, n_1 and n_2 can be estimated. Additionally, $\underline{k} = \frac{2\pi}{\lambda_{KH}} \approx 0.15\frac{\Omega_p}{v_A}$. Substitution into equation (5.2) finds the condition met, and subsequently equation (5.1) gives $\omega_{KH} \approx 0.92\Omega_p$. Note that the *local* proton gyrofrequency here will be reduced by the low magnetic field in the wake.

The derivation of equations (5.1) and (5.2) assumes an MHD description, infinitely thin boundary layer and that both regions of plasma contain only one species — non of which are applicable here. Chapter 4 has already shown the limitations of a fluid description so close to the source and the boundary in figure 5.7 is clearly not ideal. In the calculation above, the difference in species has been compensated for by taking a cometary ion to be equivalent to four protons, and using an appropriate number density for n_2. Additionally, however, the large variations in all parameters mean the result must be taken with care.

5.2 IMF in the Simulation Plane

Those simulations with $B_{IMF} = B_y$ with a planetary core were expected to be more problematic. As the planet is represented in a 2D plane, it effectively acts as a cylindrical obstacle in 3D, meaning flux tubes that are not parallel to the cylinder, such as $B_{IMF} = B_y$, cannot slip round its edges. The field then has no choice other than to diffuse through it, and as a suitable resistivity is not known *a priori* this causes problems. Due to the large size of the simulations in this section, they were performed with only 25 p.p.c.

5.2.1 Fast solar wind flow

The source used in section 5.1 was then placed in flow with $M_A = 6.6$, $\underline{B}_{IMF} = B_y$. Unfortunately, an instability was produced in the later stages of the simulation, typically as a quasi-steady state was approached. Any BS wrapping over the periodic boundaries was eliminated, resulting in the large grid size, however many particles were still being reflected upstream at high velocities at about the same time the instability set in. An example of this is shown in figure 5.8. The upstream boundary was changed to absorb backscattered ions and record how many times this occurred, to aid understanding. The velocities of these ions would have required an upstream region far in excess of that numerically possible, to allow the particles to be decelerated and flow back onto the shock. Absorption allowed the simulations to continue, albeit unphysically.

Some assumptions were made on the cause of the instability, so as to formulate an investigation. It was assumed to be due to the reflected particles forming an energetic beam. These were thought to be caused themselves by the high levels of field pile-up found upstream of the planet due to the restriction to 2D (see for example figure 5.9). Several attempts were made to investigate these assumptions,

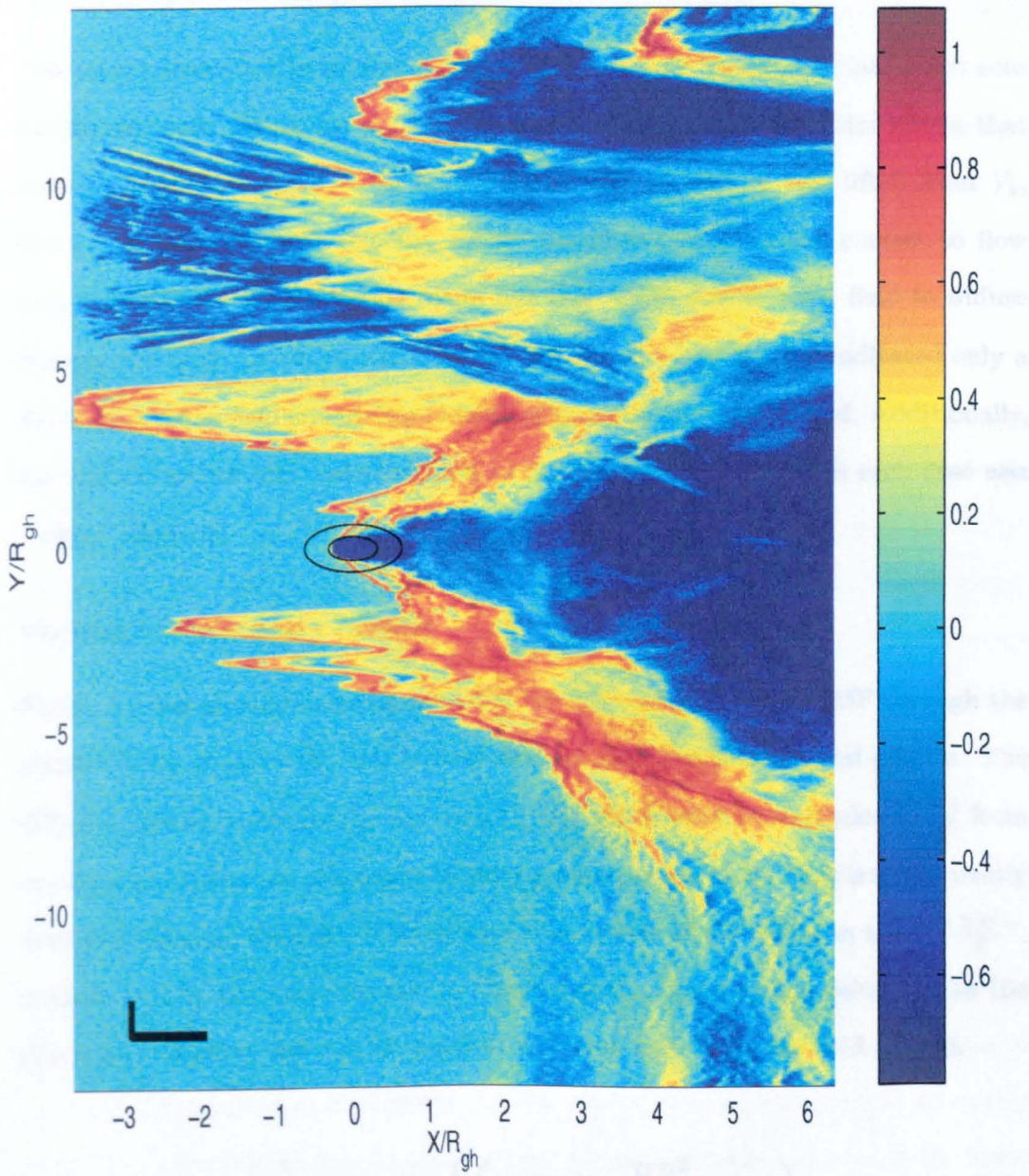

Figure 5.8: Total mass density plot, using a $\log_{10}$ scale, of a weakly ionospheric planetary source in $M_A = 6.6$ SW flow with $\underline{B}_{IMF} = B_y$. The result is typical of the instability that set-in during later, but still not quite quasi-steady, stages.

and these are now described.

Allowing $V_z \neq 0$ in the planet

The source described in section 3.4.3 enforces all bulk velocity variables are zero on the grid cells within the planet, whilst also removing any particles within that region. To reduce the level of field pile-up, this restriction was lifted from V_z, the z-component of bulk velocity, within the planet. Allowing a current to flow perpendicular to the simulation plane like this might enable some field to diffuse through the obstacle via equation (3.14). The results (not shown) indicated only a slight decrease in field pile-up from identical simulations with V_z fixed. Additionally, the number of particles reflected back to the upstream boundary in each case was roughly identical.

Varying the planetary density

Figure 5.5 has already demonstrated the low diffusion rate of the IMF through the planet. With $\underline{B}_{IMF} = B_y$ this creates massive field line draping and pile-up. The diffusion rate is controlled by equation (3.15), which upon substitution for $\underline{J}$ from equation (3.14) and use of a vector identity gives equation (5.3). This is subsequently used in advancing the field. The relative importance of the diffusion term, "$\frac{\nabla B^2}{2}$", is controlled by the mass density, ρ. Consequently, changing the value of ρ in the planet should affect the rate of magnetic diffusion and hence the field pile-up.

$$\underline{E} = -\underline{V_i} \times \underline{B} + \frac{1}{\rho}\left((\underline{B}.\nabla)\,\underline{B} - \frac{\nabla B^2}{2} - \nabla P_e\right) \tag{5.3}$$

Additionally, one notes that the skin depth, assuming waves of frequency $\omega \sim \Omega_p \ll \omega_{pe}$, is given by equation (5.4) (*Krall and Trivelpiece*, 1986). A planet of density $13\rho_0$ in the simulation then has a skin depth of roughly one-hundredth

its radius, making it highly impenetrable to waves typically present. The result is that the planet forms an impassable obstacle to the magnetic field and many waves travelling along it, such that even with $\rho = 1.3\rho_0$ in the planet, field pile-up roughly three times that observed under similar circumstances in Chapter 4 is produced, as shown in figure 5.9.

$$\delta = \frac{c}{\omega_{pe}} \tag{5.4}$$

After more experimentation with the planetary density it was found that a value of $\rho = 0.24\rho_0$ produces similar field pile-up levels to those in Chapter 4: much higher and the field struggles to diffuse through; much lower and the tail becomes more of an obstacle than the planet. By reducing the planetary density in this way, the simulations produced fewer reflected particles and almost ran to a quasi-steady state. However, the instability still appeared eventually, either through those remaining scattered particles, or some other means. Either way, the conclusion is that this orientation of IMF cannot be modeled accurately in 2D. A 3D simulation cannot presently be performed at the same level of phase space resolution.

Wake density dropping below simulation limit

In section 5.1 the wake is filled in a relatively short distance downstream, however in this orientation it remains at a very low population level far downstream. This poses two potential sources of disruption: the low numbers of particles might adversely affect the downstream boundary, and large regions within the wake reach the lower limit of grid density, described in section 3.3.1. The nature of the instability, however, does not suggest a boundary problem so a more likely one is the low resolution within the wake.

A simulation was thus performed with a planetary density of $0.24\rho_0$, but

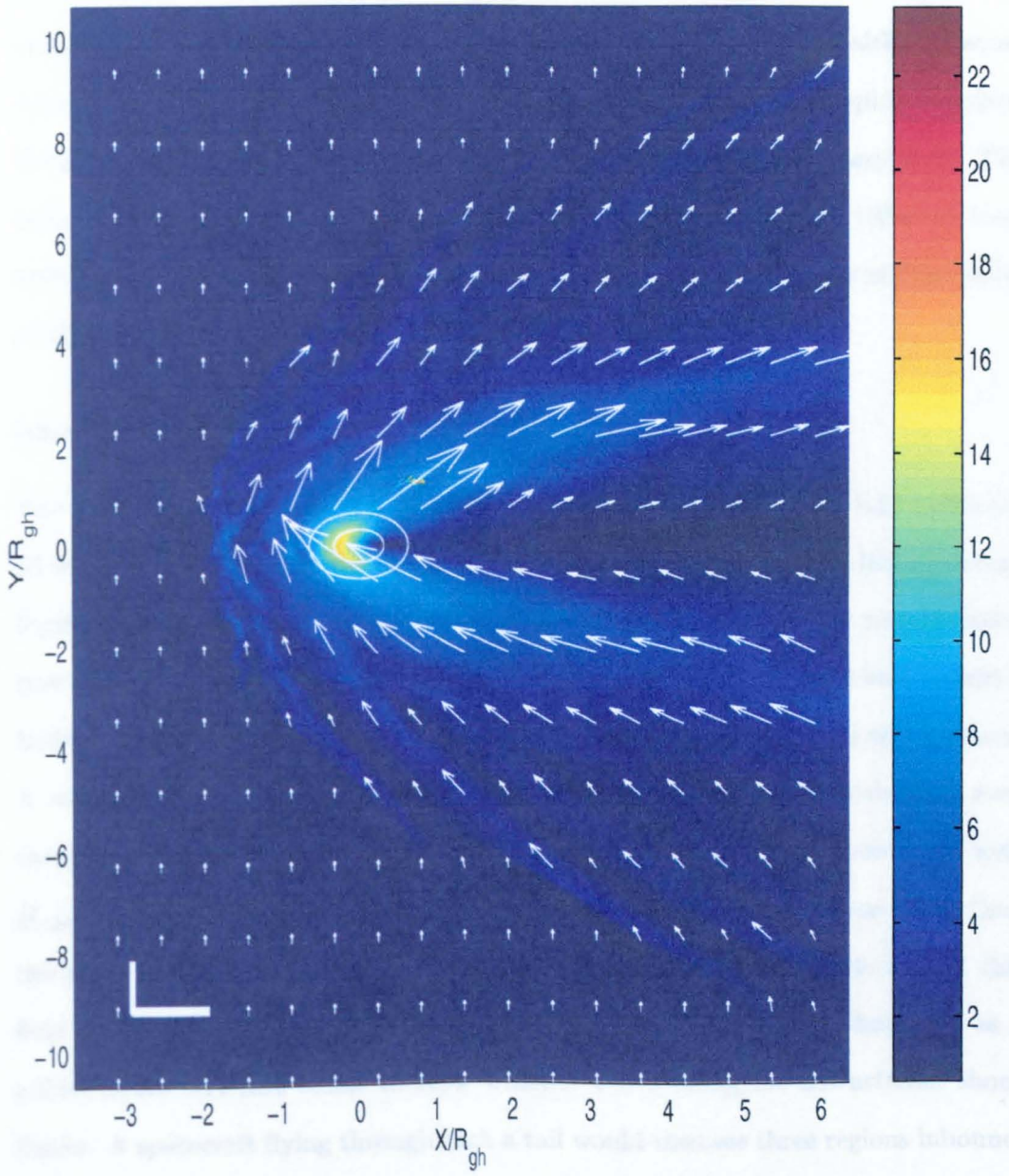

Figure 5.9: Magnetic field magnitude and components in the plane (arrows) for a simulation with $M_A = 6.6$ and $\underline{B}_{IMF} = B_y$. Notice the overall high levels of field pile-up present in addition to the fine-scaled structuring. Performed with a planetary mass density of only $1.3\rho_0$, such simulations revealed the importance of this parameter in this orientation.

producing ions on *all* sides of the planet. The rate of production was doubled to accommodate this. The result is shown in figure 5.10, which shows the mass density of planetary ions only. The wake is now well populated with particles, although some regions are still reaching the minimum level due to the particles clumping together. Consistent with this is the new variability of the number of planetary ions. The increased overall population of planetary ions now also gives more reflected ions, and the instability still sets in. The low population in the wake is thus not the cause of the instability, which remains unsolved.

Best results obtained

The best results obtained with $B_{IMF} = B_y$ are shown in figures 5.11, 5.12 and 5.13, all taken before the instability in figure 5.8 started, after $480\Omega_p^{-1}$, or 12,000 timesteps. Figure 5.14 shows the total population count of both species for the same simulation. Firstly, figure 5.11 shows the total mass density on a $\log_{10}$ scale and reveals a highly disturbed shock, with a broad central wake of very low density downstream. A comparison to figure 5.12, which shows only planetary ions, reveals that even these are sparse within the wake. Similarly to the high SW flow speed case with $\underline{B}_{IMF} = -B_z$ (section 5.1.2), the ions in the tail region are much less dense than the jump at the shock. No slow SW flow speed simulations were performed in this field orientation for comparison to those in section 5.1.1. Using Chapter 4 as a guide, figure 5.11 also seems to show whistler waves along the downstream shock flanks. A spacecraft flying through such a tail would thus see three regions inbound: disturbed SW; a turbulent shock front and shock layer of roughly $1R_{gh}$ width (at $3R_{gh}$ downstream); and an abrupt drop in density upon entering the wake.

Figure 5.12, shows that in this IMF orientation, the two tails observed in section 5.1 have merged. The planetary ions instead form a broad cone shape downstream, with roughly equal density throughout. The dependency on IMF orientation

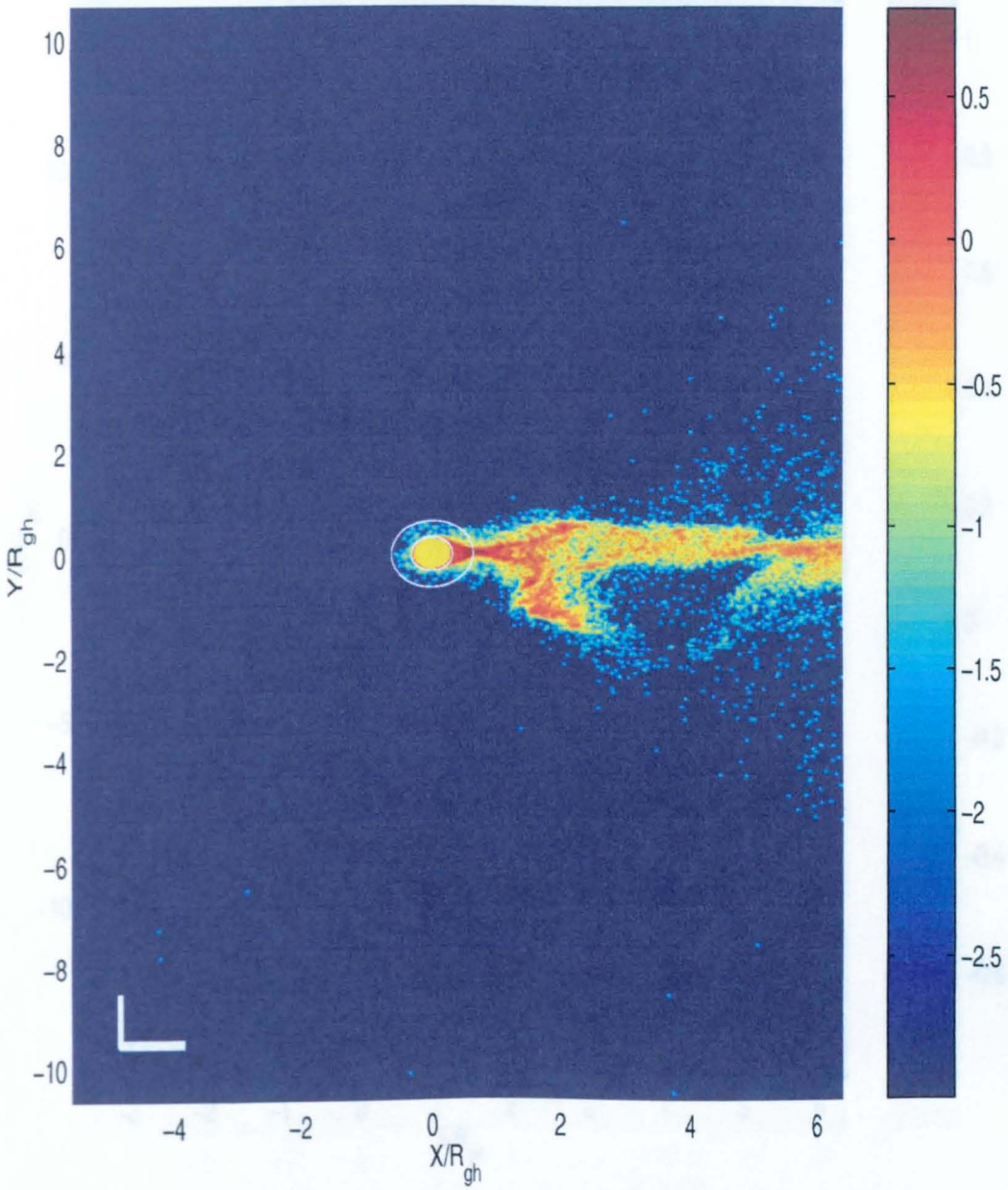

Figure 5.10: Mass density of planetary ions only, for a simulation with $M_A = 6.6$ and $\underline{B}_{IMF} = B_y$. Contrary to all other simulations in this chapter, the planet was sourced on all sides, enabling the wake to be populated much more widely than, for example, in figure 5.12.

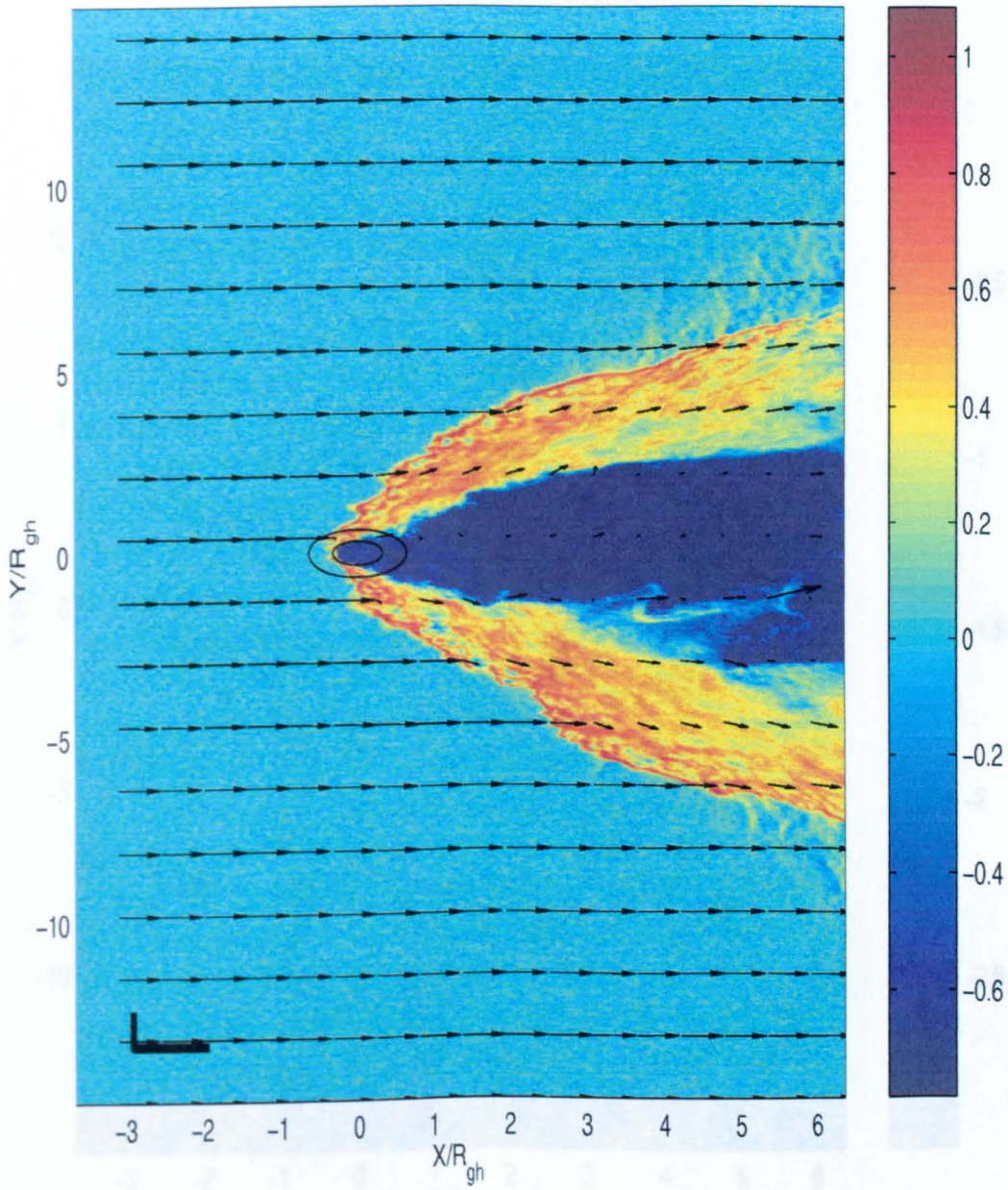

Figure 5.11: Total mass density on a $\log_{10}$ scale for a simulation with $M_A = 6.6$ and $\underline{B}_{IMF} = B_y$. Taken after $480\Omega_p^{-1}$, the simulation had not quite achieved a quasi-steady state, and suffered the instability in figure 5.8 soon after. Its structure at this point gives the closest indication available of what a quasi-steady state would look like.

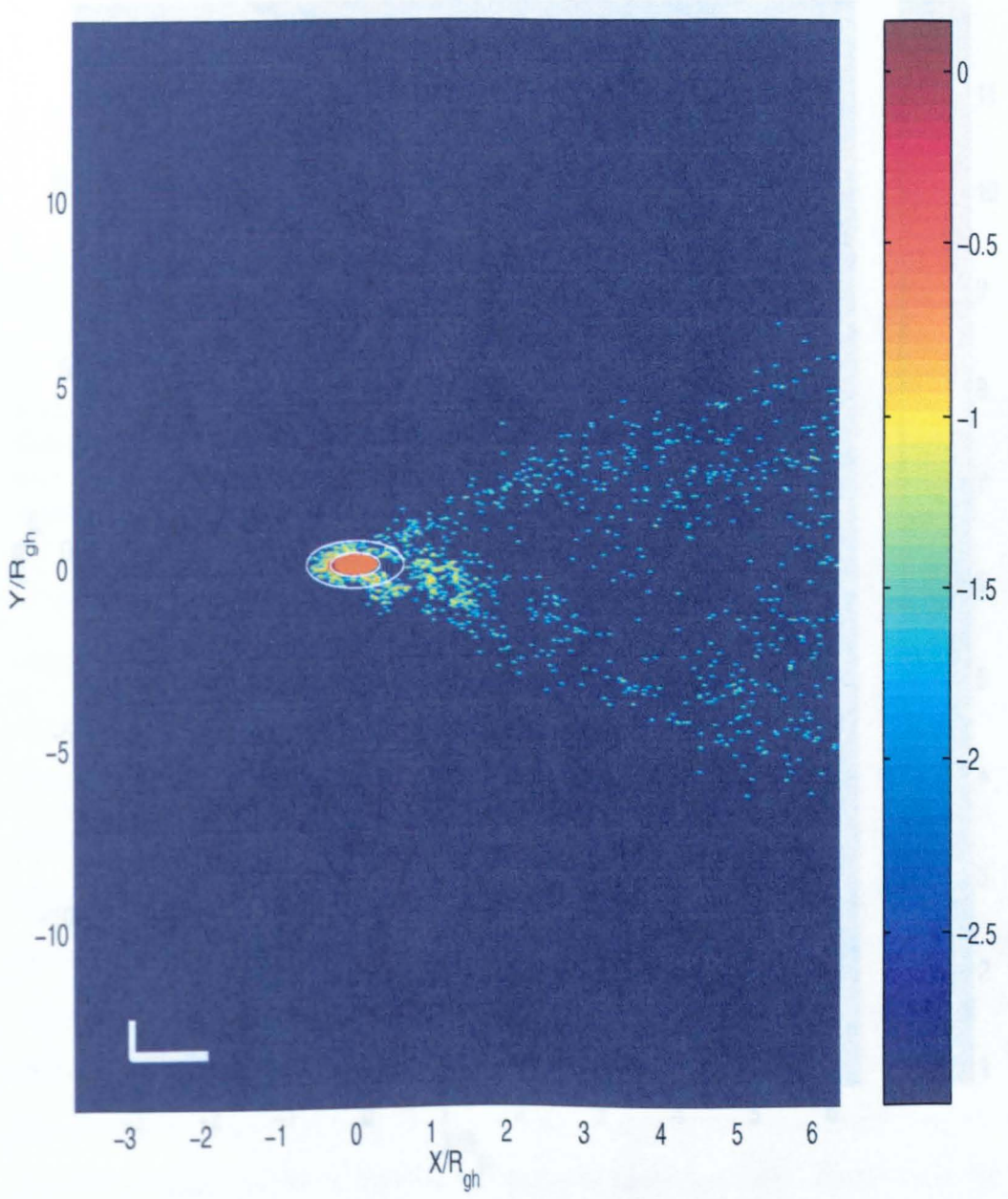

Figure 5.12: Mass density of planetary ions only, using a $\log_{10}$ scale, for the same simulation and time as figure 5.11.

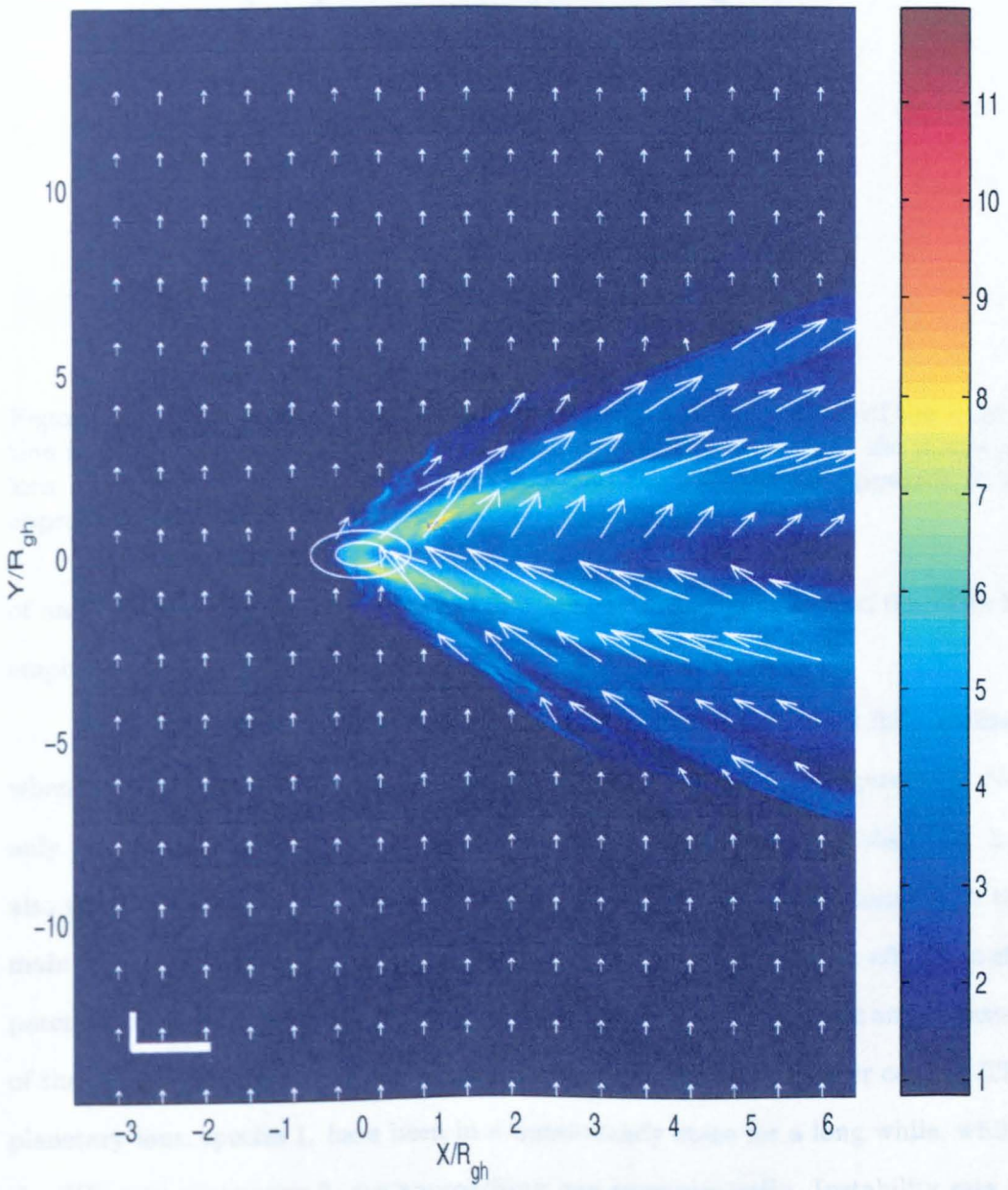

Figure 5.13: Magnetic field magnitude and components in the plane of the simulation for the same case and time as shown in figure 5.11. Notice the numerous "envelopes" of enhanced magnetic field draped over the main feature.

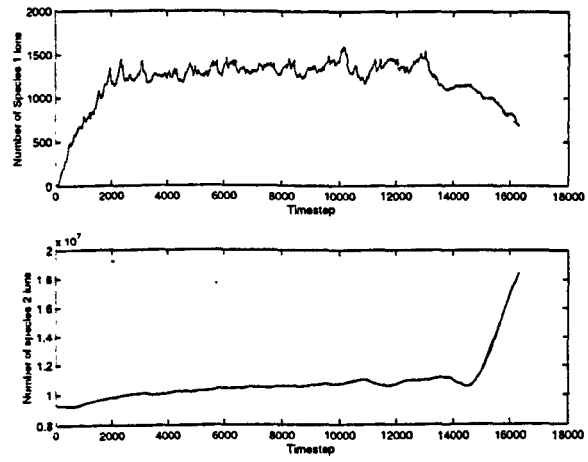

Figure 5.14: Total particle count of both ionic species over the lifetime of the simulation in figures 5.11 - 5.13. Before instability (at $\sim 13,000$ timesteps) the planetary ions had achieved a quasi-steady count rate and the SW protons appeared to be approaching one. One timestep is equal to $0.04\Omega_p^{-1}$.

of any spacecraft readings of planetary ion density in the wake should therefore be emphasized.

The true magnificence of the structure produced, however, is fully realized when considering the magnetic field magnitude, which is shown in figure 5.13. Not only the expected field line draping around the planetary core is observed, but also at least two enhanced "envelope" regions either side, draped externally to the main feature. Unfortunately, the stability of the solution was lost soon after, but the potential for interesting physical results is clearly indicated. To provide an indication of the reliability of these results, figure 5.14 shows the particle number counts. The planetary ions. species 1, have been in a quasi-steady state for a long while, whilst the SW protons. species 2, are approaching one asymptotically. Instability sets in at roughly 13.000 timesteps, or $520\Omega_p^{-1}$.

Chapter 6

Magnetized Ionospheric Planetary Simulations: Pilot Study

This chapter presents results of a pilot study performed to investigate the effect of introducing an intrinsic magnetic field to the weakly ionospheric planet used in Chapter 5. An example of such an obstacle is Mercury. A full study would require 3D, however at present this would imply significantly reduced resolution of the particle distribution functions. This 2D study prepares for possible future massively parallel simulations in 3D, by investigating the following.

1. Scaling of the source
2. Representation of the planetary dipole in the simulation
3. The interaction of the dipole field and the IMF
4. Numerical stability and equilibrium

As the plasma is non-linear, it is essential that these issues are examined before a full 3D simulation is performed, as its response to an applied field is unknown. With this goal, four scenarios are considered.

1. Weakly ionospheric source in flow with no IMF
2. Magnetized weakly ionospheric source in flow with no IMF
3. Weakly ionospheric source in SW flow with IMF present
4. Magnetized weakly ionospheric source in SW flow with IMF present

All simulations use a flow speed with $M_A = 3.0$ and both the IMF and planetary dipole field perpendicular to the plane of the simulation. This prevents the excessive field line draping seen in section 5.2 occurring, and allows for both a reconnection and non-reconnection case as shown in figure 6.1. In the hybrid algorithm used, the electron inertial term is neglected, which makes consideration of the reconnection case unsuitable. Only the non-reconnection geometry in figure 6.1 is thus considered. The little data available from Mercury suggests it possesses an offset tilted dipole field (*Ness et. al.*, 1974), however for simplicity and generality the source described in section 3.4.3 assumes a centrally located dipole.

6.1 Dipole Calculations

The obstacle is scaled to the size of Mercury compared to the planetary ion gyroradius in $M_A = 6.6$ SW flow. Note that the simulations use $m_h = 4m_p$ only, for more details see section 3.5.2. The dipole strength must thus also be reduced in accordance with this, and this is done by simply matching the field to that observed in a fly-by mission. The scaling is further complicated by the 2D nature of these simulations which in effect means that a current loop inserted in the obstacle is multiplied many times perpendicular to the plane to create a solenoidal field, as shown

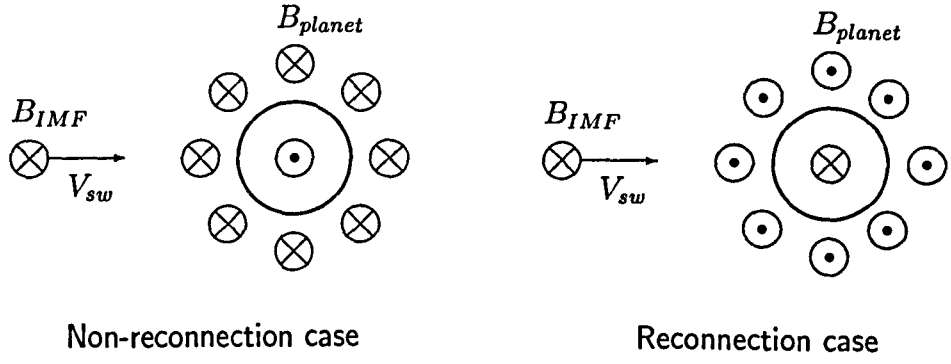

Figure 6.1: Reconnection geometries available with both the IMF and planetary field perpendicular to the simulation plane.

schematically in figure 6.2. This will affect the calculation of the current needed in such a loop to generate a given magnetic field, due to the enhancing effect of the symmetry in z.

6.1.1 Solenoid length

An infinite solenoid has a magnetic field at its centre given by equation (6.1) (*Alonso and Finn*, 1992). Here, n is the number of turns per unit length and I the current flowing through the solenoid. For this study a truly infinite solenoid will not do, as this would give zero field externally to the planet. Instead, we assume numerical diffusion will carry some field outside the planet from a long, but finite solenoid.

$$B = \mu_0 n I \tag{6.1}$$

We wish to match the field thus generated with a suitable value for Mercurys dipole. Data in *Ness et. al.* (1974) records a magnetic field of $98 \times 10^{-9} T$ at an altitude

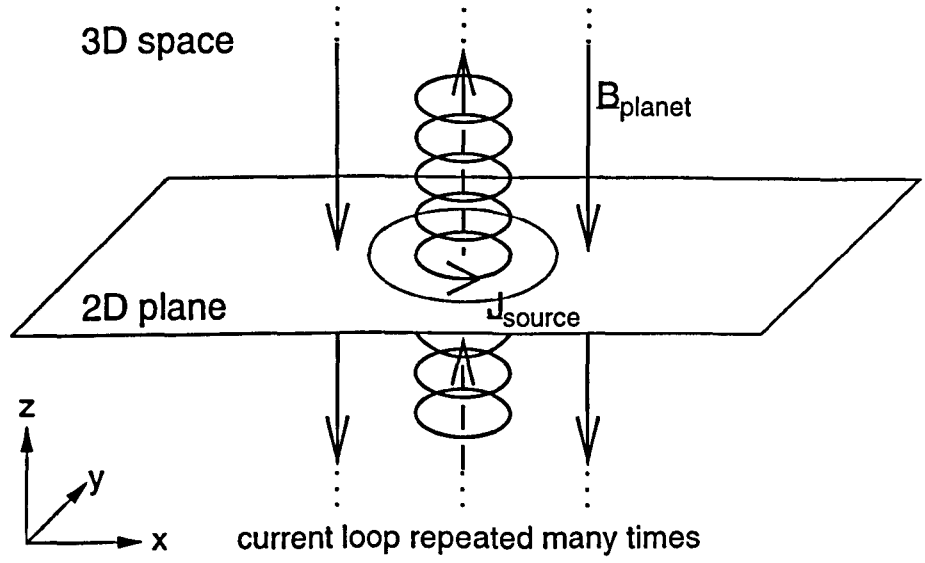

Figure 6.2: Effect in 3D of a current loop in a 2D simulation.

of $700km$, less than $\frac{1}{3}$ of a planetary radius, above Mercury. This is fairly close to the surface, so it is assumed the field strength is the same there, and that the field magnitude inside the planet is approximately equal to that outside. The field needed at the centre of the planet is thus taken as $98 \times 10^{-9}T$.

Alternatively, one could use a single current loop approach to generate the required field, by neglecting any effects of symmetry through z. However, this produces a value for the loop current which is far too large. We thus choose a value of $J_{source} = 7.0$ to be the maximum current density within the planet (see figure 3.6). In the nature of such a pilot study, this allows investigation of these issues to be undertaken.

The following sections show the results of this pilot study. Firstly, as a benchmark of the currents and fields generated in the simulation with no added fields, section 6.2 considers proton flow with no IMF past the obstacle with and without its intrinsic field. Section 6.3 then considers these variations of the obstacle in flow with an IMF. All simulations are performed in flow with $M_A = 3.0$ using

a planet of fixed density $13\rho_0$, and with the heavy planetary ions sourced only on the $x < 0$ half of the planet, as in Chapter 5. All simulations in section 6.3 use $B_{IMF} = -B_z$.

6.2 Simulations With no IMF

6.2.1 Planet with an exosphere only

This was to act as a guide to which other simulations were compared, it was performed with no IMF and no intrinsic planetary field. The results are given in figures 6.3, 6.4 and 6.5. Figure 6.3 shows a plot of total mass density on a $\log_{10}$ scale, with arrows showing the bulk velocity direction and relative magnitude. Other markings are as described in figure 4.1. The planet can be seen to create a downstream wake, which in many places reaches the limit resolvable by the simulation, namely the minimum SW density of $0.2\rho_0$, because of the absorbing planet. The halo upstream of the planet is caused by heavy source ions given off with a small radial velocity on the $x < 0$ face of the planet. As no IMF is present to perform pickup, these stream outwards indefinitely. The simulation thus did *not* reach a quasi-steady state with regards to the planetary ions, even after $720\Omega_p^{-1}$, although the proton count had leveled off. Figure 6.4 shows the only component of magnetic field experienced, B_z, at the same time. The wake contains four alternately directed regions immediately behind the planet, the middle two of which cancel out further downstream. Figure 6.5 shows the currents due to SW protons in the x-direction, J_{px}, associated with these fields. They have a peak magnitude of $|J_{px}| \sim 6.0$ and also appear on a plot of J_{py} (not shown) in which they peak at $|J_{py}| \sim 1.5$.

The presence of magnetic field in a simulation which initially contains none is surprising. Late on in the study, it was realized this is due to a numerical error in the field update step. This involves the "∇P_e" term in equation (3.20) being non-zero on

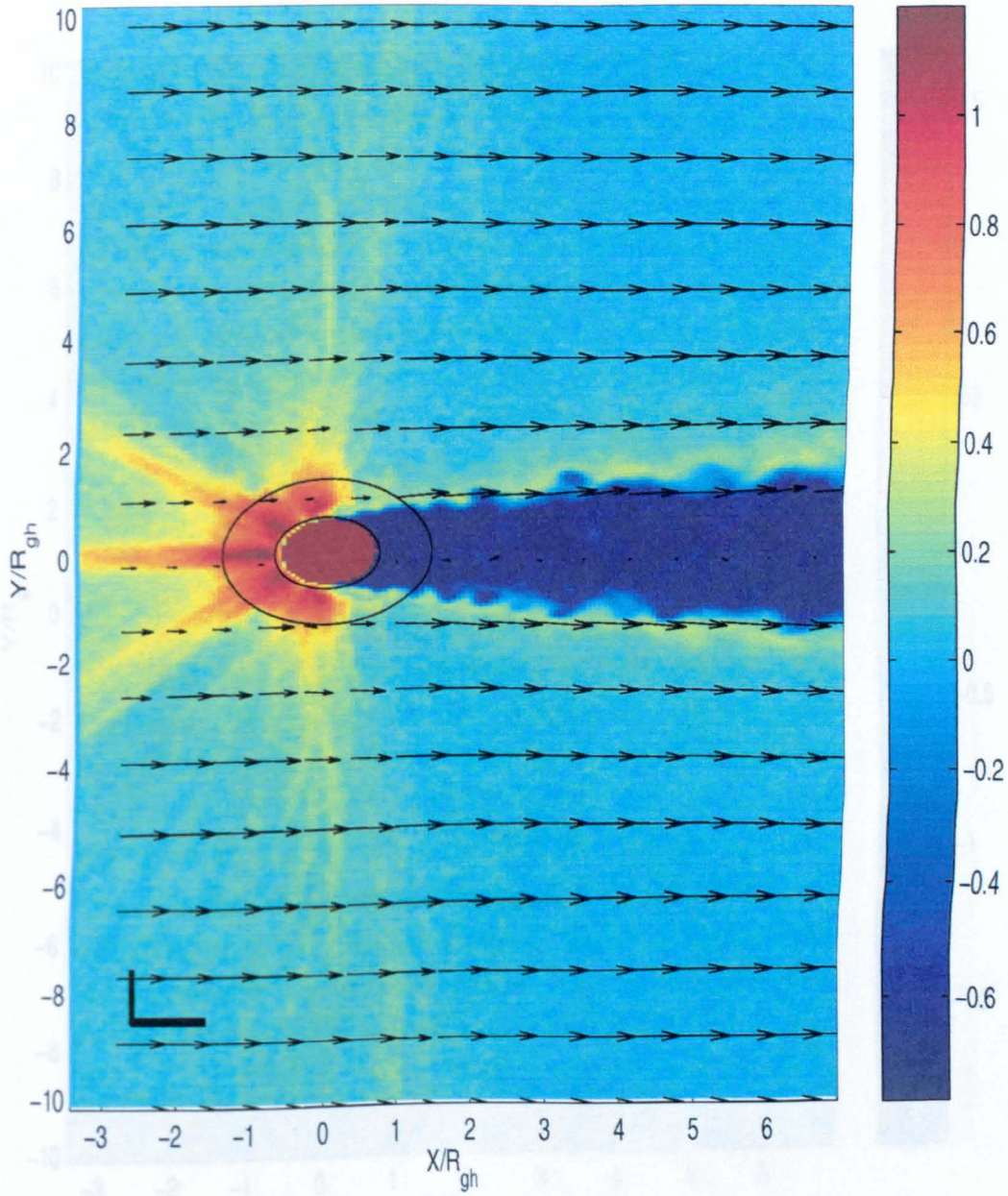

Figure 6.3: Total mass density using a $\log_{10}$ scale for a simulation with $M_A = 3.0$ and $B_{IMF} = 0$. The planet contains no current loop, so no planetary field was expected. The arrows show bulk flow velocity relative to that of the SW. The plot was taken after $720\Omega_p^{-1}$, but the planetary ion population had not leveled off due to $B_{IMF} = 0$ giving zero pickup. Other markings as in figure 4.1.

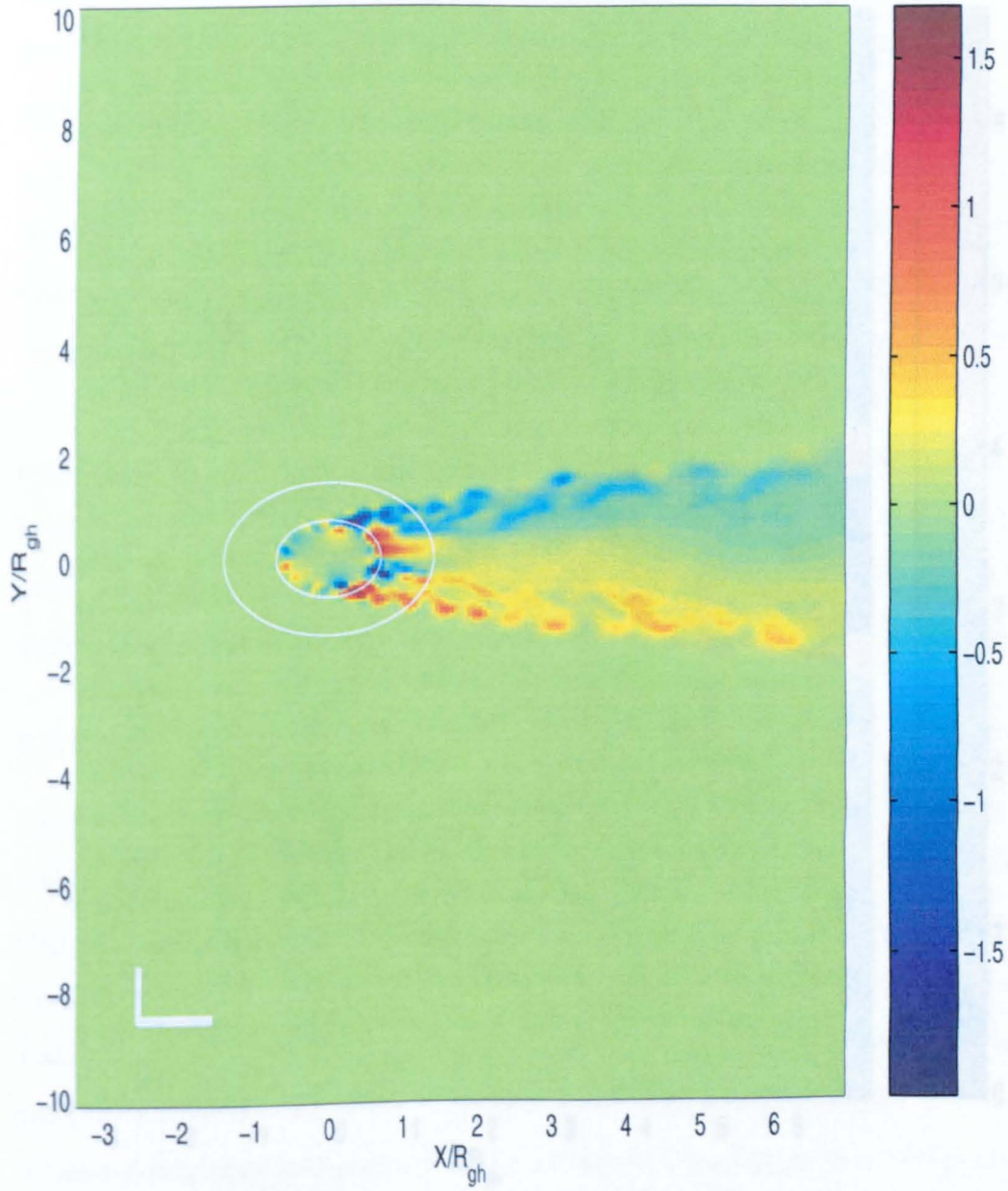

Figure 6.4: Plot of B_z, the only component of magnetic field generated, after $720\Omega_p^{-1}$ for the same simulation as in figure 6.3.

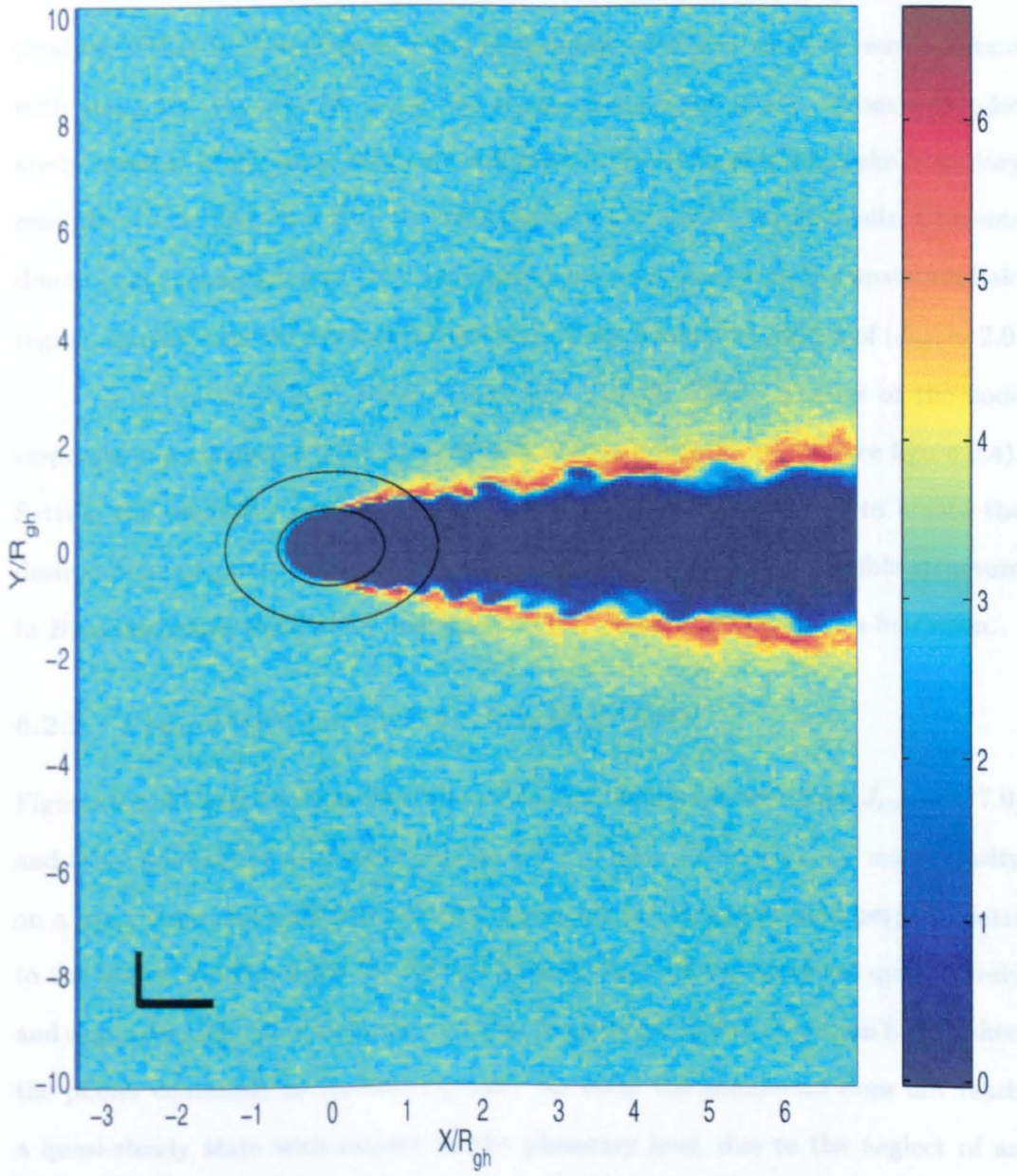

Figure 6.5: Current density carried by the protons in the x-direction, J_{px}, for the same time and simulation parameters as in figure 6.3.

a corrector step near the sharp cut-off of the planetary surface, before subsequently being reset. This allows a seed field to be present. However, the simulation may thus be more physically accurate because conditions at the planetary surface would produce $\nabla P_e \neq 0$. The error does not accumulate over time as P_e is reset constant each step, and is noted as being one result of the pilot study. From this pilot study result it is also clear that care will have to be taken over the wake boundary resolution, as at present it is a very steep gradient over only a few grid cells. Currents due to heavy planetary ions (also not shown) are concentrated in the upstream halo region, as such ions are not found elsewhere. They reach peak values of $|J_{hy}| \sim 2.0$.

It is apparent from these results that the 2D hybrid physics of the code responds to a current of $|J| \sim 6.0$ with a field of strength $|B| \sim 2.0$ (see figure 6.4). Setting the planetary current at $J_{source} = 7.0$ is therefore unlikely to create the desired field magnitude of $|B| \sim 5.5$. However, it should create a visible structure in B_z nonetheless, from which conclusions for a possible 3D study can be drawn.

6.2.2 Planet with an intrinsic magnetic field

Figures 6.6, 6.7 and 6.8 show the results of a simulation performed with $J_{source} = 7.0$, and other parameters as those in section 6.2.1. Figure 6.6 shows total mass density on a $\log_{10}$ scale and bulk flow velocity; figure 6.7 the magnetic field perpendicular to the plane; and figure 6.8 the current density J_{px}. All the plots are qualitatively and approximately quantitatively identical to those presented in section 6.2.1, when the planet contained no internal current. As then, the simulation does not reach a quasi-steady state with respect to the planetary ions, due to the neglect of an implanted IMF. The currents in other directions, and those of the heavy planetary ions (not shown) are also largely as in section 6.2.1, with those in the plane due to planetary ions now dwarfed by that present in the planetary core.

The results are so similar to those in section 6.2.1, it is apparent the planetary

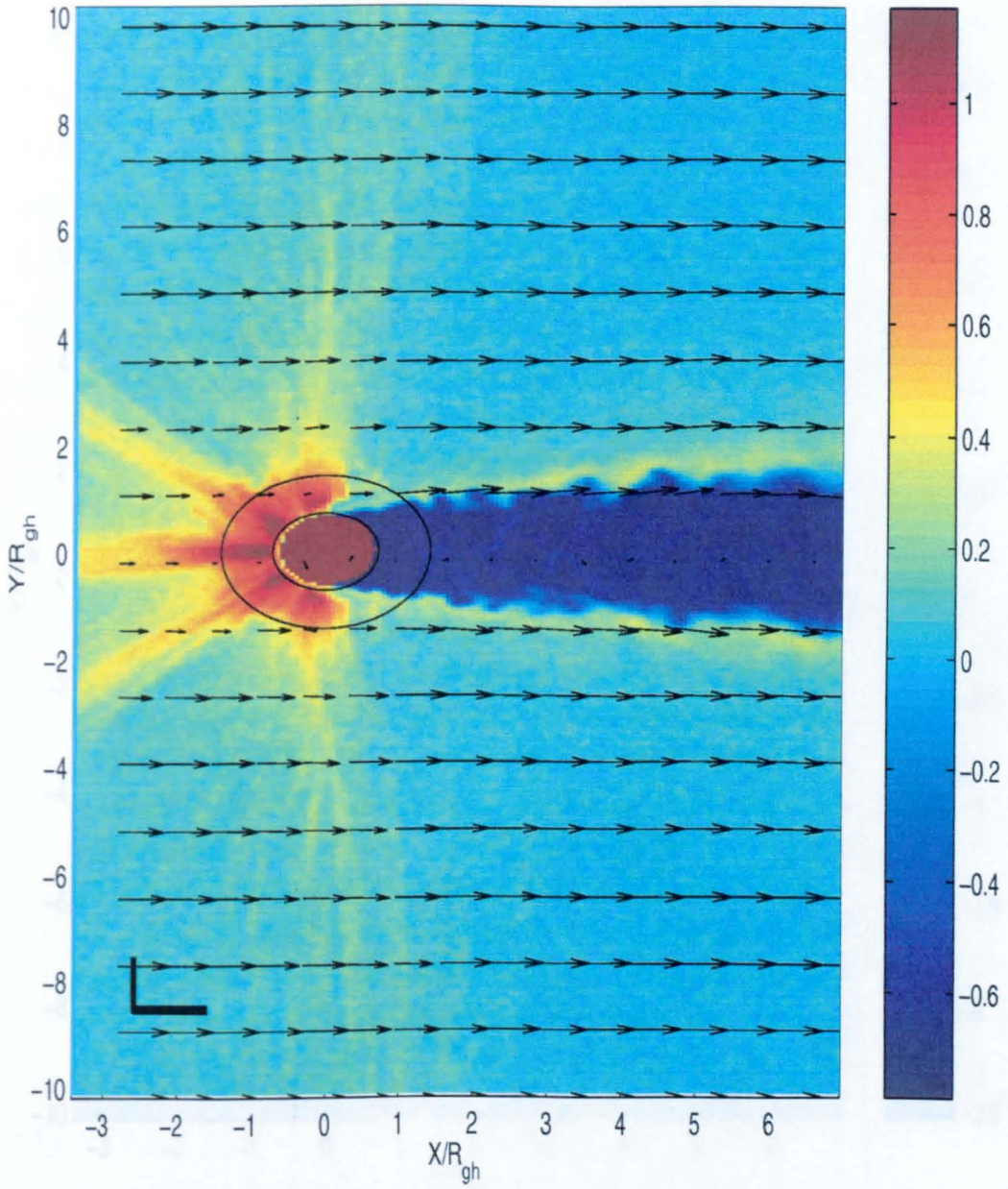

Figure 6.6: Total mass density on a $\log_{10}$ scale for a simulation with parameters identical to those in figure 6.3, except that now the planet contains a current loop designed to generate a dipole field. Again, the planetary ions had not leveled off after $720\Omega_p^{-1}$ and the arrows show bulk flow velocity in the plane of the simulation.

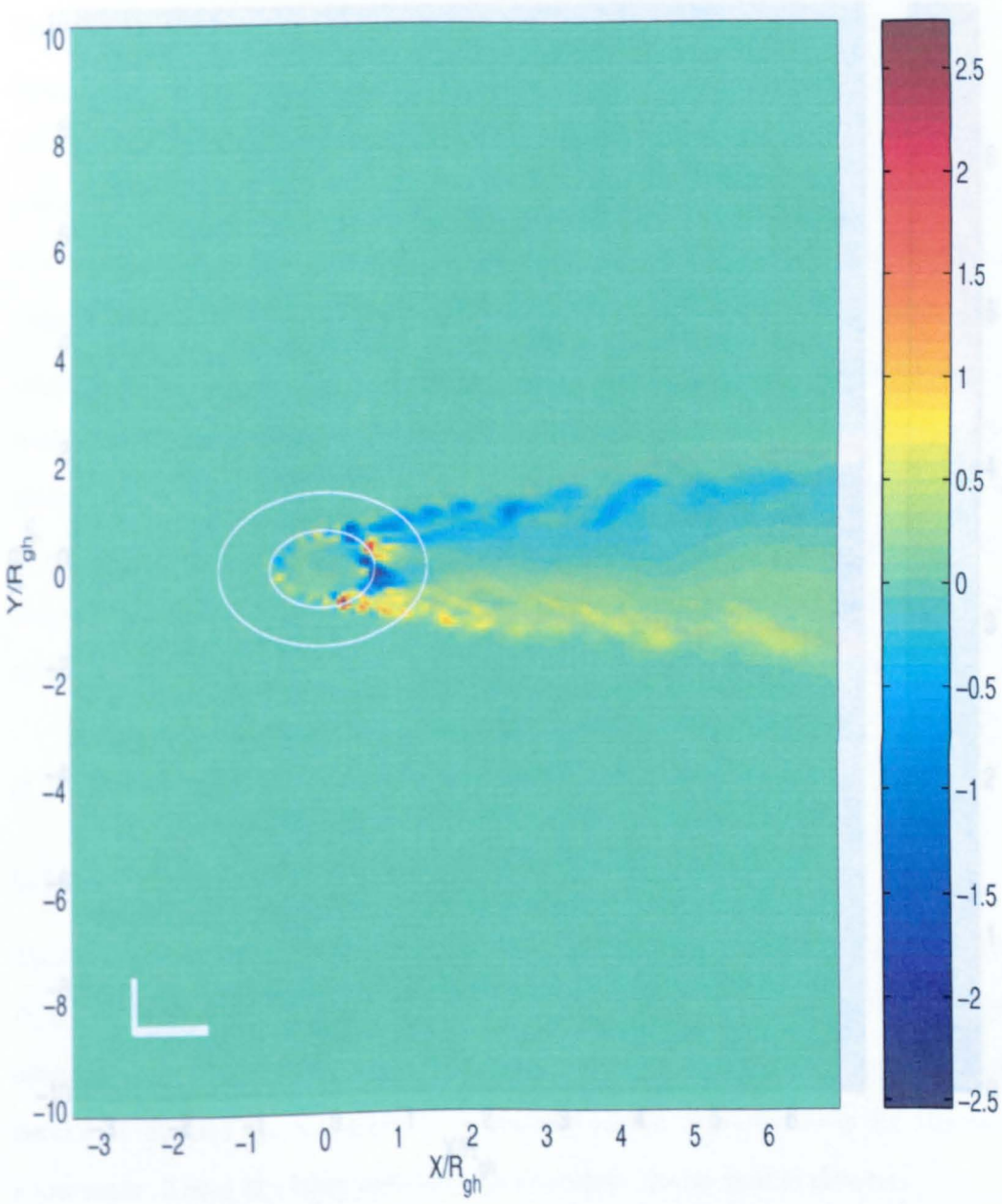

Figure 6.7: Plot of B_z for the same simulation and time as shown in figure 6.6. The dipole field expected has failed to make a significant difference when the result is compared to figure 6.4.

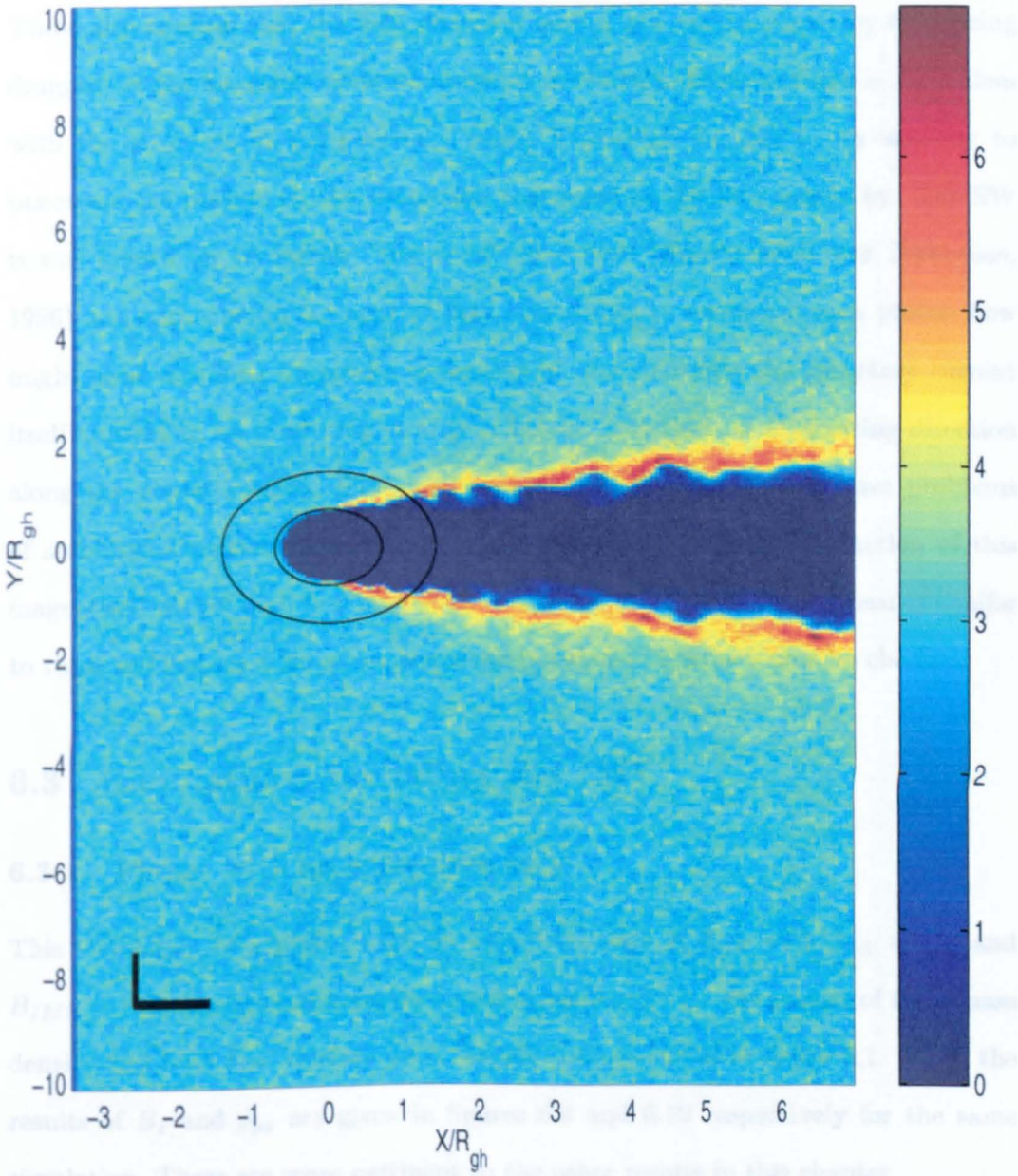

Figure 6.8: Current density carried by the protons flowing past the planet in the x-direction, or J_{px}. The planetary current loop is present, however not visible as it is labeled numerically as a planetary ion current. Taken at the same time and with the same simulation parameters as figure 6.6.

dipole field is not affecting the outcome. If the dipole field was being produced by $J_{source} = 7.0$, it would certainly be visible as the results in section 6.2.1 showed. These also confirm that the field observed here is not due to planetary field being dragged off the source as none was present previously. Clearly, there is a problem with the structure of the planetary field. This could be due to its inability to penetrate the plasma on the timescales concerned as the flow passes by. The SW is well known for its largely "frozen in" conditions (*Baumjohann and Treumann*, 1996) and consequently an applied field attempting to penetrate such proton flow might need very long timescales to achieve it. Alternatively, the planetary current itself appears to be producing strange magnetic structures of alternating direction along the planet surface. This method of dipole production may have problems of stability. One conclusion is that any attempt to model the interaction of this magnetized planet with flow embedded with IMF will likely produce results similar to those in Chapter 5 for an unmagnetized obstacle. This will now be checked.

6.3 Simulations Including the IMF

6.3.1 Planet with an exosphere only

This simulation of a planet with an exosphere only in flow with $M_A = 3.0$ and $B_{IMF} = -B_z$ has already been discussed in section 5.1.1. The results of total mass density and bulk flow velocity have already been included in figure 5.1. Here, the results of B_z and J_{px} are given in figures 6.9 and 6.10 respectively for the same simulation. These are more pertinent to the other results in this chapter.

Figure 6.9 shows the magnetic field structure produced by the unmagnetized obstacle in a quasi-steady state. There exists a smooth shock front with an increase in magnetic field magnitude downstream: the BS now dominates the field structure in comparison to the simulations in section 6.2, where no IMF resulted in no shock

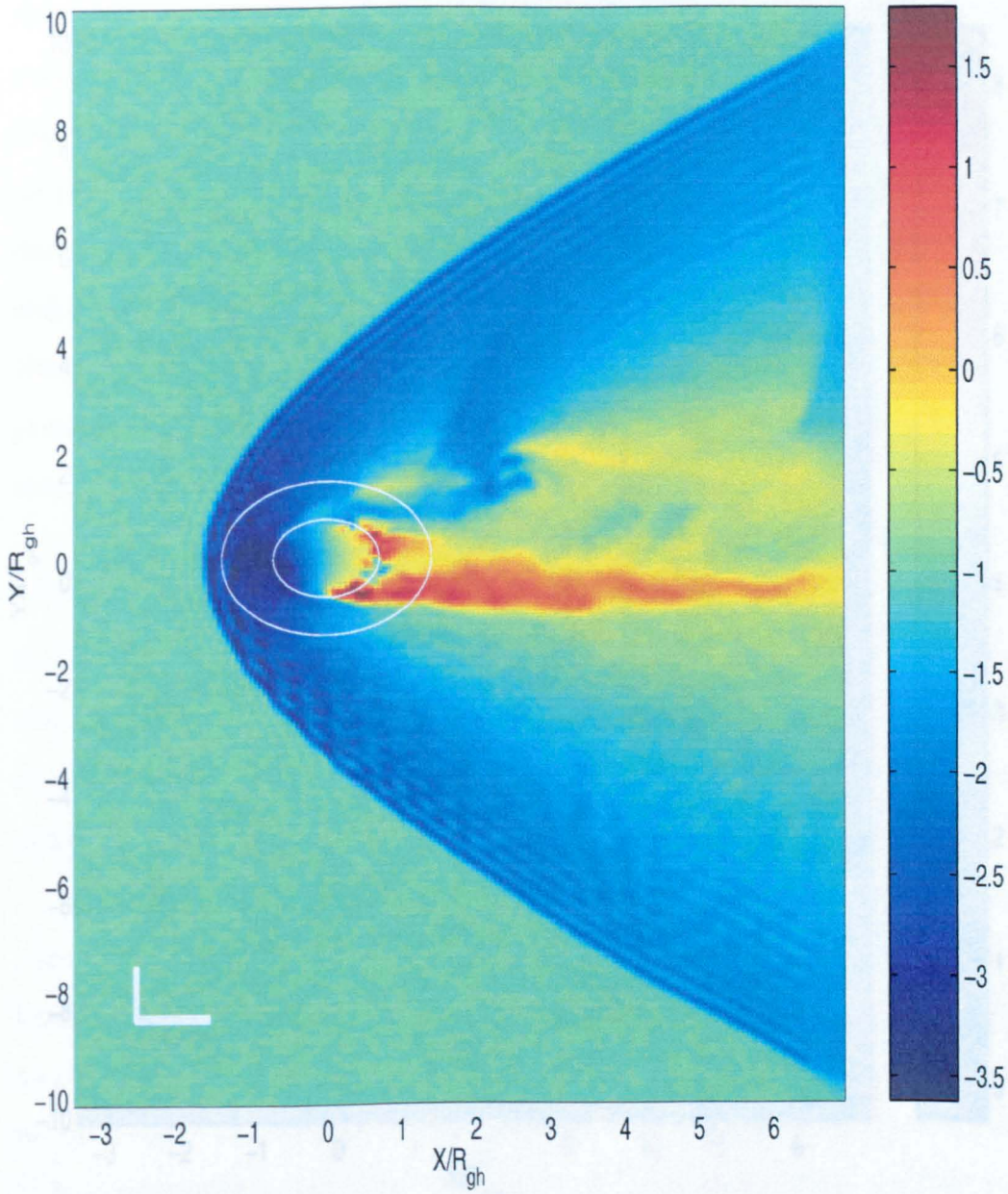

Figure 6.9: Plot of B_z for a simulation with no planetary current loop, $M_A = 3.0$ and $\underline{B}_{IMF} = -B_z$. Taken after $720\Omega_p^{-1}$, the simulation has achieved a quasi-steady state and also appears in Chapter 5.

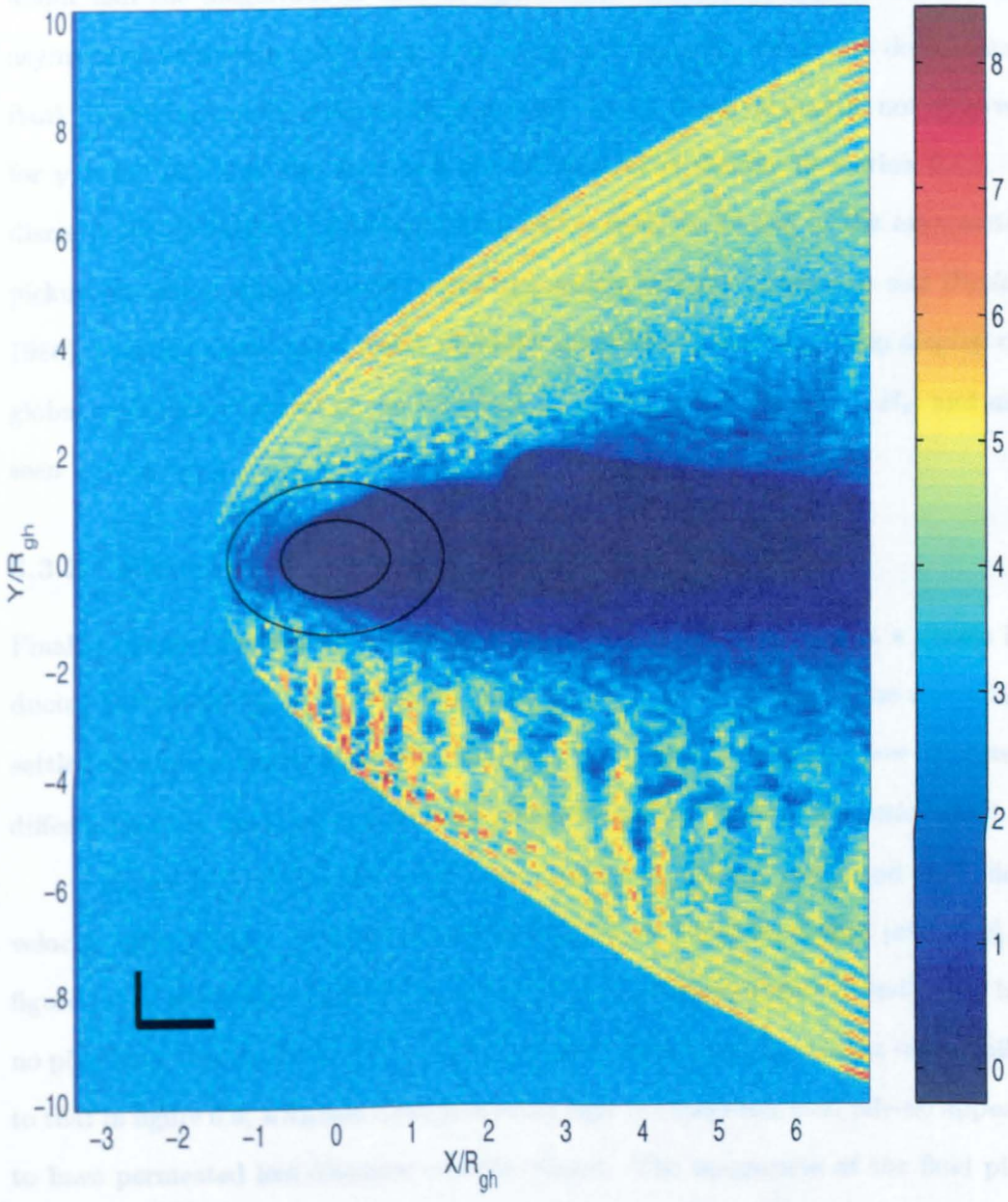

Figure 6.10: Current density carried by the SW protons in the x-direction, J_{px}, for the same simulation and time as in figure 6.9.

being formed. Figure 6.10 shows that the current density of protons now mainly flows behind the shock in the x-direction. A plot of J_{py} (not shown) peaks at about half the magnitude of that in figure 6.10. There also appears to be some asymmetry between $y > 0$ and $y < 0$ in figure 6.10, with the $y < 0$ downstream flank displaying a rippled structure in current density along its length, not observed for $y > 0$. This was also seen in a plot of total mass density in section 5.1.1. It disrupts the downstream standing waves and is likely to be due to the asymmetric pickup processes, which include lateral momentum transfer (*Chapman and Dunlop*, 1986), that are experienced under this IMF geometry. These plots also display the global asymmetry typical of the structure produced when $B_{IMF} = -B_z$, and also seen in Chapter 5.

6.3.2 Planet with an intrinsic magnetic field

Finally, results are presented of a simulation with $B_{IMF} = -B_z$ and a dipole inducing current of $J_{source} = 7.0$ in the planet. As the IMF is present, the simulation settled to a quasi-steady state after $720\Omega_p^{-1}$. The results, largely as now expected, differ little from the same run with no planetary current present in section 6.3.1.

Figure 6.11 shows the total mass density on a $\log_{10}$ scale and bulk flow velocity after $720\Omega_p^{-1}$. The structure differs only in detail from that presented in figure 5.1 of the same simulation as in section 6.3.1 with equivalent conditions, but no planetary current loop. The plot of B_z given in figure 6.12 also looks very similar to that in figure 6.9, with one difference being that the magnetic field pile-up appears to have permeated less distance into the planet. The magnitude of the field pile-up is the same. Figure 6.13 shows the planetary current loop by plotting J_{hx}, the current density due to heavy planetary ions in the x-direction. Of course, there are no ions actually within the planet, but the current is labeled as being carried by them numerically. The planetary ions are also seen to be stripped off by the SW

in the new two tail structure familiar from Chapter 5. These particles now carry a current sheet along the edge of the planetary wake, similarly to how the protons did when the IMF was neglected in section 6.2. They also carry current in the y-direction, but the magnitude is lower.

Finally, figure 6.14 shows a plot, comparable to figure 6.10 of J_{px}. Again, the overall structure remains identical, indicating the absence of any additional effect caused by the dipole inducing current. The waves observed in figure 6.10 behind the $y < 0$ shock flank have become more pronounced, however this could be coincidental. There are 13 such structures over a distance of roughly $6.5R_{gh} = 78\frac{v_A}{\Omega_p}$, giving an average wavelength of $6.0\frac{v_A}{\Omega_p}$. This is thus not identical to that of similar structures, thought to be like those in *Bogdanov et. al.* (1996), observed in figure 5.4. A plot of current density carried by the SW protons in the y-direction (not shown) gives a peak magnitude of only $|J_{py}| \sim 4.0$, with the structure similar to that in figure 6.14, without the $y < 0$ striations.

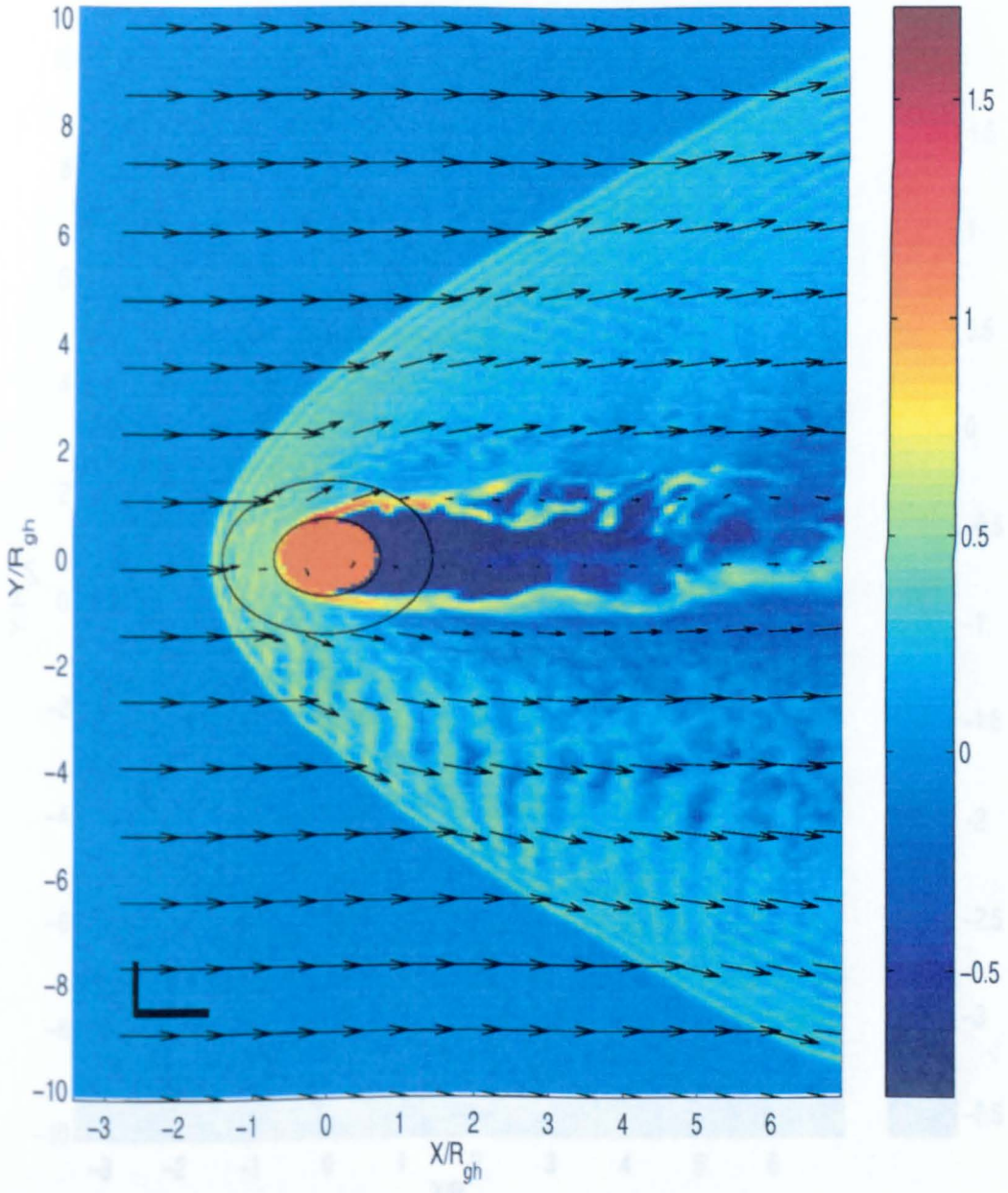

Figure 6.11: Total mass density using a $\log_{10}$ scale for a simulation like that in figures 6.9 and 6.10, except with the planetary current loop included. Arrows show bulk flow velocity. The simulation is in a quasi-steady state after $720\Omega_p^{-1}$.

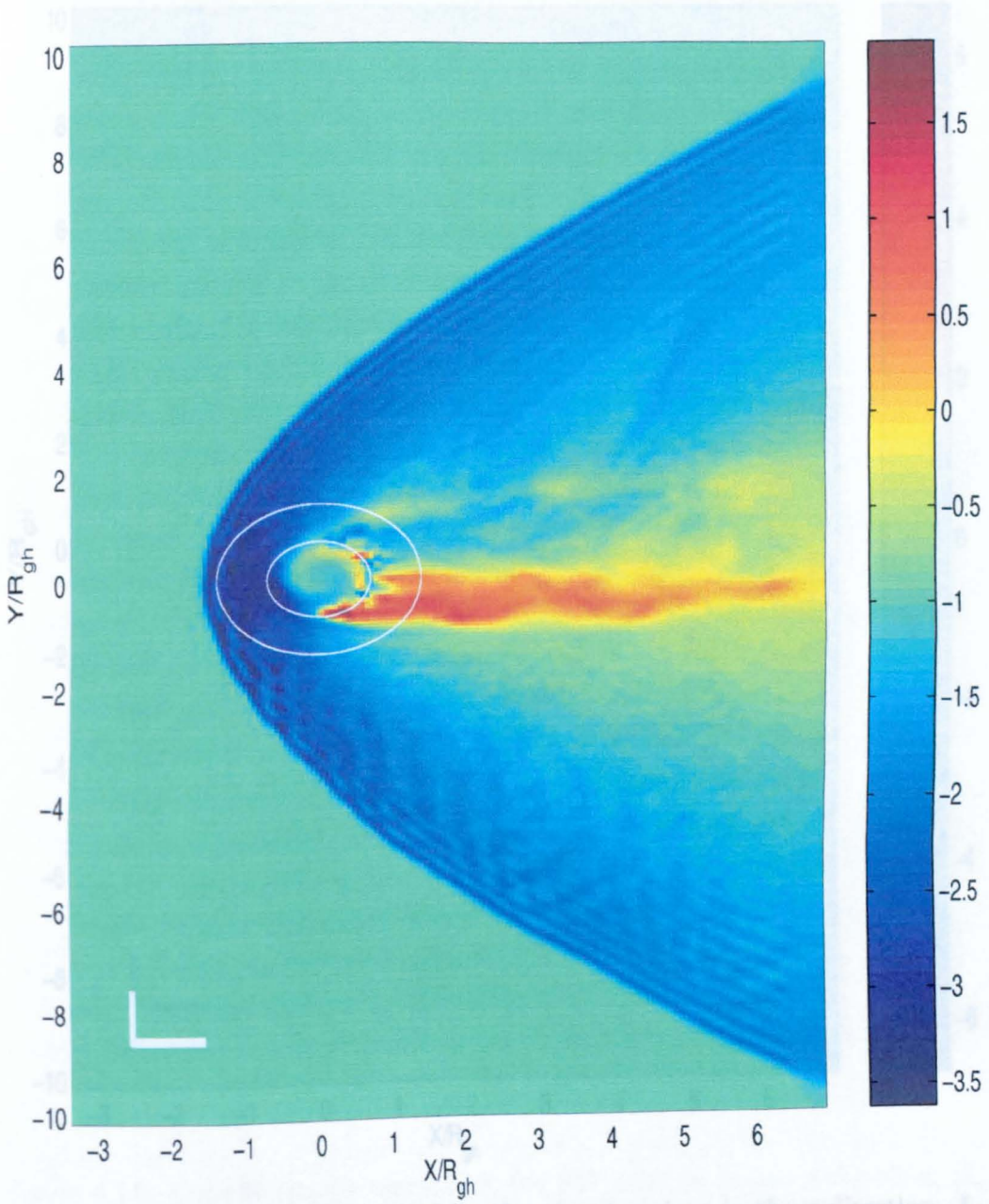

Figure 6.12: Plot of B_z for the same simulation and time as shown in figure 6.11.

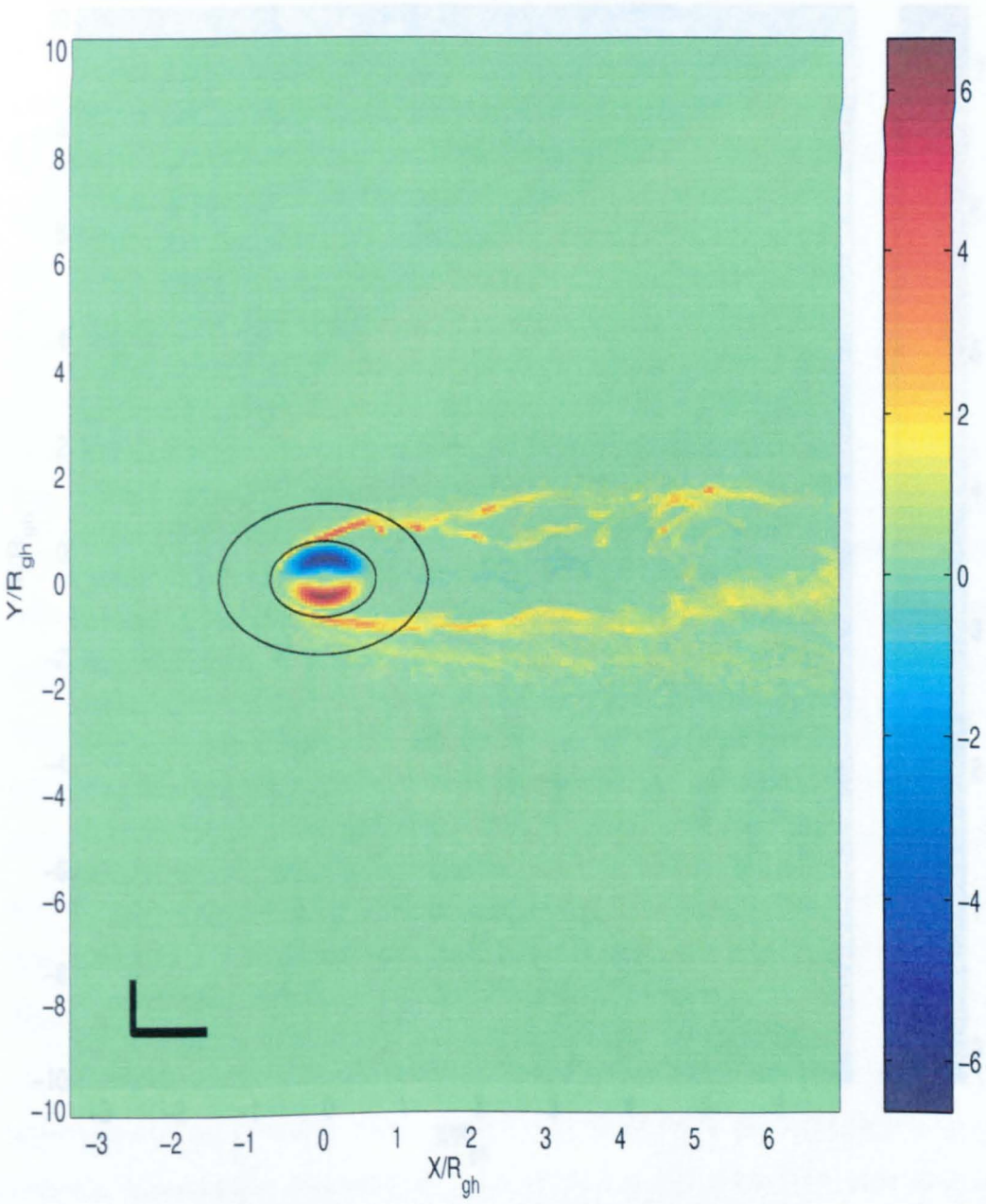

Figure 6.13: Current density carried by the planetary ions in the x-direction, J_{hx}, for the same simulation and time as in figure 6.11. The planetary current loop can now clearly be seen in the plot.

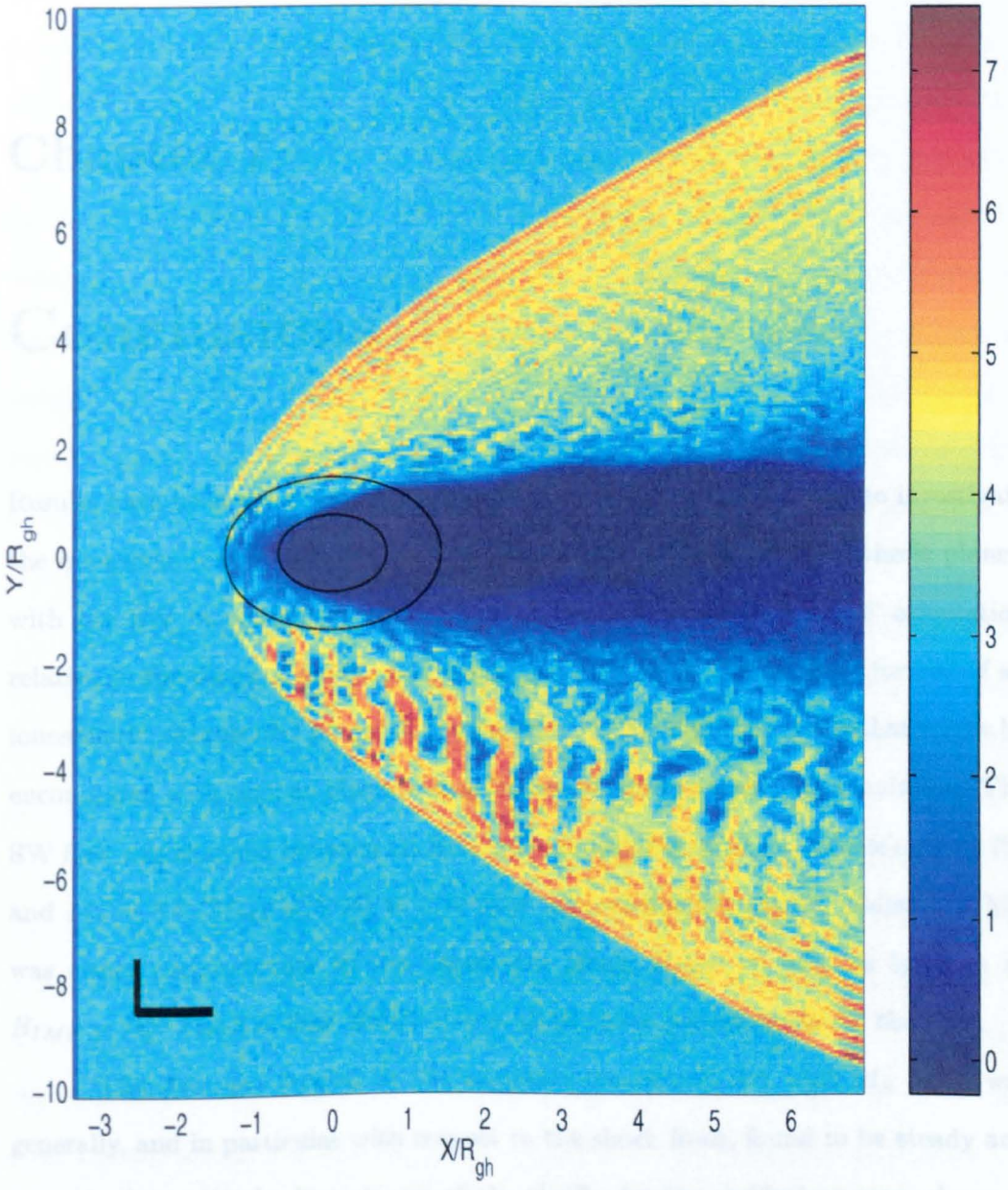

Figure 6.14: Current density carried by the SW protons in the x-direction, J_{px}, for the same simulation and time as in figure 6.11. Again, the structure remains globally similar to that in figure 6.10, despite the addition of the planetary current loop visible in figure 6.13. Notice also the downstream striations in the $y < 0$ half of the structure.

Chapter 7

Conclusions

Results have been presented of 2D hybrid numerical simulations used to investigate the interaction of two small scale sources; a comet and weakly ionospheric planet, with the SW in conditions which vary in both flow speed and IMF orientation relative to the plane of study. Additionally, a pilot study has been performed of an ionospheric, magnetized planet of similar scale, to highlight problems that might be encountered with such an obstacle in a future massively parallel 3D simulation. The SW flow was changed between an Alfvén Mach number of $M_A = 3.0$ ($M_{MS} = 2.75$) and $M_A = 6.6$ ($M_{MS} = 6.04$) to represent fast streams of plasma, whilst the IMF was either perpendicular to the simulation plane, $B_{IMF} = -B_z$, or lying in it, $B_{IMF} = B_y$. The SW flow direction was at all times perpendicular to the IMF.

The structure formed by the cometary obstacle in SW with $M_A = 3.0$ was generally, and in particular with respect to the shock front, found to be steady and smooth. Immediately downstream of the shock, density oscillations were observed which faded into low density lobe regions either side of a cometary ion tail. With $B_{IMF} = -B_z$ the tail had a much higher density due to a slower export speed of particles from the source, and incurred a KH instability. When this orientation of IMF was placed in $M_A = 6.6$ SW flow, the velocity shear between the tail

and surroundings was increased. The KH instability and global asymmetry due to preferential pickup ion motion therefore increased also, with the latter producing a "jet" upstream of the shock, of ions picked up in fast upstream flow. The shock remained intact, but much more disturbance was seen downstream of it. In this IMF orientation it could only be due to MS waves. When the IMF was positioned in the plane, $B_{IMF} = B_y$ such that waves with a component parallel to the magnetic field were possible, the disturbances again changed in nature, appearing on different length scales and being more prolific, spreading into the lobes. The shock became strongly perturbed in places and generally less clearly defined, importantly, even in regions with no cometary ion presence. Whistler waves appeared upstream of either flank. The location and direction of the disturbances suggests comparison to rays and other structures observed optically in comet tails.

Several of the observed features were discussed in the text and will be summarized here before conclusions are drawn on the nature of the interaction. A general trend was for the angle between the shock and flow to be slightly higher than that expected from fluid calculations — most probably due to an underestimate of the MS speed over the disturbed downstream region and an averaging of the flow velocity. The ripples observed immediately downstream of the shock even in the slow flow cases were shown not to be a result of proton reflection at the shock, as in *Burgess et. al.* (1989). Two acceleration mechanisms were present when $B_{IMF} = -B_z$, splitting the cometary ions into two sub-populations: the upstream pickup "jet" in flowing SW, and the majority in the slowly accelerated KH tail. This contrasted with the single mechanism when $B_{IMF} = B_y$, due to field line draping. It is also interesting to note the location of these simulations on the plot of *Bogdanov et. al.* (1996) (see figure 1.12, points (a) and (b)), and the clear presence of a BS in all cases here, compared to the "nonlinear structuring" classification expected at the higher SW flow speed from figure 1.12. Whilst the simulations performed in $M_A = 6.6$ flow

both show some nonlinear structure, the shocks present exclude a direct match to the work of *Bogdanov et. al.* (1996) (but see later planetary work).

By far the most important issue with the cometary results, however, is that of the evolving "turbulence" downstream throughout the simulations. As is the case throughout this thesis, the word "turbulence" is used in a loose sense. By examining the level of disturbance in each of the field orientations, several conclusions can be drawn about it:

1. It evolves in the presence of MS turbulence, as this first appears under fast flow conditions when $B_{IMF} = -B_z$.

2. The changed character of the turbulence when $B_{IMF} = B_y$ in fast flow implies wavemodes with a component of $\underline{k}$ parallel to $\underline{B}$ are involved, such as AIC waves.

3. Free energy is available to feed such waves from either the ring beam distribution of picked up cometary ions, or shock reflected SW protons.

4. The turbulence is present everywhere, even where no cometary ions are present, and so is either generated everywhere, or only at the nose region and requires a propagation means.

Of the two sources of energy mentioned, it is likely that the ring beam distribution of cometary ions is dominant in magnitude, and thus seems most likely. The waves must then be produced at the nose before propagating throughout. This could be via hybrid mode generation (*Treumann and Baumjohann*, 1997) and AIC propagation, or the resonant growth of AIC waves at the nose in the presence of MS waves, as described in *Winske and Gary* (1986). The latter method is considered more likely here as hybrid mode waves have not been observed: MS modes are clearly present in the $B_{IMF} = -B_z$ disturbances. According to *Winske and Gary*

(1986) the fastest growing modes would then depend on the density of unstable beam ions, here the cometary ions. This is seen to be extremely varied over the interaction region of these simulations, leading to the broadband disturbances. Finally, it is worth emphasizing that this mechanism does *not* depend on the cometary ions direct presence throughout, and as such could be seen at other obstacles.

The planetary simulations expanded the results of Chapter 4, by adding a particle absorbing planet to the source centre. The sharp boundary of this planetary region was later found to produce a small numerical error in the magnetic field in the tail. The slow flow case with $B_{IMF} = -B_z$ first displayed the new global structure shown schematically in figure 7.1. The tail is split into two, each with distinct characteristics: the UT experienced a KH instability, whilst the LT was straighter, and broader due to pickup motion. The wake was populated downstream of the planet within roughly $4R_{gh}$ whilst the global asymmetry remained due to pickup, especially noteworthy in the form of intriguing wave structures observed in the $y < 0$ half of the structure in both mass density and SW proton current plots. These are thought to be due to pickup effects. Most importantly, the ionosphere was seen to be peeled off by the IMF flowing past, a scenario repeated in the high flow speed simulation with the same IMF orientation. In this, many of the effects observed for the cometary case were also repeated: an upstream "jet" of particles picked up in fast flow; lower density tails due to faster export of particles from the source; increased KH effects in the UT; the onset of disturbances, presumably MS turbulence as before.

Interestingly, the LT also seemed to display density striations of a very similar wavelength to those observed in figure 1(b) of *Bogdanov et. al.* (1996). Again, it can be seen that the location of parameters here, point (d) in figure 1.12 after *Bogdanov et. al.* (1996) is very similar to their results, point (e). But why does the planetary simulation produce such similar structure in heavy ions, albeit with

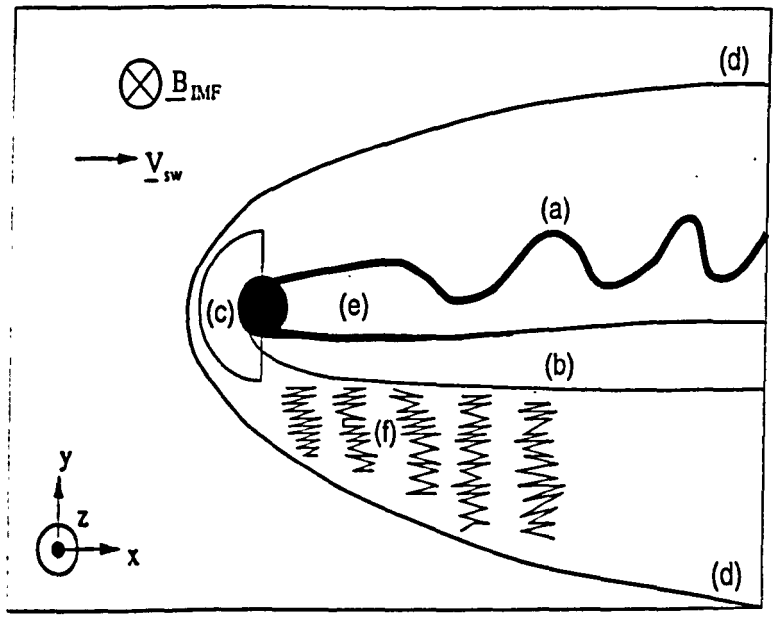

Figure 7.1: A schematic drawing of the structure obtained in planetary simulations with $M_A = 3.0$ and $B_{IMF} = -B_z$. At this speed the entire source exosphere is located behind the shock, so no upstream "jet" forms, unlike at high flow speeds. Labeled in the diagram are: (a) KH upper tail; (b) broader pickup lower tail; (c) planet and exospheric halo; (d) the asymmetric BS; (e) planetary wake; (f) wave structures in $y < 0$ half. Both (a) and (b) strip the planetary ionosphere and fill in the wake relatively quickly.

a shock still present, and the cometary simulation not? The answer must be in the source structure: the absorbing planet and split tail geometry results in the LT, which produces the striations, being effectively due to a weaker source than the cometary tail. Considered on its own, it is also more compact at its origin.

The fast flow, $B_{IMF} = B_y$ planetary simulation produced an instability. From the best results obtained, which were not quite quasi-steady, it appeared that the whistlers and disturbed shock, strongly perturbed in places, had continued from the cometary scenario. Additionally, a broad tail of sparse planetary ions formed: the only particles in a deep and long lasting downstream wake, supported by field line draping, which in this orientation proved severe. This, however, gave a striking image of "envelopes" of enhanced field magnitude draped over the planet and layered onto each other — another candidate for explaining ray type structure.

Eventually, however, all such simulations experienced instability, and although this remained a problem throughout, some tentative conclusions regarding its cause were made:

1. Allowing V_z to vary within the planet had little effect on the field pile-up, and none in stopping the instability (Usually $V_{x,y,z} = 0$ within the planet).

2. Varying the planetary density (fixed within a simulation) had a profound effect on the level of field pile-up and consequent global structure, in strong contrast to the $B_{IMF} = -B_z$ cases in which this produced little change. A lower density reduced field pile-up to levels matching those observed in the cometary case, but did not stop the instability.

3. Creating some ions on all sides of the obstacle so as to fill the wake achieved partial success in populating it, but failed to subsequently prevent the onset of instability.

Finally, simulations were performed as a pilot study for a future 3D sim-

ulation of an intrinsically magnetized planet with an ionosphere. Initially, it was important to gauge what magnetic fields and currents were produced with flow containing no IMF passing an unmagnetized planet. Predictably, the planetary ions were not picked up by the flow, but more importantly, four regions of alternately directed magnetic field formed immediately behind the planet, directed in $\pm B_z$, that extended down the wake, with the middle two soon cancelling. The remaining two were attached to the wake edge, where it was found the protons carried a current in the x-direction, generating the fields. From this it was found that a current of roughly $6.0\frac{v_A \rho_0 e}{m_p}$ generated a field of $2B_0$, where B_0 is what the scaled IMF would be. The same simulation with a current within the planet aimed at producing a planetary dipole field, gave no observable difference, such that it became clear that either the field was not able to penetrate the "frozen in" flow on the timescales concerned, or that the dipole field was not being produced correctly. With the IMF restored, the results were identical to those for the non-magnetized planetary simulations, with the wake fields still present, but dwarfed by the field jump at the shock. As the planetary ions were now stripped off the ionosphere and carried downstream, they produced the currents at the wake edges.

A future expansion of the code to 3D would necessarily imply a loss of resolution, but it is interesting for now to see what can be done in 2D. The cometary source has been comprehensively examined here and might only benefit from improved resolution or expansion of the simulation further downstream: both numerical limitations. Similar holds true for the $B_{IMF} = -B_z$ orientation of the planetary simulations, however the $B_{IMF} = B_y$ orientation clearly needs expanding to 3D. This would reduce the levels of field pile-up in a more physical way than crudely dropping the planetary density. Alternatively, a piecewise solution in the region of the low density wake, which surpasses the resolution of the current simulation, would help.

The pilot study of the interaction of a magnetized planet with the SW has helped prepare for the necessary 3D simulation which such a complex array of possible geometries needs. It has been shown that the scaling of the dipole strength, in particular, is difficult in 2D — a problem that would be solved by the absence of symmetry through z. The dipole representation was either unable to penetrate the SW in the pilot study, or its structure was flawed in 2D and requires more testing. Little information has been gained on its interaction with the IMF therefore. Either the timescale for penetration outside the planet must be increased or possibly a new generation mechanism for the planetary dipole is needed. However, it seems that such a study would be stable, at least with $B_{IMF} = -B_z$, and equilibrium would be attained.

Bibliography

Acuña, M. H., J. E. P. Connerney, P. Wasilewski, R. P. Lin, K. A. Anderson, C. W. Carlson, J. McFadden, D. W. Curtis, D. Mitchell, H. Rème, C. Mazelle, J. A. Sauvaud, C. d'Uston, A. Cros, J. L. Medale, S. J. Bauer, P. Cloutier, M. Mayhew, D. Winterhalter and N. F. Ness, Magnetic field and plasma observations at Mars: Initial results of the Mars Global Surveyor mission, *Science, 279*, p.1676, 1998.

Alonso, M. and E. J. Finn, Physics, *Addison-Wesley*, 1992.

Bagenal, F., Solar System Magnetic Fields, (Ed. E. R. Priest), *D. Reidel*, 1985.

Baumgärtel, K., K. Sauer and A. Bogdanov, A magnetohydrodynamic model of solar wind interaction with asteroid Gaspra, *Science, 263*, p.653, 1994.

Baumjohann, W. and R. A. Treumann, Basic Space Plasma Physics, *Imperial College Press*, 1996.

Bauske, R., A. F. Nagy, T. I. Gombosi, D. L. De Zeeuw, K. G. Powell and J. G. Luhmann, A three-dimensional MHD study of solar wind mass loading processes at Venus: Effects of photoionization, electron impact ionization, and charge exchange, *JGR, 103*, A10, p.23625, 1998.

Biermann, L., Kometenschweife und solare korpuskularstrahlung, *Zeitschrift für Astrophysik, 29*, p.274, 1951.

Birdsall, C. K. and A. B. Langdon, Plasma Physics via Computer Simulation, (Ed. E. W. Laing), *IOP*, 1991.

Bogdanov, A., K. Sauer, K. Baumgärtel and K. Srivastava, Plasma structures at weakly outgassing comets – results from bi-ion fluid analysis, *Planetary Space Science, 44*, 6, p.519, 1996.

Boyd, T. J. M. and J. J. Sanderson, Plasma Dynamics, *Thomas Nelson and Sons Limited*, 1969.

Brandt, J. C. and D. A. Mendis, Solar System Plasma Physics Volume 2: Magnetospheres, (Ed. E. N. Parker, C. F. Kennel and L. J. Lanzerotti), *North Holland Publishing Company*, 1979.

Brecht, S. H. and V. A. Thomas, Three-dimensional simulation of an active magnetospheric release, *JGR, 92*, A3, p.2289, 1987.

Brecht, S. H., J. R. Ferrante and J. G. Luhmann, Three-dimensional simulations of the solar wind interaction with Mars, *JGR, 98*, A2, p.1345, 1993.

Brecht, S. H., Shock formation at unmagnetized planets, *Advances in Space Research, 15*, 8/9, p.415, 1995.

Brecht, S. H.,Hybrid simulations of the magnetic topology of Mars, *JGR, 102*, A3, p.4743, 1997a.

Brecht, S. H., Solar wind proton deposition into the Martian atmosphere, *JGR, 102*, A6, p.11287, 1997b.

Burgess, D., W. P. Wilkinson and S. J. Schwartz, Ion distributions and thermalization at perpendicular and quasi-perpendicular supercritical collisionless shocks, *JGR, 94*, A7, p.8783, 1989.

Burgess, D., Foreshock-shock interaction at collisionless quasi-parallel shocks, *Advances in Space Research, 15*, 8/9, p.159, 1995.

Butler, B. J., D. O. Muhleman and M. A. Slade, Mercury: Full-disk radar images and the detection and stability of ice at the north pole, *JGR, 98*, E8, p.15003, 1993.

Chapman, S. C. and M. W. Dunlop, Ordering of momentum transfer along $\underline{V} \times \underline{B}$ in the AMPTE solar wind releases, *JGR, 91*, A7, p.8051, 1986.

Chapman, S. C. and S. J. Schwartz, One-dimensional hybrid simulations of boundary layer processes in the AMPTE solar wind Lithium releases, *JGR, 92*, A10, p.11059, 1987.

Chapman, S. C., Shock like behaviour exhibited at early times by the AMPTE solar wind/magnetosheath releases, *Planetary Space Science, 37*, 10, p.1227, 1989.

Chapman, S. C., Core Electrodynamics, *Taylor and Francis*, 2000.

Chen, F. F., Introduction to Plasma Physics and Controlled Fusion Volume 1: Plasma Physics, Second Edition, *Plenum Press*, 1984.

Cheng, A. F. and C. Paranicas, Implications of Io's magnetic signature: Ferromagnetism?, *GRL, 23*, 21, p.2879, 1996.

Choudhuri, A. R., The Physics of Fluids and Plasmas: an Introduction for Astrophysicists, *CUP*, 1998.

Cloutier, P. A., C. C. Law, D. H. Crider, P. W. Walker, Y. Chen, M. H. Acuña, J. E. P. Connerney, R. P. Lin, K. A. Anderson, D. L. Mitchell, C. W. Carlson, J. McFadden, D. A. Brain, H. Rème, C. Mazelle, J. A. Sauvaud, C. d'Uston, D. Vignes, S. J. Bauer and N. F. Ness, Venus-like interaction of the solar wind with Mars, *GRL, 26*, 17, p.2685, 1999.

Coates, A. J., A. D. Johnstone, D. E. Huddleston, B. Wilken, K. Jockers, H. Borg, E. Amata, V. Formisano, M. B. Bavassano-Cattaneo, J. D. Winningham, C. Gurgiolo and F. M. Neubauer, Pickup water group ions at comet Grigg-Skjellerup, *GRL 20*, 6, p.483, 1993.

Coates, A. J., A. D. Johnstone and F. M. Neubauer, Cometary ion pressure anisotropies at comets Halley and Grigg-Skjellerup, *JGR, 101*, A12, p.27573, 1996.

Coates, A. J., C. Mazelle and F. M. Neubauer, Bow shock analysis at comets Halley and Grigg-Skjellerup, *JGR, 102*, A4, p.7105, 1997.

Delamere, P. A., D. W. Swift and H. C. Stenbaek-Nielsen, A three-dimensional hybrid code simulation of the December 1984 solar wind AMPTE release, *GRL, 26*, 18, p.2837, 1999.

Delva, M. and E. Dubinin, Upstream ULF fluctuations near Mars, *JGR, 103*, A1, p.317, 1998.

Dubinin, E. and R. Lundin, Mass-loading near Mars, *Advances in Space Research, 16*, 4, p.75, 1995.

Dubinin, E., K. Sauer, R. Lundin, O. Norberg, J-G. Trotignon, K. Schwingenschuh, M. Devla and W. Riedler, Plasma characteristics of the boundary layer in the Martian magnetosphere, *JGR, 101*, A12, p.27061, 1996.

Dubouloz, N. and M. Scholer, On the origin of short large-amplitude magnetic structures upstream of quasi-parallel collisionless shocks, *GRL, 20*, 7, p.547, 1993.

Dubouloz, N. and M. Scholer, 2D Hybrid simulations of short large-amplitude magnetic structures (SLAMS) upstream of quasi-parallel collisionless shocks, *Advances in Space research, 15*, 8/9, p.175, 1995.

Dunne, J. A., Mariner 10 Mercury encounter, *and others in this issue, Science, 185*, p.141, 1974.

Fox, J. L., Upper limits to the outflow of ions at Mars: Implications for atmospheric evolution, *GRL, 24*, 22, p.2901, 1997.

Frank, L. A., W. R. Paterson, K. L. Ackerson, V. M. Vasyliunas, F. V. Coroniti and S. J. Bolton, Plasma observations at Io with the Galileo spacecraft, *Science, 274*, p.394, 1996.

Garcia, A. J., Numerical Methods for Physics, *Prentice-Hall*, 1994.

Giacalone, J., D. Burgess, S. J. Schwartz, D. C. Ellison and L. Bennett, Injection and acceleration of thermal protons at quasi-parallel shocks: A hybrid simulation parameter survey, *JGR, 102*, A9, p.19789, 1997.

Glassmeier, K. H., U. Motschmann, C. Mazelle, F. M. Neubauer, K. Sauer, S. A. Fuselier and M. H. Acuña, Mirror modes and fast magnetoacoustic waves near the magnetic pileup boundary of comet P/Halley, *JGR, 98*, A12, p.20955, 1993.

Goldstein, M. L. and D. A. Roberts, Magnetohydrodynamic turbulence in the solar wind, *Physics of Plasmas, 6*, 11, p.4154, 1999.

Gray, P. C., C. W. Smith, W. H. Matthaeus and N. F. Otani, Heating of the solar wind by pickup ion driven Alfvén ion cyclotron instability, *GRL, 23*, 2, p.113, 1996.

Hockney, R. W. and J. W. Eastwood, Computer Simulation Using Particles, *McGraw-Hill*, 1981.

Hopcroft, M. W. and S. C. Chapman, 2D Hybrid simulations of the solar wind interaction with a small scale comet in high Mach number flows, *GRL, 28*, 6, p.1115, 2001.

Horányi, M. and T. E. Cravens, The structure and dynamics of Jupiter's ring, *Nature, 381*, 6580, p.293, 1996.

Huddleston, D. E., A. J. Coates, A. D. Johnstone and F. M. Neubauer, Mass loading and velocity diffusion models for heavy pickup ions at comet Grigg-Skjellerup, *JGR, 98*, A12, p.20995, 1993a.

Huddleston, D. E., M. Neugebauer and B. E. Goldstein, Water group ion distributions in the midcometosheath of comet Halley, *JGR, 98*, A12, p.21039, 1993b.

Huddleston, D. E., M. Neugebauer and B. E. Goldstein, Modelling of pickup ion distributions in the Halley cometosheath: Empirical limits on rates of ionization, diffusion, loss and creation of fast neutral atoms, *JGR, 99*, A10, p.19245, 1994.

Israelevich, P. L., T. I. Gombosi, A. I. Ershkovich, D. L. DeZeeuw, F. M. Neubauer and K. G. Powell, The induced magnetosphere of comet Halley: 4. Comparison of *in situ* observations and numerical simulations, *JGR, 104*, A12, p.28309, 1999.

Johnstone, A. D., Solar System Magnetic Fields, (Ed. E. R. Priest), *D. Reidel*, 1985.

Johnstone, A. D., A. J. Coates, D. E. Huddleston, K. Jockers, B. Wilken, H. Borg, C. Gurgiolo, J. D. Winningham and E. Amata, Observations of the solar wind and cometary ions during the encounter between Giotto and comet P/Grigg-Skjellerup, *Astronomy and Astrophysics, 273*, 1, p.1, 1993.

Johnstone, A. D., Cometary ion pickup processes: Halley and Grigg-Skjellerup compared, *Advances in Space Research, 16*, 4, p.11, 1995.

Kallio, E., J. G. Luhmann and J. G. Lyon, Magnetic field near Venus: A comparison between Pioneer Venus Orbiter magnetic field observations and an MHD simulation, *JGR, 103*, A3, p.4723, 1998.

Kivelson, M. G., Z. Wang, S. Joy, K. K. Khurana, C. Polanskey, D. J. Southwood and R. J. Walker, Solar wind interaction with small bodies: 2. What can Galileo's detection of magnetic rotations tell us about Gaspra and Ida, *Advances in Space Research, 16*, 4, p.59, 1995.

Knudsen, W. C., Venus and Mars: Atmospheres, Ionospheres, and Solar Wind Interactions, (Ed. J. G. Luhmann, M. Tatrallyay and R. O. Pepin), *Geophysical Monograph 66, AGU*, 1992.

Kojima, H., H. Matsumoto, Y. Omura and B. T. Tsurutani, Nonlinear evolution of high frequency R-mode waves excited by water group ions near comets: Computer experiments, *GRL, 16*, 1, p.9, 1989.

Krall, N. A. and A. W. Trivelpiece, Principles of Plasma Physics, *San Francisco Press*, 1986.

Krankowsky, D., P. Lämmerzahl, I. Herrwerth, J. Woweries, P. Eberhardt, U. Dolder, U. Herrmann, W. Schulte, J. J. Berthelier, J. M. Illiano, R. R. Hodges and J. H. Hoffman, *In situ* gas and ion measurements at comet Halley, *Nature, 321*, 6067, p.326, 1986.

Krymskii, A. M., T. Breus and E. Nielsen, On possible observational evidence in electron density profiles of a magnetic field in the Martian ionosphere, *JGR, 100*, A3, p.3721, 1995.

Lammer, H. and S. J. Bauer, Mercury's exosphere: Origin of surface sputtering and implications, *Planetary Space Science, 45*, 1, p.73, 1997.

Leroy, M. M., C. C. Goodrich, D. Winske, C. S. Wu and K. Papadopoulos, Simulation of a perpendicular bow shock, *GRL, 8*, 12, p.1269, 1981.

Leroy, M. M., D. Winske, C. C. Goodrich, C. S. Wu and K. Papadopoulos, The structure of perpendicular bow shocks, *JGR, 87*, A7, p.5081, 1982.

Lipatov, A. S., K. Sauer and K. Baumgärtel, 2.5D Hybrid code simulation of the solar wind interaction with weak comets and related objects, *Advances in Space Research, 20*, 2, p.279, 1997.

Liu, Y., A. F. Nagy, C. P. T. Groth and K. G. Powell, 3D Multi-fluid MHD studies of the solar wind interaction with Mars, *GRL, 26*, 17, p.2689, 1999.

Luhmann, J. G., Physics of Magnetic Flux Ropes, (Ed. C. T. Russell, E. R. Priest and L. C. Lee), *AGU*, 1990.

Luhmann, J. G., Cometary Plasma Processes, (Ed. A. D. Johnstone), *Geophysical Monograph 61*, 1991.

Luhmann, J. G., C. T. Russell and N. A. Tsyganenko, Disturbances in Mercury's magnetosphere: Are the Mariner 10 "substorms" simply driven?, *JGR, 103*, A5, p.9113, 1998.

Mazelle, C., H. Rème, F. M. Neubauer and K. H. Glassmeier, Comparison of the main magnetic and plasma features in the environments of comets Grigg-Skjellerup and Halley, *Advances in Space Research, 16*, 4, p.41, 1995.

McKean, M. E., N. Omidi and D. Krauss-Varban, Wave and ion evolution downstream of quasi-perpendicular bow shocks, *JGR, 100*, A3, p.3427, 1995a.

McKean, M. E., N. Omidi, D. Krauss-Varban and H. Karimabadi, Wave and particle evolution downstream of quasi-perpendicular shocks, *Advances in Space Research, 15*, 8/9, p.319, 1995b.

Moore, K. R. and D. J. McComas, Venus and Mars: Atmospheres, Ionospheres, and

Solar Wind Interactions, (Ed.J. G. Luhmann, M. Tatrallyay and R. O. Pepin), *Geophysical Monograph 66, AGU*, 1992.

Murawski, K., D. C. Boice, W. F. Huebner and C. R. DeVore, Two-dimensional MHD simulations of the solar wind interaction with comet Halley, *Acta Astronomica, 48*, p.803, 1998.

Ness, N. F., K. W. Behannon, R. P. Lepping, Y. C. Whang and K. H. Schatten, Magnetic field observations near Mercury: Preliminary results from Mariner 10, *Science, 185*, p.151, 1974.

Ness, N. F., Solar system plasma physics III, (Ed. C. F. Kennel, L. J. Lanzarotti and E. N. Parker), *North-Holland*, 1979.

Neubauer, F. M., K. H. Glassmeier, A. J. Coates and A. D. Johnstone, Low-frequency electromagnetic plasma waves at comet P/Grigg-Skjellerup: Analysis and interpretation, *JGR, 98*, A12, p.20937, 1993.

Newbury, J. A., C. T. Russell and M. Gedalin, The ramp widths of high Mach number, quasi-perpendicular collisionless shocks, *JGR, 103*, A12, p.29581, 1998.

Ogilvie, K. W., J. D. Scudder, R. E. Hartle, G. L. Siscoe, H. S. Bridge, A. J. Lazarus, J. R. Asbridge, S. J. Bame and C. M. Yeates, Observations at Mercury encounter by the plasma science experiment on Mariner 10, *Science, 185*, p.145, 1974.

Ogilvie, K. W., M. A. Coplan, P. Bochsler and J. Geiss, Ion composition results during the International Cometary Explorer encounter with Giacobini-Zinner, *Science, 232*, p.374, 1986.

Ogino, T., R. J. Walker and M. Ashour-Abdalla, An MHD simulation of the interaction of the solar wind with the outflowing plasma from a comet, *GRL, 13*, 9, p.929, 1986.

Parks, G. K., Physics of Space Plasmas: An Introduction, *Addison-Wesley*, 1991.

Parker, E. N., Dynamics of the interplanetary gas and magnetic fields, *Asrophysical Journal, 128*, p.664, 1958.

Potter, A. E.,Chemical sputtering could produce sodium vapor and ice on Mercury, *GRL, 22*, 23, p.3289, 1995.

Press, W. H., B. P. Flannery, S. A. Teukolsky and W. T. Vetterling, Numerical Recipes - The art of Scientific Computing, *CUP*, 1986.

Queinnec, J. and P. Zarka, Io-controlled decameter arcs and Io-Jupiter interaction, *JGR, 103*, A11, p.26649, 1998.

Ray, T., Kelvin-Helmholtz instabilities in cometary ion tails, *Planetary Space Science, 30*, 3, p.245, 1982.

Reinhard, R., The Giotto encounter with comet Halley, *and others in this issue*, *Nature, 321*, 6067, p.313, 1986.

Rème, H., C. Mazelle, J. A. Sauvaud, C. D'Uston, F. Froment, R. P. Lin, K. A. Anderson, C. W. Carlson, D. E. Larson, A. Korth, P. Chaizy and D. A. Mendis, Electron plasma environment at comet Grigg-Skjellerup: General observations and comparison with the environment at comet Halley, *JGR, 98*, A12, p.20965, 1993.

Richardson, I. G., S. W. H. Cowley, R. J. Hynds, T. R. Sanderson, K. P. Wenzel and P. W. Daly, Three dimensional energetic ion bulk flows at comet P/Giacobini-Zinner, *GRL, 13*, 4, p.415, 1986.

Russell, C. T., R. C. Elphic and J. A. Slavin, Limits on the possible intrinsic magnetic field of Venus, *JGR, 85*, p.8319, 1980.

Russell, C. T., J. G. Luhmann, K. Schwingenschuh, W. Riedler and Y. Yeroshenko, Upstream waves at Mars: Phobos observations, *GRL, 17*, 6, p.897, 1990.

Russell, C. T., Venus and Mars: Atmospheres, Ionospheres, and Solar Wind Interactions, (Ed. J. G. Luhmann, M. Tatrallyay and R. O. Pepin), *Geophysical Monograph 66, AGU*, 1992.

Sauer, K., A. Bogdanov and K. Baumgärtel, Evidence of an ion composition boundary (protonopause) in bi-ion fluid simulations of solar wind mass loading, *GRL, 21*, 20, p.2255, 1994.

Sauer, K., A. Bogdanov and K. Baumgärtel, The protonopause - an ion composition boundary in the magnetosheath of comets, Venus and Mars, *Advances in Space Research, 16*, 4, p.153, 1995.

Sauer, K., A. Bogdanov, K. Baumgärtel and E. Dubinin, Plasma environment of comet Wirtanen during its low-activity stage, *Planetary Space Science, 44*, 7, p.715, 1996a.

Sauer, K., E. Dubinin, K. Baumgärtel and A. Bogdanov, Bow shock 'splitting' in bi-ion flows, *GRL, 23*, 24, p.3643, 1996b.

Sauer, K., A. Bogdanov, K. Baumgärtel and E. Dubinin, Bi-ion discontinuities at weak solar wind mass loading, *Physica Scripta, T63*, p.111, 1996.

Sauer, K. and E. Dubinin, Cometosheath structures and tail rays: Outcome of bi-ion fluid simulations, *Earth, Moon and Planets, 77*, p.271, 1999a.

Sauer, K., E. Dubinin, M. Dunlop, K. Baumgärtel and V. Tarasov, Low-frequency electromagnetic waves near and below the proton cyclotron frequency at the AMPTE Ba release: Relevance to comets and Mars, *JGR, 104*, A4, p.6763, 1999b.

Saunders, M. A. and C. T. Russell, Average dimension and magnetic structure of the distant Venus magnetotail, *JGR, 91*, p.5589, 1986.

Schmidt, H. U., R. Wegmann and F. M. Neubauer, MHD modelling applied to Giotto encounter with comet P/Grigg-Skjellerup, *JGR, 98*, A12, p.21009, 1993.

Scholer, M., Upstream waves, shocklets, short large-amplitude magnetic structures and the cyclic behaviour of oblique quasi-parallel collisionless shocks, *JGR, 98*, A1, p.47, 1993.

Scholer, M., M. Fujimoto and H. Kucharek, Two-dimensional simulations of supercritical quasi-parallel shocks: Upstream waves, downstream waves and shock re-formation, *JGR, 98*, A11, p.18971, 1993.

Scholer, M., H. Kucharek and V. Jayanti, Waves and turbulence in high Mach number nearly parallel collisionless shocks, *JGR, 102*, A5, p.9821, 1997.

Scholer, M. and H. Kucharek, Interaction of pickup ions with quasi-parallel shocks, *GRL, 26*, 1, p.29, 1999.

Schwartz, S. J., Solar System Magnetic Fields, (Ed. E. R. Priest), *D. Reidel*, 1985.

Scudder, J. D., A. Mangeney, C. Lacombe, C. C. Harvey, T. L. Aggson, R. R. Anderson, J. T. Gosling, G. Paschmann and C. T. Russell, The resolved layer of a collisionless, high-beta, supercritical, quasi-perpendicular shock-wave. 1. Rankine-Hugoniot geometry, currents, and stationarity, *JGR, 91*, A10, p.1019, 1986.

Shevchenko, V. I., V. D. Shapiro, S. K. Ride and M. Baine, Upstream wave activity at comet P/Grigg-Skjellerup, *JGR, 100*, A2, p.1735, 1995.

Siscoe, G. L. and L. Christopher, Variations in the solar wind stand-off distance at Mercury, *GRL, 2*, p.158, 1975.

Siscoe, G. L., N. F. Ness and C. M. Yeates, Substorms on Mercury, *JGR, 80*, p.4359, 1975.

Spreiter, J. R. and S. S. Stahara, Venus and Mars: Atmospheres, Ionospheres, and Solar Wind Interactions, (Ed. J. G. Luhmann, M. Tatrallyay and R. O. Pepin), *Geophysical Monograph 66, AGU*, 1992.

Srivastava, K. M., B. T. Tsurutani, B. E. Goldstein, V. Sharma and M. Okada, Acceleration of cometary H_2O group pickup ions by obliquely propagating nonlinear magnetosonic waves, *JGR, 98*, A12, p.21023, 1993.

Terasawa, T., M. Hoshino, J. Sakai and T. Hada, Decay instability of finite-amplitude circularly polarized Alfvén waves: A numerical simulation of stimulated Brillouin scattering, *and references therein*, *JGR, 91*, A4, p.4171, 1986.

Thomas, N., Detection of $O_{III}\lambda 5007$ emission from the Io plasma torus, *Astrophysical Journal, 414*, 1, p.L41, 1993a.

Thomas, N., The variability of the Io plasma torus, *JGR, 98*, E10, p.18737, 1993b.

Thomas, N., Ion temperatures in the Io plasma torus, *JGR, 100*, A5, p.7925, 1995.

Thomas, N., High resolution spectra of Io's neutral potassium and oxygen clouds, *Astronomy and Astrophysics, 313*, p.306, 1996.

Thomas, N. and G. Lichtenberg, The latitudinal dependence of ion temperature in the Io plasma torus, *GRL, 24*, 10, p.1175, 1997.

Treumann, R. A. and W. Baumjohann, Advanced Space Plasma Physics, *Imperial College Press*, 1997.

Tsurutani, B. T., R. M. Thorne, E. J. Smith, J. T. Gosling and H. Matsumoto, Steepened magnetosonic waves at comet Giacobini-Zinner, *JGR, 92*, A10, p.11074, 1987.

Tsurutani, B. T., E. J. Smith, A. L. Brinca, R. M. Thorne and H. Matsumoto, Properties of whistler mode wave packets at the leading edge of steepened magnetosonic waves: Comet Giacobini-Zinner, *Planetary Space Science, 37*, 2, p.167, 1989.

Vaisberg, O. L., Venus and Mars: Atmospheres, Ionospheres, and Solar Wind Interactions, (Ed. J. G. Luhmann, M. Tatrallyay and R. O. Pepin), *Geophysical Monograph 66, AGU*, 1992.

Valenzuela, A., G. Haerendel, H. Föppl, F. Melzner, H. Neuss, E. Reiger, J. Stöcker, O. Bauer, H. Höfner and J. Loidl, The AMPTE artificial comet experiments, *and others in this issue, Nature, 320*, 6064, p.700, 1986.

Verheest, F., G. S. Lakhina and B. T. Tsurutani, Intermediate electromagnetic turbulence at comets, *JGR, 104*, A11, p.24863, 1999.

Von Rosenvinge, T. T., J. C. Brandt and R. W. Farquhar, The International Cometary Explorer mission to comet Giacobini-Zinner, *and others in this issue, Science, 232*, p.353, 1986.

Wambecq, A., Rational Runge-Kutta methods for solving systems of ordinary differential equations, *Computing, 20*, p.333, 1978.

Wang, Z., M. G. Kivelson, S. Joy, K. K. Khurana, C. Polanskey, D. J. Southwood and R. J. Walker, Solar wind interaction with small bodies: 1. Whistler wing signatures near Galileo's closest approach to Gaspra and Ida, *Advances in Space research, 16*, 4, p.47, 1995.

Wang, Z. and M. G. Kivelson, Asteroid interaction with solar wind, *JGR, 101*, A11, p.24479, 1996.

Whipple, F., A comet model: 1. The acceleration of comet Encke, *Astrophysical Journal, 111*, p.375, 1950.

Winske, D., S. P. Gary, Electromagnetic instabilities driven by cool heavy ion beams, *JGR, 91*, A6, p.6825, 1986.

Woolliscroft, L. J. C., M. P. Gough, P. J. Christiansen, A. G. Darbyshire, H. G. F. Gough, D. S. Hall, D. Jones, S. R. Jones and A. J. Norris, Plasma waves and wave-particle interactions seen at the UKS spacecraft during the AMPTE artificial comet experiment, *Nature, 320*, 6064, p.716, 1986.

Zank, G. P., T. R. Story and F. M. Neubauer, The structure of mass loading shocks: 1. Comets, *JGR, 99*, A7, p.13335, 1994.

Paginated blank pages are scanned as found in original thesis

No information is missing